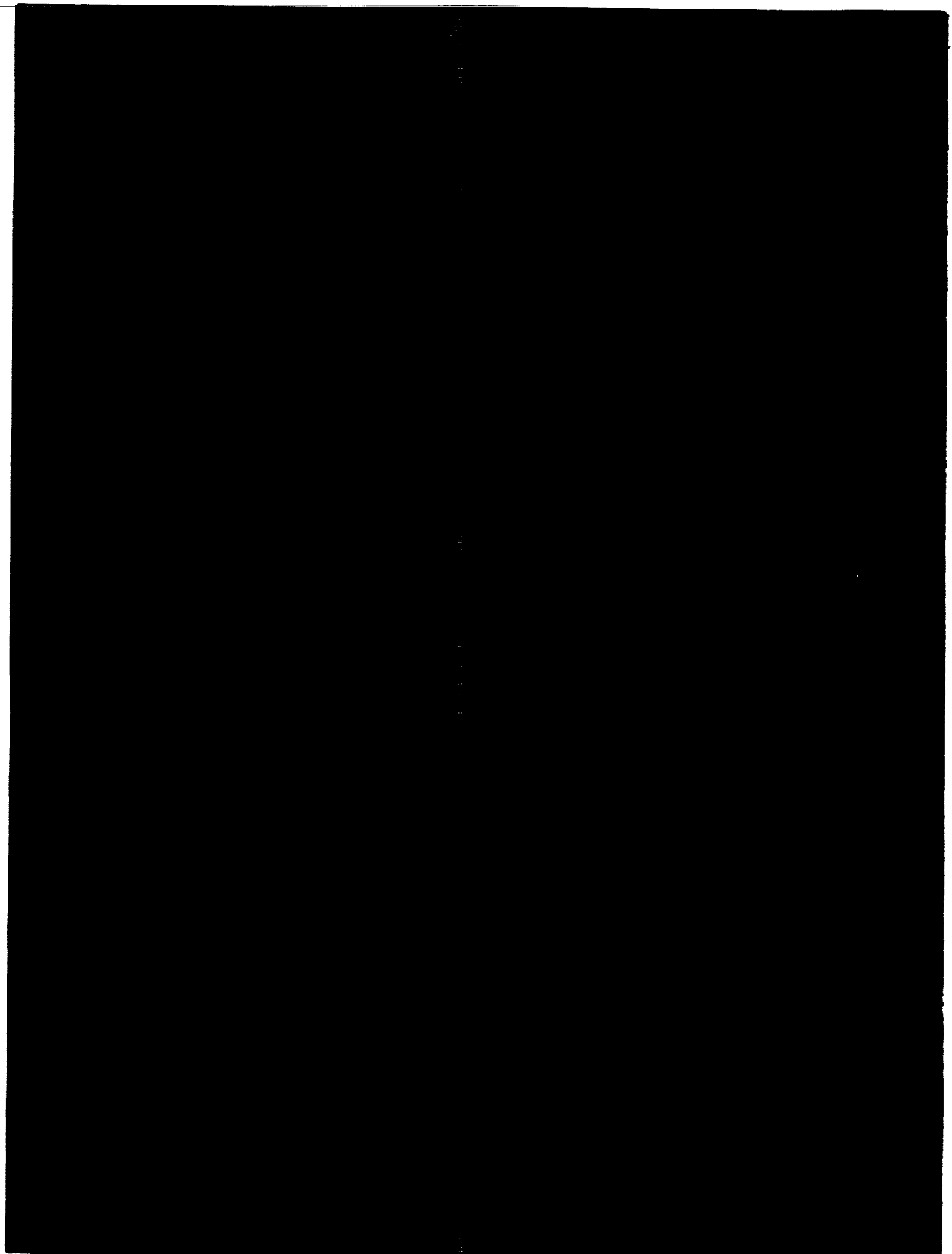

Damage Tolerance of Pressurized Graphite/Epoxy Tape Cylinders Under Uniaxial and Biaxial Loading

by

Stacy Marie Priest

Submitted to the Department of Aeronautics and Astronautics on January 14, 1994
in partial fulfillment of the requirements for the Degree of Master of Science.

ABSTRACT

The damage tolerance behavior of internally pressurized, axially slit, graphite/epoxy tape cylinders was investigated. Specifically, the effects of axial stress, structural anisotropy, and subcritical damage were considered. In addition, the limitations of a methodology which uses coupon fracture data to predict cylinder failure were explored. This predictive methodology was previously shown to be valid for quasi-isotropic fabric and tape cylinders but invalid for structurally anisotropic $[\pm 45/90]_s$ and $[\pm 45/0]_s$ cylinders. The effects of axial stress and structural anisotropy were assessed by testing tape cylinders with $[90/0/\pm 45]_s$, $[\pm 45/90]_s$, and $[\pm 45/0]_s$ layups in a uniaxial test apparatus, specially designed and built for this work, and comparing the results to previous tests conducted in biaxial loading. Structural anisotropy effects were also investigated by testing cylinders with the quasi-isotropic $[0/\pm 45/90]_s$ layup which is a stacking sequence variation of the previously tested $[90/0/\pm 45]_s$ layup with higher D_{16} and D_{26} terms but comparable D_{16} and D_{26} to D_{11} ratios. All cylinders tested and used for comparison are made from AS4/3501-6 graphite/epoxy tape and have a diameter of 305 mm. Cylinder slit lengths range from 12.7 to 50.8 mm. Failure pressures are lower for the uniaxially loaded cylinders in all cases. The smallest percent failure pressure decreases are observed for the $[\pm 45/90]_s$ cylinders, while the greatest such decreases are observed for the $[\pm 45/0]_s$ cylinders. The relative effects of the axial stress on the cylinder failure pressures do not correlate with the degree of structural coupling. The predictive methodology is not applicable for uniaxially loaded $[\pm 45/90]_s$ and $[\pm 45/0]_s$ cylinders, may be applicable for uniaxially loaded $[90/0/\pm 45]_s$ cylinders, and is applicable for the biaxially loaded $[90/0/\pm 45]_s$ and $[0/\pm 45/90]_s$ cylinders. This indicates that the ratios of D_{16} and D_{26} to D_{11}, as opposed to the absolute magnitudes of D_{16} and D_{26}, may be important in the failure of these cylinders and in the applicability of the methodology. Discontinuities observed in the slit tip hoop strains for all the cylinders tested indicate that subcritical damage can play an important role in the failure of tape cylinders. This role varies with layup and loading condition and is likely coupled to the effects of structural anisotropy. Biaxial failure pressures may exceed the uniaxial values because the axial stress contributes to the formation of 0° ply splitting (accompanied by delamination) or similar stress-mitigating subcritical damage. The failure behavior of similar cylinders can also vary as a result of differences in the role of subcritical damage as observed for the case of a biaxially loaded $[90/0/\pm 45]_s$ cylinder with a 12.7 mm slit. For this case, the methodology is valid when the initial coupon and cylinder fracture modes agree. However, the methodology underpredicts the failure pressure of the cylinder when a circumferential fracture path, suggestive of a 0° ply split, occurs at one slit tip. Thus, the failure behavior of some tape cylinders may be highly sensitive to the initial subcritical damage mechanism. Finite element analyses are recommended to determine how structural anisotropy and axial stress modify the slit tip stress states in cylinders from those found in flat plates since similarity of these stress states is a fundamental assumption of the current predictive methodology.

Thesis Supervisor: Professor Paul A. Lagace
Title: Associate Professor of Aeronautics and Astronautics

Acknowledgments

In the last two and a half years, I have been through some of the most difficult experiences of my life ranging from spending nine days in the hospital to losing my home in Hurricane Andrew. Somehow it seems fitting that during the most emotionally challenging period of my life I would also be at the best engineering school in the country working on the most ambitious intellectual undertaking that I've ever attempted. I'll probably never fully understand how I survived my time at MIT, but I certainly couldn't have done it without the encouragement and support of some very special people.

The manufacturing and testing of composite cylinders is a long, complicated, and labor-intensive process that requires a great deal of dedication and patience. This is why I am deeply grateful to everyone who participated in my experimental work. I especially want to thank my UROPers Kerry Forbes, Matt Libby, Malee Lucas, Michael Oh, and Corinne Ilvedson. I share this accomplishment with them and hope that they will remember their work on this project as a positive and worthwhile experience.

Several people I met during my undergraduate years at Georgia Tech continue to stay in touch and will always be an important part of my life. I want to thank Denise Martin, Kent Britton, Rich Franks, Del Brooks, Andy Johns, and Scott Olcott for the great memories and for caring enough to call me frequently while I was writing this monster thesis. Thanks to Del for patiently teaching me how to use a Mac toy at a time when I still hated them and frequently thought of throwing a heavy object at the screen.

I wish to thank Dr. Armanios at Georgia Tech for cultivating my interest in composites. It is because of his guidance and enthusiasm that I chose to specialize in composites and pursue my Master's degree at MIT.

I will dearly miss all of my friends from TELAC, but there are a few special names that I would like to mention here. To Aaron, Brian, Rich, Yew-Poh, and Mary, and especially to Hari, Wilson, Narendra, and Steve, thanks for being there for me during some rough times, for helping me immeasurably, and for making me happy (which isn't easy to do).

Several of my friends from MIT deserve special recognition for their contributions to this effort. Thanks to Debbie Bowser for helping me keep track of Paul and to Ping Lee for taking care of the money. I thank Don and Earle in the Aero Projects Lab for teaching me how to put precision holes in large pieces of metal and for helping me to manufacture the uniaxial test apparatus. I am deeply grateful to Al Supple for teaching me how to be a practical engineer and for helping me to overcome my fear of the large, noisy machines in the basement of Building 37.

I thank my advisor, Paul Lagace, for being a mentor as well as a good friend. I think this project took a couple of years off of both of our lives, but I'm happy to say that, largely as a result of Paul's efforts, I emerged from this experience a little bit stronger, a little bit more confident, and much more competent as an engineer.

I can never fully express my gratitude to my family, and especially to my parents, for their love and support throughout the years. I just want my family to know that I am as proud of them as they are of me and that it is because of them that I have been able to succeed.

I dedicate this thesis to David Tew who is probably the kindest person I've ever known. His endless patience and support throughout this experience will always be deeply appreciated and he will always have a special place in my heart.

Foreword

The research described herein was conducted in the Technology Laboratory for Advanced Composites (TELAC) of the Department of Aeronautics and Astronautics at the Massachusetts Institute of Technology. This investigation was sponsored by the NASA Langley Research Center under NASA Grant NAG-1-991.

Additional support was provided by the National Science Foundation through a Graduate Research Fellowship. Any opinions, findings, conclusions, or recommendations expressed in this thesis are those of the author and do not necessarily reflect the views of the National Science Foundation.

Table of Contents

List of Figures

List of Tables

Nomenclature

a	Half-notch length perpendicular to loading direction in coupon or half-slit length in axially-slit cylinder
a_o	Characteristic length from Whitney-Nuismer Average Stress Criterion
D_{ij}	Terms in bending stiffness matrix from Classical Laminated Plate Theory
d_o	Characteristic length from Whitney-Nuismer Point Stress Criterion
E	Extensional modulus of isotropic or quasi-isotropic material
E_L	Longitudinal extensional modulus
E_T	Transverse extensional modulus
E_{11}	Hoop direction extensional modulus in cylinder
G	Shear modulus of isotropic or quasi-isotropic material
G_{LT}	Shear modulus
H_c	Composite fracture parameter from Mar-Lin equation
K_{Ic}	Critical stress intensity factor for cracked plate in Mode I loading
K_I^e	Folias curvature correction factor for extensional stresses perpendicular to axial slit in cylinder
K_{Icyl}^e	Folias extensional stress intensity factor for isotropic cylinder with axial crack
K_{Iplate}^e	Stress intensity factor for cracked plate in Mode I loading
L	Cylinder length
L''	Overall length of cylinder angle ply
m	Order of stress singularity at fiber/matrix interface and exponent of Mar-Lin equation

p	Internal cylinder pressure
P	Cylinder circumference
$p_{f\,cyl}$	Cylinder failure pressure
$p_{f\,plate}$	Far-field plate failure stress expressed as equivalent cylinder failure pressure
r	Cylinder radius
t	Laminate thickness
t_{ply}	Ply thickness
W	Overall width of cylinder angle ply
δ	Orthotropy parameter used to calculate specially orthotropic shell parameter
ε_{11}	Hoop direction extensional strain in cylinder
ε_{22}	Axial direction extensional strain in cylinder
ε_{12}	Shear strain in cylinder
ζ	Ratio of slit length to extended slit length in Whitney-Nuismer Point and Average Stress Criteria
θ	Cylinder ply angle
λ_i	Isotropic shell parameter
λ_o	Specially orthotropic shell parameter
ν	Poisson's ratio of isotropic or quasi-isotropic material or geometric mean of major and minor Poisson's ratios
ν_{LT}	Major Poisson's ratio
ν_{TL}	Minor Poisson's ratio
ν_{12}	Major Poisson's ratio of cylinder
σ_e	Far-field effectively applied hoop stress in cylinder or far-field applied tensile stress in plate

σ_f Far-field failure stress of notched plate

σ_o Far-field failure stress of unnotched plate

$\sigma^e_{f\,cyl}$ Far-field hoop direction extensional stress at failure of cylinder with slit

$\sigma^e_{f\,plate}$ Far-field failure stress of plate with slit

σ_{11} Hoop direction extensional stress in cylinder

σ_{22} Axial direction extensional stress in cylinder

σ_{12} Shear stress in cylinder

CHAPTER 1

Introduction

Recent years have brought an increase in the demand for advanced, fiber-reinforced composite materials, especially graphite/epoxy, in the aerospace industry. The many benefits of composites, such as their high specific stiffness and strength, their high fatigue and corrosion resistance, and the ability to tailor their properties to specific applications, are well-recognized and appreciated. However, the use of composites in the aerospace industry has not reached initial expectations, due both to the high cost of materials and their manufacture as well as the risk associated with a fundamental lack of understanding of much of the behavior of composite structures and a lack of analytical tools with which to predict this behavior.

One area of particular importance in the use of composites is damage tolerance, or the ability of a structure to continue to perform after it experiences damage. Currently, damage tolerant design of composite structures relies heavily on expensive and time-consuming experimentation to determine needed properties and ensure the high level of safety that is required, especially if these structures are used for aerospace applications. A better understanding of the effects of damage on the performance of composite structures and better analytical tools to predict this performance are required to make composites more economical and trustworthy, and to allow composites to be utilized to their maximum potential.

Damage tolerant design is inherently more complicated for composite structures than for structures made from conventional materials, such as isotropic metals. Composites are laminated, inhomogeneous, and generally

orthotropic to anisotropic in nature. This results in a more complicated loading response and more varied failure modes than in the isotropic and homogeneous case. Damage in composites can take on many forms, such as matrix cracking, fiber breakage, and interply delamination, and it is still unclear as to how these damage types individually affect residual strength and how they interact to cause ultimate failure of a composite structure. It is known, however, that the types of damage that occur and the interaction of this damage are highly dependent on the loading condition, the structural geometry, and the nature of the stress-raiser in the structure where the damage initiates.

Damage tolerant design using composites is further complicated by many factors including the susceptibility of composites to manufacturing defects, the difficulties in locating damage using nondestructive inspection, the notch sensitivity that composites have been shown to exhibit, and the numerous notches and cutouts that most structures contain as part of their function but which serve as stress concentrations in the material. In order to understand the damage tolerant behavior of composites and eventually develop tools to predict this behavior, it is obvious that many effects must be considered and isolated. One approach to this is to consider a known structural defect and to determine the effect of structural geometry, loading condition, and material system on the failure stress and the initial fracture path.

The internally pressurized, thin-walled cylinder is a structure of particular importance to the aerospace industry because of its similarity to a transport aircraft fuselage. Transport aircraft manufacturers have shown great interest in using composites for fuselage structure due to the potential for large cost and weight savings. The relative benefits of the application of

composites to the fuselage are higher than those for other components, since the fuselage of a typical large transport aircraft currently accounts for the greatest cost per pound of structure and can represent as much as 40% of the total structural weight [1]. Realizing the potential advantages of composites use for fuselage structure, Boeing and NASA initiated the Advanced Technology Composite Aircraft Structure (ATCAS) program, with the stated objective to "Develop an integrated technology and demonstrate a confidence level that permits the cost and weight-effective use of advanced composite materials in transport fuselage structures for future aircraft" [2]. ATCAS is funded through the NASA Advanced Composite Technology (ACT) program and receives technical support from NASA Langley and industrial and university subcontractors. Since an especially critical technical issue identified by the ATCAS program is to understand the damage tolerance behavior of composite fuselages, research concerning the damage tolerance behavior of internally pressurized graphite/epoxy cylinders is highly appropriate and timely. Additional justification for this type of research stems from the fact that the Beech Starship, a small transport aircraft, was certified with an all-composite graphite/epoxy fuselage. The Learfan 2100, which did not go into production, also contained graphite/epoxy composites in its fuselage structure. Fuselages contain many windows, doors, and other required cutouts which are part of their function, and may experience damage during flight and ground operations from rock impacts, turbine blade punctures, mishandled tools, or other unforeseen events. Thus, the diversity and quantity of potential stress concentration points, or potential damage initiation sites, in fuselages makes predicting the damage tolerance behavior of these structures particularly challenging and important. Research concerning the damage tolerance of composite cylinders is also applicable to

other pressurized structures of this general shape including rocket motor casings, fuel tanks, and oil pipelines.

A methodology has been developed which allows the failure pressures of notched, internally pressurized composite cylinders to be predicted from notched coupon fracture data and the material properties [3]. This methodology, which assumes that the stress state responsible for fracture at the notch tip is comparable for the cylinder and coupon, accounts for a difference in stress intensity between the two specimen types that is basically of geometric origin. This type of approach is highly preferable to one that attempts to directly characterize cylinder failure, since cylinder analyses and tests are very costly and difficult to implement compared to those for coupons. The methodology was originally developed, and has been verified, for quasi-isotropic fabric cylinders. An investigation has also been undertaken to assess the applicability of the methodology to quasi-isotropic and structurally anisotropic tape cylinders [4]. The results of this investigation suggest that more work is needed to isolate and understand effects in some of these cylinders that are neglected by the predictive methodology and, therefore, cause the methodology to be invalid in the general case. Once more is known about these effects, it is possible that they may be incorporated into a similar predictive methodology that can be used for composite cylinders of general configuration.

Thus, in the present investigation, the limitations of using this methodology to predict failure in quasi-isotropic and structurally anisotropic tape cylinders are further explored, primarily through a change in loading condition on the previously tested cylinders. Failure stresses for coupons with through-thickness slits from tests in the past and current investigations are used to predict the failure pressures of graphite/epoxy AS4/3501-6 tape

cylinders with axial slits. In order to understand how axial stresses, which are ignored in the predictive methodology, may affect the failure of tape cylinders, these cylinders are tested to failure in uniaxial (hoop) loading using a test apparatus that was designed and built especially for this investigation. The failure pressures of these uniaxially loaded cylinders are compared to the predicted values as well as to the experimentally obtained values from the past investigation for a biaxial loading condition. Additionally, the failure modes of these cylinders are compared to those of the coupons and biaxially loaded cylinders with the same layups. In a second approach used in this investigation, the stacking sequence is varied for the previously tested quasi-isotropic layup to increase the degree of anisotropy with respect to the bending properties of the laminate, and coupon and cylinder tests are used to determine the effects on the fracture behavior as well as on the applicability of the predictive methodology.

Previous experiments and analyses which are relevant to the current investigation are summarized in Chapter 2. Particular emphasis is given to experiments involving the failure prediction methodology for cylinders, which is also described in detail in this chapter. The problem definition, experimental goals, and test plan for the current investigation, as well as descriptions of the test specimens, are provided in Chapter 3. A summary of the failure prediction methodology for cylinders is also contained in this chapter. Experimental procedures for manufacturing, instrumenting, and testing composite cylinders and coupons are described in Chapter 4. However, all aspects of these procedures which are specific to the uniaxial loading of cylinders are reserved for Chapter 5, where a full description of the uniaxial test apparatus is provided. All results for the current investigation are provided in Chapter 6, followed by discussion in Chapter 7, including

comparisons with past results and possible explanations. In Chapter 8, the conclusions of the present investigation are summarized and recommendations are made for further work. An appendix follows with tabulated experimental data from the current investigation.

CHAPTER 2

Background

Experiments and analyses that have been conducted to understand damage tolerance behavior in composite plates and shells are briefly described in this chapter. Related theories and analytical tools which characterize the stress state responsible for fracture and aid in failure prediction in composite and isotropic materials are also presented. Both plates and shells are considered since the failure prediction methodology considered in this investigation utilizes flat plate failure behavior to predict failure in a pressurized cylinder.

2.1 Notched Flat Plates in Tension

Numerous models have been proposed to predict failure in composite plates with various types of notches, especially slits and holes. The variety in the models and techniques used to characterize failure in composites is, in part, a result of the complexity and diversity of the failure modes in these materials and the lack of consensus on the proper set of failure criteria to be used. Also, no one model has been shown to have general applicability to a wide range of composite laminates.

Initially, attempts were made to directly apply the well-established Linear Elastic Fracture Mechanics (LEFM) techniques to composites with discouraging results. LEFM was developed to model the failure of homogeneous, isotropic materials with through-thickness cracks, where failure implies a colinear, self-similar crack extension. The far-field failure stress, σ_f, of a cracked plate is given by the equation:

$$\sigma_f = K_{Ic} (\pi a)^{-0.5} \tag{2.1}$$

where K_{Ic} is the critical stress intensity factor, or fracture toughness, of the material in Mode I loading, a is the half-crack length, and 0.5 is the order of the stress singularity at the crack tip. Problems arise when applying this equation to composites since composites generally violate the fundamental assumption of self-similar crack growth [5], and the order of the stress singularity on a microscopic level is known to be a function of the material system [6]. Most results to date indicate that the LEFM techniques for the in-plane fracture of composite laminates are only valid for very limited cases [5].

In an attempt to maintain the simplicity and ease of implementation of LEFM techniques, many 'modified,' semi-empirical LEFM approaches for composites have also been proposed. The problem with these failure prediction models is that they ignore the complex micro- and macro-damage interaction in the crack-tip damage zone that leads to crack extension in composites. Some of the LEFM models and expanded LEFM models that have been applied to composites have bypassed the details of the damage state surrounding the crack tip by simulating the damage as an 'effective' zone which is then assumed to increase in a self-similar manner. Since it is very difficult to determine the actual stress state in the damaged area ahead of the crack tip, these models are usually based on approximate stress distributions. Other models have also been proposed which rely on the elastic stress distributions but do not involve LEFM techniques.

The numerous empirically based methods to predict the failure strength of notched composite laminates are generally limited to uniaxial

loadings and involve parameters which are a function of the lamination geometry. Thus, in order to lend operational generality and allow more complex loading conditions to be considered, pure analytical methods, such as progressive failure prediction via finite element modeling, have also been pursued [7]. In this type of approach, the ply properties, lamination geometry, loading conditions, and crack length are treated as input parameters to the model and a failure criterion is utilized to determine when a localized ply failure occurs. Each progressive ply failure is accompanied by stiffness degradation in the model and corresponding stress redistributions until the ultimate failure of the laminate occurs. In order to maintain the tractability of the analysis, simplifying assumptions are introduced concerning the types and sizes of ply damage that are induced and the corresponding effects of this damage on the stresses and stiffnesses. The validity of this type of progressive failure analysis for certain configurations has been demonstrated experimentally for flat composite laminates under several loading conditions with both through-thickness cracks and holes [7]. However, these methods are computationally expensive and are currently employed much less frequently than the experimentally based techniques.

Awerbuch and Madhukar [5] have reviewed many of the available and commonly used techniques for modeling failure in composite laminates. They emphasized semi-empirical fracture models that are easy to implement and comparisons were made with extensive experimental data to assess the applicability of the models. Two of these techniques which represent different and relatively successful approaches to predicting composite failure are summarized in this section. The method of Mar and Lin [8] is emphasized, since this is the method that is employed in the current investigation. The method of Whitney and Nuismer [9] is also discussed,

since this method has also been used as part of a failure prediction methodology for pressurized composite cylinders.

Mar and Lin [8] modified the basic Linear Elastic Fracture Mechanics equation for use with composites. Following several investigators, such as Corten [10], who suggested that the exponent of 0.5 in the classical equation was inappropriate for composites, Mar and Lin proposed a new exponent, m, to account for the inhomogeneity of the material. The resulting equation for the failure stress of a notched composite coupon under uniaxial loading has the form:

$$\sigma_f = H_c\,(2a)^{-m} \tag{2.2}$$

where σ_f is the far-field stress at failure, 2a is the notch length perpendicular to the loading direction, and H_c is the composite fracture parameter [11]. Note that unlike the LEFM equation, the Mar-Lin equation is applicable for more notch shapes than just slits oriented perpendicular to the loading direction, as has been demonstrated in numerous experiments involving holes and angled slits [11-16]. This, of course, is a consequence of the notch sensitivity that composites have been shown to exhibit. It is also important to understand that this theory implies that the failure stress of a given coupon depends only on the length of the notch measured perpendicular to the loading direction and not on the notch geometry. This assertion has also been verified experimentally [14].

Mar and Lin proposed that the new exponent, m, is the value of the stress singularity at the tip of a discontinuity lying at a fiber/matrix interface. Fenner [6] used a micromechanical approach to solve for this stress singularity and he determined that m is a function of the ratio of the shear

moduli of the constituent materials as well as their respective Poisson's ratios. The theoretical value of m for graphite/epoxy, as originally determined for AS1/3501-6 from the Fenner solution, is 0.28. This value of m is valid for both fabric and tape systems since the value depends only on the properties of the fiber and matrix and not on their arrangement in the laminate [15]. The appropriateness of the use of the theoretical value of 0.28 for m has been experimentally verified for graphite/epoxy laminates with both holes and slits that were made from AS1/3501-6 and AS4/3501-6 fabric and tape material systems [4, 11-13, 15, 17].

The composite fracture parameter, H_c, is somewhat analogous to the fracture toughness, K_{Ic}, of isotropic materials. However, H_c is not called the composite fracture toughness since it is presently used for composites only to curve-fit the experimental data [11]. These two variables also have different units, due to the difference between the exponents of the two equations in which the variables appear. The composite fracture parameter is dependent on the laminate and stacking sequence. However, numerous investigations have shown that the value is invariant with notch geometry [3, 12, 15].

The Mar-Lin equation has been used in several investigations to correlate the failure stresses of fabric and tape coupons with different notch types. The majority of these investigations have involved graphite/epoxy material systems and notches in the form of holes, slits, and angled slits. In most cases, the Mar-Lin equation was shown to be a good correlative model for the experimental failure stresses. However, Lagace has noted that the Mar-Lin equation may not be valid for laminate failures in which delamination or out-of-plane effects are important [11].

Utilizing a different approach, Whitney and Nuismer [9] proposed two criteria to predict the failure of uniaxially loaded composite coupons with

through-thickness notches. These criteria were used to develop failure models which rely on the exact stress distribution near the notch, but do not involve LEFM techniques. The first, known as the Point Stress Criterion, assumes that failure will occur when the stress at a characteristic distance from the notch tip, d_o, reaches or exceeds the unnotched strength of the laminate. The characteristic distance, d_o, is analogous to the plastic process zone length at the tips of notches in metals, and it represents the distance over which the material must be critically stressed in order for failure to occur. The second, known as the Average Stress Criterion, assumes that failure occurs when the average stress over another critical distance from the notch tip, a_o, equals the unnotched laminate strength. The basis for this criterion is the assumption that the material can redistribute the stress concentration at the notch tip through local failure. Thus, a_o approximates the distance from the notch tip over which local damage is assumed to have occurred. Both of the characteristic dimensions, d_o and a_o, were originally assumed to be material properties that were independent of the laminate construction and stress distribution. However, experiments have shown that these parameters can also be a function of layup [5].

Whitney and Nuismer's proposed failure models using the Point Stress and Average Stress Criteria take on different forms for different notch geometries since the stress field near a notch is modified by a change in notch geometry. For through-thickness slits using the Point Stress Criterion, the far-field failure stress, σ_f, can be determined from the equation:

$$\sigma_f = \sigma_o \left[1 - \zeta^2\right]^{0.5}. \tag{2.3}$$

Using the Average Stress Criterion this equation becomes:

$$\sigma_f = \sigma_o \left[\frac{1-\zeta}{1+\zeta}\right]^{0.5}. \qquad (2.4)$$

In both equations, σ_o is the unnotched fracture stress and ζ is the ratio of the slit length, 2a, to the extended slit length, $2(a+d_o)$ or $2(a+a_o)$, depending on which criterion is being used. The unnotched strength and characteristic dimension are experimentally determined for both models in order to correlate the coupon failure data.

Like the Mar-Lin equation, the Whitney-Nuismer equations have been shown to be good correlative models for notched coupon failure stresses [5, 11, 12]. This should be expected since these methods are semi-empirical and essentially provide a curve-fit to the experimental data. The Mar-Lin model is more general, since it is independent of notch geometry, but in some cases the Whitney-Nuismer models have provided a better correlation to the experimental data. Furthermore, it should be noted that the Mar-Lin model requires one material parameter, m, and one laminate parameter, H_c, while the Whitney-Nuismer models each require two laminate parameters, σ_o and a_o or d_o.

2.2 Curvature Correction Factors for Notched Pressurized Shells

The state of stress near a notch is inherently more complicated in a pressurized shell than in a similarly loaded flat plate (under in-plane and uniform lateral loading) due to geometrical effects. In the flat plate case, the differential equations governing the stress and displacement functions are uncoupled and, thus, the extensional and bending problems may be treated

separately. In contrast, the governing differential equations for a shell are coupled such that bending loads generally produce both bending and extensional stresses and extensional loads induce both extensional and bending stresses [18]. This membrane-bending coupling effect, which is characteristic of curved structures, results in greater stress intensification at a notch in a shell than in a flat plate with a similar far-field loading condition [19]. Curvature correction factors to account for the differences in stress intensity between shells and flat plates have been proposed for various notch types, under different loading conditions, in several shell geometries. However, due to the complexities of analyzing shell behavior, most work to date has been limited to isotropic shells with very simple geometries and simple notch types such as slits and holes.

Many of the proposed curvature correction factors have been based on solutions by Folias [19-21] for the stress state near a through-thickness crack in a pressurized shell. Folias started with coupled fourth-order differential equations governing the stress function and the displacement function and was able to derive closed form solutions for the extensional and bending stresses at the crack tips, in asymptotic form, for several shell geometries and loading conditions. Simple geometries such as a cylinder or sphere were mainly considered, but it was stated that the stress solution could be obtained for more complex geometries through a proper superposition of the more simple solutions. In all cases, shallow shell theory was used to analyze elastic, isotropic, homogeneous, constant thickness shells which undergo small deformations and strains.

Folias noted that the stress distributions near the crack in a cylinder or sphere maintain the same square-root-of-r singularity and angular orientation as do flat plate stresses [20]. The difference between the shell

and flat plate solutions lies solely in a change in intensity of the extensional and bending stresses. As mentioned previously, this change is of geometric origin. The coupled stress intensity factors for the extensional and bending stresses in the shell are functions of the crack size, shell geometry, material properties, and loading conditions. As the radius goes to infinity, the uncoupled flat plate stress intensity factors are recovered.

For the case of a through-thickness axial crack in a pressurized cylinder with or without axial loading, the extensional stress intensity factor may be approximated within 7% error [21] by:

$$K_{Icyl}^{e} = \left(1 + 0.317\lambda_i^2\right)^{0.5} \sigma_e \sqrt{a} \tag{2.5}$$

where σ_e is the far-field effectively applied hoop stress in the cylinder and a is the half-crack length. The subscript and superscript 'e' is used in this and subsequent equations to denote that a factor is related to extensional behavior, as opposed to bending behavior, of a structure. The isotropic shell parameter, λ_i, is determined from the equation:

$$\lambda_i^2 = \frac{a^2 \left[12\left(1 - \nu^2\right)\right]^{0.5}}{rt} \tag{2.6}$$

where t is the cylinder thickness, r is the cylinder radius, a is the half-crack length, and ν is the Poisson's ratio of the material. Folias notes that the stress intensity factor for bending, and thus the bending stresses, are small in comparison with the extensional stress intensity factor and stresses, and therefore the bending stresses may be neglected. This is a valid assumption for most crack lengths of interest. However, bending stresses may become

significant as the crack length increases. The range of ratios of cylinder radius to crack length for which bending stresses are negligible was not indicated by Folias.

The extensional stress intensity factor determined by Folias may be used to define a 'curvature correction factor' for the extensional stresses perpendicular to the axial crack in the cylinder. The curvature correction factor is defined by taking the ratio of the extensional stress intensity factors for the cylinder and the flat plate as follows:

$$K_I^e = \left(1 + 0.317\lambda_i^2\right)^{0.5} = \frac{K_{I\,cyl}^e}{K_{I\,plate}^e}. \tag{2.7}$$

In this equation, K_I^e is the defined curvature correction factor, K_{Icyl}^e is the stress intensity factor for the cylinder (equation 2.5) and K_{Iplate}^e is the stress intensity factor for the plate. This plate stress intensity factor is defined by the equation:

$$K_{I\,plate}^e = \sigma_e \sqrt{a} \tag{2.8}$$

where σ_e is the far-field applied tensile stress in the plate and a is the half-crack length. Other curvature correction factors may be defined in a similar manner for any shell geometry and loading condition for which the stress intensity factor has been determined. For example, closed-form solutions for a pressurized spherical cap with a through-thickness crack and for a cylinder with a through-thickness circumferential crack under axial loading or axial loading with internal pressure have been derived [21]. Other solutions for the stress intensity factor may be determined numerically.

Krenk [22] expanded Folias' work on stress intensity factors for cylinders with an axial crack by using tenth-order shell theory to account for transverse shear effects. Krenk's analysis is, however, limited to specially orthotropic materials. A specially orthotropic material is different from other orthotropic materials since its in-plane shear modulus is a function of the Young's moduli and Poisson's ratios rather than being an independent material constant. As in the isotropic case, the stress intensity factors are functions of a shell parameter, λ. The specially orthotropic shell parameter, λ_o, differs from the isotropic value, λ_i, only by the presence of an extra term, δ, to account for the special orthotropy of the material and by the definition of an 'average' Poisson's ratio, ν. The orthotropy parameter, δ, has the following form:

$$\delta^4 = \frac{E_L}{E_T} = \frac{\nu_{LT}}{\nu_{TL}} \tag{2.9}$$

where E_T and E_L are the transverse and longitudinal Young's moduli, and ν_{LT} and ν_{TL} are the major and minor Poisson's ratios. The special orthotropy of the material is accounted for in the Poisson's ratio by expressing it as the geometrical mean of the major and minor values, ν_{LT} and ν_{TL}, as follows:

$$\nu = \sqrt{\nu_{LT}\nu_{TL}} \tag{2.10}$$

The specially orthotropic shell parameter is calculated using ν and δ from the equation:

$$\lambda_o^4 = \frac{a^4\left[12\left(1-\nu^2\right)\right]}{\delta^2 t^2 r^2} \tag{2.11}$$

where a is the half crack length, r is the cylinder radius, and t is the cylinder thickness. Unfortunately, the stresses, and thus the stress intensity factors, can only be determined numerically. Krenk [22] presents stress intensity factors as a function of the specially orthotropic shell parameter for various values of the ratio of cylinder radius to cylinder thickness. It is noted that this theory generally predicts smaller bending stresses near the crack than the classical eighth-order theory used by Folias. Thus, as in the isotropic case, the bending stress intensity factor may be neglected in comparison with the extensional factor. It is noted that as the ratio of the cylinder radius to cylinder thickness increases, these results approach the isotropic case.

2.3 Previous Work with Pressurized Cylinders

Most of the work concerning fracture in pressurized cylinders has focused on isotropic metals. As discussed previously, the stress state at the notch tip in a thin-walled, homogeneous, isotropic cylinder can be determined in closed form for several different notch geometries and loading conditions. Also, well-established Linear Elastic Fracture Mechanics (LEFM) techniques may be used to describe damage tolerance behavior in shells when the material is isotropic and homogeneous.

Many investigators have attempted to predict the failure of metallic cylinders with through-thickness axial cracks or slits using the critical stress intensity factor, or fracture toughness, of the material in Mode I loading as determined from flat plate failure tests [23-26]. The far-field hoop stress in a cylinder at failure was predicted from a stress intensity factor equation for the extensional stresses perpendicular to and near the crack or slit by setting this factor equal to the flat plate fracture toughness. As cited by Broek [26],

many investigators have used the extensional stress intensity factor (equation 2.5) determined by Folias [21] for a cylinder with an axial crack. Other investigators [24, 25] have proposed semi-empirical relations for this cylinder stress intensity factor. Plastic zone correction factors were incorporated into the stress intensity factor for the cylinder in many of these investigations [23-26], and the experiments that were conducted cover a wide range of material types, cylinder sizes, notch lengths, and cylinder temperatures. Reasonable correlation was obtained between the predicted hoop stresses at failure in the cylinders and the experimental values in all of the aforementioned investigations.

For composite cylinders, no closed-form solutions exist to determine the stress state near a notch. Thus, numerical techniques must be utilized. Furthermore, the available techniques to analyze the damage tolerance behavior are not as well-established as those of LEFM. Attempts have been made to directly characterize composite cylinder failure using LEFM techniques as well as techniques that were developed for composite flat plates. There has also been a strong focus on developing methodologies which predict cylinder failure from flat plate failure data. The second approach is more desirable and easier to implement since full-scale testing of composite cylinders is a very tedious and costly process, and a wealth of experimental data already exists for composite coupons. The second approach could also lead to efficient failure prediction methodologies for more complex structures. In the following, investigations are described which utilize both approaches to describe failure in composite cylinders made from graphite/epoxy material systems.

Rogers [27] was the first investigator to work with pressurized graphite/epoxy composite cylinders and their fracture toughness. He tested

graphite/epoxy tape cylinders with a $[\pm 45/0]_s$ layup, a radius of 152 mm, and axial slit lengths from 6 to 51 mm. Unnotched specimens were sealed with bonded endcaps and then pressurized to predetermined pressure levels at which point a guillotine knife of preset dimensions was used to instantaneously introduce an axial slit into the cylinder. If the knife did not cause catastrophic failure, the slit was patched and the whole process was repeated with a larger knife, in a location on the cylinder away from any patches, until catastrophic failure was achieved. Rogers thus determined a range of cylinder lengths that would potentially cause cylinder failure at a give pressurization level.

The Mar-Lin equation (2.2) and the LEFM equation (2.1) were used to correlate the hoop failure stresses of his cylinders, with similar results. In determining the 'best-fit' to his experimental data, Rogers calculated both the composite fracture parameter, H_c, and the exponent, m, in the Mar-Lin equation. The Mar-Lin equation was able to correlate the data well. However, the experimentally determined value of m differed significantly from the theoretical value as determined from the Fenner solution [6]. Also, Rogers did not use any type of curvature correction factor to account for stress intensification near the slit tips in the cylinders.

The difference between the value of m as determined from Rogers' cylinder tests and the theoretical value was reconciled by Graves and Lagace [3] by using the curvature correction factor derived by Folias [21]. The curvature correction was implemented as part of a failure prediction methodology which allowed the failure pressures of cylinders with axial slits to be predicted from flat plate failure data. Failure in both the cylinder and the coupon was assumed to be caused by the extensional stresses near the slit tips and perpendicular to the slit. Cylinder failure was predicted when the

magnitude of these extensional stresses reached the value that caused failure in the coupon with the same slit length. Mathematically this condition reduces to:

$$\sigma^{e}_{f\,cyl} = \frac{\sigma^{e}_{f\,plate}}{K^{e}_{I}} \tag{2.12}$$

where $\sigma^{e}_{f\,cyl}$ is the far-field circumferential stress required for cylinder failure, $\sigma^{e}_{f\,plate}$ is the failure stress of a plate in uniaxial tension with the same slit length, and K^{e}_{I} is the Folias curvature correction factor, defined in equation (2.7), for the extensional stresses. Once the hoop stress at failure has been predicted for the cylinder, it is a simple step to determine the corresponding failure pressure from the expression:

$$p_{f\,cyl} = \frac{\sigma^{e}_{f\,cyl}\, t}{r} \tag{2.13}$$

where $p_{f\,cyl}$ is the failure pressure of the cylinder, r is the cylinder radius, t is the cylinder thickness, and $\sigma^{e}_{f\,cyl}$ is the hoop stress at failure. The coupon failure stresses may be correlated prior to implementing the curvature correction using the Mar-Lin equation or any other equation which is appropriate for composite plates. This makes the methodology for predicting failure in composite cylinders particularly flexible and general.

Several key assumptions were made in the implementation of this methodology. Most importantly, the stress state at the tips of an axial slit in a biaxially loaded cylinder must be comparable to that for a uniaxially loaded coupon with a slit perpendicular to the loading direction. Graves [13] noted that the Folias solution for the extensional stresses at the slit tips in the

cylinder showed the same square-root-of-r singularity and angular distribution as the flat plate solution. He also noted that the bending stresses from the Folias solution are small in comparison with the extensional stresses and may therefore be neglected. Additionally, Folias' analysis has shown that the axial load in the cylinder has no effect on the stress state perpendicular to the slit. With the bending stresses and axial load ignored (i.e. only the hoop midplane stress is considered), the stress state near the slit resulting from pressure loading in a cylinder and the in-plane tensile loading in the direction perpendicular to the slit in a coupon are similar in nature. However, ignoring the axial load in the cylinder also requires that this load does not contribute to failure. This assumption is reasonable, since numerous investigations have shown that loading parallel to a slit in a flat plate does not affect the failure strength of the plate [e.g. 13, 14]. It is also important to note that the assumption that the extensional stresses near and perpendicular to the slit cause failure in both cylinders and coupons is coupled to an additional assumption that the initial failure mode is the same in both specimen types for a given layup.

Graves [3, 13] used the methodology to predict the failure pressures of quasi-isotropic fabric cylinders with axial slit lengths from 38 to 69 mm. Two layups were considered, $[0_f/45_f]_s$ and $[45_f/0_f]_s$, and the cylinders had the same length and radius as those used by Rogers. Failure data was obtained for coupons and correlated with the Mar-Lin equation. The Folias and Krenk correction factors were used to determine the corresponding cylinder failure pressures. The use of both correction factors is valid for the layups considered, since they are both quasi-isotropic and specially orthotropic. Cylinders were tested using Rogers' [27] pressurization technique and guillotine mechanism to introduce the slits. The predicted cylinder failure

pressures agreed well with the experimental values. The main deficiency of this experimental work was the lack of a direct correlation between slit sizes and failure pressures for the layups considered due to the use of the guillotine method to introduce the slits.

Chang and Mar [28] developed a patch technique which allowed preflawed cylinders with various notch geometries to be pressurized monotonically to failure. Thus, the exact internal pressure required for failure could be determined for a given notch dimension. This technique was used in testing quasi-isotropic fabric cylinders with holes, holes with longitudinal slits, elongated holes, colinear longitudinal slits, and slits rotated at various angles to the longitudinal axis. For cylinders with rotated slits, an extended version of the method used by Graves was employed to predict cylinder failure from flat plate failure behavior. This extended method involved a superposition of the Folias curvature correction factors for axial and circumferential slits, in order to obtain the curvature correction factor for the rotated slit in the cylinder. Analytically obtained curvature correction factors for the other notch geometries were used in conjunction with the Mar-Lin coupon correlation to predict cylinder failure. Acceptable correlation was obtained between the experimental and analytical results.

Sawicki [29] used the same methodology to predict the failure pressures of graphite/epoxy $[0_f/45_f]_s$ cylinders with axial slits from 52 to 178 mm. Slits were precut into the cylinders and a rubber bladder system was used in lieu of the patch system of Chang and Mar. The experimental cylinder failure pressures were slightly higher than the predicted values; however, reasonable correlation was achieved.

Saeger and Lagace [12] used two different methodologies to predict the failure of $[0_f/45_f]_s$ cylinders with axial slits from 50 to 150 mm. These

cylinders differed from those of previous investigations in that they used a high strain-to-failure, or 'tough,' epoxy matrix: American Cyanamid's CYCOM 907. The same methodology as used by Graves was employed to predict cylinder failure pressures in order to see if a change in material system would affect the applicability of the methodology. The results indicate that the methodology involving the Mar-Lin coupon correlation with the Folias curvature correction factor somewhat overpredicts the failure pressures of cylinders made from the toughened epoxy. Another failure prediction method that relies on parameters from coupon tests and involves the previously described Whitney-Nuismer Average Stress Criterion was also employed. The characteristic distance from the notch tip, a_o, that is required by this criterion was experimentally determined from coupon tests. Failure was predicted in the cylinder when the average hoop stress over this experimentally determined distance reached the unnotched strength of the material, which was also determined from coupon tests. In order to determine the average stress over the distance a_o, an accurate knowledge of the hoop stress as a function of the distance from the notch tip was required. A finite difference solution to determine the hoop stresses and strains in the cylinder was developed and experimental strain data were used to verify the accuracy of the analysis [30]. This failure prediction methodology provides excellent correlation with the experimental results. However, this method is much less general and desirable than the one previously used, since the Whitney-Nuismer Average Stress Criterion takes on different forms for different notch shapes and the computationally expensive finite difference solution must be calculated for each notch size and material system in question.

All of the investigations described up to this point involve cylinders with a radius of 152 mm. Ranniger [17] addressed scaling issues by testing $[0_f/45_f]_s$ cylinders with a radius of 76 mm. Axial slits ranging in length from 38 to 76 mm were precut into the cylinders and pressurization was achieved using a rubber bladder system. As in the previous investigations, the experimental failures pressures agree well with the predicted values, as determined from the method employing the Mar-Lin coupon correlation coupled with the Folias curvature correction factor.

The previous discussion has shown that methodologies exist which utilize flat plate failure behavior to successfully predict failure in composite cylinders with through-thickness notches. Different size cylinders and different notch types and sizes have been considered. However, most work to date has focused on quasi-isotropic layups and fabric material systems. Since these cylinders represent only a small portion of the potential types, it is also important to understand how tape material systems and anisotropy affect the applicability of the methodologies.

Ranniger et al. [4, 31] used the previously described methodology to predict the failure pressures of tape cylinders with through-thickness axial slits. Quasi-isotropic $[90/0/\pm45]_s$ and structurally anisotropic $[\pm45/0]_s$ and $[\pm45/90]_s$ layups were considered. The latter two layups are referred to as structurally anisotropic since the anisotropy that they exhibit, in the form of bending-twisting coupling, is not an inherent ply property and is expressed only when the plies are laminated together in a structure. Coupons and cylinders, with a diameter of 152 mm, were manufactured from AS4/3501-6 graphite/epoxy tape. Slits with lengths between 9.5 and 19.1 mm were cut into some of the coupons perpendicular to the loading direction. The notched and unnotched coupons were tested to failure in uniaxial tension. The failure

stresses of the notched coupons with the same layup were correlated using the Mar-Lin equation. The Folias curvature correction term was applied to each correlation to establish the failure prediction curves for the cylinders. Axial slits with lengths between 12.5 and 63.5 mm were cut into the cylinders and rubber bladders were used to internally pressurize the cylinders to failure. The predicted far-field hoop stresses at failure were compared to the experimentally obtained values and the initial failure paths were compared for coupons and cylinders with the same layup, to assess the applicability of the methodology to the cylinders considered.

The failure pressures of the $[90/0/\pm45]_s$ cylinders with slit lengths between 25.4 and 63.5 mm agree well with the predicted values. However, it is interesting to note that all of the experimental values exceed the predictions by 1% to 15%. In contrast, the methodology inadequately predicts the failure pressure of the $[90/0/\pm45]_s$ cylinder with the 12.7 mm slit as the failure pressure for this cylinder is higher than the predicted value by 18%. Furthermore, the experimental value is also greater than the equivalent failure pressure for a plate with the same slit size. This equivalent failure pressure was determined by taking the correlated far-field coupon stress and using equation (2.13) to determine what cylinder pressure would give a far-field hoop stress of the same magnitude.

The predicted failure pressures for the $[\pm45/0]_s$ and $[\pm45/90]_s$ cylinders were not expected to match the experimental results, since the applied curvature correction factor was derived for isotropic materials and aspects of the structural properties, such as bending-twisting coupling, were neglected. The experimental failure pressures were compared to the predicted values since the quantitative difference between these values can be used to infer differences in the failure of cylinders which are quasi-isotropic from those

that are structurally anisotropic. The discrepancy between the experimental and predicted values is also indicative of the degree of applicability of the predictive methodology to cylinders which are structurally anisotropic. For both layups, the experimental failure pressures are well above the predicted values by 31% to 93% and most of the cylinder failure pressures fall between the plate and shell prediction curves when the plate curves are displayed in terms of equivalent pressures. However, as with the $[90/0/\pm45]_s$ layup, the failure pressures of the structurally anisotropic cylinders with the 12.7 mm slits are higher than the corresponding values from the coupon correlation curves.

Due to the results for tape cylinders with the 12.7 mm slit length, a fabric $[0_f/45_f]_s$ cylinder with the same fiber and matrix types and a 12.7 mm slit was also manufactured and tested to failure. Coupon data from a previous investigation [17] was used to predict the failure pressure of this cylinder. Unlike with the tape cylinders, the methodology accurately predicts the failure pressure of the quasi-isotropic fabric cylinder with a 12.7 mm slit.

A comparison of the initial failure modes of cylinders and coupons with the same layup reveals that the methodology is unable to predict the failure pressure of the cylinder whenever the failure modes differ. The initial failure modes of all of the structurally anisotropic cylinders and the quasi-isotropic tape cylinder with the 12.7 mm slit are different from those of the coupons with the same laminate types. This is a highly significant result since a difference between the initial failure modes in coupons and cylinders with the same layup implies that a different failure mechanism operates in the two specimen types. Since this condition violates a fundamental assumption of the predictive methodology, more work is needed to identify and understand effects present in tape cylinders that are currently neglected, but should be

included, in this methodology. One primary effect cited that warrants further consideration relates to the potential role of the axial stress in the failure of tape cylinders [4]. The axial stress is neglected in the predictive methodology, but it may influence the failure of tape cylinders due to the possible presence of localized damage at the slit tips prior to the ultimate failure of the cylinders. The role of the axial load may also become more important in laminates which exhibit a high degree of bending-twisting coupling, such as the $[\pm 45/0]_s$ and $[\pm 45/90]_s$ laminates, especially when such slit tip damage is present. Additionally, more research is needed to understand how different degrees of bending-twisting coupling affect the failure of tape cylinders, since the presence of such coupling may significantly alter the stress state at the slit tips in a cylinder from that which is found in a flat plate. Due to the limited experimental data which currently exist for pressurized tape cylinders, more research is also needed to further establish this database and identify areas for further work.

CHAPTER 3

Overall Approach

In this chapter, the issues raised by previous work and the resulting goals of the present experimental investigation are clearly identified. The configurations and layups for the coupon and cylinder specimens considered in this investigation are described and the rationale for their selection is explained. The experimental plan is outlined and test matrices are presented for both cylinder and coupon specimens.

3.1 Problem Definition

As discussed in Chapter 2, problems have been encountered in applying the current failure prediction methodology to tape cylinders with axial slits. Specifically, the methodology inaccurately predicts the failure pressures of a quasi-isotropic $[90/0/\pm45]_s$ cylinder with a 12.7 mm slit and structurally anisotropic $[\pm45/0]_s$ and $[\pm45/90]_s$ cylinders with slit lengths between 12.7 and 63.5 mm. The initial failure modes of these cylinders are also different than those of slit coupons with the same layups, which violates a fundamental assumption of the methodology and indicates that the methodology is inappropriate for these cylinders. Thus, the challenge for the current investigation is to explore possible reasons why the current methodology is valid for some tape cylinders, such as for $[90/0/\pm45]_s$ cylinders with slit lengths between 25.4 and 50.8 mm, but is invalid for others. The primary differences between the quasi-isotropic and structurally anisotropic tape cylinders which have been tested and the quasi-isotropic $[0_f/45_f]_s$ fabric cylinders for which the methodology has been shown to be valid are that the

former cylinders have a nonwoven fiber architecture and a higher degree of anisotropy with respect to their bending properties. Thus, the discrepancies between the predicted and experimental failure pressures and the coupon and cylinder failure modes for many of the tape cylinders in the previous investigation are most likely caused by effects related to these fundamental differences between the fabric and tape laminates.

As mentioned in Chapter 2, one possible effect in laminates that exhibit bending-twisting coupling is that local bending near the slit in the cylinder results in an altered stress state near the slit tips from that which is found in the flat plate. Thus, in laminates that exhibit this type of structural coupling, not only is the laminate behavior not properly accounted for in the isotropic curvature correction factor, the extensional stresses perpendicular to the slit may no longer be solely responsible for the initiation of failure. These extensional stresses might be supplemented by nonnegligible bending stresses perpendicular to the slit, or the stress state at the slit tips might be altered in such a fashion that failure could also be induced through tearing or shearing action. The effects of bending-twisting coupling are expected to be most apparent in the structurally anisotropic layups. However, these effects might also be present in a more limited sense in the quasi-isotropic tape layup, since it has some, although a much smaller degree of, bending-twisting coupling. The quasi-isotropic fabric layup tested in most of the previous investigations does not exhibit this type of coupling. Thus, more work is needed using tape laminates with different degrees of structural anisotropy, with respect to their bending properties, so that the effects of bending-twisting coupling can be better understood.

Another potential effect that must be considered is the role of the axial stress in the failure of tape cylinders. As described in Chapter 2, the axial

stress was ignored in the development of the failure prediction methodology. This requires that the axial stress not affect the stress state in the hoop direction near the slit or contribute to the cylinder failure. However, localized damage initiated at the slit tips prior to the final cylinder failure, primarily in the form of ply splitting, may cause the axial loading to become involved and, thus, violate these assumptions. A localized damage effect involving ply splitting is limited in fabric laminates due to the woven nature of the fibers. However, previous work with tape laminates loaded in uniaxial tension [32] has shown that localized damage in the form of splitting in the 0° plies and delamination can mitigate stress at the notch tip and result in reduced notch sensitivity. Thus, a localized damage effect at the slit tips in the quasi-isotropic cylinder with the 12.7 mm slit and the structurally anisotropic cylinders, which might or might not be influenced by the axial load, could account for the difference in failure modes between cylinders and coupons and cause stress mitigation that explains the higher than expected experimental failure pressures. A circumferential fracture path, suggestive of a 0° ply split, that was observed at the slit tip in the quasi-isotropic cylinder with the 12.7 mm slit [4] supports this explanation. However, since this effect is present only at the 12.7 mm slit size in the quasi-isotropic tape cylinders and only one data point exists for this slit size, the data point should be repeated to increase the level of confidence in the previous results and conclusions. The axial loading may play a more important role in the structurally anisotropic tape cylinders, especially when localized damage is induced at the slit tips, due to the high degree of structural coupling. Thus, experiments are needed where quasi-isotropic and structurally anisotropic cylinders are tested in hoop loading only, so that the role of the axial load in the failure of these cylinders can be assessed.

The relative influences of axial stress and bending-twisting coupling on the failure of tape cylinders are currently unknown. It is also unclear if and how these potential effects influence each other. Thus, in order to fully understand the failure process in tape cylinders with axial slits and explain the results of the past work, both axial stress effects and bending-twisting coupling effects need to be addressed in further work.

3.2 Experimental Approach

In the current investigation, an experimental approach is utilized to address the issues raised in the past work concerning the roles of axial stresses and bending-twisting coupling in the failure of tape cylinders with axial slits. The effects of axial loading and bending-twisting coupling on the applicability of the current failure prediction methodology for tape cylinders are also addressed. The primary goal of this investigation is to assess the role of axial stress in the failure of tape cylinders. This is accomplished by testing cylinders of the same configuration and layups as in past work [4] to failure in hoop loading only. A secondary goal is to determine how a change in the degree of anisotropy with respect to the bending properties of a laminate affects the cylinder failure behavior. This is accomplished by testing quasi-isotropic tape cylinders with a different stacking sequence from those in the past work [4] to failure in biaxial loading.

The uniaxial loading experiments were undertaken to eliminate the axial stress as a potential cause of observed effects in the failure of tape cylinders. The $[90/0/\pm45]_s$, $[\pm45/0]_s$, and $[\pm45/90]_s$ layups and AS4/3501-6 unidirectional tape material system were chosen for these experiments so that direct comparisons could be made with the results for biaxially loaded cylinders with these layups and material system from the past work [4]. The

cured ply properties for this material system are shown in Table 3.1 along with those for the fabric material used in much of the previous research (see Chapter 2). Cylinders with the quasi-isotropic $[90/0/\pm45]_s$ layup and structurally anisotropic $[\pm45/0]_s$ and $[\pm45/90]_s$ layups and slit lengths of 12.7, 25.4, and 50.8 mm were manufactured and tested to failure in hoop loading only, using a test apparatus designed and built especially for this investigation. Calculated extensional properties for each layup from Classical Laminated Plate Theory (CLPT) are listed in Table 3.2.

The test matrix for the cylinders tested under uniaxial loading is shown in Table 3.3. The slit lengths were chosen to match those in the past investigation and to focus the current investigation on the lower end of the range of slit lengths that have been tested to date. This focus was desired due to the unexpectedly high failure pressures for cylinders with 12.7 mm slits in the past investigation which are even higher than the corresponding values from the coupon correlation curves, as described in Chapter 2.

The quasi-isotropic cylinder with the 50.8 mm slit was first tested several times as an unnotched specimen to a low percentage of its failure stress in order to verify the uniaxial test apparatus design. It was then tested to failure as a notched specimen. These verification tests were necessary to ensure the proper loading condition on the cylinder and apparatus and to establish the effects of a cylinder explosion on the apparatus before it was used to conduct the general uniaxial failure tests. The $[90/0/\pm45]_s$ cylinder with the 50.8 mm slit was chosen for the verification tests since the curvature correction factor is theoretically valid for this quasi-isotropic layup and the cylinder with the 50.8 mm slit length has the lowest predicted failure pressure of the three cylinders with this layup that are considered in the current work.

Table 3.1 Cured Material Properties

Material	E_L [GPa]	E_T [GPa]	ν_{LT}	G_{LT} [GPa]	t_{ply} [mm]
AS4/3501-6	142.0	9.8	0.30	6.0	0.134
AW370-5H/ 3501-6S	74.1	73.1	0.06	6.5	0.350

Table 3.2 Calculated Laminate Extensional Properties

Laminate	E_L [GPa]	E_T [GPa]	ν_{LT}	G_{LT} [GPa]
$[\pm 45/90]_s$	26.7	61.8	0.30	26.5
$[\pm 45/0]_s$	61.8	26.7	0.69	26.5
$[90/0/\pm 45]_s$	55.5	55.5	0.30	21.4
$[0/\pm 45/90]_s$	55.5	55.5	0.30	21.4
$[0_f/45_f]_s$	54.2	53.7	0.30	20.6

Table 3.3 Test Matrix for Uniaxially Loaded Cylinders

Slit Size, mm	Laminate		
	$[\pm 45/90]_s$	$[\pm 45/0]_s$	$[90/0/\pm 45]_s$
12.7	1[a]	1	1
25.4	1	1	1
50.8	1	1	1[b]

[a] indicates number of cylinders tested

[b] indicates cylinder used for test apparatus verification

Coupon failure data from the past investigation for the three layups considered were correlated using the Mar-Lin equation. The Folias curvature correction factor was applied to establish the failure pressure prediction curves for the cylinders. As a check on the validity of using this coupon data for the current work, coupons with the $[90/0/\pm45]_s$ layup and through-thickness slits oriented perpendicular to the loading direction were also manufactured and tested to failure in uniaxial tension. The test matrix for these notched coupons is shown in Table 3.4. The coupon correlation and cylinder failure pressure prediction curves for the $[90/0/\pm45]_s$ layup were determined separately for these coupons and are compared to those obtained using the coupon data set from the past investigation. The specially orthotropic curvature correction factor discussed in Chapter 2 is also valid for the $[90/0/\pm45]_s$ layup, but it is not considered in the current work since it provides essentially the same results as using the factor derived by Folias (equation 2.7). The experimental failure pressures are compared to the predicted values as well as to the experimental values obtained in the past investigation for a biaxial loading condition. The initial fracture paths are also compared for coupons, uniaxially loaded cylinders, and biaxially loaded cylinders of the same laminate type. Failure pressure and fracture path comparisons are used to draw conclusions concerning the effects of the axial load and the applicability of the methodology to uniaxially loaded quasi-isotropic and structurally anisotropic tape cylinders.

The three layups considered in the uniaxial loading experiments were originally chosen in the past work for specific reasons. The quasi-isotropic and specially orthotropic $[90/0/\pm45]_s$ tape layup was selected since it has fibers in the same directions and in a similar distribution through the thickness of the laminate as the $[0_f/45_f]_s$ fabric layup that has been used in

Table 3.4 Test Matrix for Tensile Coupons

	Slit Length, mm				
Laminate	Unnotched	9.5	12.7	15.9	19.1
$[0/\pm45/90]_s$	4[a]	4	4	4	4
$[90/0/\pm45]_s$	--	2	2	2	2

[a] indicates number of specimens tested

previous research. The structurally anisotropic $[\pm 45/0]_s$ and $[\pm 45/90]_s$ layups were chosen since they are simple and relatively easy to manufacture, and they are layups for which much coupon failure data has already been compiled [11]. These two layups are comprised of subsets of the plies in the $[90/0/\pm 45]_s$ layup and differ from each other only in that the $[\pm 45/0]_s$ layup has fibers along the hoop direction while the $[\pm 45/90]_s$ layup has fibers along the axial direction of the cylinder. Thus, by testing these two complementary layups, the effects of having fibers in one of the two primary loading directions, circumferential or axial, can be investigated. Ranniger [4] also noted that using these two layups helps to separate effects which are specific to the laminates from those which can be attributed to their structural anisotropy. This is possible since the values of D_{16} and D_{26}, the bending-twisting coupling terms from the 'D' matrix in Classical Laminated Plate Theory, are the same for both layups. However, the ratio of D_{16} and D_{26} to D_{11}, the hoop direction bending stiffness, for the $[\pm 45/0]_s$ layup is 10% lower than the value of 0.33 for the $[\pm 45/90]_s$ layup and this may also be a factor. The components of the 'D' matrix are listed in Table 3.5 for the laminates investigated in this work.

A second approach was also used to isolate the effects of structural anisotropy in the previously tested tape cylinders. Quasi-isotropic cylinders with the $[0/\pm 45/90]_s$ layup and slit lengths of 12.7 and 25.4 mm were manufactured from AS4/3501-6 tape prepreg and tested to failure in biaxial loading. This investigation was only meant to be preliminary, since a full investigation into the effects of bending-twisting and other types of structural coupling should involve a number of laminates showing a wide range in the magnitudes of structural coupling as well as detailed finite element analyses to determine the stress states near the slit tips. In the current work, the

Table 3.5 Calculated Laminate Bending Properties

	Bending Property, GPa*mm^3					
Laminate	D_{11}	D_{22}	D_{12}	D_{16}	D_{26}	D_{66}
$[0/\pm45/90]_s$	10.40	2.72	1.58	0.64	0.64	1.90
$[90/0/\pm45]_s$	5.53	9.37	0.70	0.32	0.32	1.01
$[\pm45/0]_s$	2.13	1.92	1.41	0.64	0.64	1.54
$[\pm45/90]_s$	1.92	2.13	1.41	0.64	0.64	1.54
$[0_f/45_f]_s$	15.79	15.81	1.84	0.00	0.00	1.87

$[0/\pm45/90]_s$ layup was chosen so that direct comparisons could be made with the previously tested $[90/0/\pm45]_s$ layup. The Folias curvature correction factors are the same for both layups since they have the same in-plane properties, as indicated in Table 3.2, and these factors are theoretically valid for both layups since they are both quasi-isotropic. However, the use of the $[0/\pm45/90]_s$ layup allows stacking sequence effects to be examined, as well as the effects of having a higher degree of anisotropy with respect to the bending properties of the laminate. These bending properties are indicated in Table 3.5 for both layups. The bending properties of the quasi-isotropic fabric layup used in the previous work are also listed in the table for comparison. As can be seen in this table, the $[0/\pm45/90]_s$ layup has values of D_{16} and D_{26} with twice the magnitudes of those for the $[90/0/\pm45]_s$ layup. However, the ratio of D_{16} and D_{26} to D_{11} for the $[0/\pm45/90]_s$ layup is only 6% higher than the value of 0.058 for the $[90/0/\pm45]_s$ layup. The $[0/\pm45/90]_s$ layup was chosen over the $[45/90/0/-45]_s$ layup, which has the highest values of D_{16} and D_{26} for any symmetric combination of the plies in the $[90/0/\pm45]_s$ layup, specifically because it maintains this ratio. This was done since it is currently unknown how changes in this ratio may affect the failure behavior of cylinders and the applicability of the predictive methodology. It should be noted that the ratios of D_{16} and D_{26} to D_{11} for the two structurally anisotropic layups exceed those of the $[0/\pm45/90]_s$ and $[90/0/\pm45]_s$ layups by a factor of approximately five. This ratio is zero for the fabric layup used in past work since it has zero values of D_{16} and D_{26}.

The test matrix for the cylinders with the $[0/\pm45/90]_s$ layup is shown in Table 3.6. Coupons with the same layup and through-thickness slits oriented perpendicular to the loading direction were also manufactured and tested to failure in uniaxial tension. These tests were necessary since no failure data

Table 3.6 Test Matrix for Biaxially Loaded Cylinders

	Laminate	
Slit Length, mm	$[90/0/\pm45]_s$	$[0/\pm45/90]_s$
12.7	2[a]	1
50.8	--	1

[a] indicates number of cylinders tested

for coupons with the same slit lengths and configuration as those in the past work were previously available for this layup. Unnotched coupons were tested to failure to determine the laminate properties. The test matrix for these coupons is indicated in Table 3.4. The previously described methodology was applied to the coupon failure stresses to predict the failure pressures of the cylinders. The specially orthotropic correction factor discussed in Chapter 2 is not used for this layup even though it is theoretically valid, since it provides essentially the same prediction curve as does the Folias curvature correction factor. Comparisons are made between failure modes in the coupons and cylinders and cylinder failure pressures are compared for the $[90/0/\pm45]_s$ and $[0/\pm45/90]_s$ layups, to infer differences that are caused by the change in degree of anisotropy and stacking sequence.

In order to substantiate the results of the past investigation for the quasi-isotropic tape cylinder with the 12.7 mm axial slit, two cylinders with the $[90/0/\pm45]_s$ layup and this slit length were manufactured from AS4/3501-6 tape prepreg and tested to failure in biaxial loading. Failure pressure and failure mode comparisons are again made and conclusions are drawn based on the results. Two cylinders were tested to see if repeatable results could be obtained and to further establish the predominating effects.

3.3 Specimen Configurations

The coupon configuration chosen for this investigation is the same as that used in previous work. Thus, direct comparisons can be made with these results. As shown in Figure 3.1, the coupons have an overall length of 350 mm with a test section length of 200 mm, and a width of 70 mm. The $[90/0/\pm45]_s$ coupons were cut 305 mm long due to an error. Glass/epoxy loading tabs with a length of 75 mm (53 mm for the $[90/0/\pm45]_s$ coupons) and

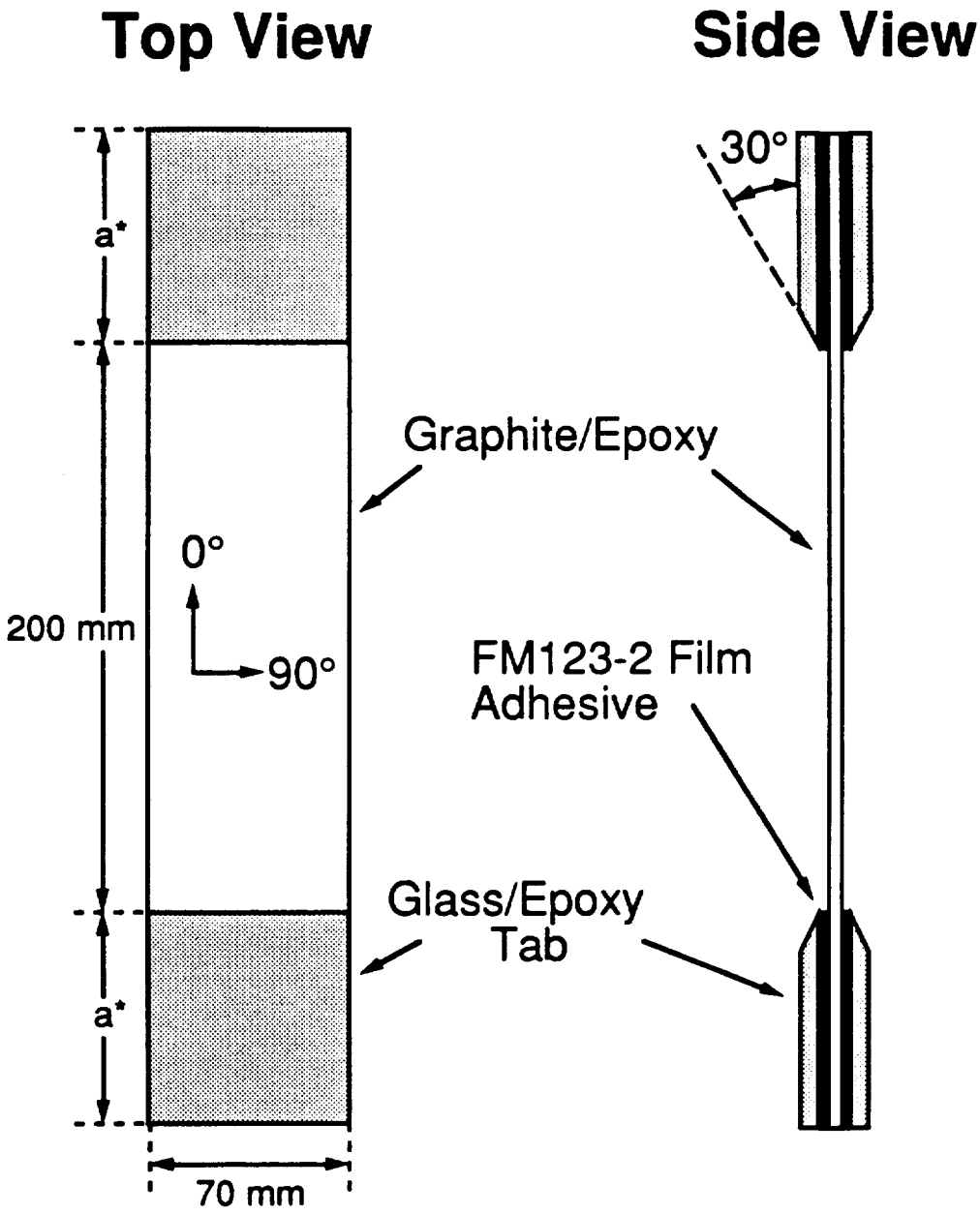

* $[0/\pm45/90]_s$ Coupons: a = 75 mm

$[90/0/\pm45]_s$ Coupons: a = 53 mm

Figure 3.1 Configuration of coupon specimen.

the same width as the specimen were bonded to both sides of the specimen at each end. A 30° beveled edge on each tab allowed for smooth load transfer from the tabs to the specimen. Both notched and unnotched coupons were tested to failure in this investigation. The notched coupons always contain through-thickness slits centered in the test section and oriented perpendicular to the loading direction. The four slit lengths considered, which vary from 9.5 to 19.1 mm, were chosen to avoid finite width effects on the 70 mm wide coupon. Slits were chosen so that the notch geometry would be consistent for both coupons and cylinders and their failure modes could be directly compared. The ply angles in the coupons are referenced to a right-handed coordinate system with the 0° axis in the direction of loading, which is also the direction perpendicular to the slits.

The cylinder configuration used in this investigation, as shown in Figure 3.2, is also exactly the same as that used in the previous work. The cylinder radius is 152 mm and the cylinder length is 750 mm, which is longer than necessary for the present investigation. The only requirement for the present investigation is that the cylinder has to be long enough so that the boundary zone at the cylinder ends does not interfere with the stress state near the slit. In the previous work, the length of 750 mm was needed so that stiffening bands could be added to some of the cylinders, outside the area of influence of the slits, as part of an investigation into damage containment and arrest. This length was maintained in the current work for consistency. Through-thickness axial slits with lengths between 12.7 and 50.8 mm were cut into all of the cylinders, with the slits centered along the cylinder length. The coordinate system for the cylinders was defined as shown in Figure 3.2 with the 0° axis along the circumferential direction. Thus, the 0° direction for both coupons and cylinders is perpendicular to the slits.

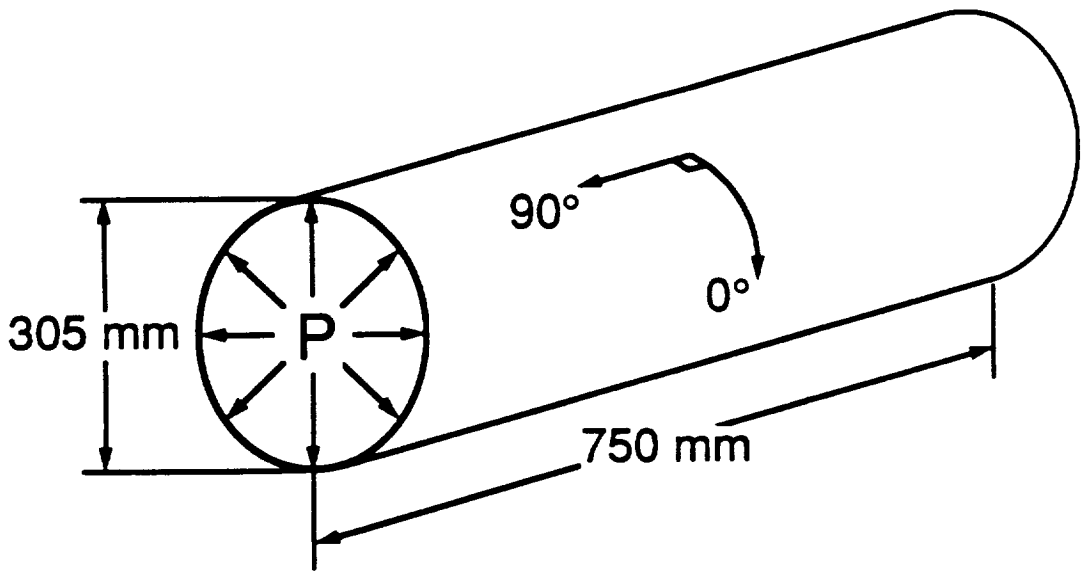

Figure 3.2 Configuration of cylinder specimen.

The boundary zone mentioned in the preceding paragraph is a region of high stress and strain gradients at the ends of the cylinder due to the constraint imposed by the boundary condition. For an unnotched cylinder with bonded endcaps that is internally pressurized to achieve a two-to-one biaxial loading condition, the boundary zone can be seen in a plot of the radial deflection [13]. Such a plot is provided in Figure 3.3 for a $[\pm 45/90]_s$ cylinder. As can be seen in this plot, the radial deflection is constant along most of the length of the cylinder, but increases dramatically and then abruptly falls to zero in a region approximately 75 mm from each endcap. A similar region of constant radial deflection and boundary zones should exist for a cylinder loaded in the hoop direction only since this case differs from the one for biaxial loading only in the degree of constraint on the cylinder ends. The boundary zones in a uniaxially loaded cylinder develop since the ends of the cylinder are placed into grooves in the endplates, but are not bonded, and the portion of the cylinder in these grooves is not exposed to the internal pressure loading in the cylinder. Stress redistribution and a corresponding strain gradient near the ends of the cylinder are necessary to satisfy equilibrium and compatibility and provide the zero stress condition along the free edge at both cylinder ends. The boundary zones for a uniaxial and biaxial loading condition are expected to be different sizes since, in the former case, the stresses go to zero at the ends of the cylinder and, in the latter case, the radial deflection is forced to zero. However, the relative sizes of these boundary zones are not known. Strain readings are therefore taken during the verification tests to ascertain the size of these zones and to be sure they do not interfere with the stress state around the notch.

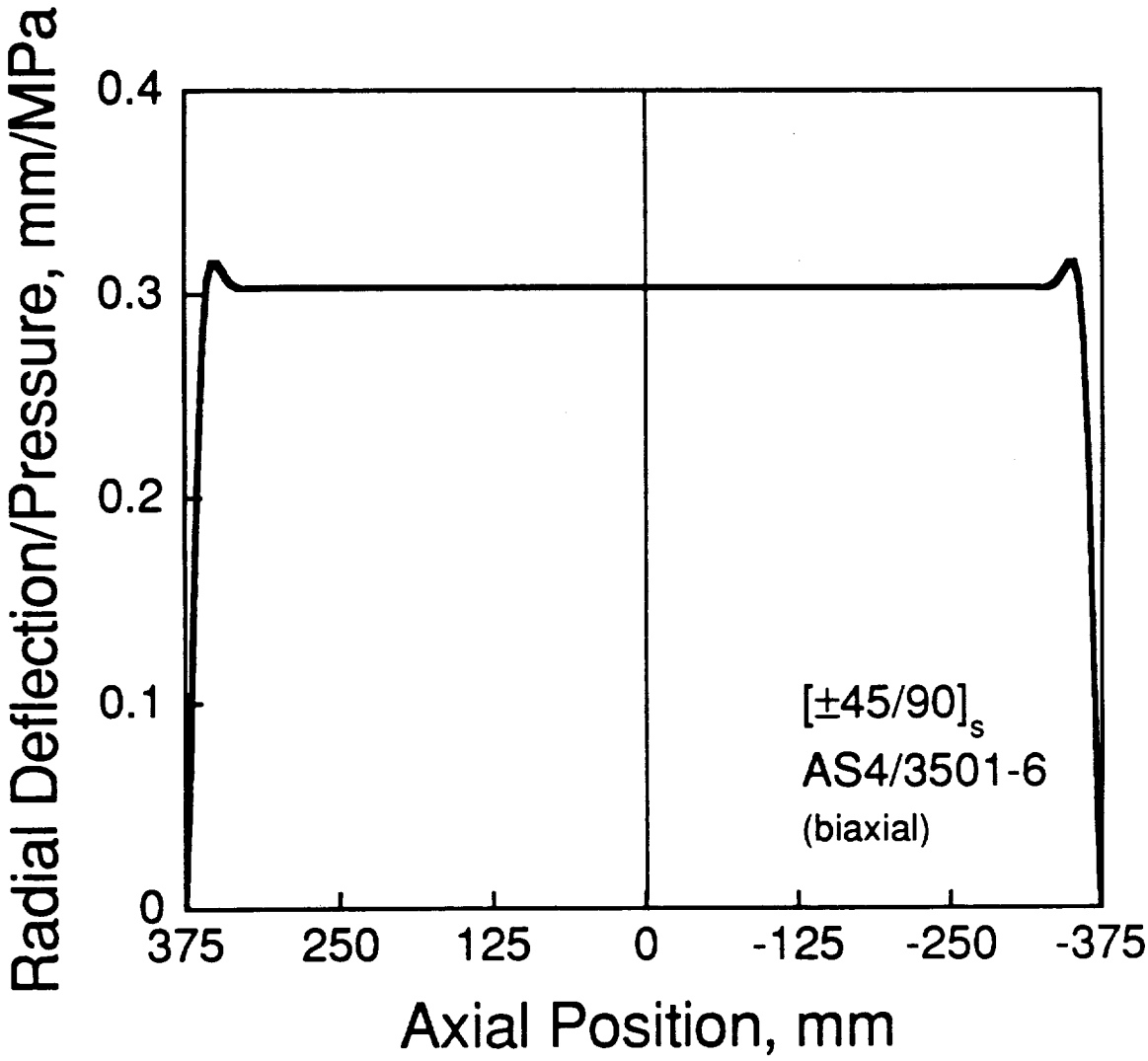

Figure 3.3 Plot of radial deflection versus axial position for unnotched, biaxially loaded $[\pm 45/90]_s$ tape cylinder with bonded endcaps.

3.4 Summary of Predictive Methodology

The methodology utilized in this investigation to predict cylinder failure pressures, which is described in detail in Chapter 2, is summarized here for convenience.

The experimental far-field failure stresses of notched coupons in uniaxial tension are correlated using the Mar-Lin equation:

$$\sigma^{e}_{f\,plate} = H_c\,(2a)^{-m} \tag{3.1}$$

where the variables are defined as follows:

$\sigma^{e}_{f\,plate}$ = far-field failure stress of coupon (MPa),

H_c = composite fracture parameter (MPa*mm^m),

2a = length of notch perpendicular to loading direction (mm),

m = order of stress singularity at bimaterial interface.

The theoretical value of m used in the current investigation, as determined from the Fenner solution [6] for graphite/epoxy, is 0.28. The composite fracture parameter, H_c, is determined individually for each coupon with a given layup and these values are averaged to establish the H_c value for the coupon correlation curve. This curve may be expressed in terms of equivalent pressures by taking the far-field coupon stresses and determining what cylinder pressures would give far-field hoop stresses of the same magnitudes. The equivalent cylinder failure pressure, $p_{f\,plate}$, for a far-field coupon failure stress, $\sigma^{e}_{f\,plate}$, may be determined from the equation:

$$p_{f\,plate} = \frac{\sigma^{e}_{f\,plate}\,t}{r} \tag{3.2}$$

where r is the cylinder radius (mm) and t is the cylinder/coupon thickness (mm). By substituting this expression into equation (3.1), the Mar-Lin equation may be expressed as follows:

$$p_{f\,plate} = \frac{H_c\, t}{r}(2a)^{-m}. \tag{3.3}$$

The use of the Mar-Lin equation in this form allows the coupon correlation and cylinder failure prediction curves to be plotted together on the same graph for comparison purposes.

Cylinder failure is predicted when the magnitude of the extensional stresses near the slit tips and perpendicular to the slit reaches the value that caused failure in the coupon with the same slit length. The far-field applied hoop stress in the cylinder for which this condition is satisfied is related to the far-field failure stress of the flat plate by the following equation:

$$\sigma^e_{f\,cyl} = \frac{\sigma^e_{f\,plate}}{K^e_I} \tag{3.4}$$

where $\sigma^e_{f\,cyl}$ is the predicted far-field cylinder hoop stress at failure (MPa), $\sigma^e_{f\,plate}$ is the correlated far-field failure stress of the flat plate (MPa), and K^e_I is the Folias curvature correction factor for the extensional stresses. Equivalently, the predicted cylinder failure pressure, $p_{f\,cyl}$, is related to the plate failure pressure, $p_{f\,plate}$, by the expression:

$$p_{f\,cyl} = \frac{p_{f\,plate}}{K^e_I} \tag{3.5}$$

where $p_{f\,plate}$ is determined using equation (3.2).

The Folias curvature correction factor for the extensional stresses accounts for geometrical effects which result in a difference in stress intensity at the slit tips in a cylinder and flat plate. This correction factor, which was derived from linear shallow shell theory for isotropic materials, may be approximated using the equation:

$$K_I^e = \left(1 + 0.317\lambda_i^2\right)^{0.5} . \tag{3.6}$$

The isotropic shell parameter, λ_i, is determined from the equation:

$$\lambda_i^2 = \frac{a^2\left[12\left(1-\nu^2\right)\right]^{0.5}}{rt} \tag{3.7}$$

where t is the cylinder thickness (mm), r is the cylinder radius (mm), a is the half-crack length (mm), and ν is the Poisson's ratio of the material. In the current investigation, the Poisson's ratio for a structurally anisotropic laminate is expressed as the geometrical mean of the major and minor values, ν_{LT} and ν_{TL}, as follows:

$$\nu = \sqrt{\nu_{LT}\,\nu_{TL}} . \tag{3.8}$$

The values of ν for the quasi-isotropic layups considered in the current investigation and the values of ν_{LT} and ν_{TL} for the structurally anisotropic layups were calculated from Classical Laminated Plate Theory and are indicated in Table 3.2.

CHAPTER 4

Experimental Procedure

The manufacturing, instrumentation, and testing procedures, as well as the post-test documentation, for the coupon and cylinder test specimens of this investigation are described in this chapter. However, aspects of the experimental procedure which are specific to uniaxially loaded cylinders are reserved for the next chapter, where a full description of the uniaxial test apparatus is provided.

4.1 Coupon Experimentation

Twenty coupons with the $[0/\pm45/90]_s$ layup and eight coupons with the $[90/0/\pm45]_s$ layup were manufactured and tested for this investigation. The configuration of these specimens is discussed in Section 3.3 and is shown in Figure 3.1. All coupon experimentation was conducted in the Technology Laboratory for Advanced Composites (TELAC) according to standard laboratory procedures, as outlined in the TELAC Manufacturing Class Notes [33].

4.1.1 Coupon Manufacture

The manufacturing procedure for composite coupons involved constructing seven 355 mm by 305 mm laminates, five with the $[0/\pm45/90]_s$ layup and two with the $[90/0/\pm45]_s$ layup, and cutting each laminate into four coupons 70 mm wide and 350 mm long. The $[90/0/\pm45]_s$ coupons were cut 305 mm long due to an error. Glass/epoxy loading tabs were also cut and bonded to both ends of each coupon. Thickness measurements and width

measurements were taken for all coupons, and through-thickness slits of varying lengths were cut in some coupons as indicated in Table 3.4.

As mentioned previously, the graphite/epoxy material system used for the coupons is AS4/3501-6. The cured properties of the material are provided in Table 3.1. This unidirectional preimpregnated tape material was provided by Hercules in 305 mm wide rolls and was stored in a freezer at a temperature below -18°C until it was ready to be used. Individual plies were cut from the rolls using special teflon-coated aluminum templates and a utility knife. The templates are designed so that a 355 by 305 mm ply of a given angle may be formed from a maximum of two pieces of material using only matrix joints. A matrix joint implies that the cut is made parallel to the fibers. This ply layup is illustrated in Figure 4.1 for a +45° ply.

Layup was accomplished by hand in a jig with two raised perpendicular sides. All plies were butted against these raised sides during layup in order to maintain their proper angular orientation in the laminate. The corner of the laminate at the intersection of the raised sides was designated as the 'good corner' for reference purposes. It is assumed that the plies are closest to their nominal orientation in this 'good corner'. The completed laminate was carefully removed from the jig and covered on both sides with 330 mm by 420 mm pieces of peel-ply fabric. The attached peel-ply sheets were trimmed on three sides to the exact dimensions of the laminate. The fourth side was not trimmed to facilitate laminate removal from the cure assembly. The 'good corner' of each laminate was marked on the peel-ply for future reference.

The $[0/\pm45/90]_s$ and $[90/0/\pm45]_s$ laminates were cured on two separate occasions. For both runs, the laminates were arranged in the standard TELAC cure assembly illustrated in Figure 4.2. As shown in this figure, a

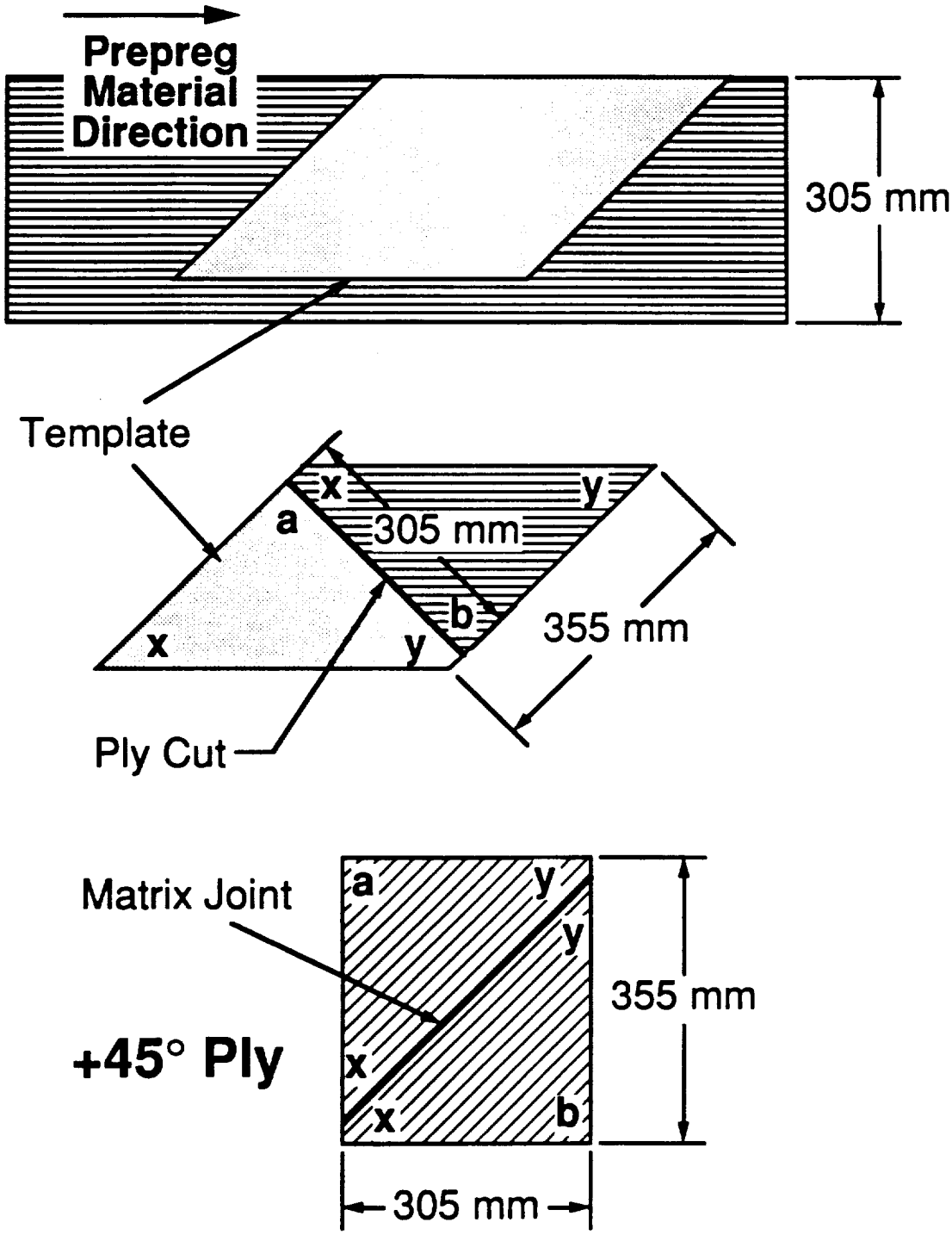

Figure 4.1 Illustration of +45° ply layup for composite coupons.

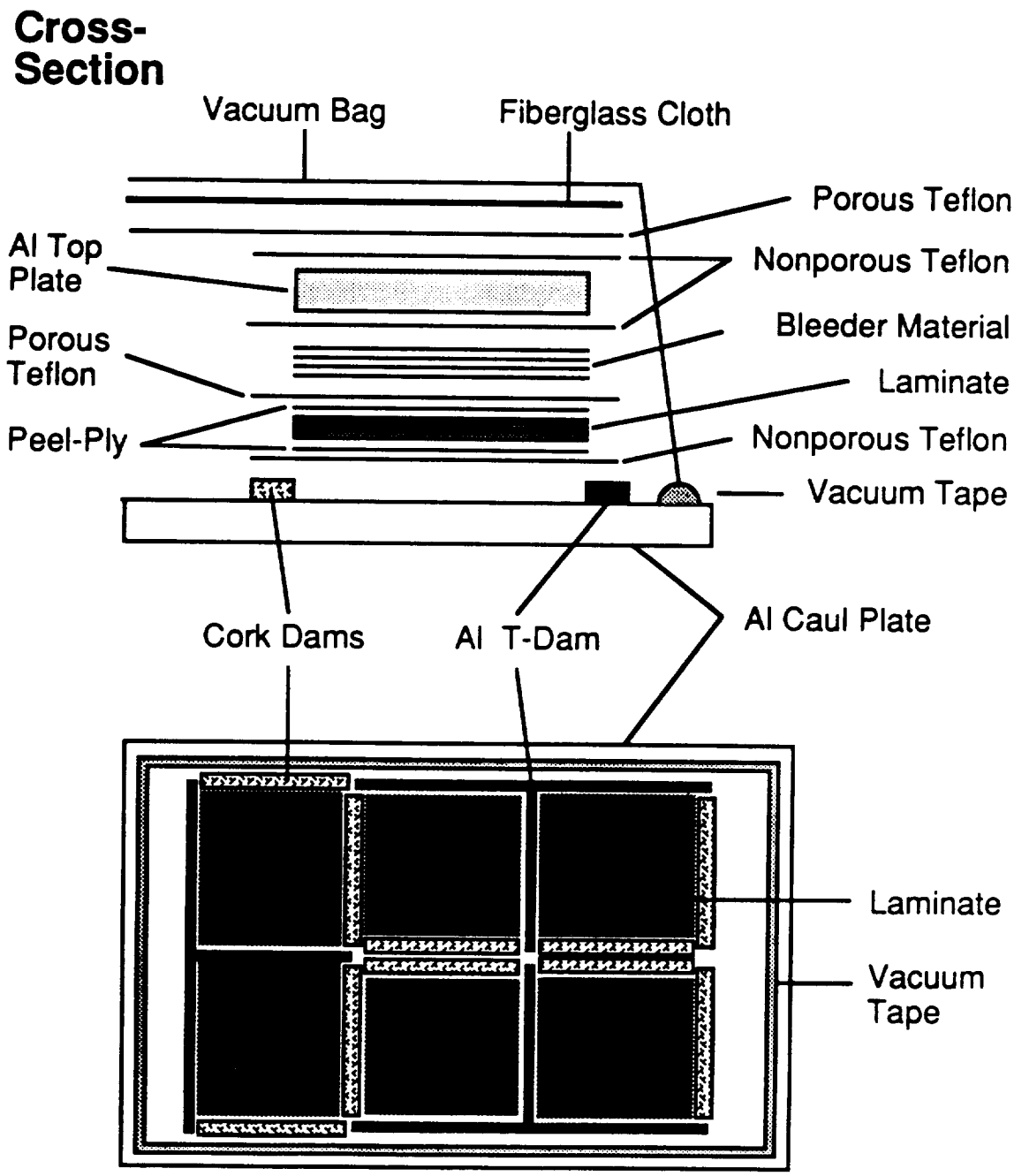

Figure 4.2 Laminate cure assembly setup.

maximum of six laminates may be cured at any one time. A clean, 1.4 m by 0.8 m by 9.5 mm thick, aluminum caul plate on a special cart was prepared by coating it with mold release and a sheet of guaranteed nonporous teflon (GNPT). One aluminum T-dam for every two laminates was placed on the cure plate so that each laminate had enough room. A 355 mm by 305 mm rectangular bay was formed for each laminate, with one side of a T-dam forming two sides of the bay and two layers of cork dam forming each of the other two sides. Each bay was lined with a 355 mm by 405 mm piece of GNPT followed by the laminate. The 'good corner' of the laminate was always placed in the bay corner formed by the aluminum T-dam. Since the material system in question bleeds resin as part of the consolidation process, bleeder paper plies were also required to soak up the resin. A piece of porous teflon was placed between the laminate and the bleeder plies to prevent the two from sticking to each other. One sheet of bleeder paper was used for every two graphite/epoxy plies in the laminate. Another sheet of GNPT was placed on top of the bleeder plies followed by a clean, 9.5 mm thick, aluminum top plate. Like all of the other aluminum components of the cure assembly, all top plates were coated with mold release before they were added to the assembly. The top plates provide uniform pressure to the laminate during the consolidation process resulting in a smooth laminate surface. Another sheet of GNPT was placed over the top plate, and then the overlap from the teflon materials in the bay was taped to this sheet to seal in the laminate and minimize epoxy flow to other parts of the cure assembly. The entire cure assembly was covered with porous teflon and two layers of fiberglass airbreather. These materials prevent the vacuum bag from rupturing on the edges of the T-dams and cork dams and allow the vacuum, which is applied through two holes in the ends of the baseplate, to effectively

consolidate and remove volatiles from the laminates. The final step in the cure assembly set-up was to attach the vacuum bag to the baseplate with vacuum tape. The laminates were then ready to be cured.

The laminates were cured in the TELAC autoclave using the cure cycle recommended by Hercules for AS4/3501-6, as shown in Figure 4.3. Prior to wheeling the cure cart into the autoclave, a vacuum test was performed to ensure that there were no leaks in the bag. A full vacuum of 760 mm Hg was pulled and then the vacuum pump was shut off for five minutes. If the strength of the vacuum fell by more than 75 mm Hg in this time period, steps were taken to repair or replace the bag. The vacuum test was repeated until the bag performance was satisfactory. The cure cart was then wheeled into the autoclave, the door was secured, the pressure safety lock was activated, and the cure process continued. Full vacuum and 0.59 MPa of autoclave pressure were applied immediately and maintained throughout the entire cure. After the pressure reached this value of 0.59 MPa, the heaters were turned on and the temperature was ramped up to 116°C at a rate of 3°C per minute. This temperature was held for one hour and then it was ramped up to 177°C at the same rate. After two hours at 177°C, the autoclave was slowly cooled at an approximate rate of 3°C per minute to avoid thermal shock to the laminates. The autoclave pressure and vacuum were not relieved until the autoclave was cooled to 66°C. The laminates were carefully removed from the cure assembly. The laminates were postcured in an oven for an additional eight hours at 177°C. No pressure or vacuum was applied during the postcuring process.

The coupons were cut from the laminates using a 254 mm diameter diamond-coated abrasive cutting wheel on a milling machine. The laminates were clamped to the milling machine table and the table was automatically

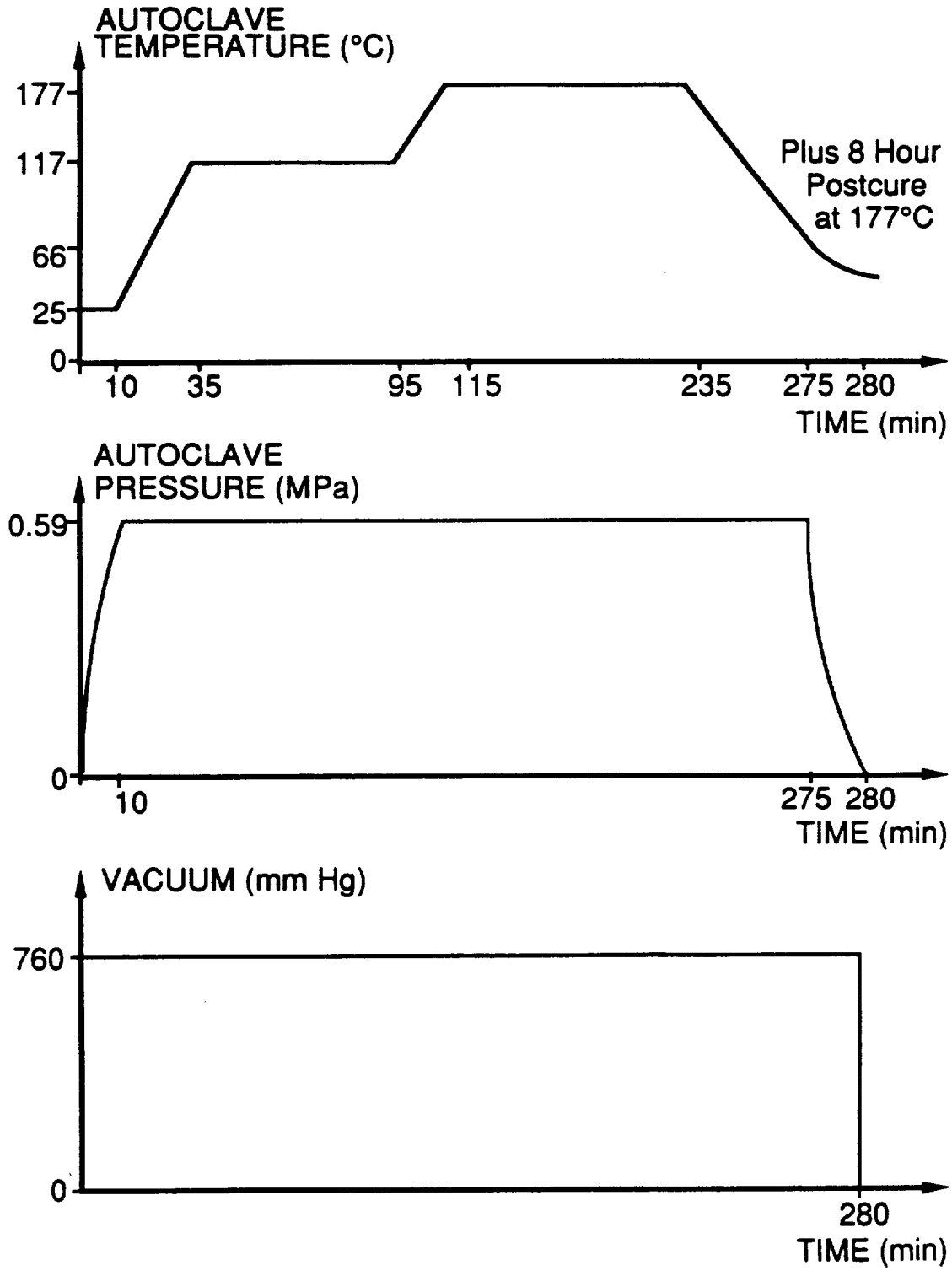

Figure 4.3 Standard cure cycle for AS4/3501-6 graphite/epoxy laminates.

fed at 280 mm per minute under the cutting wheel while it spun at 1100 rpm. Water was used to cool the cutting wheel and minimize dust during the cutting process. The first cut was made along an edge next to the 'good corner' and care was taken to ensure that the cut coupons had the same ply angles as the original laminate. Three width measurements and nine thickness measurements were taken for each specimen at the locations shown in Figure 4.4. These locations were marked using a cardboard template and a paint pen before the measurements were taken. The average thickness for the $[0/\pm45/90]_s$ coupons is 1.10 mm with a coefficient of variation of 2.1%. The average width of these coupons is 70.1 mm with a coefficient of variation of 0.1%. For the $[90/0/\pm45]_s$ coupons, the average thickness is 1.08 mm with a coefficient of variation of 2.3%. The average width of these coupons is 70.2 mm with a coefficient of variation of 0.1%. The nominal thickness of 1.072 mm and nominal width of 70 mm were used for all subsequent calculations in this investigation. Average thickness and width measurements for each coupon are tabulated in Appendix A.

Fiberglass loading tabs were bonded to both sides of both ends of each coupon in order to reinforce the coupon so it would not be damaged by the hydraulic gripping force of the testing machine. The 70 mm wide by 75 mm long tabs for the $[0/\pm45/90]_s$ specimens, and 70 mm wide by 53 mm long tabs for the $[90/0/\pm45]_s$ specimens, were cut on the milling machine from purchased 380 mm by 600 mm sheets of Scotchply 1002 glass/epoxy. The sheets used had 15 or 13 plies in a 0/90 type stacking sequence. In order to provide smooth load transfer from the tabs to the coupon, the top edge of each tab closest to the coupon test section was beveled to a 30° angle before being bonded. This process was accomplished using a belt sander. American Cyanamid's FM123-2 film adhesive was used to attach the loading tabs to the

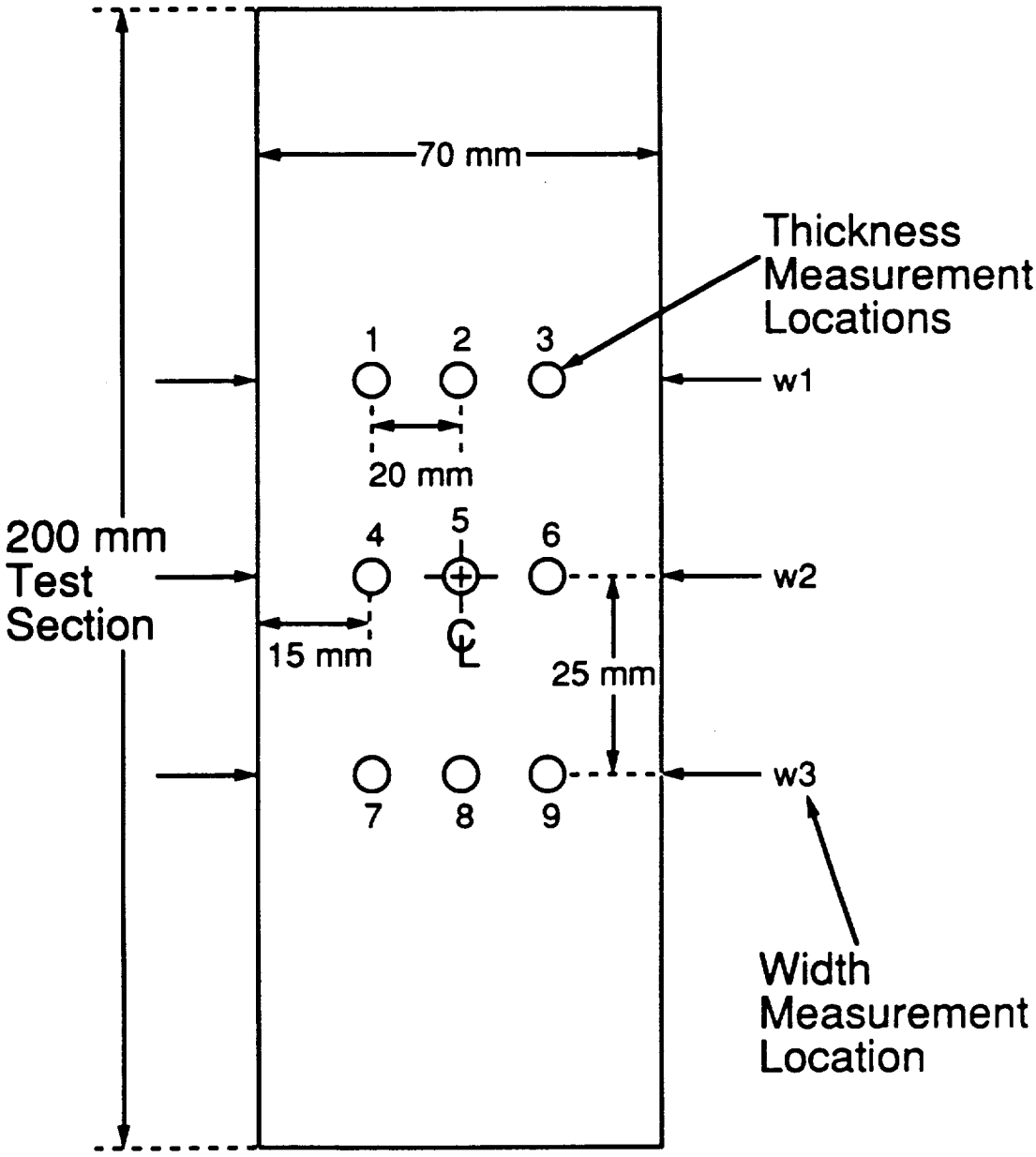

Figure 4.4 Measurement locations for coupons.

coupons. Tabs that were carefully cleaned with methanol and gauze were placed on the film and a utility knife was used to cut around each tab. The tabs were positioned along the length of the coupon so that they were 100 mm from the specimen centerline and care was taken to ensure that the beveled edges of the tabs lined up on both sides of the coupon.

Two bond cures, one for each layup, were conducted in the autoclave to permanently attach the loading tabs to the coupons. The coupons with attached tabs were placed on the aluminum baseplate covered with mold release and GNPT. Scrap glass/epoxy material, the same thickness as the loading tabs, was placed under the test section of each coupon to prevent it from deflecting downward due to pressurization during the cure. All coupons were covered with GNPT followed by a layer of steel top plates. The top plates are necessary for uniform loading on the tabs during the cure. The top plates were covered by a sheet of porous teflon followed by four layers of fiberglass airbreather and a vacuum bag. These materials serve the same purposes as in the laminate curing process. The vacuum test was conducted as previously described, and then the cure was conducted for two hours at 107°C. Full vacuum and 0.07 MPa of autoclave pressure were applied throughout the entire bond cure. This pressure is based on a needed pressure of 0.28 MPa on the loading tabs and depends on the ratio of the area of the steel plates to the area of the tabs. As in the laminate cure, the temperature was not applied until the final pressure was achieved. Heating and cooling of the autoclave were again conducted at 3°C per minute.

Slits were cut perpendicular to the loading direction and centered on the test section in 16 of the 20 $[0/\pm45/90]_s$ coupons and in all 8 of the $[90/0/\pm45]_s$ coupons. As indicated in Table 3.4, four $[0/\pm45/90]_s$ coupons and two $[90/0/\pm45]_s$ coupons all received the same slit size with one of the

following lengths: 9.5, 12.7, 15.9, or 19.1 mm. The slit location was established perpendicular to the long edge of the specimen that was originally closest to the 'good corner', or the 'good edge' of the specimen, using a level and a ruler. A scribe was used to mark the slit location on each coupon. Masking tape was placed just inside of the ends of the marked slit location so that it would be easier to see where to stop cutting.

Cutting of the slits was accomplished using a 0.74 mm diameter, 220 grit, diamond-coated endmill that was mounted in a DREMEL™ rotary tool and spun at 30,000 rpm. The set-up schematic for coupon slit cutting is shown in Figure 4.5. Scrap glass/epoxy material was placed under the coupon test section for support and a master square was used to align the 'good edge' of the coupon so that it was perpendicular to the long edge of the milling machine table. After the coupon was aligned and supported, it was clamped to the table using a C-clamp and a clamping bar. The DREMEL™ was vertically attached to the milling machine arm after a master square was used to position this arm perpendicular to the machine table. The alignment of the endmill with respect to the coupon was also checked with a master square and adjustments were made as necessary to ensure that the endmill was perpendicular to the coupon. The final alignment check was to position the endmill over one end of the slit and move the table sideways to pass the endmill down to the other end of the slit. If the endmill stayed over the etched slit location line, the slit was ready to be cut.

Slit cutting was started at one end of the slit by moving the table up towards the endmill. A 0.18 mm deep cut was made in the coupon, and then the table was slowly moved sideways to cut the slit. When the other end of the slit was reached, another 0.18 mm deep cut was made and the table was moved back in the other direction. This process continued until the endmill

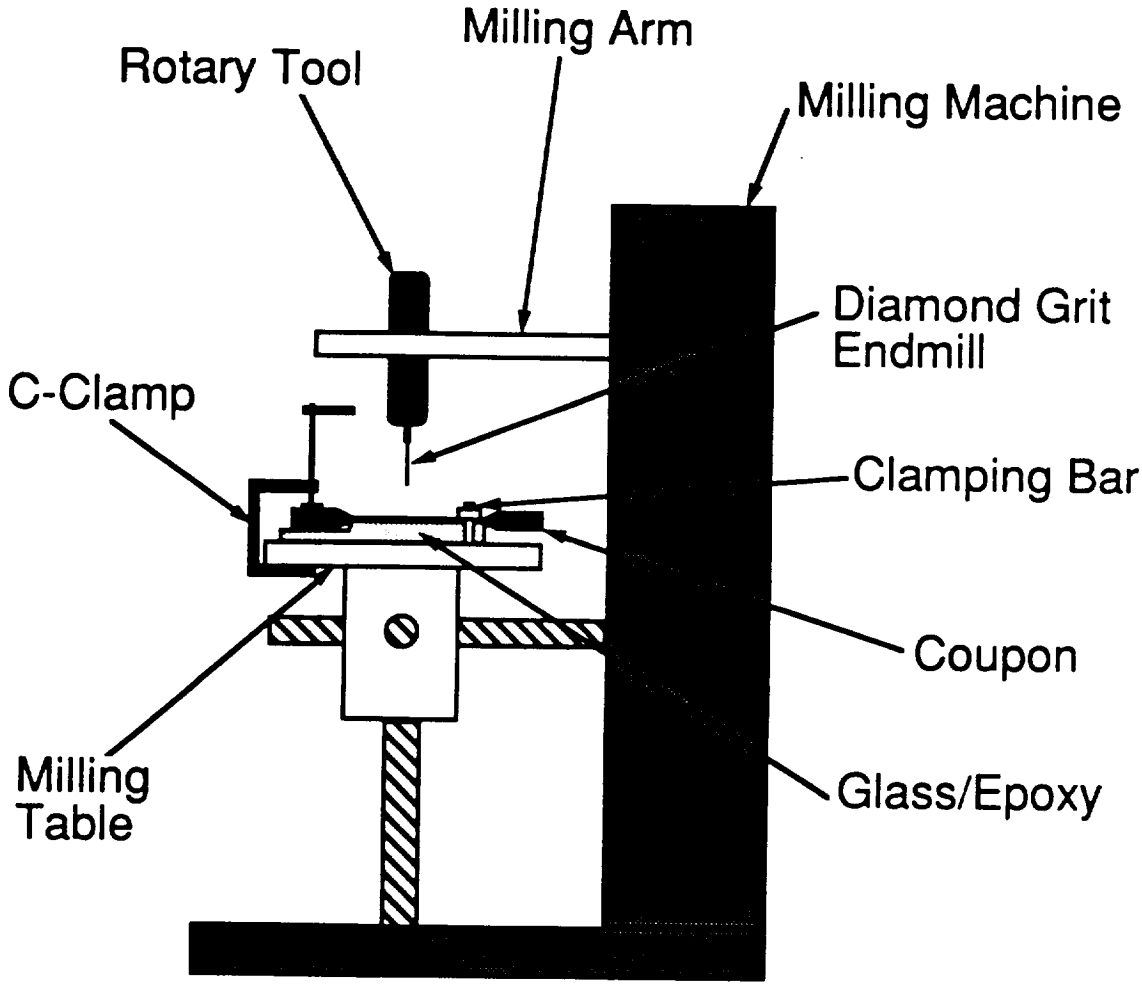

NOTE: Not to Scale

Figure 4.5 Illustration of coupon slit cutting setup.

passed all the way through the thickness of the coupon. Deeper cuts were not used for each cutting pass since this would put too much stress on the endmill and would cause it to break. Water from a bottle was used to cool the endmill during the cutting process. The slits were finished and the slit tips were sharpened using jeweler's saws that were sharpened on a grinder. These saws are initially 0.5 mm thick. One pass of the saw across the grinder was made on each side to decrease the thickness. An additional pass was made on each side, with the saw held at an angle, to sharpen the teeth to a point. The post-grinding thicknesses of the saws were not measured. The slits were inspected under a microscope and the slit lengths were measured to the nearest 0.1 mm with an eye-piece micrometer. The measured slit lengths are tabulated in Appendix A and were used in all subsequent calculations in this investigation.

4.1.2 Coupon Instrumentation

All 28 coupons tested in this investigation were instrumented with EA-06-125-AD-120 strain gages from the Micromeasurements Company. One transverse and one longitudinal gage were bonded to the unnotched specimens so that the Poisson's ratio and longitudinal modulus could be determined and compared to the predicted values from Classical Laminated Plate Theory. The gages on these specimens were centered across the width of the specimen and the center of each gage was placed 13 mm from the horizontal centerline as shown in Figure 4.6. Notched coupons were each instrumented with one longitudinal gage. This gage was located 17.5 mm in from the specimen edge and 50 mm from the horizontal centerline as shown in Figure 4.7. The gage on each notched $[0/\pm45/90]_s$ specimen was used to ensure that the far-field behavior of the coupon was the same as that of the

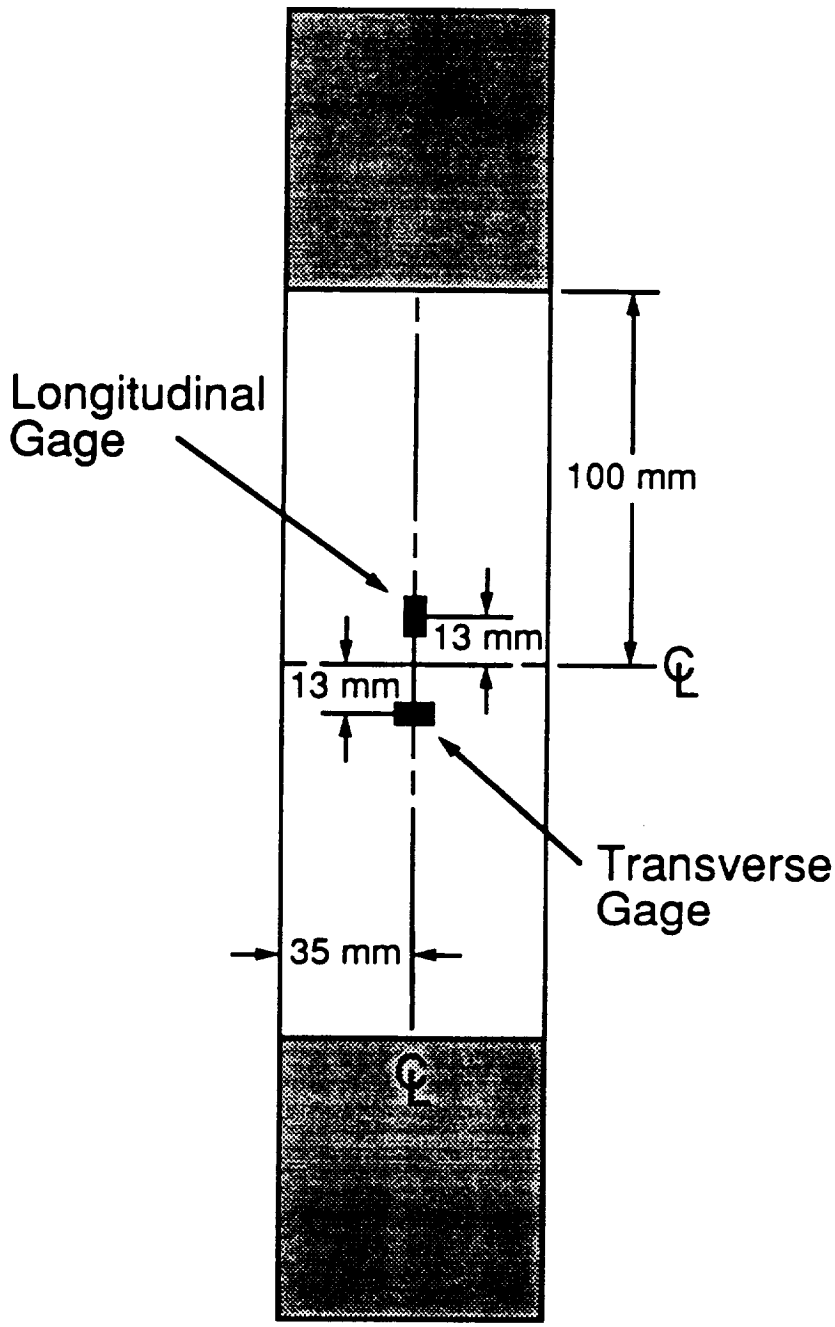

Figure 4.6 Strain gage locations for unnotched coupons.

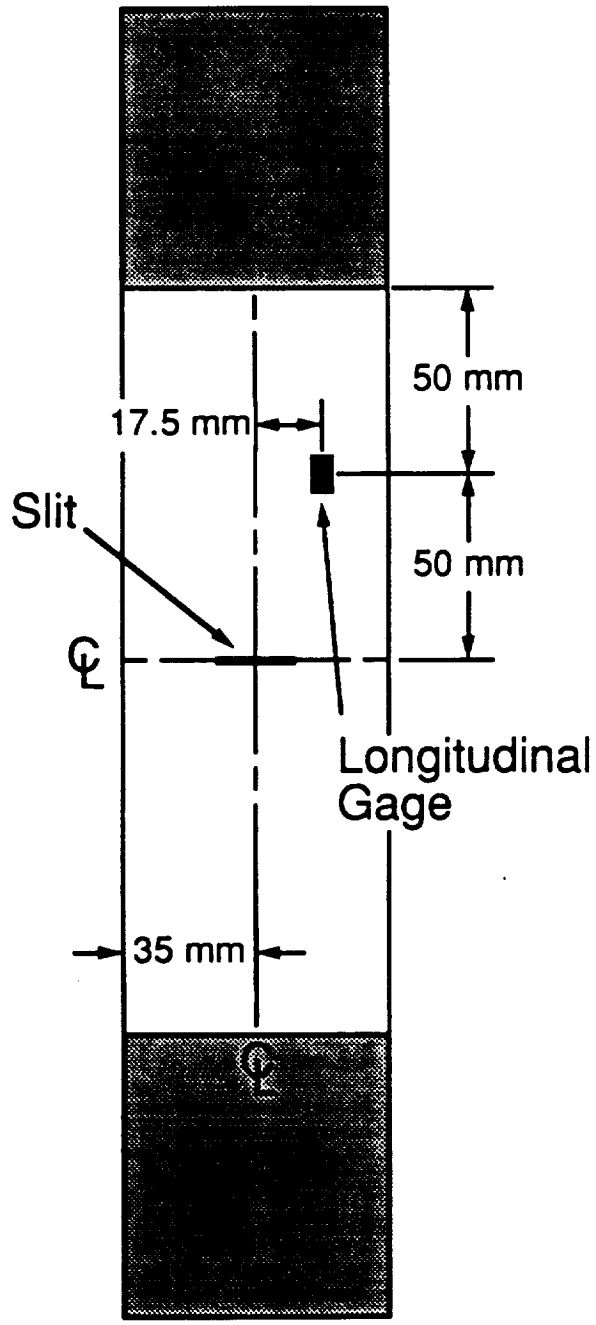

Figure 4.7 Strain gage locations for notched coupons.

unnotched specimens. The gages on the notched $[90/0/\pm45]_s$ specimens were used to determine the longitudinal modulus since no unnotched specimens of this layup were tested.

4.1.3 Coupon Testing

All coupons were tested to failure using an MTS 810 testing machine equipped with hydraulic grips. The coupons were inserted into the upper grip first and were pushed in far enough so that the loading tabs would be entirely covered. A square was used to align each coupon with the loading direction and then the upper grips were closed. The upper crosshead of the testing machine was lowered until the bottom loading tabs of the coupon were completely within the bottom grips. Before the bottom grips were closed, the strain gages on the specimen were zeroed and calibrated. These two steps are done in this order since closing the bottom grips can induce a small preload in the specimen.

Coupons were loaded monotonically to failure under stroke control at a rate of 0.018 mm/sec. This loading rate corresponds to a strain rate of 90 μstrain/sec in the test section of the coupon. A Macintosh IIx computer equipped with Labview data acquisition software was used to record the stroke, load, and strain data at a frequency of 2 Hz. Any audible 'clicks' heard during the test were also recorded by the software by clicking on a computer screen icon with the mouse. A new data file was generated for each coupon tested.

Immediately following a coupon test, the maximum load indicator on the testing machine was read and the load value was noted so that the failure stress could be determined for the coupon. This load value was compared with the highest value in the computer data file to ensure that the values

were similar. However, the testing machine value was used for all subsequent calculations since it was based on a higher sampling frequency. All coupons were photographed to record their failure modes and failure paths were compared to assess the consistency of the results. The strain data for each coupon were examined and compared to those of other specimens. Any unusual or inconsistent results were noted.

4.2 Cylinder Experimentation

A total of 13 cylinders were manufactured for this investigation with the following layups: $[90/0/\pm45]_s$, $[0/\pm45/90]_s$, $[\pm45/0]_s$, and $[\pm45/90]_s$. The calculated extensional properties for these layups from Classical Laminated Plate Theory are provided in Table 3.2. The configuration of these specimens was discussed in Section 3.3 and is shown in Figure 3.2. All cylinder experimentation was conducted in TELAC according to standard laboratory procedures. As previously mentioned, information specific to the uniaxial loading of cylinders is presented in the next chapter.

4.2.1 Cylinder Manufacture

The manufacturing process for composite cylinders involves numerous steps including cylinder construction, trimming and leveling of the cylinder ends, gridding, and bladder construction. Thickness measurements were taken for each specimen and through-thickness axial slits of varying lengths were cut in the cylinders as indicated in Tables 3.3 and 3.6. Also, endcaps were bonded to the cylinders that were tested in biaxial loading.

Cylinders were constructed using an aluminum mandrel with a length of 1.2 m, an outer diameter of 305 mm, and a wall thickness of 6.4 mm. During the layup procedure, the mandrel was supported 1.15 m off the

ground by a motorized tubewinder, as shown in Figure 4.8. A footpedal connected to the tubewinder was used to rotate the mandrel in either direction at 3 rpm. A vacuum port is located on the mandrel near one end and two holes on opposite sides of the mandrel at both ends allow rods to be inserted so that the mandrel may be carried and suspended in the autoclave.

The same 305 mm wide rolls of AS4/3501-6 graphite/epoxy material were used in the manufacture of cylinders as were used in the manufacture of coupons. The required overall ply dimensions for an angle ply may be determined via the following formulation. The geometry is shown in Figure 4.9. The required ply width, W, is calculated using the equation:

$$W = P\cos\theta \tag{4.1}$$

where P is the circumference of the cylinder and θ is the ply angle. The overall ply length required, L", is calculated from:

$$L" = \frac{L}{\cos\theta} + P\sin\theta \tag{4.2}$$

where L is the length of the cylinder. The required overall ply dimensions for 0° and 90° plies are shown in Figure 4.10. The hoop length of the 0° plies is 12.7 mm longer than the circumference of the cylinder to allow for an overlapped fiber joint in the back of the tube, defined as the side opposite the slit location and manufactured on the vacuum port side of the mandrel. This joint provides a path for smooth load transfer through shear between the fibers on both sides of the joint. It also prevents a gap from developing

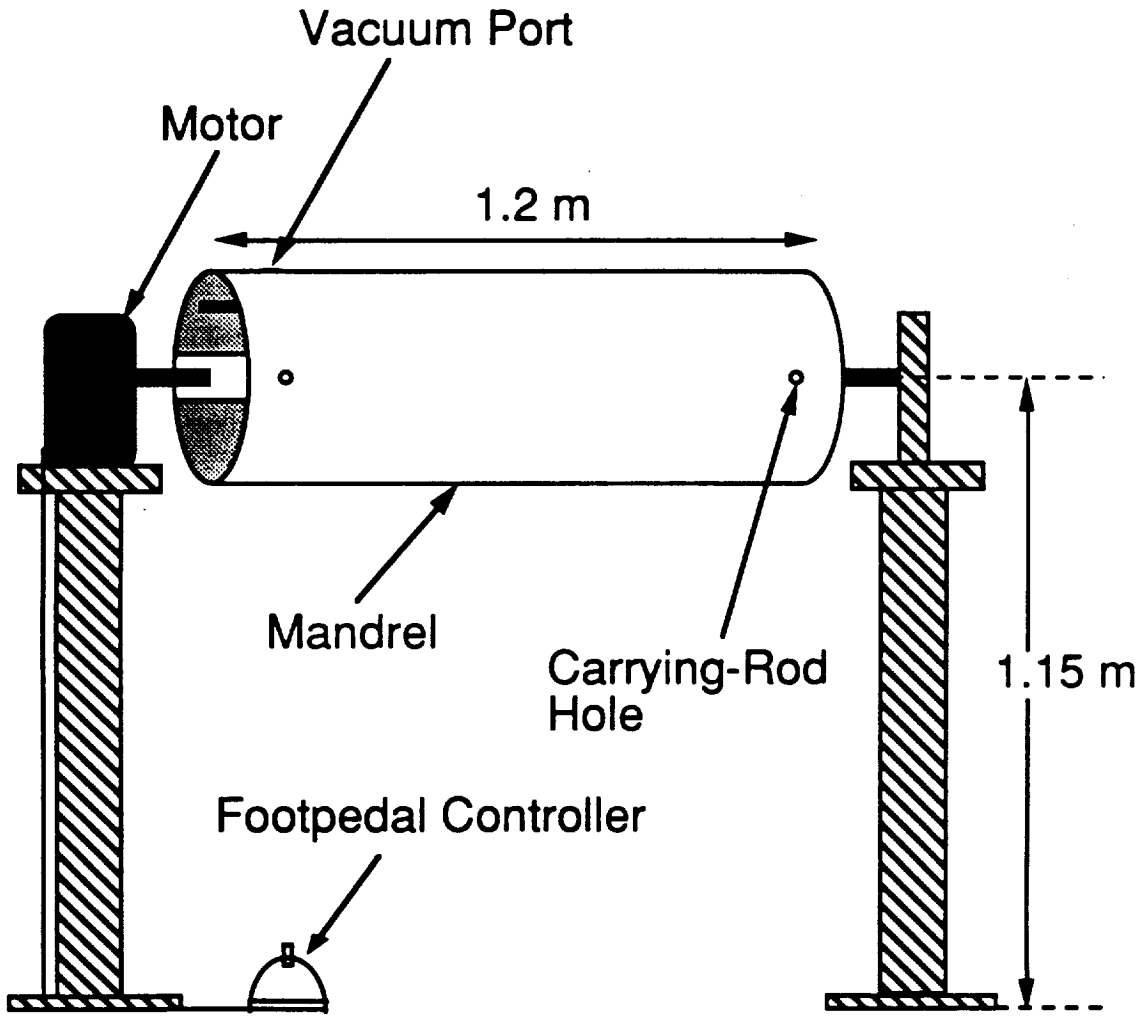

Figure 4.8 Illustration of motorized tubewinder and mandrel.

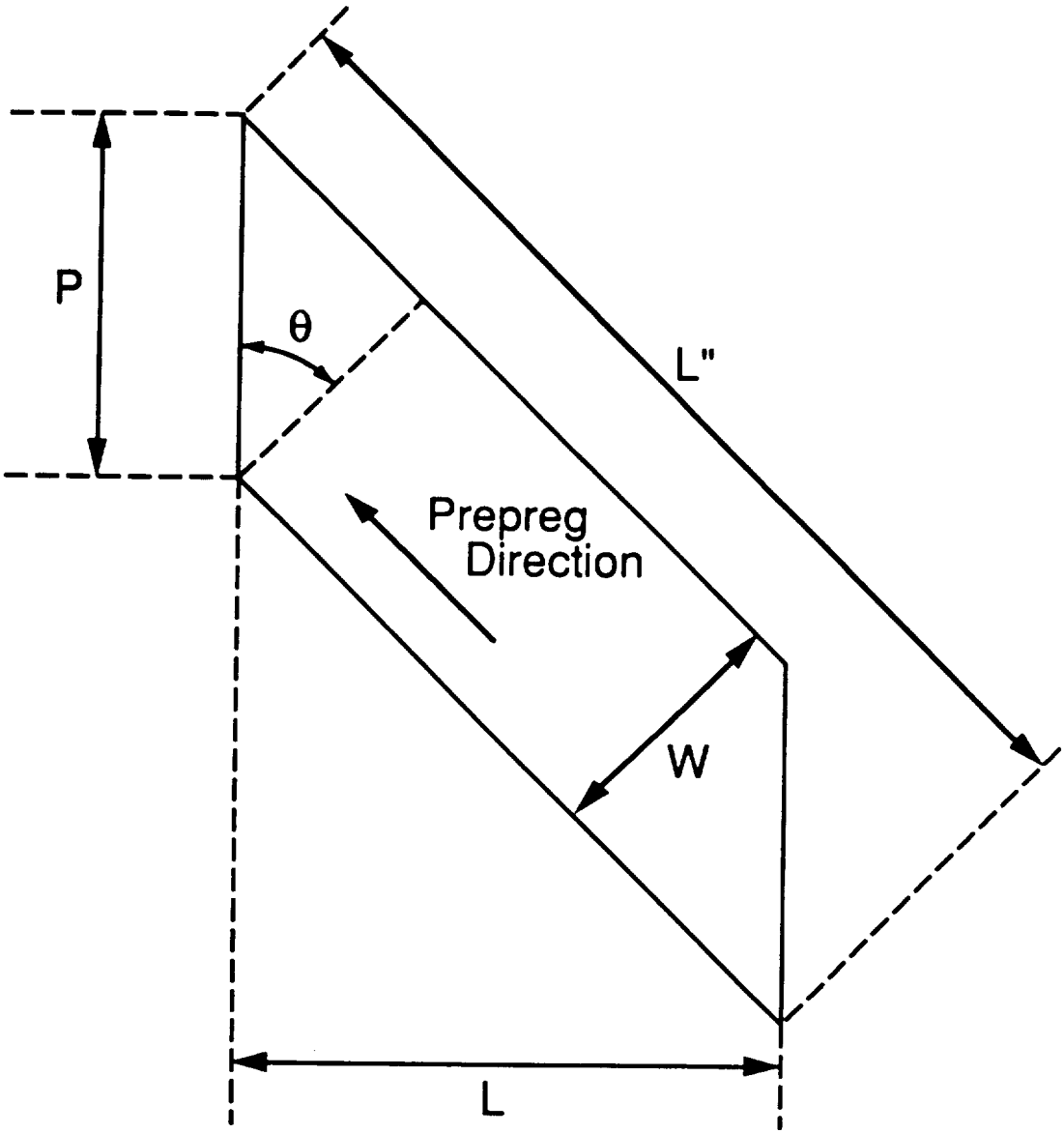

θ = Ply Angle
P = Cylinder Circumference
W = Width of Ply
L = Cylinder Length
L" = Overall Ply Length

Figure 4.9 Important geometric parameters for angle ply dimension calculations.

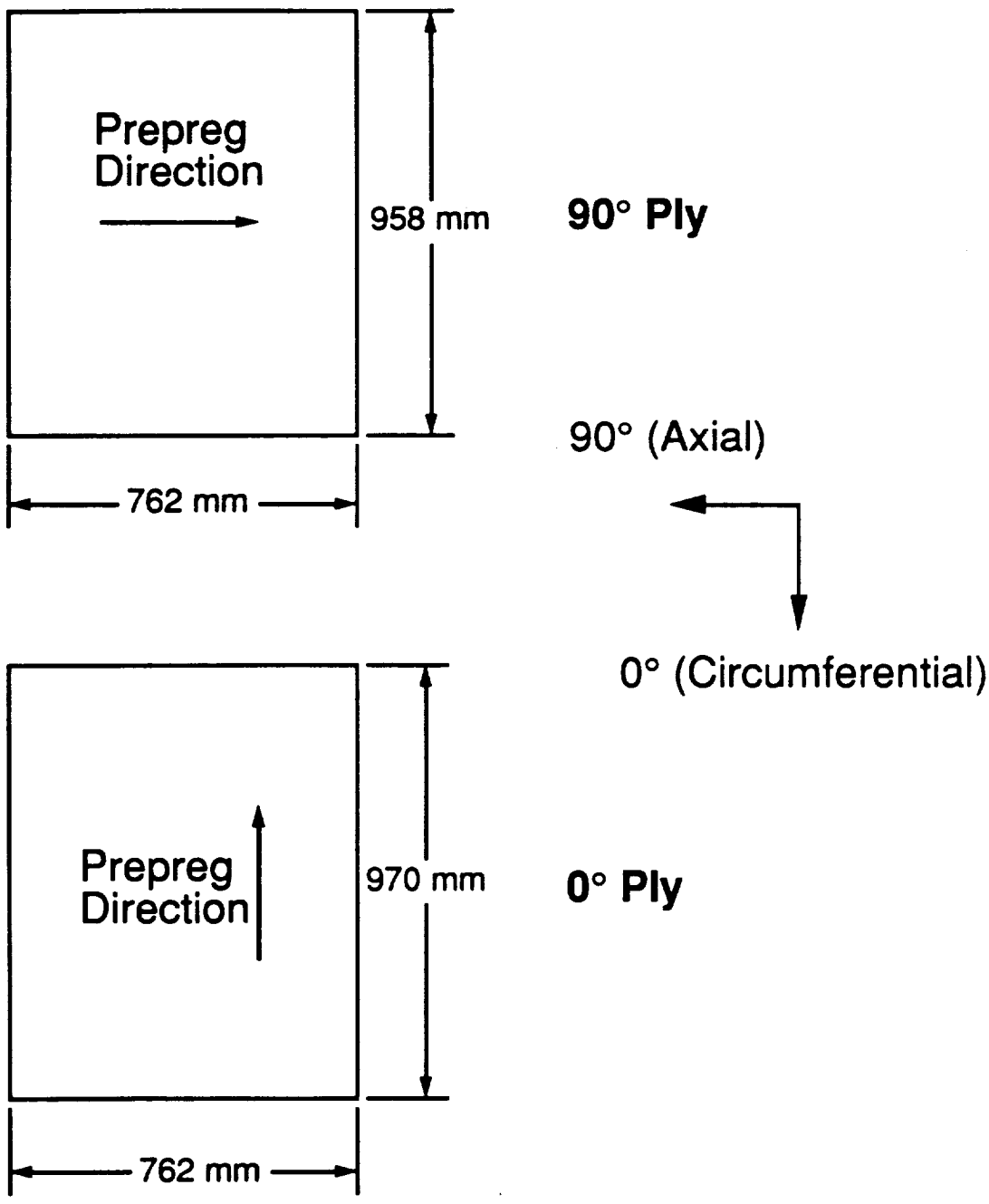

Figure 4.10 Geometry of *(top)* 90° and *(bottom)* 0° plies.

between the fibers during the loading process due to the circumferential expansion.

Since the rolls of material used were only 305 mm wide, several large pieces of the unidirectional tape material, or subplies, were needed to make up each ply in the cylinder. Each subply was cut with a teflon-coated aluminum template and a utility knife. The dimensions and orientations of the subplies in a 0° and 90° ply are shown in Figure 4.11. The 0° ply is formed from two pieces of material that are the width of the roll (305 mm) and 970 mm long and one piece that is half the width of the roll (152 mm) and 970 mm long. The 90° ply is formed from three pieces of material that are the width of the roll (305 mm) and 762 mm long and one piece that is 43 mm wide and 762 mm long. The dimensions and orientations of the subplies in +45° and -45° plies are shown in Figure 4.12. Each of these angle plies is formed from two pieces of material that are the width of the roll (305 mm) and have an overall length of 1382 mm and from one piece of material with a width of 68 mm and an overall length of 1146 mm. The ends of the subplies for the angle plies were cut at +45° and -45° angles with respect to the fiber direction, as appropriate for the ply in question. The dimensions of the subplies for all plies in the cylinder were chosen to minimize material waste and the number of joints in each ply. All of these joints are matrix joints made parallel to the fibers, except for the aforementioned fiber joint for the 0° plies.

Before starting a cylinder layup, the mandrel was cleaned, coated with mold release, and covered with a sheet of GNPT. This GNPT sheet was wrapped tightly around the mandrel to avoid wrinkles and secured to the back of the mandrel using flash tape and transfer tape. The front, back, and ends of the cylinder and mandrel were designated as indicated in Figure 4.13,

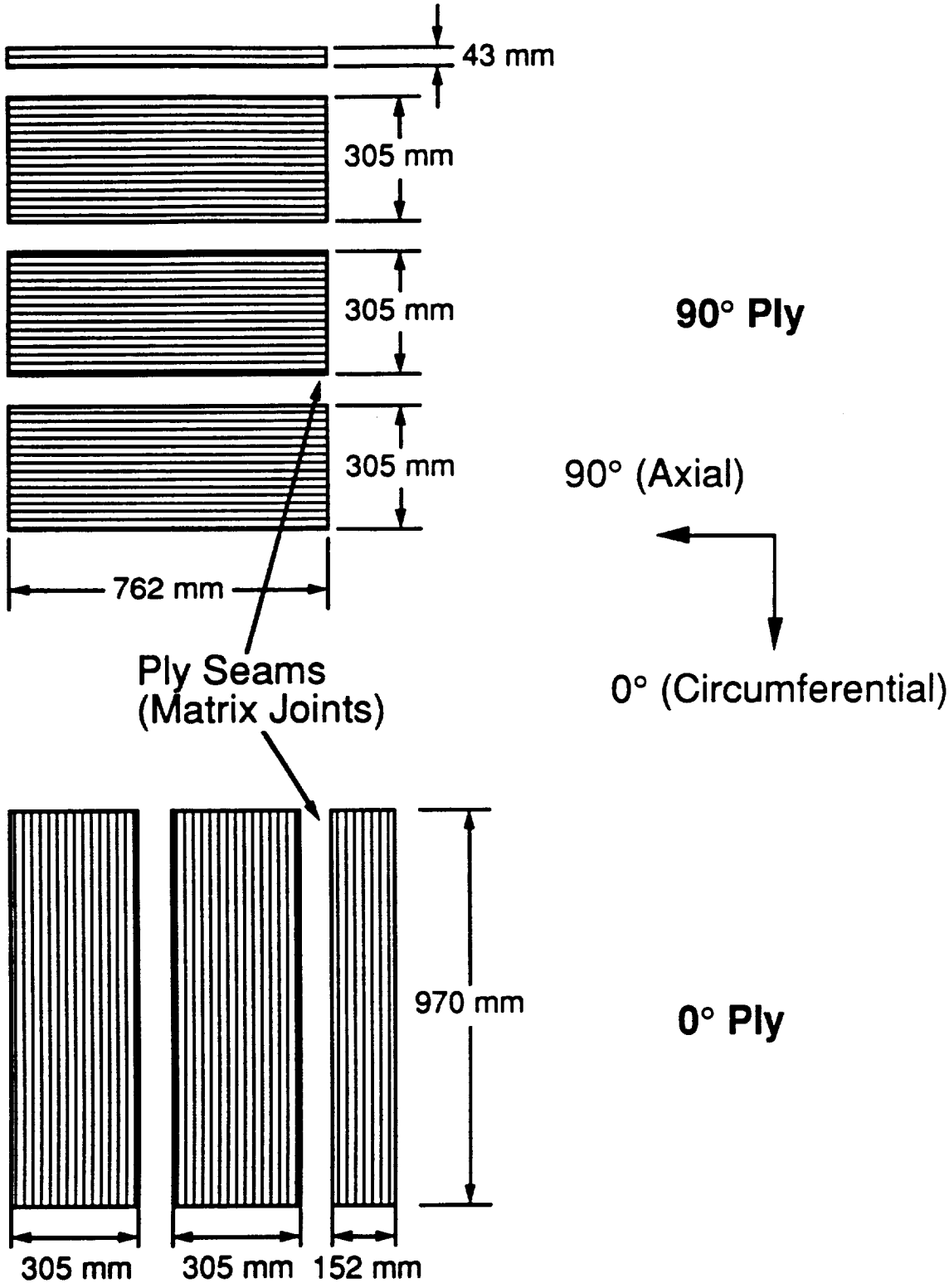

Figure 4.11 Subply dimensions and orientations for *(top)* 90° and *(bottom)* 0° plies.

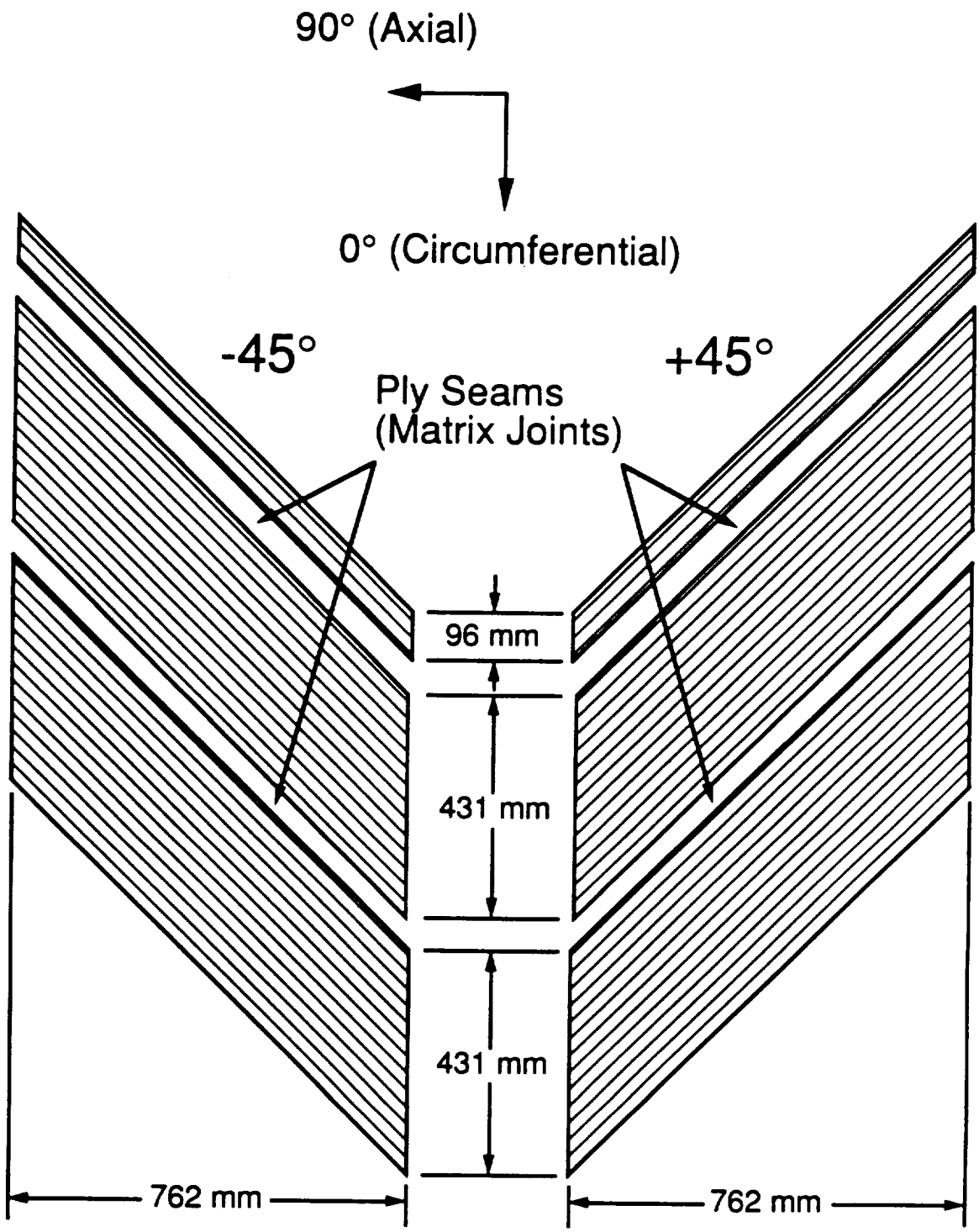

Figure 4.12 Subply dimensions and orientations for +45° and -45° plies.

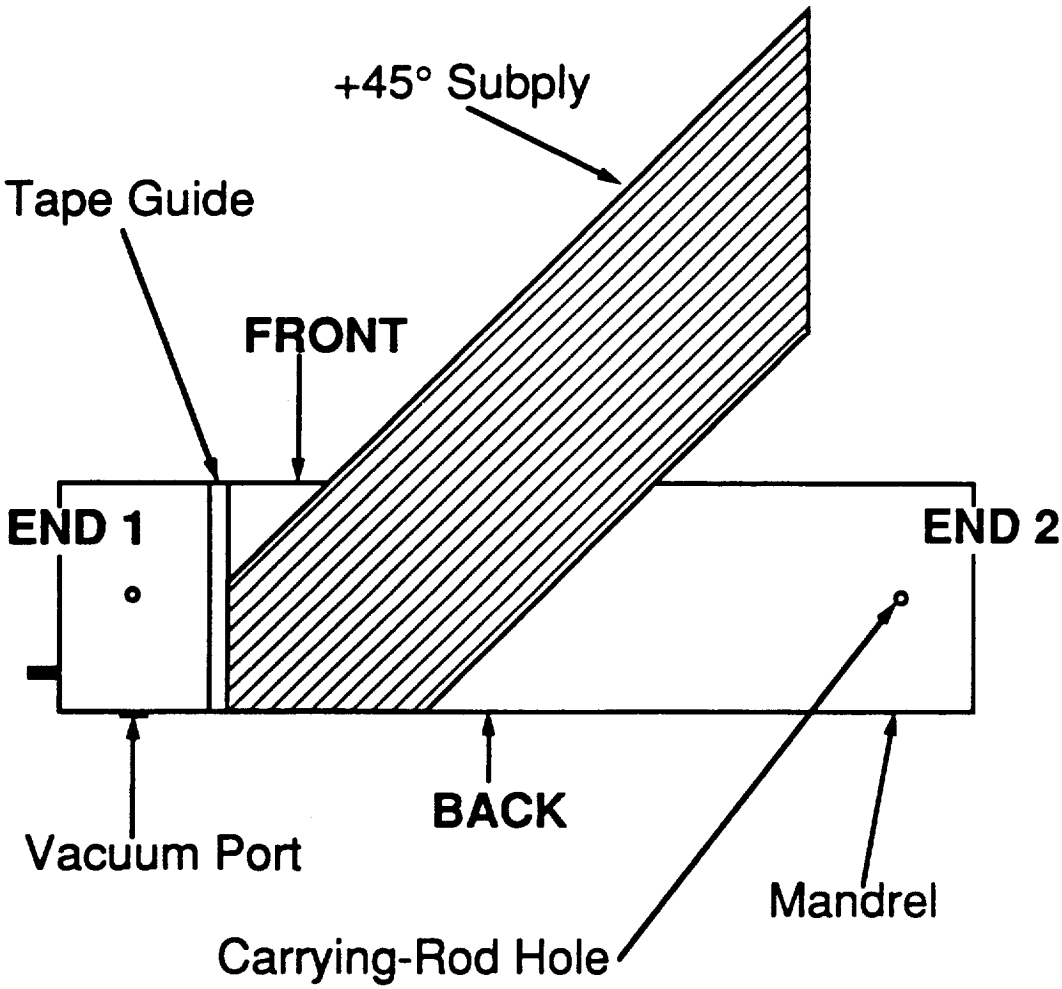

Figure 4.13 Illustration of cylinder layup procedure.

for reference purposes. These locations for both the cylinder and mandrel always coincided during the layup process. The back of the mandrel, as well as the back of the cylinder, were designated as the side of the mandrel where the vacuum port is located. The front of the cylinder and mandrel, or test section of the cylinder, were designated as the side of the mandrel opposite the vacuum port hole. This is the location where the slit was later machined. End 1 of the cylinder and mandrel were designated as the end of the mandrel where the vacuum port is located. A tape guide, as shown in Figure 4.13, was positioned in the circumferential direction at End 1 of the mandrel to aid in the orientation of the subplies. A wide strip of GNPT with straight, parallel sides was wrapped around the mandrel before the tape guide in order to establish the circumferential direction. The guide was established by wrapping a continuous strip of flash tape around the mandrel so that its edge was flush with the edge of the GNPT strip. The GNPT strip was removed after the tape guide was in place.

Subplies were applied to the mandrel one at a time by hand, starting at the tape guide end of the cylinder. This process is illustrated for a +45° subply in Figure 4.13. The first subply for each ply was oriented using the tape guide. Subsequent subplies were oriented to achieve smooth joints with the previously attached plies. Accidental seam overlaps or underlaps were corrected after the whole ply was laid down by trimming or filling with thin 'gap filler' strips. These 'gap filler' strips are long pieces of unidirectional material, generally less than 5 mm wide, that were cut from prepreg that was left over from when the subplies were cut. 'Gap filler' strips were cut whatever length and width was necessary to fill the gap in question. Consequently, in some instances discontinuous fibers were present along the seam between adjacent subplies. To minimize any adverse effects from these

discontinuous fibers, care was taken to place the subplies so that joints would not coincide for similar plies and joints would be as far removed as possible from the cylinder test section.

The cure assembly for composite cylinders used most of the same materials as that previously described for coupons. After all the plies were laid up, the cylinder was covered with peel-ply and then a sheet of porous teflon. A continuous sheet of bleeder paper was also wrapped around the cylinder to soak up the excess epoxy that the material system bleeds as part of the consolidation process. This sheet was wrapped around the cylinder three times for the six-ply cylinders and four times for the eight-ply cylinders. All of the materials mentioned above were wrapped tightly to prevent wrinkles from being formed on the cylinder surface during the cure, and the materials were always overlapped and attached in the back of the cylinder. A continuous strip of 152 mm wide fiberglass airbreather was wrapped around the mandrel starting at the vacuum port and ending 60 mm along the length of the cylinder on the end closest to the vacuum port. The vacuum port was covered fully by the airbreather. This airbreather allowed the vacuum to effectively consolidate and remove volatiles from the cylinder during the cure. The final step in the cure assembly setup was to attach the vacuum bag using vacuum tape. Extreme care was used to achieve a tight, wrinkle-free bag since any wrinkles of the bag appear as wrinkles in the cylinder.

The cylinders were cured in the TELAC autoclave using the same cure cycle described in Section 4.1.1 for composite coupons (see Figure 4.3). The vacuum bag test that is also described in this section was conducted before the cure. After the cure, the external cure materials had to be chipped off with a knife and spatula before the cylinder could be removed from the mandrel. The cylinder was loosened by banging End 2 of the mandrel on the

floor several times. The cylinder was then removed from the mandrel by sliding it off on End 2. The peel-ply was removed from the cylinder and the cylinder was postcured in an oven for eight hours at 177°C.

Both ends of each cylinder were trimmed and leveled using a DREMEL™ rotary tool with a 25.4 mm diameter cutting wheel and files. A wide strip of GNPT with straight parallel edges was wrapped around the circumference of the tube to establish the cutting line, and a paint pen was used to mark the line. The GNPT strip was lined up carefully before each line was drawn in order to maximize the degree of parallelness of the two ends and ensure that the cut would be made along the hoop direction. The DREMEL™ was hand-held during the cutting process, and the cutting was done carefully to minimize the need for subsequent filing. The levelness of the cylinder was checked by placing it on a flat surface and using a master square to see how close the cylinder walls were to vertical. Filing was done cautiously and sparingly to prevent damage to the ends of the cylinder. The trimming and leveling process resulted in slightly different lengths for each cylinder that are all within 18 mm of the average length of 749 mm. The average lengths of the cylinders, as determined from several measurements on each tube, are tabulated in Appendix A.

To aid in the reassembly of the cylinder fragments after the test, a square grid, 51 mm by 51 mm per square, was drawn on the cylinder with a paint pen. Each square in the grid was labeled with a letter and number, as shown in Figure 4.14. Columns in the axial direction received the same letter and rows in the circumferential direction received the same number. The square receiving the identifier 'A1' was located at End 1 of the cylinder to the right of the axial slit location line. Numbers increased towards End 2 of the cylinder and letters increased in the counter-clockwise direction when End 1

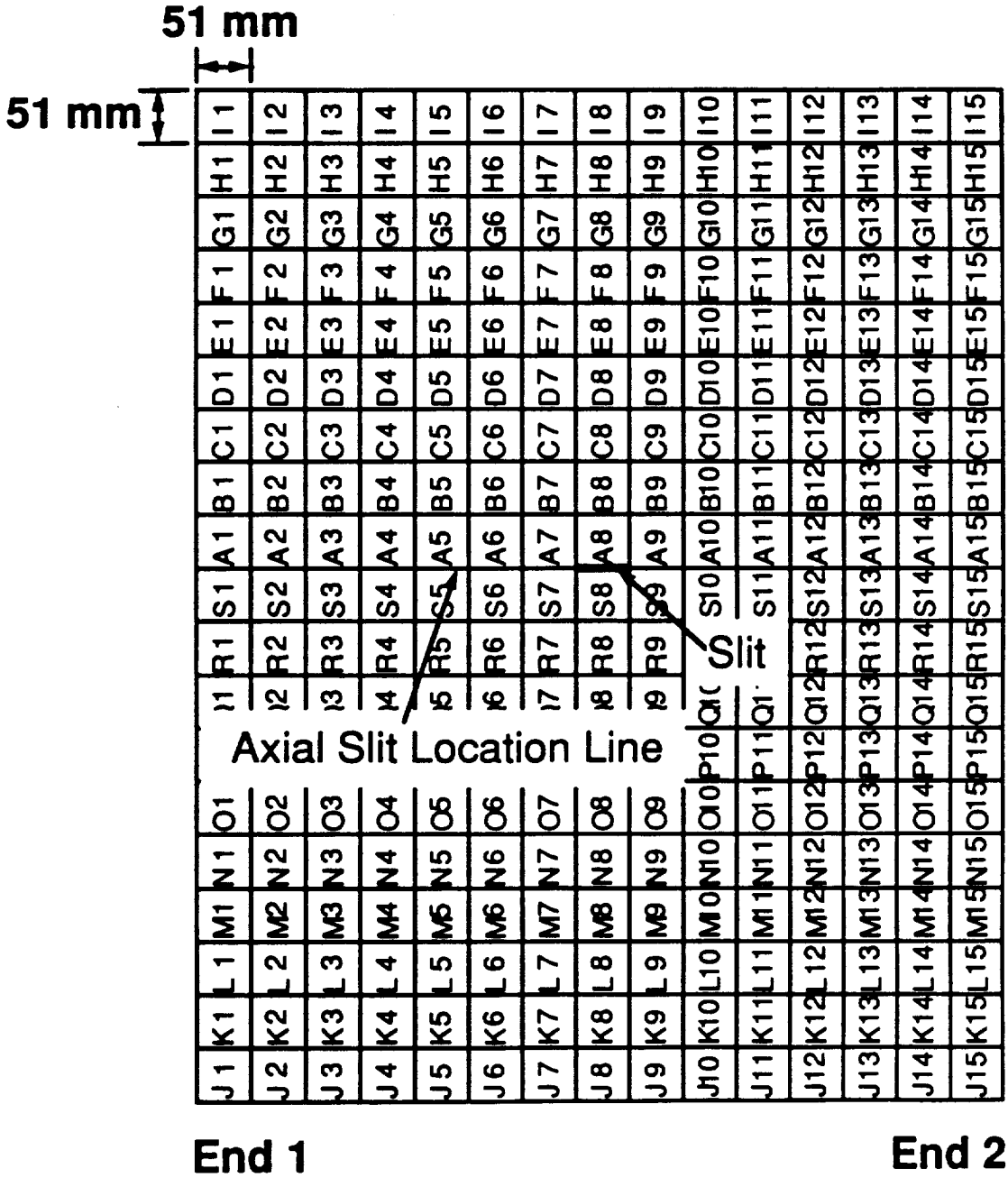

Figure 4.14 Cylinder paint identification grid.

of the cylinder was up. The slit is located on the line between the grid squares marked 'S8' and 'A8'.

Nine thickness measurements were made for each cylinder in the locations indicated in Figure 4.15. All measurements were made approximately 51 mm in from the ends of the cylinder using a micrometer. A measurement was taken on End 1 of the cylinder every 90° starting from the axial slit location line. On End 2, a measurement was taken at the axial slit location line, and then measurements were taken every 90° starting from the location +45° from the slit line location. The average thickness for the six-ply specimens is 0.81 mm with a coefficient of variation of 0.7%, while the average thickness for the eight-ply specimens is 1.08 mm with a coefficient of variation of 1.3%. The nominal thicknesses of 0.804 mm for the six-ply specimens and 1.072 mm for the eight-ply specimens are used for all subsequent calculations in this investigation. Average thicknesses for each cylinder are tabulated in Appendix A.

The axial slit location line, that was previously mentioned, was established on the front of the cylinder. A wide strip of GNPT with straight, parallel edges was wrapped around the center of the tube to establish the circumferential direction. Another strip of GNPT with perpendicular edges was aligned with the first strip to determine the axial direction. A ruler and paint pen were then used to mark the axial slit location line. The slit was scribed in the center of the tube along this line. Masking tape was placed just inside of the ends of the marked slit location so that it would be easier to see where to stop cutting.

Slits with lengths between 12.7 and 50.8 mm were cut into the cylinders using the TELAC milling machine set-up shown in Figure 4.16. The ends of a cylinder were placed in complementary convex and concave

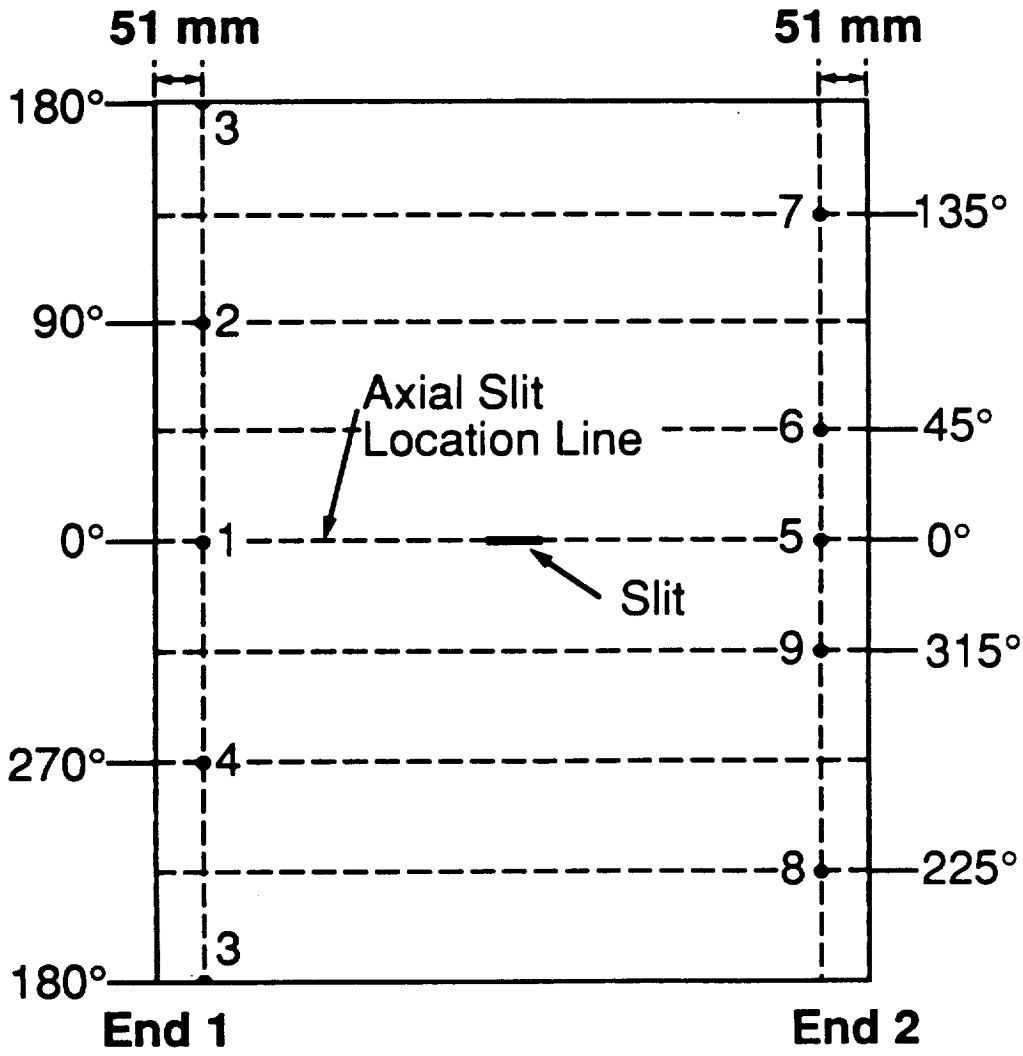

Figure 4.15 Cylinder thickness measurement locations.

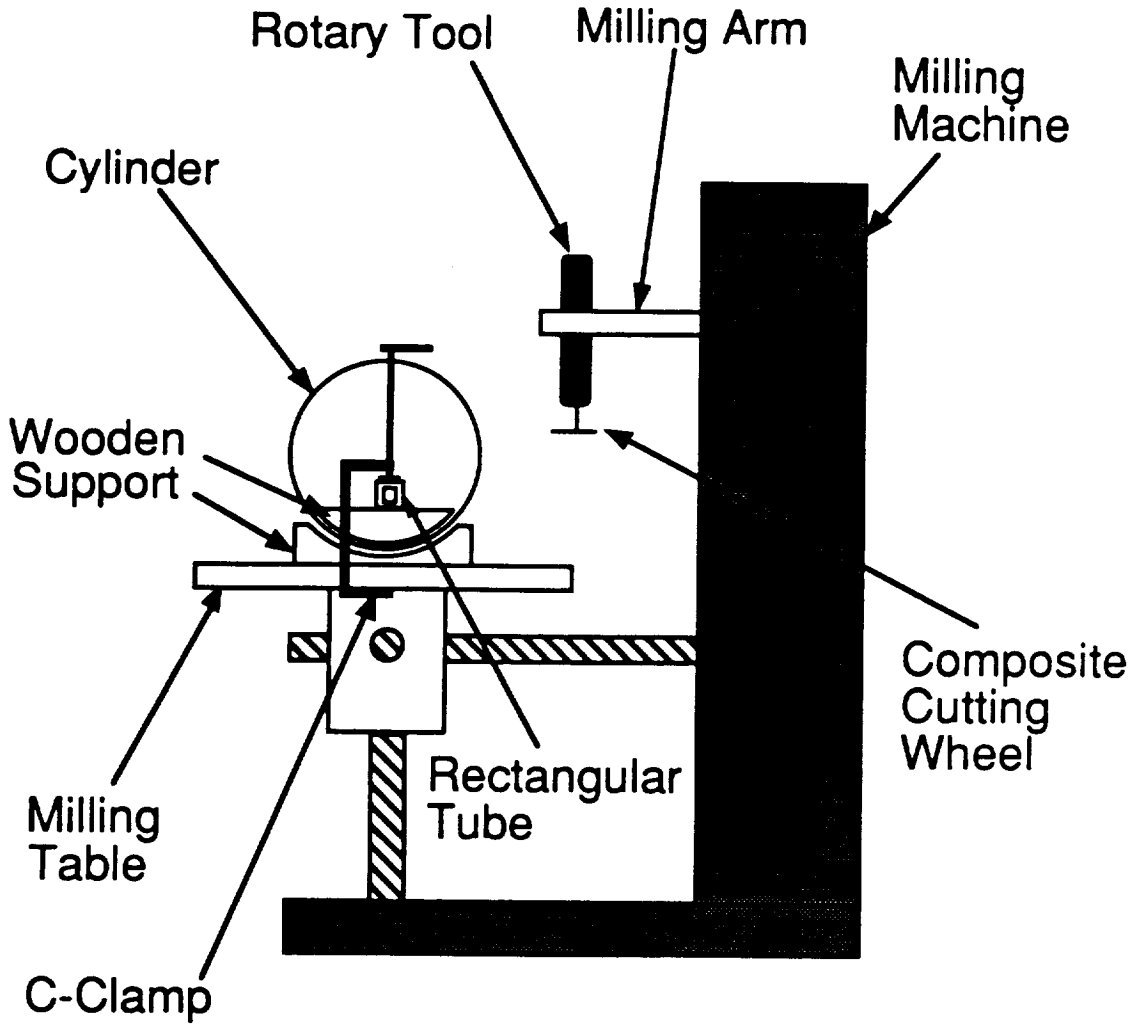

NOTE: Not to Scale

Figure 4.16 Illustration of cylinder slit cutting setup.

wooden holders on the milling machine table. These holders were designed to provide support for the cylinder and prevent deformation during the clamping process used to hold the cylinder to the table. The cylinder was rotated so that the axial slit location line was 90° from the lowest point of the cylinder on the table. The proper orientation of this line was visually verified using a master square. The square was also used to align the line and, thus, the cylinder the same distance from the table's edge all the way along its length. A long rectangular tube was placed through the center of the cylinder and was allowed to rest on the wooden holders. C-clamps were used to clamp the rectangular tube and, thus, the cylinder to the table. Care was taken not to disturb the alignment of the cylinder during the clamping process.

A DREMEL™ rotary tool with a 25.4 mm diameter, 0.64 mm thickness, cutting wheel spinning at 30,000 rpm was used to cut the slits. The DREMEL™ was vertically attached to the milling machine arm after a master square was used to position this arm perpendicular to the machine table. A master square was used to ensure that the plane of the cutting wheel was parallel to the surface of the table. The table was positioned so that the cutting wheel was in the proper location to cut the scribed slit. Before the slit was cut, the table was moved sideways back and forth to ensure that the blade stayed over the scribed line. Slit cutting started in the middle of the slit. Unlike in the previous investigation [4], slits were cut by moving the head of the machine with the attached DREMEL™ into the cylinder, instead of moving the table with the attached cylinder into the cutting wheel on the stationary DREMEL™. This change was made since it is difficult to move the table smoothly by hand and the crank to move the head of the machine is in a better position to view a slit as it is cut. After the cutting wheel cleared the other side of the cylinder wall, the table was slowly

moved sideways both ways to cut the body of the slit. After the cutting was complete, the wheel was withdrawn completely from the cylinder before the DREMEL™ was shut off. Another difference between slit cutting in the current and former investigations is that the procedure described above was also used to cut the 12.7 mm slits. However, the cutting wheels used to cut slits this size were ground down first on a steel grinding bar to make them approximately 21 mm in diameter. Also, it was not necessary to move the table sideways to cut the 12.7 mm slits. The cutting wheel was passed through the cylinder wall a single time as far as it could go without overcutting the slit length. Since the wheel is curved, this resulted in a varying depth cut along the length of the slit with a through-thickness cut in the middle. All slits were finished and the slit tips were sharpened using 0.5 mm thick jeweler's saws that were sharpened on a grinder in the same manner as described in Section 4.1.1. The slits were inspected under a microscope, and the slit lengths were measured to the nearest 0.1 mm with a digital caliper. A magnified photograph of a slit tip taken using the microscope is shown in Figure 4.17. The measured slit lengths are tabulated in Appendix A and were used in all subsequent calculations in this investigation.

For two of the cylinders tested in this investigation (the $[0/\pm45/90]_s$ cylinder with the 25.4 mm slit and the second biaxially loaded $[90/0/\pm45]_s$ cylinder with a 12.7 mm slit) the first slit cut was not satisfactory. Both slits were patched using a wet layup of two layers of fiberglass fabric and Epoxy-Patch™ two-part matrix, and a new slit was cut in a different location on both cylinders. A patched cylinder ready for testing is shown in Figure 4.18. This patching technique was first shown to be effective by Graves [13]. The bottom layer of each patch was cut to extend at least twice the slit length

Figure 4.17 Photograph (27 X magnification) of tape cylinder slit tip.

Figure 4.18 Photograph of patched, biaxially loaded tape cylinder ready for testing.

from each slit tip in the axial direction and 32 mm above and below the slit in the circumferential direction. The dimensions of the second layer were cut 12.7 mm smaller than those of the bottom layer. Before the patch was attached, the area where it was to be located was sanded just enough to remove the paint from the identification grid. Methanol was used sparingly to remove the graphite dust after the sanding was complete. Flash tape was also placed over the slit on the inside of the cylinder to prevent the epoxy from running through the slit. Both layers of the patch were attached individually after they had been thoroughly coated on both sides with the epoxy. Each layer was carefully smoothed to remove wrinkles and air bubbles. After both layers were attached, the patch was allowed to cure at room temperature for one hour. This initial setting period was followed by a cure in the autoclave for two hours at 60°C. The new slit location was established in a smooth area on the cylinder approximately halfway between the patch location and the back of the cylinder. The new slits were cut in the same manner as described before.

The biaxially loaded cylinders required bonded endcaps to achieve the proper loading condition due to internal pressure. A schematic of the aluminum endcaps used is shown in Figure 4.19. Each endcap is 25.4 mm thick and 330 mm in diameter. The ends of the cylinder fit into 12.7 mm deep and 4.75 mm wide circular grooves that are located in each endcap. These grooves are cut so that the inside edge of the groove is located at a radius of 152 mm from the center of the endcap. One of the endcaps also has a rounded, stepped, rectangular hole for the pressure-fitting plate. The pressure-fitting plate contains a brass fitting which allows the pressurizing gas to enter the cylinder and the plate is removable so that it can be bonded to the bladder to prevent leaking at the bladder inlet. The shape of the plate

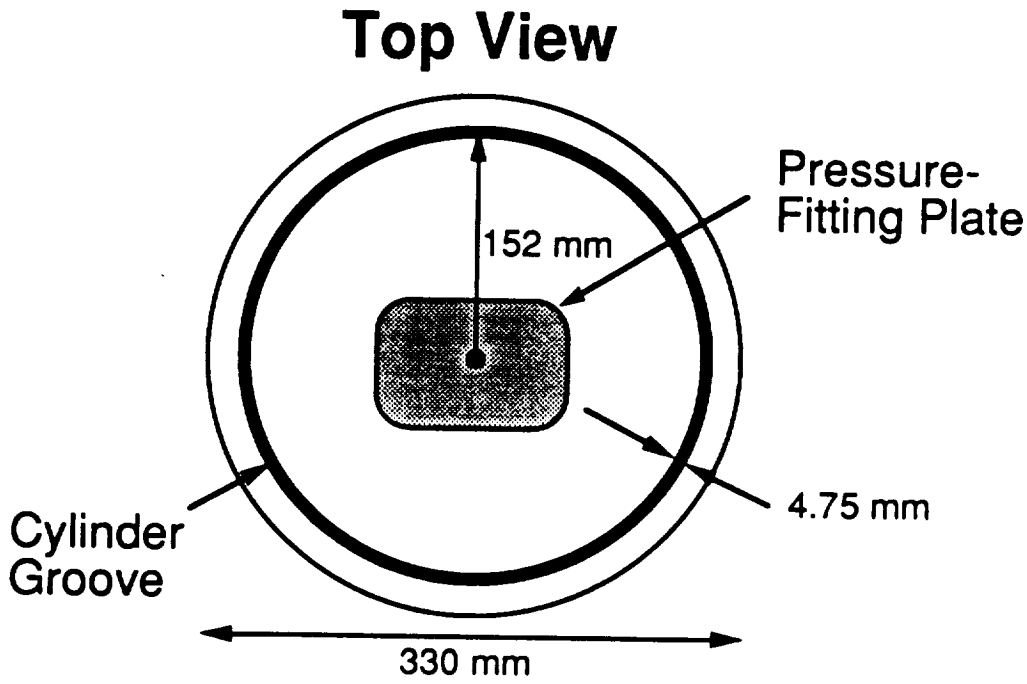

Figure 4.19 Illustration of cylinder endcaps for biaxial loading tests.

and the fact that it is removable allow the bladder to be inserted in the cylinder after the endcaps are bonded.

The endcaps are bonded to the cylinder one at a time using Scotch-Weld 2216 B/A epoxy adhesive from 3M. This two-part epoxy system is mixed in the specified weight ratio of seven parts resin to five parts hardener in plastic hexagonal boats. For each end of the cylinder, a plastic boat is filled with 105 grams of resin and 75 grams of hardener and tongue depressors are used to stir the mixture well. Before an endcap is bonded, it is carefully cleaned with methanol and heated to 80°C. Immediately after the endcap is removed from the oven, the epoxy mixture is poured into the groove of the cylinder until it slightly overflows. This process is done while the endcap is hot so that the viscosity of the epoxy is lowered and air bubbles can be removed from it more easily. The mixture is also used to coat both sides of the end of the cylinder to be bonded to a depth of 25 mm. It should also be noted that the region on the inner side of the cylinder within 25 mm of the end is lightly sanded and then cleaned with gauze and methanol before the bonding process takes place. The cylinder is pushed down into the groove on the endcap as far as it goes and toothpicks are used to center the cylinder in the groove. Tongue depressors are used to make fillets with the epoxy mixture at the endcap/cylinder junction on both the inside and outside of the cylinder. These fillets allow for smooth load transfer from the endcap to the cylinder. The toothpicks are removed and the cylinder and endcap are heated in the autoclave for one hour at 80°C. The entire process is then repeated with the other endcap. The endcap with the hole is bonded to the cylinder first to provide access to the inside of the cylinder during the second bonding process.

After the cylinder test, the endcaps have to be cleaned so that they can be reused. The endcaps are placed in an oven and heated for several hours at 260°C to char the bonding epoxy. Hammers and scribes are then used to chip the epoxy out of the grooves. The endcaps are returned to the oven occasionally since it is very difficult to chip the epoxy when the endcaps are cool. Vice grips are used to pull the cylinder remnants from the groove as soon as it is physically possible to do so. Scribes, cotton swabs, and solvents are used in the final stage of the cleaning process to remove as much of the cured epoxy as possible.

Rubber bladders were constructed to line the cylinders so that the nitrogen gas does not leak while the cylinders are pressurized. The standard TELAC bladder manufacturing process used is described in more detail in an internal TELAC document [34]. Each bladder is made from four pieces of 1/32" (0.8 mm) thick pure gum rubber which are cut from a 915 mm wide roll. These pieces are held together by vacuum tape and rubber adhesive. The main body of each bladder is formed from a rectangular piece 1041 mm by 800 mm. Two strips of 13 mm wide vacuum tape, #213-3 made by General Sealants, are placed side-by-side along one of the two shorter edges. The other short edge is lapped over the tape by 25.4 mm to form a 1016 mm circumference rubber tube. Two more strips of vacuum tape are placed side-by-side around the circumference of the main bladder piece at each end. These strips of tape are used to connect the toothed circular endpieces that are shown along with the other bladder pieces in Figure 4.20. Each circular endpiece is 458 mm in diameter and has triangles with a base of approximately 25 mm and a height of 51 mm cut from it to form 16 teeth. Teeth are connected one at a time in an alternating fashion to the main bladder piece. One of the endpieces has a 25 mm diameter hole cut into the

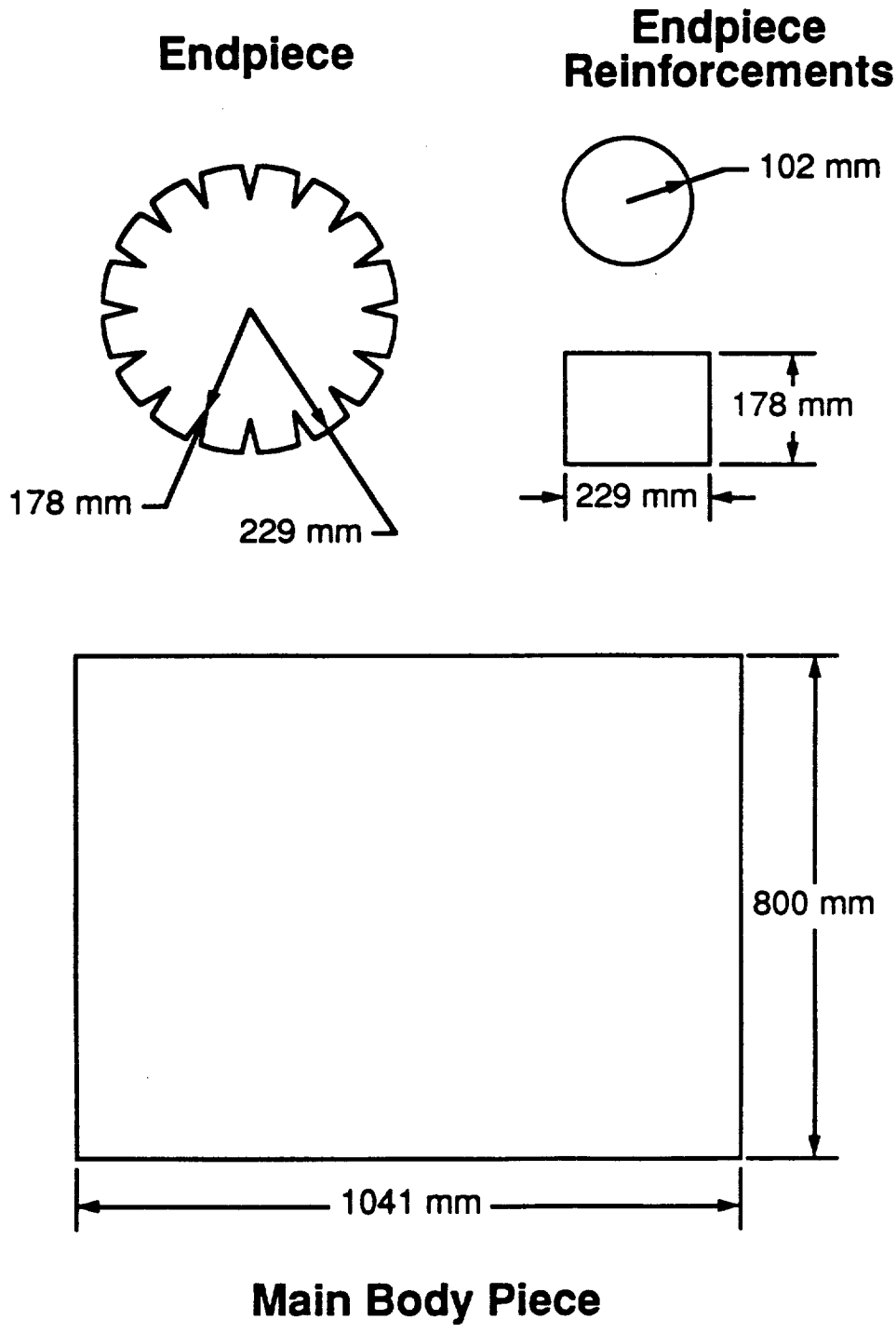

Figure 4.20 Rubber pieces for cylinder bladders.

center of it and then Globe Rubber Works Utility Adhesive Number 503 or 3M Scotch-Grip 1300 rubber adhesive is used to bond the pressure-fitting plate over the hole. An extra piece of rubber with a 25 mm diameter hole in its center is connected to the pressure-fitting plate before it is attached to the bladder in order to reinforce the connection. As shown in Figure 4.20, the endpiece reinforcement pieces have two different shapes. Circular reinforcement pieces are used with the circular pressure-fitting plate that is part of the uniaxial test apparatus, while rectangular reinforcement pieces are used with the previously described rectangular pressure-fitting plate. All seams on the bladder are painted with adhesive to reinforce them and to cover exposed areas of the vacuum tape which are very sticky otherwise and tend to cause the bladder to stick to itself and to the inside of the cylinder.

Each bladder is tested by fully inflating it with compressed air and using Snoop Liquid Leak Detector™, which bubbles if a leak is present. All leaks are patched with vacuum tape and adhesive after the bladder is deflated and dried. The bladders are constructed slightly larger than the cylinders to reduce the chance of premature bladder failure during a cylinder test. The bladders are also protected by taping two layers of bonded rubber to the inside of the cylinder over the slit (to prevent the bladder from bulging through the slit) and by not testing the bladder or inserting it in the cylinder until the day of the cylinder test.

4.2.2 Cylinder Instrumentation

All cylinders tested in this investigation were instrumented with strain gages from the Micromeasurements Company. On all cylinders, except the one used for the uniaxial test apparatus verification tests, two EA-06-125AD-120 gages were placed near and perpendicular to each other in the axial and

circumferential directions to monitor the far-field behavior. Since the location of the far-field gages is arbitrary as long as these gages are located in a region on the cylinder that experiences far-field loading, strict attempts were not made to standardize the far-field gage locations. The far-field gages on the biaxially loaded and first-tested $[90/0/\pm45]_s$ cylinder with the 12.7 mm slit and the $[0/\pm45/90]_s$ cylinder with the 12.7 mm slit were placed approximately 191 mm in the axial direction from the edge of the cylinder on End 1 and 318 mm in the circumferential direction from the axial slit location line. The far-field gages on the biaxially loaded and second-tested $[90/0/\pm45]_s$ cylinder with the 12.7 mm slit and the $[0/\pm45/90]_s$ cylinder with the 25.4 mm slit were placed in a different location since these cylinders were patched, as previously described. The gages on both of these cylinders were placed approximately halfway down the length of the cylinder and 318 mm in the circumferential direction from the center of the patch. The direction along the circumference of the cylinder from the patch to the gages was opposite of that from the patch to the new slit.

Far-field gages on the uniaxially loaded cylinders were located in or near the paint grid square marked 'D10'. The location of this square relative to the slit location can be seen in Figure 4.14. The center of this square was located approximately 114 mm from the center of each cylinder along its length and 178 mm from the axial slit location line in the circumferential direction. This location was chosen for the far-field gages so that all of the gages on each cylinder could be viewed simultaneously and, thus, could be protected more easily, during the installation of the cylinder into the uniaxial test apparatus. After the tests of the $[90/0/\pm45]_s$ cylinders with the 25.4 mm and 50.8 mm slits and the $[\pm45/90]_s$ cylinder with the 50.8 mm slit, an extra far-field circumferential gage was added to the remaining six uniaxially

loaded cylinders since there was concern that the first sets of 'far-field' gages were too close to the slits. These extra gages were located in or near the paint grid square marked 'F5' (see Figure 4.14). The center of this square was located approximately 254 mm from the edge of the cylinder in the axial direction and 280 mm in the circumferential direction from the axial slit location line. The strain data from each of these gages were compared to those for the other circumferential gage on the cylinder to determine if the output from the first set of gages could be treated as true far-field values. There are some slight variations in the locations of the far-field gages from cylinder to cylinder since these gages were placed to avoid any wrinkles and paint on the cylinder surface.

In addition, EA-06-031DE-120 gages, with a 1 mm long by 0.8 mm wide gage element, were oriented in the circumferential direction as close as possible to all of the slit tips in an attempt to monitor damage. Damage to the cylinder or the gage is indicated by discontinuities and other odd behavior in the stress/strain curve. The substrate on these gages was trimmed on one side almost to the gage element, as shown in Figure 4.21, so that the gages could be placed closer to the slit tips.

On the two cylinders with a patch, an additional circumferential EA-06-125AD-120 gage was placed halfway between the patch and the new slit location so that hoop strains from this location could be compared to the far-field hoop strains. If the hoop strains at both locations were comparable, it would indicate that far-field conditions were present between the patch and the slit; a condition which would verify that the patch did not interfere with the loading condition near the slit. The patch gage on the $[0/\pm45/90]_s$ cylinder with the 25.4 mm slit was located 108 mm in the circumferential direction from the new slit while the patch gage on biaxially loaded $[90/0/\pm45]_s$ cylinder

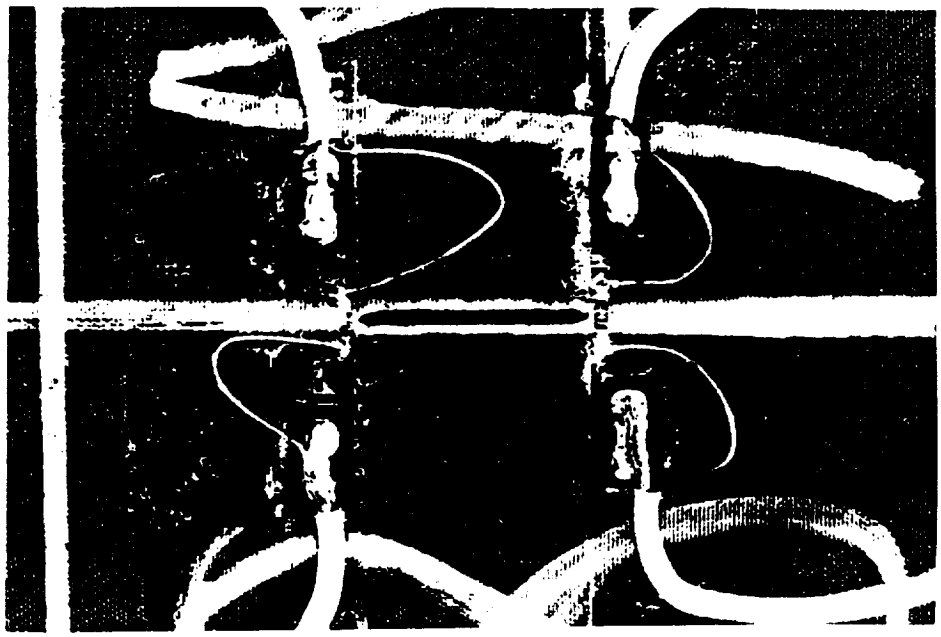

Figure 4.21 Photograph of slit in tape cylinder instrumented with trimmed, circumferential slit tip gages.

with the 12.7 mm slit was located 135 mm in the circumferential direction from the slit. Both patch gages were centered along the length of the cylinder. The cylinder used for the uniaxial test apparatus verification testing was instrumented with the two types of gages mentioned above as well as EA-06-125RA-120 rosettes. The purposes and locations of the eleven gages on this cylinder are described in more detail in the next chapter.

In addition to the strain gages, a pressure transducer was used to collect data during the cylinder tests. This pressure transducer was connected to the pressurizing line leading from the nitrogen tank to the cylinder. The transducer relies on a calibrated metal diaphragm, instrumented with a full Whetstone bridge of strain gages, to determine the pressure in the line. The pressure transducer was needed to monitor the pressurization rate of the cylinders during the tests and to determine the pressures when the cylinders failed.

4.2.3 Cylinder Testing

All cylinder testing was conducted in a blast chamber. The only difference between uniaxial and biaxial testing involved the setup procedure of the test apparatus. For biaxial tests, the bladder was inserted into the cylinder with bonded endcaps and then the cylinder endcaps were simply rested horizontally on a steel I-beam on the blast chamber floor. For the uniaxial tests, the cylinder as well as the bladder had to be installed in the test apparatus on the day of the test, and then this apparatus was also rested horizontally on two special supports. The cylinders were always oriented on the supports so that the slits were up and such that the simply supported boundary condition of the endcaps for both types of tests placed no restrictions on the axial expansion of the cylinder. Two to three layers of

sandbags were stacked all the way around the cylinder for the biaxial tests and only along the sides for the uniaxial tests. The sandbags were always placed so that there was no contact between them and the test apparatus. The sandbags were used to absorb the shock of the explosion, protect the instrumentation in the blast chamber, and contain the endcaps when the cylinder failed (in the biaxial tests). A schematic of the blast chamber setup is shown in Figure 4.22 for a biaxially loaded cylinder. All additional testing procedures were the same for both types of tests.

The cylinders were pressurized via nitrogen gas that was supplied from a bottle located outside the blast chamber. Nine and a half meters of copper tubing and flexible hose were used to feed the nitrogen through a port hole in the side of the blast chamber to a wooden box containing the pressure transducer. An additional 2 m of 6.5 mm inside-diameter copper tubing was used to feed the nitrogen from the pressure transducer location to the cylinder. The previously mentioned wooden box also contained attachment points for the strain gage wires and the instrumentation required to send the strain and pressure data back to the X-Y plotter and computerized data acquisition system via the testing machine.

During a cylinder test, nitrogen was manually introduced into the cylinder at an approximate rate of 0.40 MPa/min. Strain and pressure data were recorded at a frequency of 1 or 2 Hz by a Macintosh IIx computer equipped with Labview data acquisition software. Additionally, the pressure data was recorded by an analog X-Y plotter. The real-time pressure plot and computer-displayed pressure data were monitored during the test to ensure that the proper pressurization rate was maintained. After the cylinder failed, the fragments were collected for further analysis and the blast chamber was cleaned for the next test.

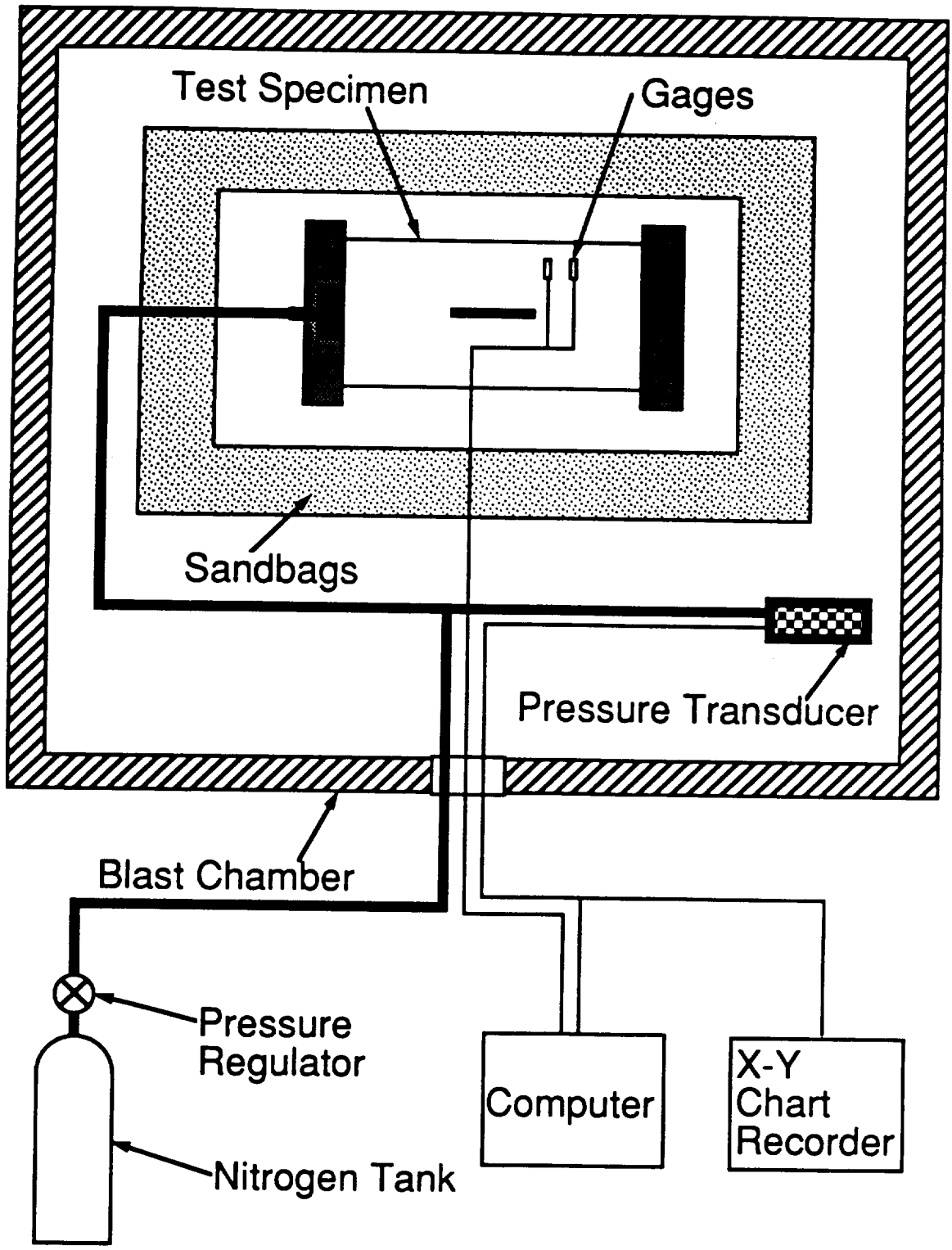

Figure 4.22 Illustration of blast chamber setup for biaxially loaded cylinders.

Following each cylinder test, the maximum pressure from the pressure plot was compared to the maximum pressure indicated in the computer data file to ensure that the values were similar. The value from the data file was used as the failure pressure of the cylinder in subsequent comparisons. The plot was also inspected to see if the proper pressurization rate was maintained throughout the test. The plots from all of the cylinder tests indicate that the cylinders were pressurized at average rates between 0.26 MPa/min and the nominal rate of 0.40 MPa/min. Cylinder fragments were pieced back together, with the help of the paint identification grid, and photographs were taken to record the failure path of the specimen. Pressure/strain data from gages at the slit tips were plotted and inspected for qualitative behavior which might indicate slit tip damage prior to the ultimate failure of the cylinder. Pressure levels when any strain gages went inactive on the cylinder were also noted. Far-field strain data were compared for similar specimens to assess the consistency of the results, and any unusual behavior was noted.

CHAPTER 5

Uniaxial Test Apparatus

All aspects of the experimental procedure which are specific to the apparatus that was designed and manufactured for this investigation to test pressurized cylinders to failure in hoop loading only are described in this chapter. In addition, a full description of the apparatus is provided and the design and manufacturing processes are explained. The initial testing that was conducted to verify the apparatus design is described, except for the actual testing procedure which is summarized in Chapter 4.

5.1 Design Process Overview

The uniaxial test apparatus is also referred to as the anti-axial load device (AALD) since its main purpose is to provide a path for pressure loading applied in the axial direction such that none of this load is carried in the test specimen. The design of this device involved numerous considerations and compromises. A simple design was required which would allow internally pressurized cylinders to be loaded only in the circumferential direction without major modifications to the existing TELAC cylinder manufacturing and testing procedures. The apparatus needed to be modular so that it could be moved and stored easily, and it was also desirable to minimize the number of parts as well as the weights of the parts. The apparatus needed to be durable to withstand the cylinder explosions and had to accommodate a range of cylinder lengths. The maximum pressure that the device needed to withstand for this investigation is approximately 2.1 MPa. However, a value of 6.9 MPa was kept in mind throughout the design process

so that the device could potentially be used at higher pressures in future investigations. A factor of safety was, furthermore, taken into account.

The AALD design was driven by several limitations such as the availability of materials, minimum required orders, and price. Also, due to difficulties in analyzing the behavior of the apparatus, it was necessary to rely heavily on symmetry and make as many comparisons to the biaxial test apparatus as possible, since this is a proven design. The design was effected by potential difficulties and requirements associated with the AALD set-up procedure, by the length of time and availability of equipment required to manufacture the device, as well as by the complexity of the manufacturing procedure itself. The merits and potential pitfalls of the proposed design were carefully analyzed before any manufacturing took place. However, due to some unforeseen developments, several design modifications were made as required or warranted even after the first uniaxial cylinder tests were conducted.

5.2 Description and Manufacturing

The assembled uniaxial test apparatus is illustrated in Figure 5.1. The cylinder is enclosed in a symmetric 'cage' formed by two aluminum endplates connected to each other by eight continuously threaded steel rods. The cylinder is placed into circular grooves in both endplates but is not bonded to the endplates. Since the cylinder and the endplates are not rigidly connected, all of the internal pressure loading on the endplates that would induce an axial load in a bonded cylinder is taken by the continuously threaded rods. Three rod support plates, which are steel rings with holes for the continuously threaded rods, are distributed along the length of the cylinder to prevent the rods from being damaged during the cylinder explosions. These

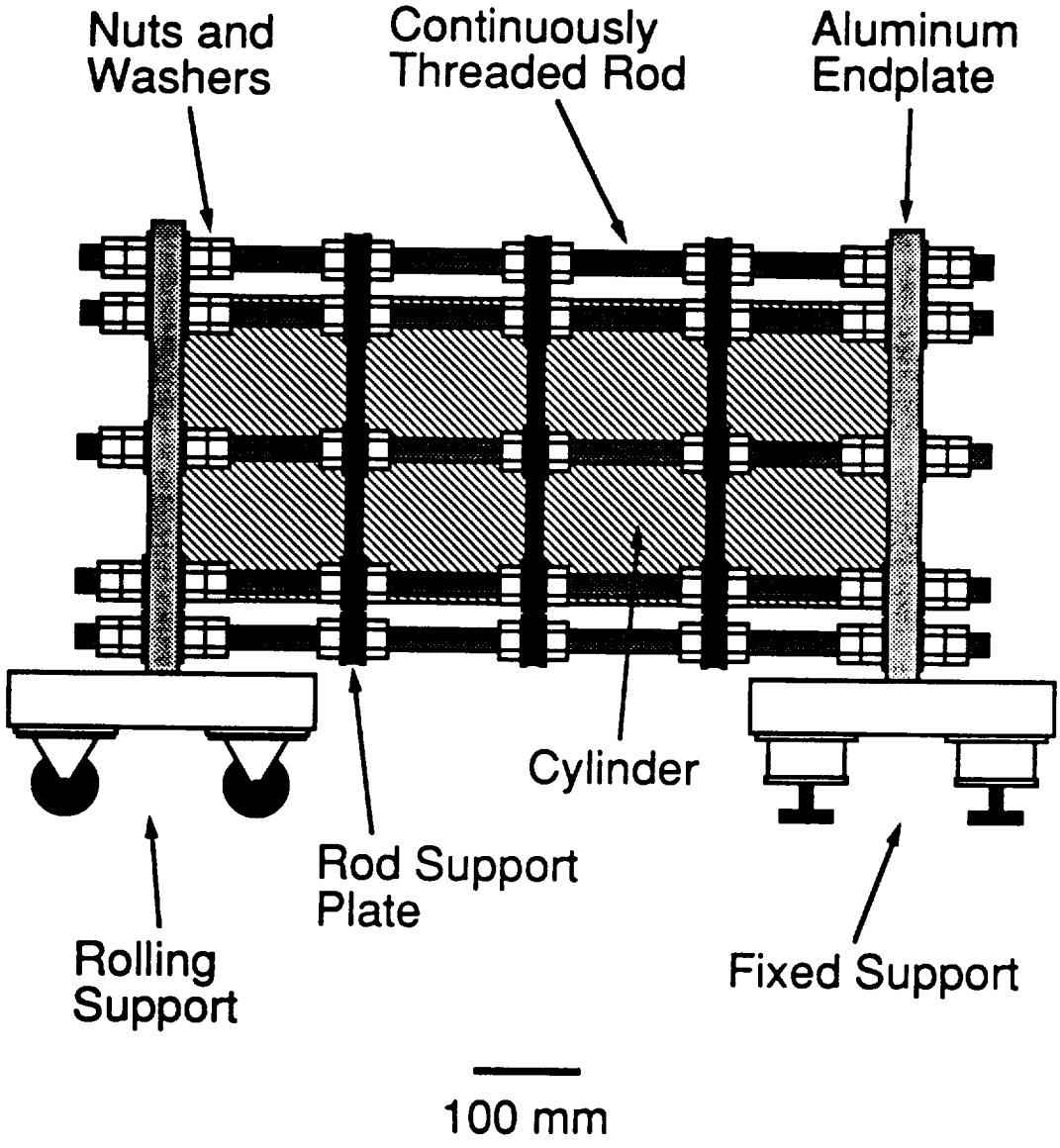

Figure 5.1 Schematic of assembled uniaxial test apparatus.

plates were added to the AALD design after the first cylinder failure test since some of the original rods were damaged during this test. As with the biaxial test apparatus, the AALD has a pressure-fitting plate in one endplate and supports to hold it horizontally in the blast chamber during the cylinder test.

In the following discussion of the design specifications for the AALD, dimensions are presented first in English units if the part was milled or purchased using these units. The equivalent SI units for all English dimensions are also presented. Otherwise, all dimensions are presented in SI units.

The AALD endplates are required to contain the bladders in the cylinders so that the cylinders can be internally pressurized. Each endplate is a disk of 6061-T651 aluminum with a thickness of 1.25" (32 mm), a diameter of 18" (457 mm), and a mass of approximately 14 kg. One of the endplates is illustrated in Figure 5.2. The ends of the cylinder fit into 3/16" wide (5 mm) and 0.5" (13 mm) deep circular grooves that were cut so that the center of each groove is 6.07" (154 mm) from the center of the endplate. The diameter of the circle defining the centerline of the groove was chosen so that the cylinder would be centered in the groove. This dimension was based on circumference measurements of actual cylinder specimens as well as on measurements of the outer diameter and circumference of the mandrel on which the specimens are cured. A bolt circle, which is a ring of holes for the continuously threaded rods, was cut into each endplate. The bolt circle has a radius of 7.56" (192 mm) and is concentric with the endplate. Each of the eight evenly distributed holes around the bolt circle has a diameter of 29/32" (23 mm), which is 1/32" (0.8 mm) larger than the nominal outer diameter of the rods. The holes were sized to allow for deviations in the diameter and

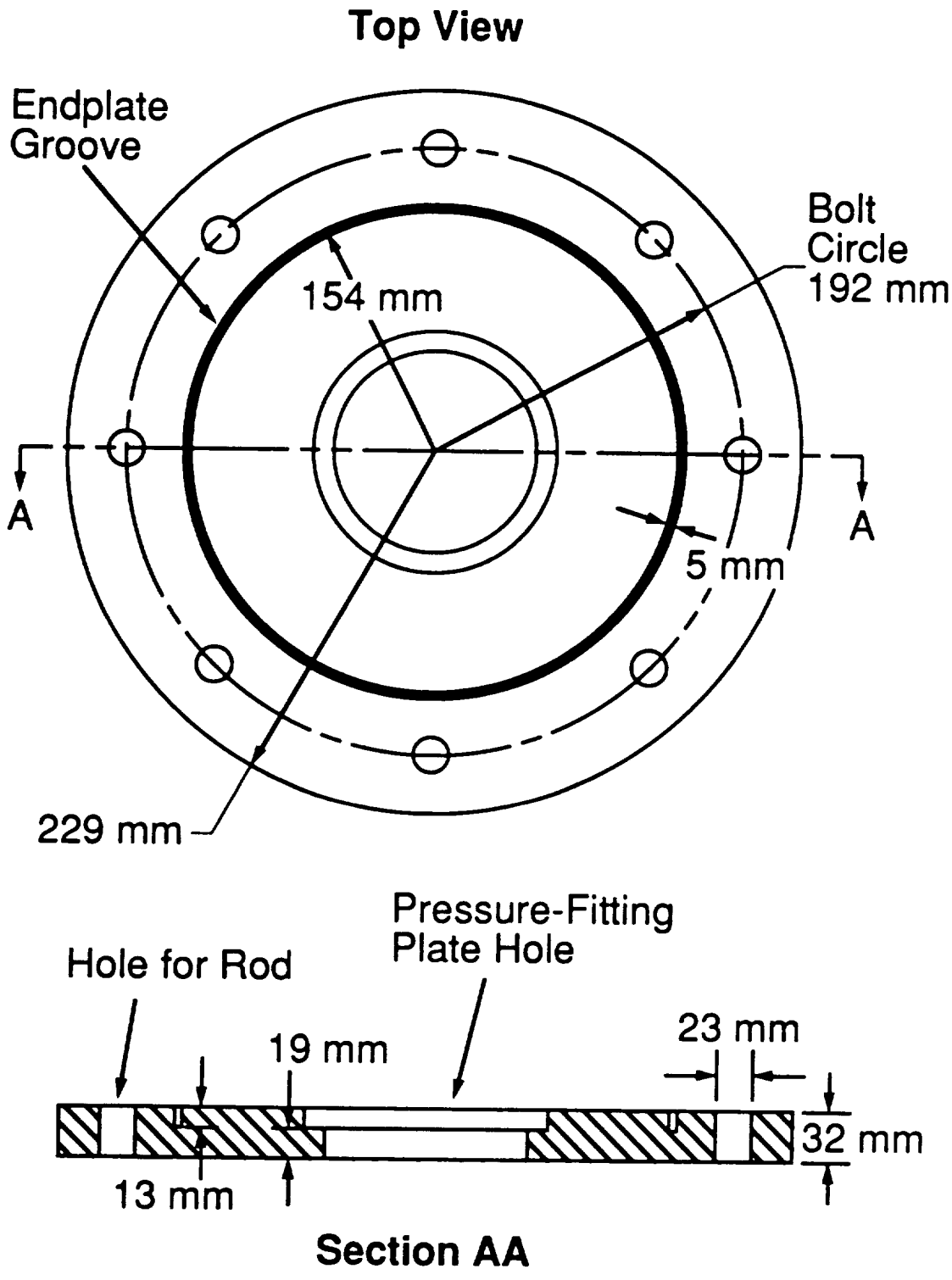

Figure 5.2 Illustration of uniaxial test apparatus endplate.

degree-of-straightness of the rods from the nominal values due to manufacturing tolerances. One of the endplates also has a stepped circular hole cut in the middle of it for the pressure-fitting plate.

The pressure-fitting plate is shown in Figure 5.3. This plate is a stepped disk of 6061-T651 aluminum with the same overall thickness as the endplates. It is removable so that it may be bonded to the bladder to prevent leaking at the bladder inlet. The lower step on the plate has a diameter of 6" (152 mm) and a thickness of 0.5" (13 mm). The upper step has a diameter of 5" (127 mm) and a thickness of 0.75" (19 mm). The step is required for load transfer from the plate to the endplate and the plate is sized to allow access to the inside of the cylinder once it is installed in the AALD. Two steel 'clips' attached to the plate with 1/4" (6 mm) thumb screws hold the pressure-fitting plate securely in the endplate. A threaded hole down the center of the plate accommodates the brass fitting which is used to connect the pressure line to the AALD.

Two accommodations were made at the junction between the cylinder and the endplate to protect the cylinder and the bladder. These are shown in Figure 5.4. First, in order to cushion the ends of the cylinder and hold them stationary after the AALD is assembled, latex tubing with an outer diameter of 3/16" (5 mm) and a wall thickness of 1/32" (0.8 mm) is used to line the endplate grooves. The rings of tubing are held in the grooves using a thin film of vacuum grease. Highly compliant tubing was chosen to maximize the degree of cushioning and sealing between the cylinder and the endplate and so that the axial contraction and hoop expansion of the pressurized cylinder are not restricted. Second, to prevent the bladder from protruding into the space between the cylinder wall and the inner edge of the groove, a circular 3/16" (5 mm) thick neoprene rubber mat was attached to each endplate with

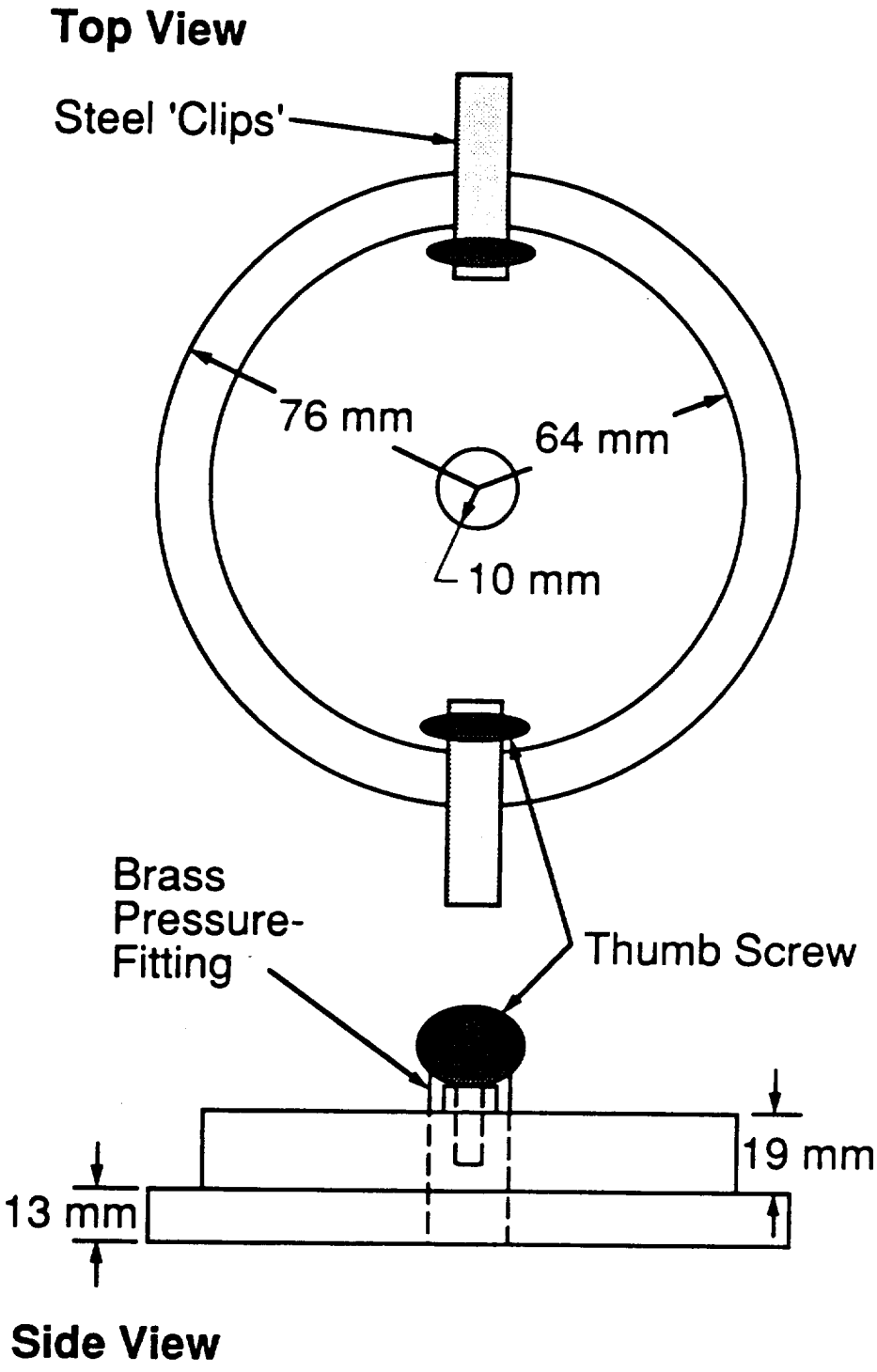

Figure 5.3 Illustration of uniaxial test apparatus pressure-fitting plate.

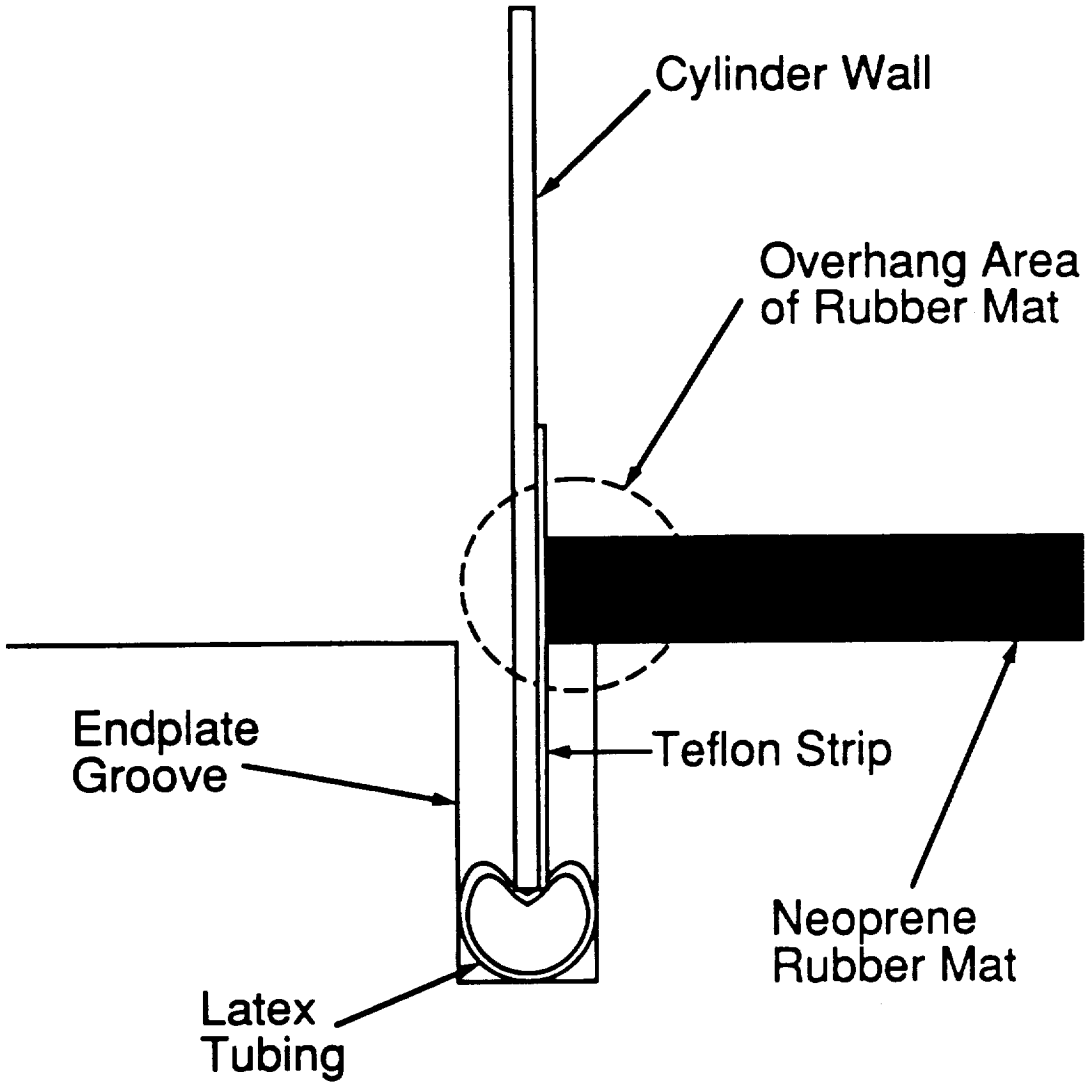

Figure 5.4 Illustration of accommodations at cylinder/endplate junction.

double-sided tape to block the entrance to the gap. It is important to keep the bladder out of the gap since the bladder could rupture on the sharp corner at the inner edge of the groove. If the bladder did successfully enter the gap, it might interfere with the loading condition on the cylinder or protrude out from under the cylinder ends. The mats were carefully cut using a utility knife and a circular plexiglass template. A 7" (178 mm) diameter hole was cut in the center of one of the mats so that the pressure-fitting plate could still be inserted in its endplate. The plexiglass template has a diameter of 12 3/64" (306 mm) and a thickness of 0.5" (13 mm). Since a very tight fit is required between the cylinder wall and the mat, the template was sized using circumference measurements on actual cylinder specimens. It was assumed that any small remaining gap between the cylinder wall and the mat would be sealed by the radial expansion of the mat when it was under pressure loading. To reduce friction between the cylinder wall and the mat which might induce shear loading in the cylinder, a strip of teflon film was taped to the inside of the cylinder near each end. The teflon also aided in sliding the cylinder over the mat and into the groove during the AALD set-up procedure.

The rod support plates, shown in Figure 5.5, were added to the AALD design after the design verification tests since some of the rods were damaged during the first test of a cylinder to failure using the original design. The rod damage is described in more detail in Section 5.5.2. The purpose of the plates is to prevent excessive deflection and, thus, permanent deformation of the rods due to buckling or bending induced by the cylinder explosion. The three plates were purchased as steel rings with an inner diameter of 13.5 -1/8" (343 -3 mm), an outer diameter of 17 +1/8" (432 +3 mm), a thickness of 5/8" (16 mm), and a mass of 6 kg. Each of the eight holes for the continuously threaded rods was drilled through all three plates at the same time using a

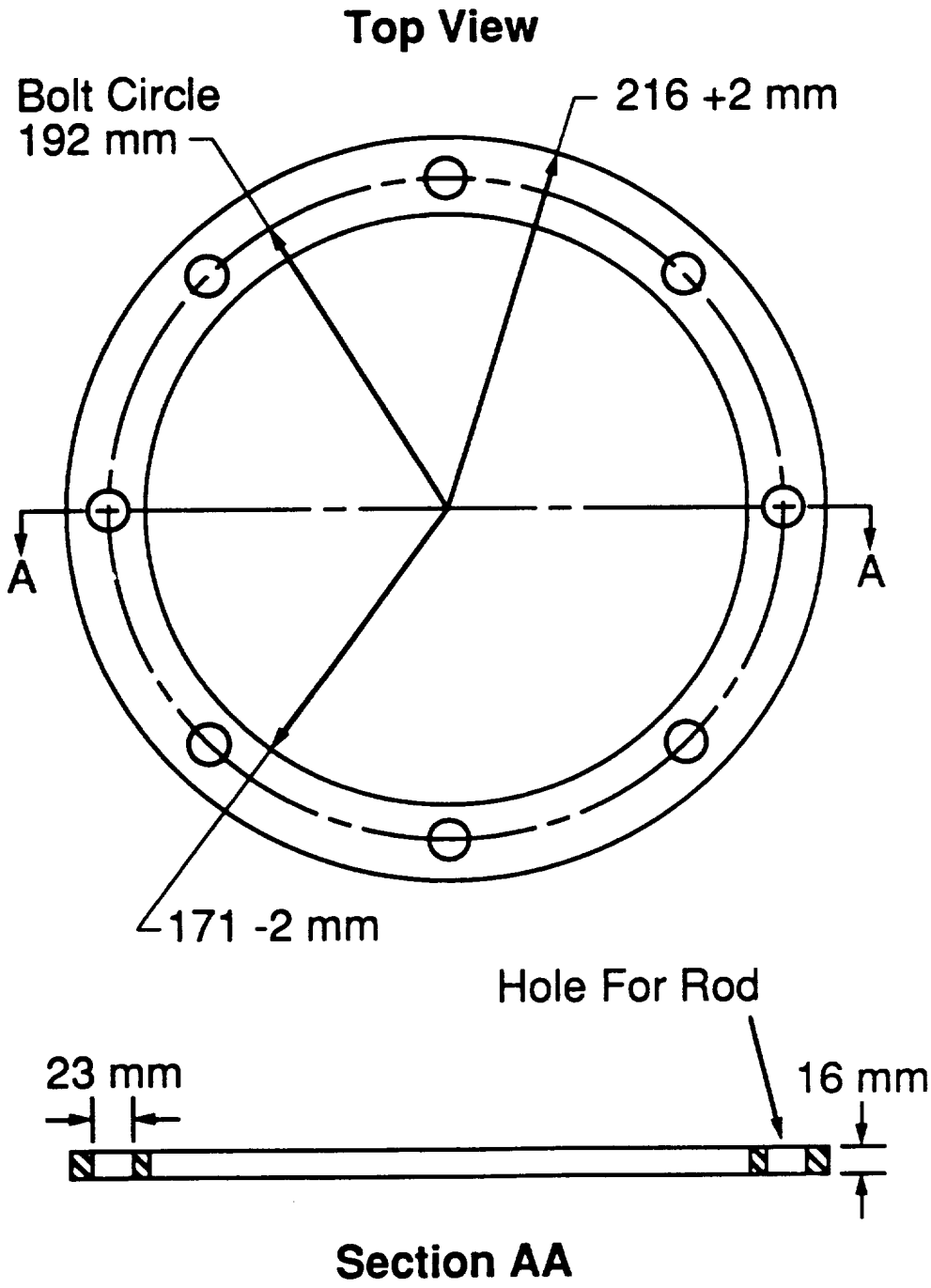

Figure 5.5 Illustration of uniaxial test apparatus rod support plate.

milling machine. The endplate with the pressure-fitting plate hole was used to establish the locations for these 29/32" (23 mm) diameter holes so that they would line up precisely with those in the endplates. An etcher was used to mark each hole in the rings with the same letter as was used to identify the corresponding guide hole from the endplate, so that the proper orientation of the rings with respect to the endplates could be identified easily. A heavy hexagonal nut and a washer are used on both sides of each rod support plate at all eight hole locations to hold the plate at a certain location along the continuously threaded rods. The three plates are located during the AALD set-up procedure so that they are evenly distributed between the endplates. Since the washers used are wider than the rings, one side of all of the washers used was trimmed down, as shown in Figure 5.6, so that the washers would not overhang the inner edge of the rings. It was particularly undesirable for the washers to overhang on this side of the rings since the washers might be damaged by the cylinder explosion or cause additional damage to the cylinder during the explosion.

The eight continuously threaded rods used to connect the endplates together are made of grade 2 steel and have an overall diameter of 7/8" (22 mm) and a root diameter of 0.77" (20 mm). Each rod has a length of 36" (914 mm), a mass of 2.3 kg, and 9 threads per inch (9 threads per 25.4 mm). Two sets of rods had to be purchased, since several rods in the first set were damaged, as previously mentioned. A section was milled flat on four of the rods in the first set halfway down their lengths so that longitudinal strain gages could be attached to these rods. The milled section on each rod is rectangular with a length of 1" (25.4 mm) and a width of 10 mm, excluding the width of the threads. The flat, exposed area on the rod is just large enough to accommodate the gage and the terminals for the wires. Strain

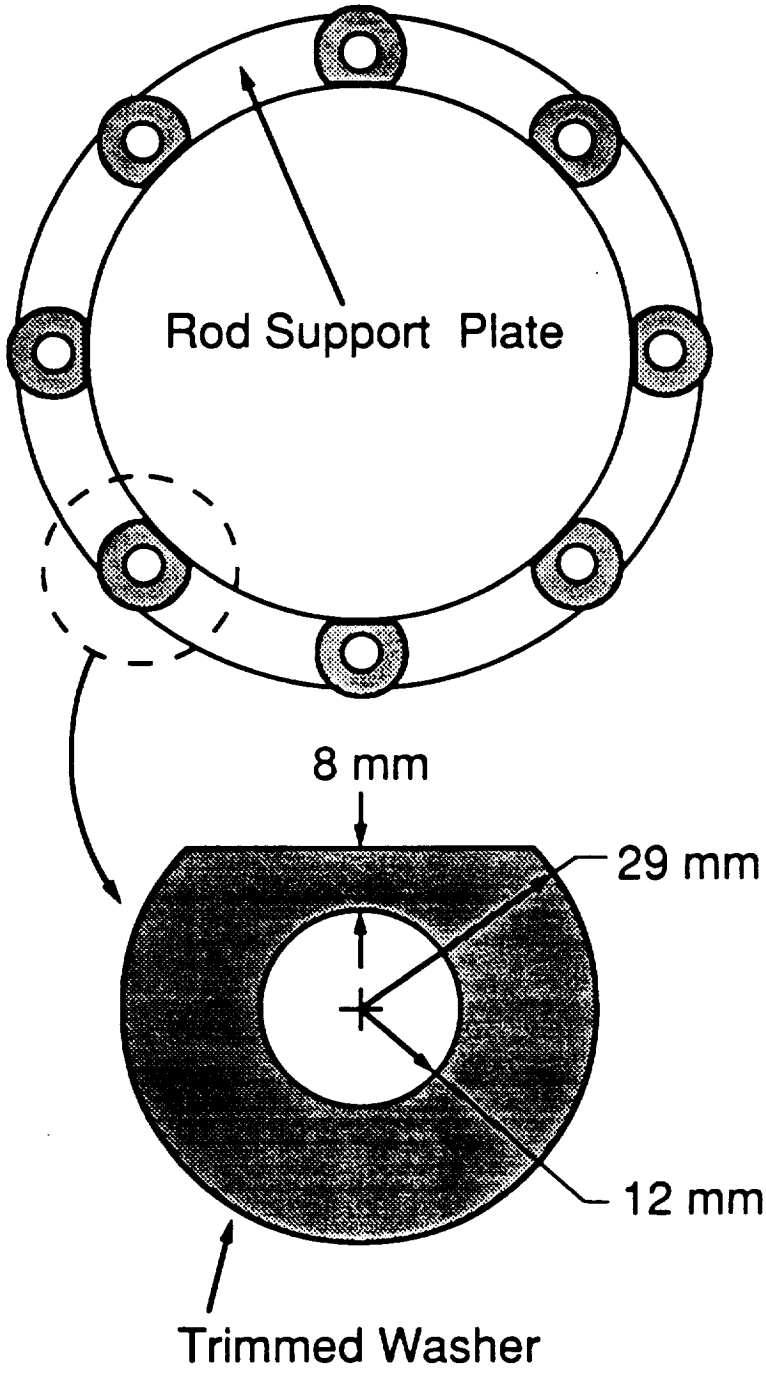

Figure 5.6 Schematic of trimmed washer.

gages were not attached to any of the rods in the second set, since this would interfere with the attachment of the rod support plates to the rods during the AALD set-up procedure. Heavy hexagonal nuts and flat washers in addition to those used with the rod support plates were purchased for the rods so that connections could be made with the AALD endplates. Each rod in both sets was assigned a pair of matched endplate holes where it was always located, and it was marked with the same letter as was used for its assigned holes.

Two independent supports were manufactured to simply support the AALD horizontally above the blast chamber floor. These supports are shown in Figures 5.7 and 5.8. The supports are identical except that one rests on rigid casters while the other rests on legs with attached screw-action machine mounts. Two supports were needed, since the AALD was designed to accommodate a range of cylinder lengths. Furthermore, the fixed-rolling boundary condition on the supports was chosen so that the AALD could expand in the axial direction without restriction. The machine-leveling mounts are required on the fixed support so that it can be stabilized on an uneven floor and its height can be adjusted to the level of the other support. Both supports are 12" (305 mm) long, 14.25" (362 mm) wide, and have a span of 10" (254 mm) between the contact points for the AALD. The rolling support is 144 mm high. These dimensions reflect the need for stable supports that could each hold several times the AALD weight.

The main frame of each support and the legs on the fixed support were manufactured from 4" (102 mm) wide by 1/4" (6 mm) thick steel flats and 3" by 3" by 1/4" thick (76 x 76 x 6 mm) steel angles. Individual steel pieces were cut from stock lengths and trimmed to the proper dimensions on a milling machine. The pieces were tackwelded together to form the frames prior to the attachment of the casters or the machine-leveling mounts.

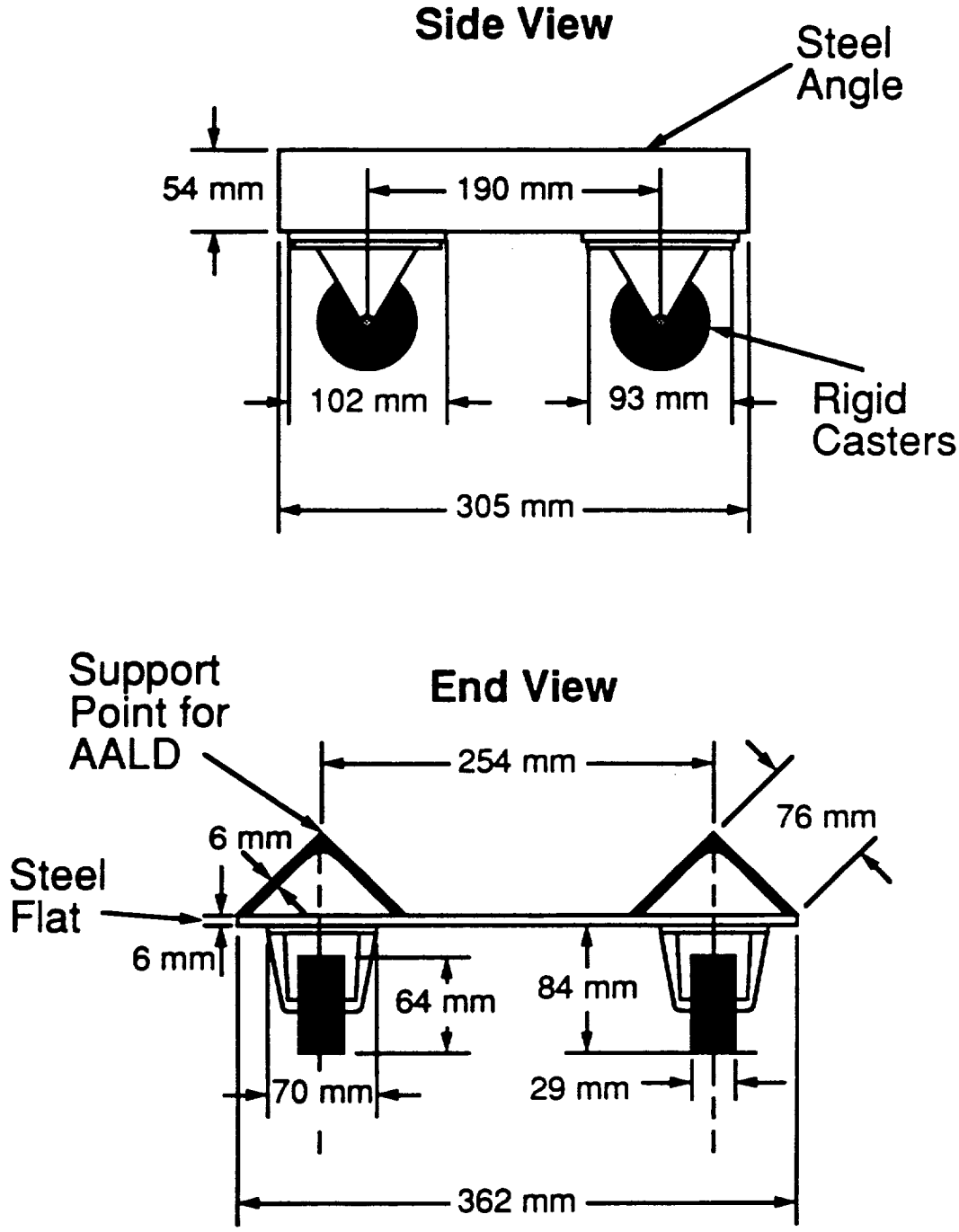

Figure 5.7 Illustration of rolling AALD support.

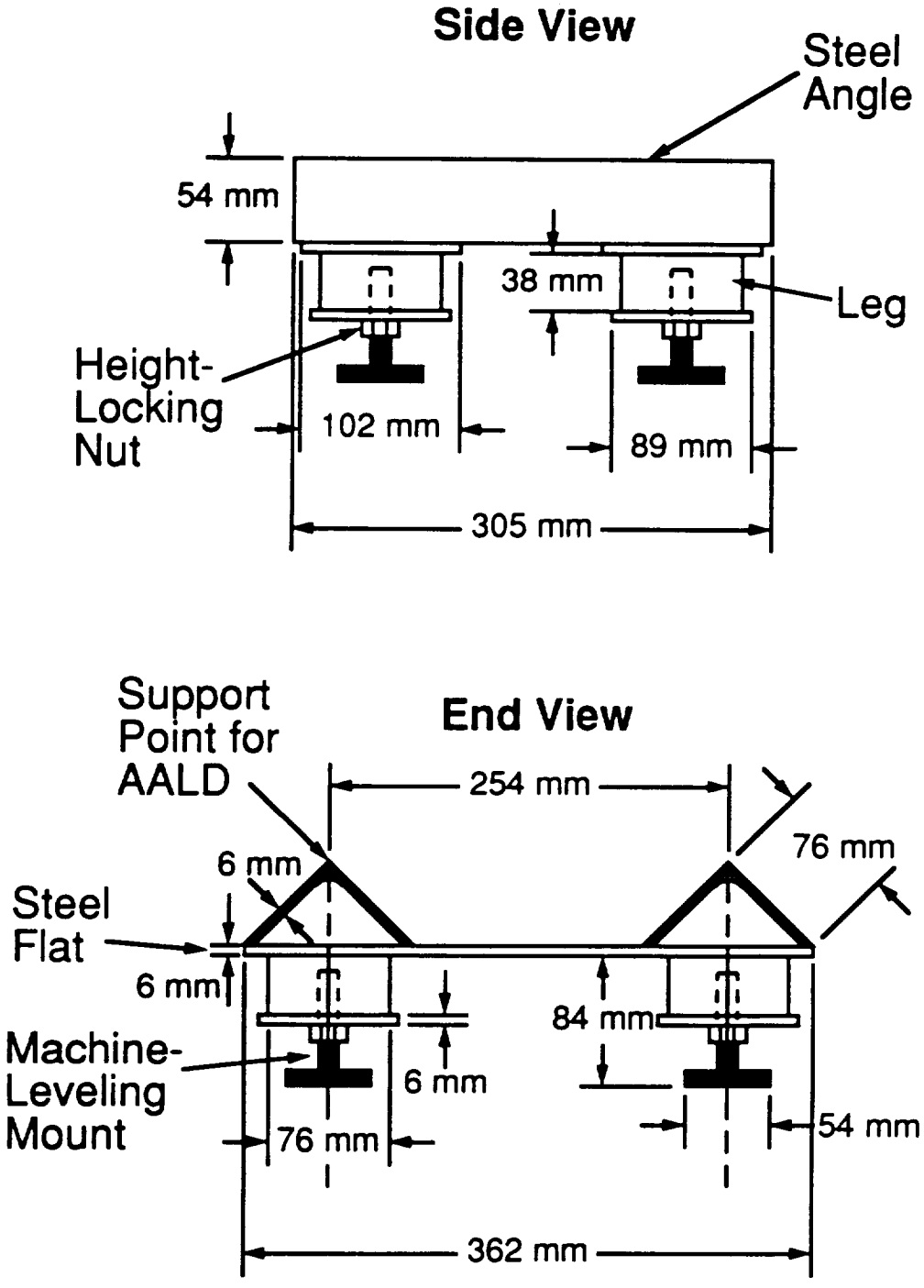

Figure 5.8 Illustration of stationary AALD support.

The four machine-leveling mounts on the fixed support were screwed into threaded holes in the flat rectangular pieces of steel that were used to form the bottoms of the legs. These mounts can each take a maximum load of 300 lbs (1334 N). Their dimensions are a base diameter of 2 1/8" (54 mm), a 1/2" (13 mm) bolt diameter with 13 threads per inch (13 threads per 25.4 mm), and an overall height of 2 7/8" (73 mm). Each mount can be adjusted by using a wrench on a hexnut type connection at the base, and a nut on each mount can be tightened against the bottom plate on the leg to lock the mount at any height.

Each of the four rigid casters on the rolling support was bolted through four holes that were drilled in the bottom of the frame after it was welded together. Each caster has a capacity of 175 lbs (778 N) and an overall height of 3 5/16" (84 mm). The wheels on the casters are 2 1/2" (64 mm) in diameter and 29 mm wide and are made from Atlasite™ rubber. Care was taken to align the casters properly on the frame so that the support would roll in the correct direction with ease.

A stand was manufactured to support the AALD vertically above the blast chamber floor during the set-up procedure. This stand, which is shown in Figure 5.9, was made from wood and steel Dexion™ angle pieces and has a height of 267 mm. The top of the stand was formed in the shape of a cross from two 470 mm long, 60 mm wide, and 38 mm thick pieces of wood. The Dexion™ pieces were bolted together to form four legs, and sheet metal screws were used to attach the legs to the wood cross. The top of the stand was designed so that it would pass between the holes in the endplates for the continuously threaded rods and would not interfere with the attachment of washers and nuts to the rods during the AALD set-up procedure.

Figure 5.9 Photograph of AALD on support stand during set-up procedure.

5.3 Cylinder Preparation

Cylinders used in the uniaxial loading experiments were manufactured and instrumented as described in Chapter 4. The uniaxially loaded cylinders were easier to prepare for testing than the biaxially loaded cylinders, since it was not necessary to bond endcaps to these specimens. However, since the cylinders without endcaps were unsupported and could easily be deformed, it was difficult to attach strain gages to them. This problem was solved by carefully putting each cylinder back on the mandrel and then attaching the mandrel to the tubewinder shown in Figure 4.8. Thus, the cylinder was held stationary during the strain gaging process and firm pressure could be applied without damaging the cylinder.

The only other step required to prepare the uniaxially loaded cylinders for testing was to attach the previously mentioned teflon strip to each end. The teflon strips were needed to reduce friction between the cylinder wall and the neoprene mats used to prevent the bladder from protruding into the endplate grooves. The 0.04 mm thick, 38 mm wide, and 965 mm long strips were cut from a 1225 mm wide roll of teflon using a ruler and a utility knife. A continuous length of flash tape was used to tape the strip around the circumference at the end of the cylinder so that all of the tape was on the cylinder and most of the teflon strip was overhanging the edge. The strip was folded over the edge to the inside of the cylinder and another continuous length of flash tape was used to finish attaching the teflon. Flash tape was chosen over other kinds of tape since it is very thin and smooth and it sticks fairly well to the cylinders. Attempts were made to minimize wrinkling of the teflon strips. However, even with some wrinkles, the strips made it easier to insert the cylinder in the endplate grooves after the neoprene mats were attached.

5.4 Set-up Procedure

Several requirements were identified in designing a set-up procedure for the AALD. Most importantly, the set-up procedure needed to be consistent and easily repeatable. Also, in order to achieve the proper loading condition on the cylinder and a fairly symmetric loading condition on the AALD, it was important to develop a method for aligning the endplates and rod support plates parallel to each other and the continuously threaded rods perpendicular to the endplates. To prevent movement of the cylinder once it was installed in the apparatus, it was desirable for the endplates to be flush with the cylinder ends. It was necessary to minimize any risk of damage to the cylinder during the set-up procedure, and, of course, a procedure was sought that was convenient and relatively quick and easy to implement.

The set-up procedure that was developed to satisfy these requirements involves two people and is performed in the blast chamber. As mentioned previously, the rods and the holes in the endplates and rod support plates were marked with letters so that the apparatus could always be put together with the endplates, rod support plates, rods, and cylinder in the same orientation with respect to each other as illustrated in Figure 5.10. The procedure was practiced and modified prior to the verification testing of the apparatus, and complete instructions, except for those for the rod support plates, were established before the first tests took place. After the verification tests, additional steps were added to the procedure for the rod support plates, but none of the preexisting steps were affected. The major steps of the set-up procedure for the fully dismantled apparatus are summarized here. Once the apparatus was set up the first time, only the top endplate was disconnected between tests and the procedure was conducted on the day of the cylinder test starting from the point when the cylinder was

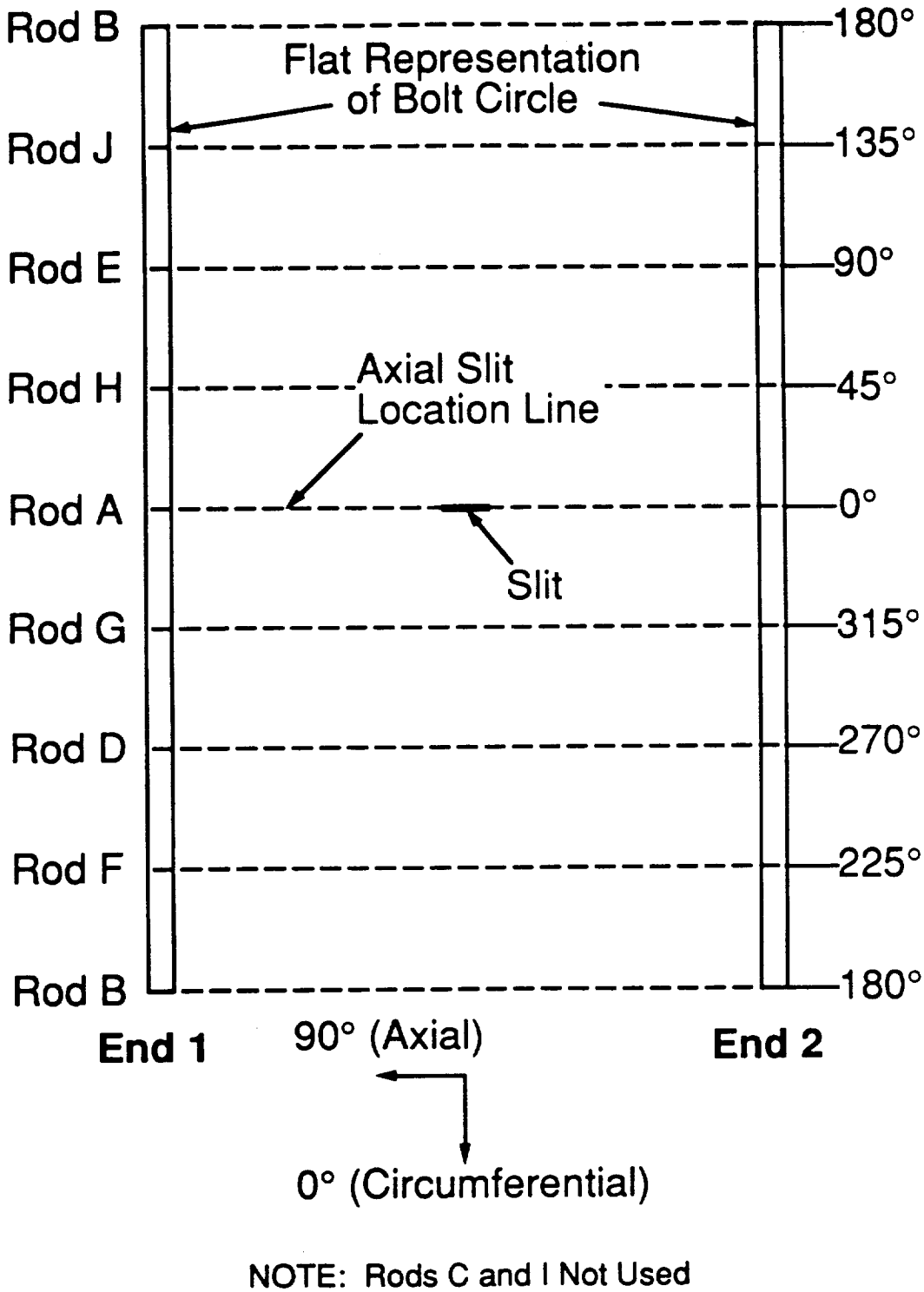

Figure 5.10 Relative orientations of rods/endplates to cylinder in assembled AALD.

installed in the device. An internal TELAC document describes the set-up procedure in more detail [35].

The AALD is put together vertically on a special stand that was designed and built for this purpose and is described in Section 5.2. The set-up procedure begins by leveling and stabilizing this stand on the blast chamber floor using shim stock. The endplate without the hole for the pressure-fitting plate is placed on the support groove side up and is oriented so that the support does not interfere with the attachment of washers and nuts to the continuously threaded rods. The bottom endplate is then loosely attached to the rods using two nuts and a washer on both sides of the endplate. The nuts are located on the rods so that 60 mm of each rod protrudes from the bottom of the endplate. Prior to tightening the nuts against the bottom endplate, the upper endplate is rested groove side down on resistance nuts and washers at the upper ends of the rods. The resistance nuts are turned to level this plate and thereby properly align the rods with respect to the endplates. Nuts with washers are finger-tightened on the other side of the top endplate to hold the rods in place. The nuts are then tightened on the bottom endplate in a consistent manner by holding a nut on one side of the endplate stationary with a wrench and using a wrench to turn a nut on the other side until it is hand tight. The nuts are tightened so that a similar amount of resistance is felt for each nut. The upper endplate is removed after the tightening of the bottom nuts is complete.

The rod support plates are then connected to the continuously threaded rods, one plate at a time. One resistance nut and washer are placed on each rod at the height where the plate is to be located. The plate locations are determined so that the plates will be equally distributed between the endplates after the cylinder is installed. The plate is then guided onto the

rods and is allowed to rest on the nuts and washers. The resistance nuts are adjusted until the plate is level and, thus, parallel to the bottom endplate. Another nut and washer is finger-tightened on all eight rods on the top of the plate to hold the plate stationary with respect to the rods. The whole process is repeated with the next plate until all three plates are in place. Each of the twenty-four rod/plate connections for all three rod support plates is then consistently tightened using two wrenches by holding the bottom nut stationary and turning the top nut. The nuts are turned hand tight so that a similar amount of resistance is felt for each nut.

The next step in the set-up procedure is to install the cylinder in the 'cage' formed by the continuously threaded rods and the rod support plates. The cylinder is slowly and carefully lowered into the 'cage' from the top to prevent scraping the cylinder on the rods or rod support plates or damaging the strain gages. One person holds the cylinder while another guides it down the hole, over the neoprene mat, and into the endplate groove. In the current work, the axial slit location line of the cylinder was always oriented directly under rod 'A', except in two of the verification tests. For consistency, End 2 of the cylinder was always placed into the bottom endplate.

Before the top endplate is placed on End 1 of the cylinder, the pressure-fitting plate with a bonded bladder is attached to the top endplate using the previously mentioned steel 'clips.' The top endplate is held groove side down when the pressure-fitting plate is attached, and the bladder is allowed to hang freely from the endplate. The pressure-fitting plate is rotated in the endplate so that the seam on the main body of the bladder will be located in the back of the cylinder. The bladder is guided into the cylinder and then the endplate is lowered over the rods and onto the end of the cylinder.

The resistance nuts on the top endplate are backed off so that the entire weight of the endplate is taken by the cylinder. This is done to ensure that the endplates are flush with both cylinder ends. The resistance nuts are moved up so that they just barely touch the bottom of the endplate and then the resistance nuts on rods 'A' and 'B' are turned by three-twelfths of a full rotation to lift the endplate 0.7 mm off the cylinder end. This is done to minimize the compressive preload that is induced in the cylinder by the weight of the endplate. Nuts are finger tightened on the top of the endplate at the 'A' and 'B' locations to hold the endplate in place, and then the rest of the resistance nuts are again moved up so that they just barely touch the bottom of the endplate. Two rows of nuts are then finger tightened on all rods on the top of the top endplate, followed by the final tightening of all of the nuts on the top endplate in a specific order. These nuts are tightened in the same manner as described previously for the nuts on the bottom endplate.

With the AALD set up as described, the only remaining step is to lift the apparatus and rest it horizontally on the supports. This is the only step in the procedure that requires more than two people. The pressure-fitting end of the apparatus is located on the fixed support, and the apparatus is oriented so that the slit is up. The procedure for cylinder testing using the AALD is the same as that for the biaxially loaded cylinders and is described in Chapter 4. After the cylinder test, the AALD was returned to the leveled stand and the top endplate was disconnected so that the cylinder fragments could be removed and the apparatus could be prepared for the next test.

5.5 Verification Testing

Before the AALD could be confidently used to test cylinders to failure in hoop loading only, the design had to be verified through experiments. The

primary goal of the verification testing was to ensure that no axial or torsional loads were induced in the cylinder test section. It was also important to establish that any boundary effects were restricted to a small range at the cylinder ends and that the bladder and the cylinder ends were not damaged significantly during the testing. It was also necessary to show that repeatable results could be achieved, especially when the AALD was taken apart and put back together. A maximum of seven channels of strain gage data could be collected during any one test, due to limitations of the A/D board in the testing computer.

One unnotched $[90/0/\pm45]_s$ cylinder was used in four tests conducted to different pressurization levels using different combinations of active strain gages. Strain data from two gages on the continuously threaded rods and eleven strategically placed gages on the cylinder were used to verify that the proper loading condition was achieved. Three control gages were designated, and the strain data from these gages were compared for all four tests to assess the repeatability of the results. The top endplate was disconnected and then reconnected and the cylinder was rotated by +22.5° with respect to the continuously threaded rods between the second and third tests, again to see if repeatable results could be achieved. Each test was also monitored for unusual results which might indicate bladder failure or unexpected cylinder damage. Once the strain data from the unnotched cylinder tests were analyzed and the operation of the AALD was shown to be satisfactory, the second part of the plan was to test the same cylinder to failure with a 50.8 mm slit and see how the cylinder failure would affect the AALD. The apparatus and cylinder strain gage locations and the five verification tests are described, followed by a discussion of the strain data analyses for all five tests.

5.5.1 Verification Test Plans

The strain gage locations for the $[90/0/\pm45]_s$ cylinder used in the verification testing are shown in Figure 5.11. The orientations and designations of these gages are indicated in Figure 5.12. The strain gages were distributed on the cylinder so that strain data could be collected from varied locations at different relative orientations to the continuously threaded rods. However, strain gages were not placed in the back of the cylinder due to the previously described fiber joint in the 0° plies. The center rosette was located 356 mm in the circumferential direction from the axial slit line location and was centered along the cylinder length. The three gages in this rosette, as well as those in the other two rosettes on the cylinder, were oriented in the circumferential and longitudinal directions and in the direction at 45° with respect to the other two. This rosette was used to characterize the far-field strain state in the cylinder and the circumferential and longitudinal gages were designated as controls. This rosette was placed sufficiently far from the planned slit location for this cylinder so that it could still be used to collect far-field strain data during the failure test. The End 1 and End 2 rosettes were both located 17 mm from the ends of the cylinder, so that they would just clear the endplate groove when the cylinder was installed in the AALD. The End 2 rosette was located on the axial slit location line at End 2 of the cylinder, while the End 1 rosette was located 356 mm in the circumferential direction from the axial slit location line at End 1 of the cylinder, as defined in Chapter 4. These rosettes were used to look at the strain state in the boundary zone on the cylinder at two different locations. As mentioned in Chapter 3, the boundary zone near the ends of the cylinder is a region of high strain gradients induced by the constraint of the

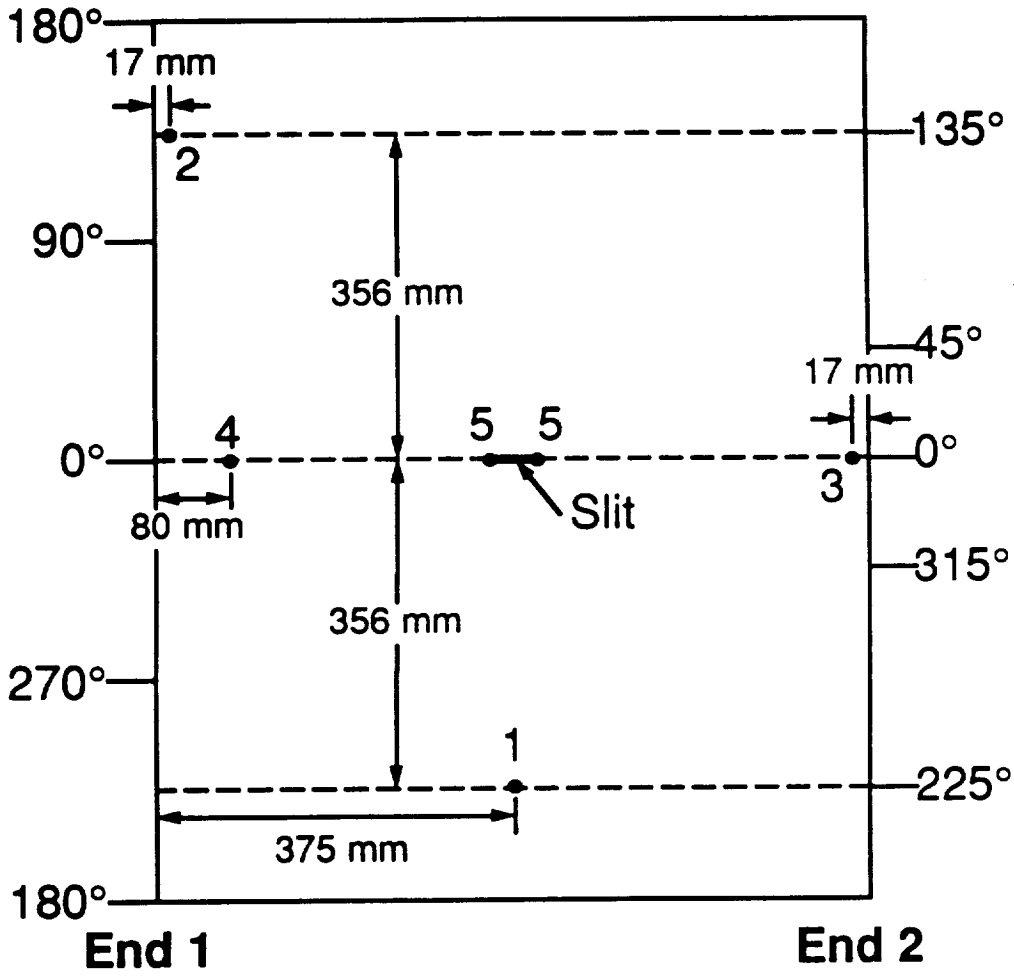

- Gage Locations:
  1 Far-Field Rosette
  2 End 1 Boundary Rosette
  3 End 2 Boundary Rosette
  4 Edge Zone Pair
  5 Slit Tip Gages

Figure 5.11 Illustration of cylinder strain gage locations for AALD verification tests.

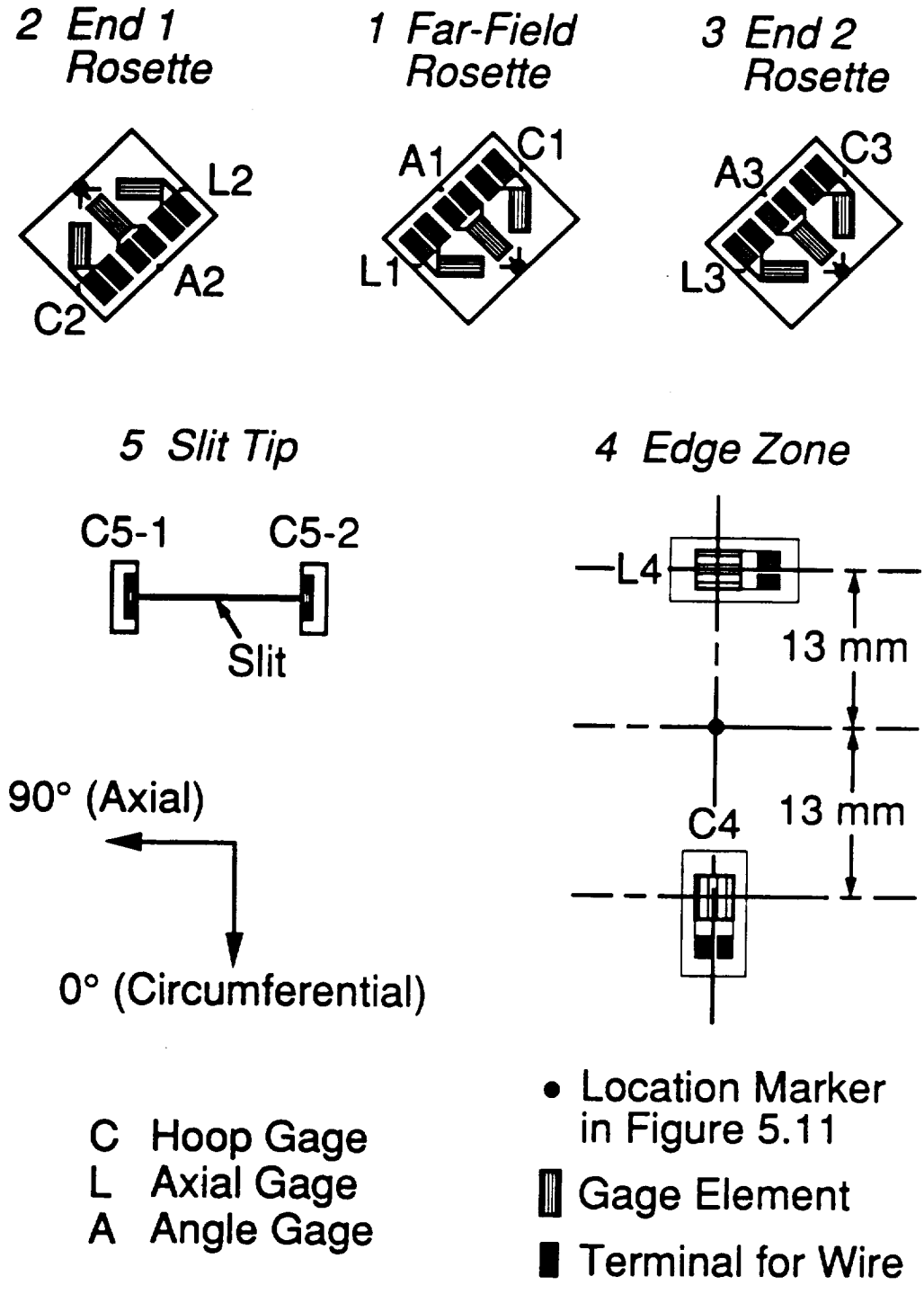

Figure 5.12 Illustration of cylinder strain gage orientations for AALD verification tests.

endplates. These two boundary zone rosettes were thus used to see if observed effects in this zone are consistent around the circumference of the cylinder. Longitudinal and circumferential edge zone gages were located 80 mm from End 1 of the cylinder on the axial slit location line. These gages were placed near the edge of the known boundary zone for the biaxially loaded cylinders, as discussed in Chapter 3, to see if the size of these zones is comparable for the two loading conditions. Finally, a small circumferential gage with its substrate trimmed to the gage element on one side was placed directly at each slit tip before the cylinder was tested to failure with the 50.8 mm slit, in an attempt to monitor slit tip damage.

Additional strain data were taken from a longitudinal gage on the rod marked by the letter 'A', which was located either directly above the slit location line or +22.5° in the hoop direction from this line, and from a longitudinal gage on the rod marked 'D', which was located 90° from the rod marked 'A' in the direction toward the center rosette. The strain data from the rod gages was used to determine if the loading on the rods is repeatable from test to test and if the loading on the endplate is equally distributed between the rods. The gage on rod 'A' was designated as a control.

The test sequence and active strain gages for the AALD verification testing are indicated in Table 5.1. Seven strain channels were used during each test to maximize the amount of data collected. The three control gages were active during each test. The three gages in each rosette were active at the same time in at least one test so that the stress state could be calculated in the three primary zones on the cylinder.

Tests 1 and 2 were conducted on the same day to internal cylinder pressures of 0.34 and 0.69 MPa, respectively, and the top endplate was not disconnected between the tests. The cylinder was oriented in the apparatus

Table 5.1 Active Strain Gages for Uniaxial Test Apparatus Verification Tests

Gage		Test 1 0.34 MPa[b]	2 0.69 MPa	3 0.69 MPa	4 1.21 MPa	5 0.57 MPa
Center Rosette	C1[a]	X	X	X	X	X
	L1[a]	X	X	X	X	X
	A1	X				X
End 1 Rosette	C2		X	X		
	L2	X	X	X		
	A2		X			
End 2 Rosette	C3				X	
	L3	X			X	
	A3				X	
Edge Zone	C4		X	X	X	X
	L4			X		
Slit Tip Gages	C5-1					X
	C5-2					X
Rod Gages	L6-1[a]	X	X	X	X	X
	L6-2	X				

[a] indicates control gage

[b] indicates maximum test pressure

for these tests such that the axial slit location line was located directly under rod 'A'. The primary purpose of Test 1 was to see if there would be any immediate problems with the bladder or obvious damage to the cylinder. All three gages in the far-field rosette, the two boundary zone axial gages, and the two bar gages were active. This test was also used to get an initial feel for the loading condition on the cylinder and the apparatus. Test 2 was conducted to further establish these loading conditions at a higher cylinder pressure and to check the repeatability of the control gage data. The far-field circumferential and longitudinal gages, the three gages in the End 1 boundary zone rosette, the edge zone circumferential gage, and the bar gage above the slit location line were active. Circumferential strain data from the boundary, edge, and far-field zones were collected during this test to determine the variation of circumferential strain along the length of the cylinder.

Following Tests 1 and 2, the top endplate was disconnected and the cylinder and bladder were removed from the test apparatus. The bladder was carefully examined and no damage was observed. This indicated that the neoprene mats were successful in keeping the bladder out of the endplate grooves. The neoprene mats, latex tubing used to line the endplate grooves, and cylinder were also examined and appeared to be undamaged. A preliminary analysis of the strain data from Tests 1 and 2 was conducted, and the desired loading condition was verified before proceeding to the third and fourth tests.

Tests 3 and 4 were conducted on the same day to internal cylinder pressures of 0.69 and 1.21 MPa, respectively, and the top endplate was not disconnected between the tests. The same bladder was used for these tests as was used for Tests 1 and 2. The main difference between these and the

previous tests is that the cylinder was rotated in the apparatus by +22.5° so that the axial slit location line was halfway between bars 'A' and 'H'. The primary purpose of Test 3 was to determine if the change in orientation of the cylinder with respect to the continuously threaded rods and the disconnection of the top endplate between the second and third tests would affect the control gage results. This test was conducted with the far-field circumferential and longitudinal gages, the boundary zone circumferential and longitudinal gages at End 1 of the cylinder, both edge zone gages, and the bar gage on rod 'A' active. Circumferential and longitudinal strain data from the boundary, edge, and far-field zones were collected to determine the variation of these strains along the length of the cylinder. Following the test, the apparatus and cylinder were examined and no damage was observed. Test 4 was conducted to a pressure level that is close to the average predicted failure pressure for the uniaxially loaded cylinders considered in this investigation and is 175% of the predicted failure pressure for the same cylinder with a 50.8 mm slit. The main purpose of this test was to obtain strain data for the unnotched specimen and to verify the proper operation of the apparatus in a representative range of pressures that were expected during the failure tests. Strain data from the control gages could also be directly compared to those that were measured during the failure tests of the notched $[90/0/\pm45]_s$ specimens. Test 4 was conducted with the far-field circumferential and longitudinal gages, all three gages in the boundary zone rosette near End 2 of the cylinder, the edge zone circumferential gage, and the bar gage on rod 'A' active. As in previous tests, circumferential strain data were collected from all three zones on the cylinder to establish the variation of these strains along the length of the cylinder. Following the test, the cylinder and bladder were removed from the apparatus and carefully

examined. As in the previous tests, no cylinder or bladder damage was observed.

Following the four tests on the unnotched $[90/0/\pm45]_s$ cylinder, a 50.8 mm axial slit was cut in the cylinder halfway down its length, on the line between paint grid columns 'S' and 'A', according to the procedure described in Chapter 4. Extreme care was taken to ensure that the eleven gages that were already on the cylinder were not damaged during the slit cutting procedure or the attachment procedure for the subsequently installed slit tip strain gages. The purpose and location of these slit tip gages is described earlier in this chapter as well as in Chapter 4. The cylinder was tested to failure in the uniaxial test apparatus with the three far-field rosette gages, the edge zone circumferential gage, the longitudinal gage on the rod marked 'A', and the two slit tip gages active. The cylinder was oriented in the device so that the slit was located directly below bar 'A', and the same bladder was used in this test as was used in Tests 1 through 4.

5.5.2 Verification Test Results

The strain data were analyzed throughout the verification tests to ensure that the desired loading condition was achieved and that the results were repeatable from test to test. The primary method of checking the repeatability of the results was to plot all the strain data obtained for a given gage that was active during more than one test on the same graph and to compare the results. Particular attention was given to the three control gages, since these gages were active during all five tests. Using this method, the repeatability of the results was shown to be excellent and, thus, only representative strain results are presented here.

The far-field strain state in the cylinder during the failure test (Test 5) is shown in Figure 5.13. The hoop and axial strains in this figure are direct outputs from the circumferential and longitudinal gages, respectively, in the far-field rosette, while the shear strains are calculated values based on strain readings from all three rosette gages. As can be seen in this figure, the pressure-strain curves for all three strain components are essentially linear throughout the test. Also, the results show that there is virtually no shear strain. This verifies that no torsional loading was induced in the cylinder, as is desired for the hoop loading only condition.

Hoop and axial strain output from the edge zone gages in Test 3 are shown in Figure 5.14. These results are comparable in magnitude and degree of linearity to the far-field results provided in Figure 5.13. However, the strains from the edge zone hoop gage are approximately 5% lower than those from the far-field hoop gage. This may indicate that the edge zone gage may have been slightly misaligned with respect to the cylinder's circumferential direction. Another possible explanation is that the edge zone gages may have been located slightly inside the boundary region at the end of the cylinder. Even if this were the case, the strain results suggest that the boundary region is comparably sized to or somewhat smaller than that for the biaxial loading condition. Thus, based on past experience with biaxially loaded cylinders, the cylinder length chosen for the current work is more than adequate to ensure that the boundary zones at the ends of the cylinder will not interfere with the loading condition near the slit.

Strain results for the boundary zone rosette near End 2 of the cylinder from Test 4 are displayed in Figure 5.15. As in Figure 5.13, the shear strain results in this figure were calculated using strain output from all three gages in the rosette. The pressure-strain curves for the three strain components in

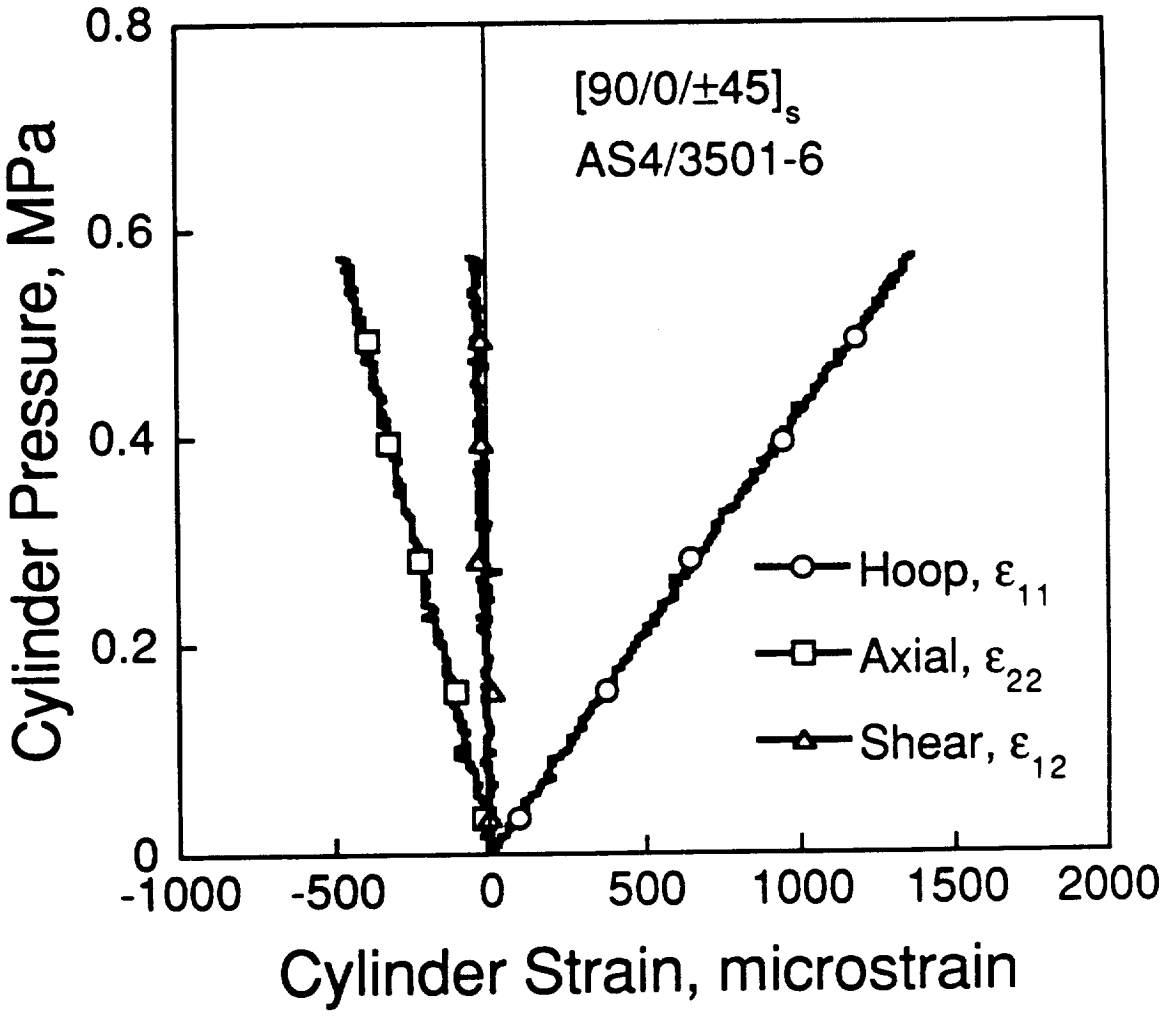

Figure 5.13 Far-field rosette strains from failure test of uniaxially loaded $[90/0/\pm45]_s$ cylinder with 50.8 mm slit.

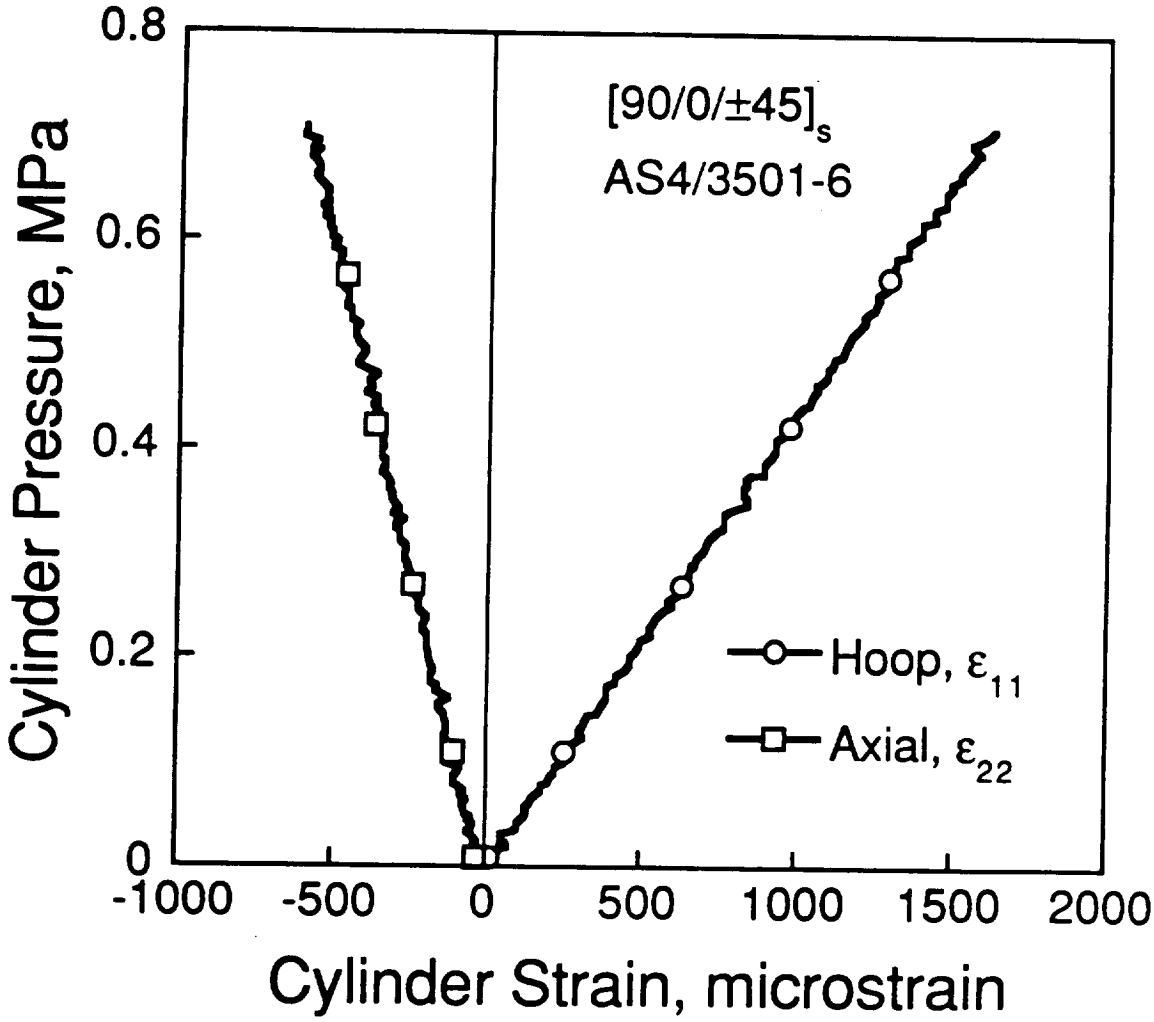

Figure 5.14 Edge zone strains from AALD Verification Test 3 of unnotched $[90/0/\pm45]_s$ cylinder.

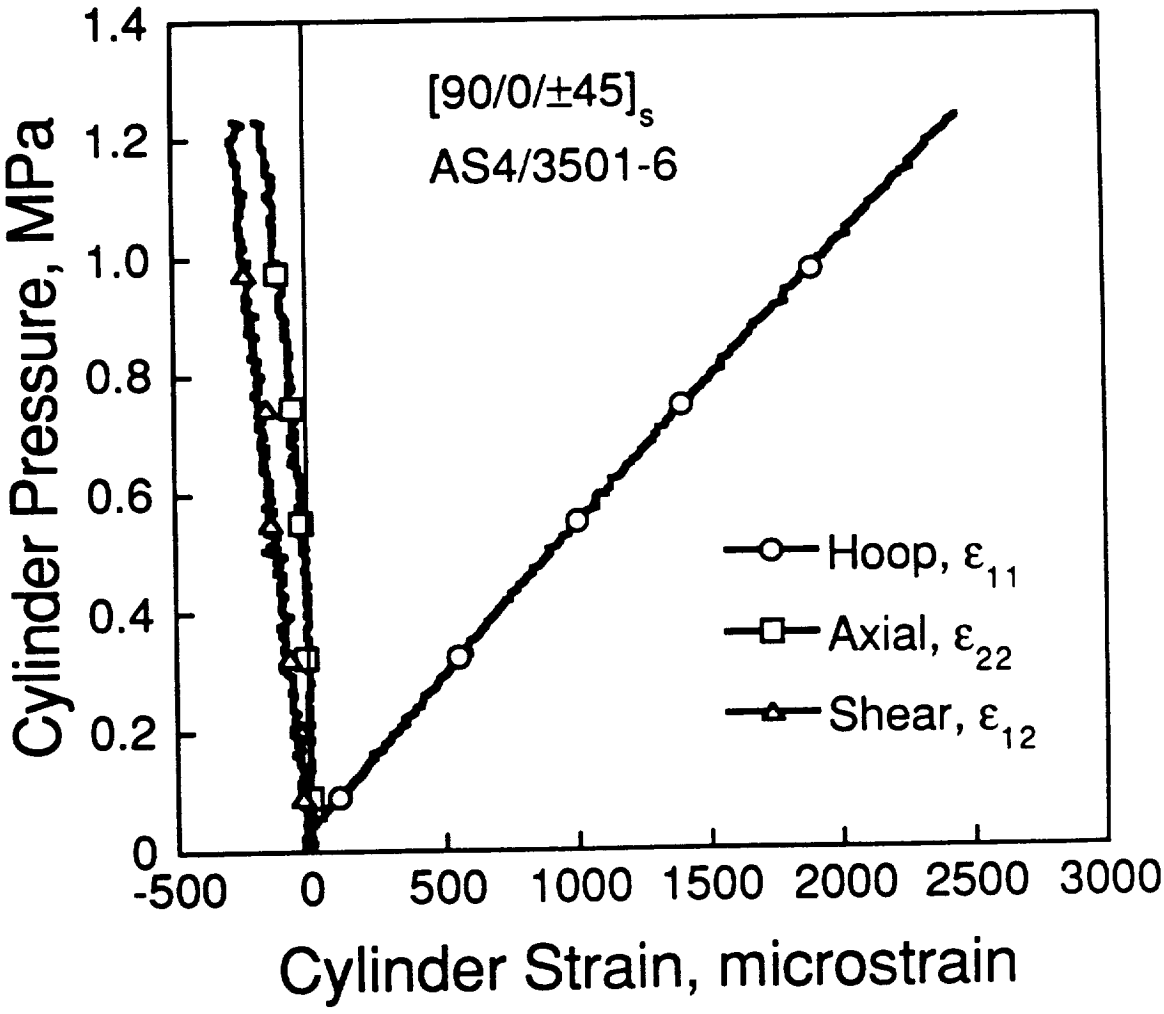

Figure 5.15 End 2 boundary zone rosette strains from AALD Verification Test 4 of unnotched $[90/0/\pm45]_s$ cylinder.

the boundary zone do not show the same degree of linearity as those for gages elsewhere on the cylinder. This is not surprising since many factors may cause slight changes in the boundary condition on the end of the cylinder during the test and, thus, result in slope changes in the boundary zone strain data. Such changes could be caused by shifting and settling of the cylinder in the endplate grooves during the test or interaction of the cylinder with the latex tubing used to line the endplate grooves, the neoprene mats, the ends of the bladder, or the walls of the endplate grooves. This behavior is likely since the cylinder material in and near the endplate grooves expands circumferentially and also contracts in the axial direction due to the Poisson's effect when it is under loading. The circumferential strains in the boundary zone are lower and the axial strains are higher than the far-field values, and the shear strains are nonzero, although small, which indicates that all three stress components are present in the boundary zone. As discussed in Chapter 3, this type of stress redistribution from the far-field hoop stress only condition is necessary to satisfy equilibrium since the material inside the endplate groove is not exposed to the pressure loading. Similar trends were observed for the rosette in the boundary zone at the other end of the cylinder, however, the magnitudes of the strains are somewhat different. This result is understandable since the rosettes are located in high gradient regions such that a small change in gage location or orientation could have a relatively large effect on the strain readings. Thus, the strain results confirm the presence of a boundary region of high stress and strain gradients near each end of the cylinder that is similar to that observed in a cylinder with bonded endcaps.

Strain readings obtained in Test 4 from the longitudinal gage on rod 'A' are provided in Figure 5.16. As can be seen in this figure, the general trend

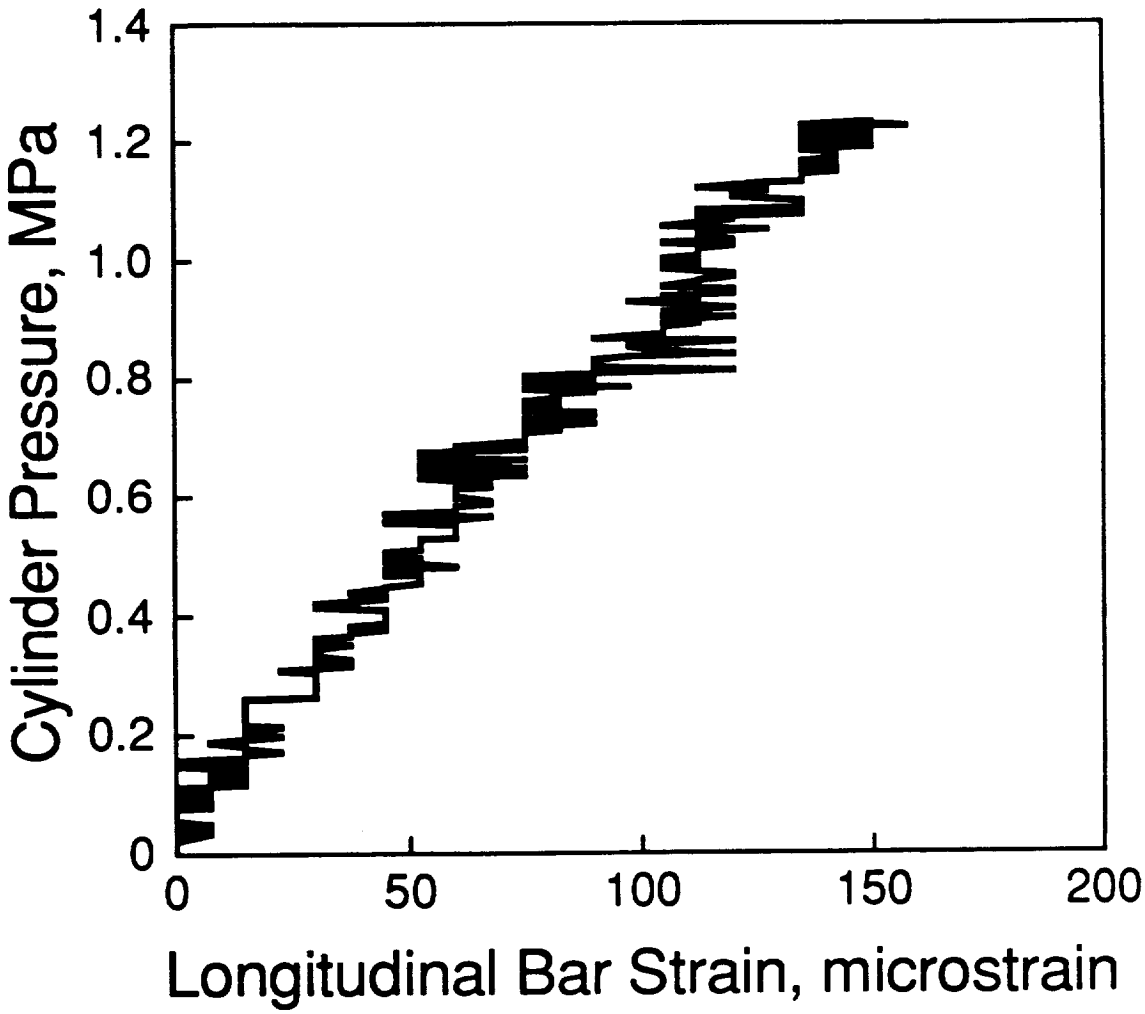

Figure 5.16 Rod 'A' longitudinal strains from AALD Verification Test 4 of unnotched $[90/0/\pm45]_s$ cylinder.

in the pressure-strain data is linear. The large fluctuations observed in the strain data are due to low resolution resulting from the conversion factor of 7.5 μstrain/computer unit that was used for all of the active gages in this test and the relatively low bar strains that were encountered compared to those for the cylinder. Strains of similar magnitudes and scatter ranges were obtained in Test 1 for the gage on rod 'D' and in the other tests in which the rod 'A' gage was active.

The longitudinal bar strain data shown in Figure 5.16 were used to calculate the stresses in the bar as a function of cylinder pressure so that they could be compared to predicted values. The experimental and predicted stress curves for rod 'A' from Test 4 are shown in Figure 5.17. Experimental stresses were calculated assuming a bar modulus of 207 GPa, while predicted values were calculated assuming that the bar load was carried only in the root diameter of the rod and that one-eighth of the total load on the endplate was taken by each rod. The root diameter used in the bar stress calculations is 0.77" (20 mm). As can be seen in Figure 5.17, the experimental bar stresses are approximately 20% lower than the predicted values. This discrepancy is artificially high, since the threads on the rods were neglected in the predicted stress calculations even though they carry some load and, thus, the predicted stresses should be lower. Also, due to the previously described issue concerning low resolution in the experimental strain data, shifting the strains in the positive direction by only one computer unit, which corresponds to 1.6 MPa of bar stress, decreases the discrepancy by approximately 6%. Thus, considering the known sources of error, the experimental bar stresses correlate reasonably well with the conservative predicted values.

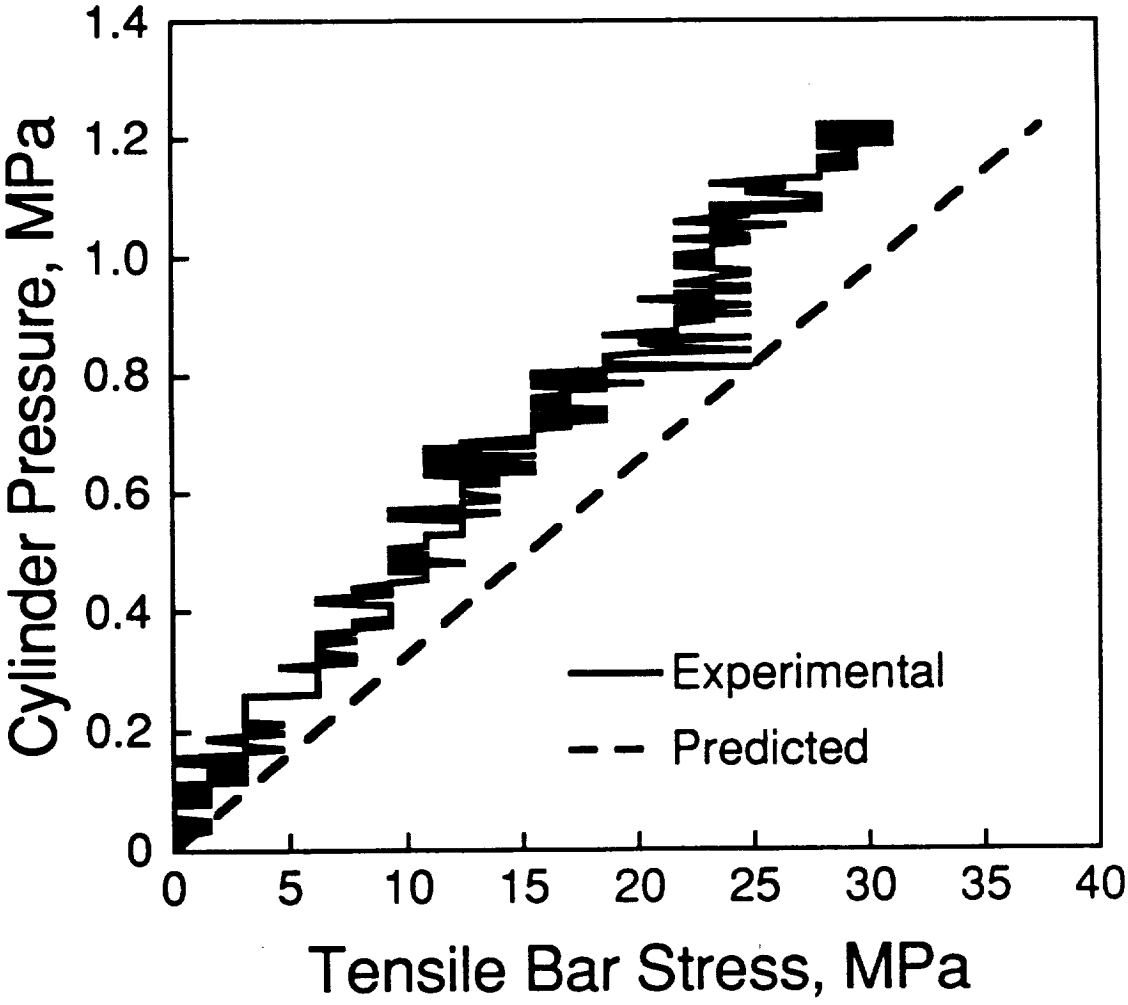

Figure 5.17 Experimental and predicted Rod 'A' longitudinal stresses from AALD Verification Test 4 of unnotched $[90/0/\pm45]_s$ cylinder.

In order to determine if only hoop loading was applied to the cylinder far-field, the experimental data were further analyzed. A uniaxial stress state was assumed to exist. Thus, hoop stresses were determined from the experimental cylinder pressures using the equation:

$$\sigma_{11} = \frac{pr}{t} \tag{5.1}$$

where σ_{11} is the hoop stress, p is the cylinder pressure, r is the radius of the cylinder, and t is the cylinder thickness. Nominal values of cylinder radius and thickness were used in all calculations. The slope of the hoop stress versus hoop strain data, or E_{11}, for all data sets involving edge zone and far-field circumferential gages were determined using a least squares linear curve fitting program called LIN6 [36]. A predicted value for E_{11} was determined to be 55.5 GPa using Classical Laminated Plate Theory and the basic ply properties of Table 3.1. If uniaxial loading was not achieved in the experiments, the experimental and predicted values would not agree.

The experimentally determined hoop moduli are listed in Table 5.2. The consistency of the moduli determined for each gage supports the previous conclusion that the results were repeatable from test to test. Furthermore, the close agreement between the moduli obtained from the far-field circumferential gage data and the predicted value indicates that a far-field, uniaxial, hoop loading condition was successfully achieved.

One final check on this assertion was to use LIN6 to determine experimental values of the major Poisson's ratio, ν_{12}, from the slopes of axial strain versus hoop strain data for the edge zone and far-field gages. The experimentally determined values of ν_{12} are listed in Table 5.3. Reasonable agreement with the predicted value of 0.30 was achieved considering common

Table 5.2 Experimental Hoop Moduli from Uniaxial Test Apparatus Verification Tests

Test	Hoop Modulus, E_{11}, GPa	
	Far-Field	Edge Zone
1	59.2	--
2	59.3	58.9
3	58.9	62.4
4	58.8	62.7
5	59.4	62.2

Table 5.3 Experimental Poisson's Ratios from Uniaxial Test Apparatus Verification Tests

	Poisson's Ratio, ν_{12}	
Test	Far-Field	Edge Zone
1	0.35	--
2	0.35	--
3	0.35	0.36
4	0.34	--
5	0.34	--

effects, such as transverse gage sensitivity, which make it difficult to accurately measure the Poisson's ratio.

The desired uniaxial loading condition was also verified by using the constitutive equations and the Test 5 strain data from the far-field rosette, shown in Figure 5.13, to calculate the far-field stress state in the cylinder. The experimentally obtained stress state is displayed in Figure 5.18 along with the predicted hoop stresses for a uniaxial loading condition as determined from equation 5.1. The experimental hoop and axial stresses in the quasi-isotropic cylinder, σ_{11} and σ_{22}, were calculated from the equations:

$$\begin{Bmatrix} \sigma_{11} \\ \sigma_{22} \end{Bmatrix} = \frac{E}{1-\nu^2} \begin{bmatrix} 1 & \nu \\ \nu & 1 \end{bmatrix} \begin{Bmatrix} \varepsilon_{11} \\ \varepsilon_{22} \end{Bmatrix} \tag{5.2}$$

where ε_{11} and ε_{22} are the hoop and axial strains, respectively, E is the in-plane modulus and ν is the in-plane Poisson's ratio. The experimental shear stresses, σ_{12}, were calculated from the equation:

$$\sigma_{12} = G\,\varepsilon_{12} \tag{5.3}$$

where G is the in-plane shear modulus and ε_{12} is the shear strain calculated using all three rosette gage strains. The nominal E, ν, and G values of 55.5 GPa, 0.30, and 21.4 GPa, respectively, as calculated from Classical Laminated Plate Theory were used to generate all three experimental stress curves in Figure 5.18. As can be seen in this figure, the experimentally obtained far-field hoop stresses are approximately 8% lower than the predicted values. The axial and shear stresses are essentially zero, as desired. Thus, the experimental far-field stress results further confirm that the far-field uniaxial loading condition was obtained.

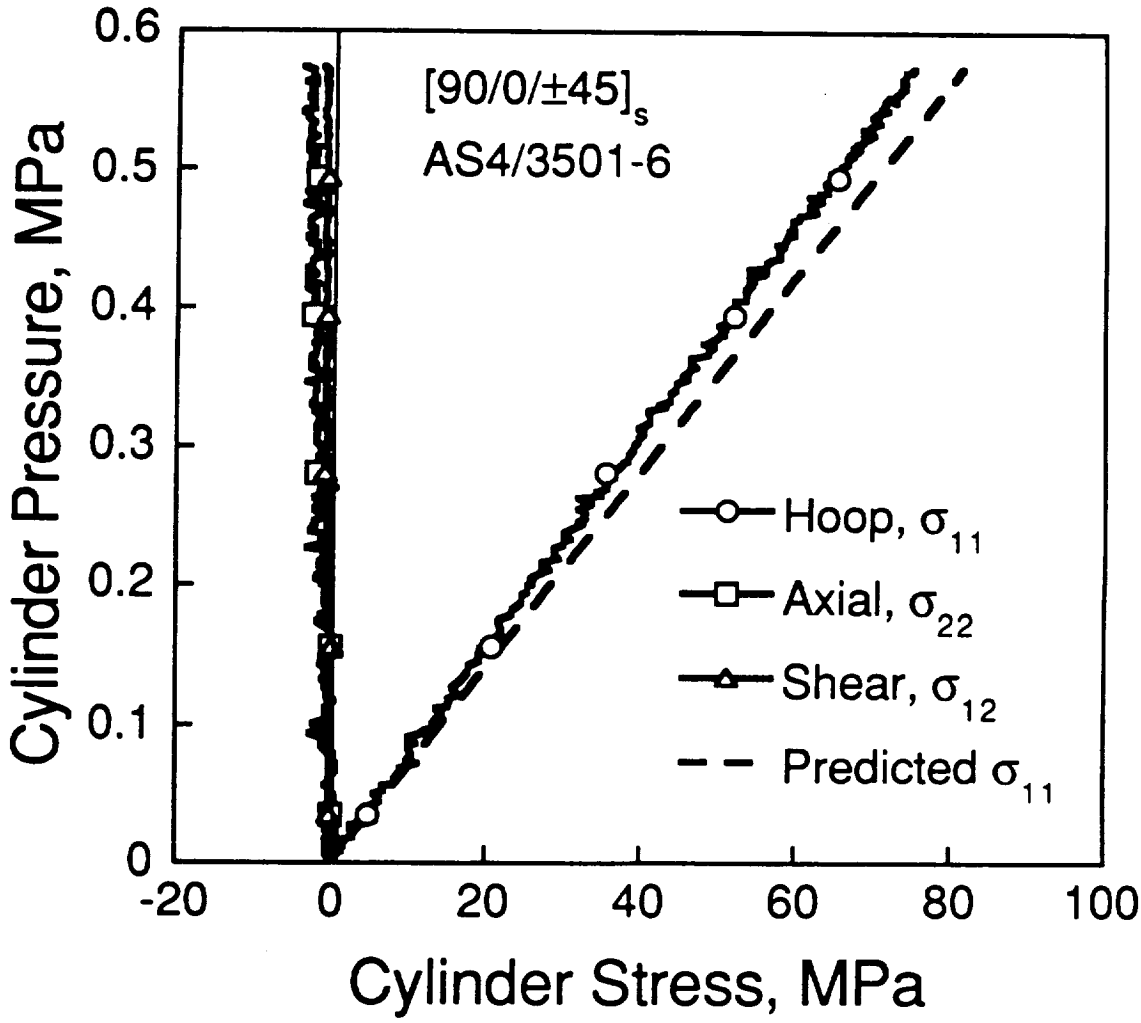

Figure 5.18 Experimental and predicted far-field stresses from failure test of uniaxially loaded $[90/0/\pm45]_s$ cylinder with 50.8 mm slit.

The $[90/0/\pm45]_s$ cylinder with the 50.8 mm axial slit failed at an internal pressure of 0.57 MPa. A photograph of the cylinder and apparatus immediately following the test is provided in Figure 5.19. A full presentation of the results along with similar results for other cylinders is provided in Chapter 6. What is of importance to note in terms of verification of the device is that obvious permanent deformation was observed in five of the eight continuously threaded rods, with the worst damage observed in rods 'H' and 'G'. These rods were located on both sides of rod 'A', which is the rod that was located directly over the slit. No damage was observed for the neoprene mats or the endplates, and no problems were encountered in disconnecting the damaged rods from the endplates.

The rods were placed on a flat surface and a ruler was used to measure the maximum permanent deflection in each rod. The largest deflection of 10 mm was observed in rod 'H'. Permanent deformation could not be confirmed visually in rods 'F', 'B', and 'J', which are the three rods that were located the farthest from the slit location. It is unknown whether yielding occurred in these three rods. It is also unclear whether the damage observed in the other rods was caused by a bending or buckling effect, or both. However, since the rods were in tension when the cylinder failed, the most likely explanation is that the addition of bending stresses induced by the cylinder hitting the rods as it exploded caused the yield strength to be exceeded in most of the rods. This explanation is supported by the fact that the direction of permanent deflection in the rods was always observed to be away from the cylinder in essentially the radial direction. Also, distinct impressions left by the rod threads on the main remaining piece of the cylinder and the retrieved cylinder fragments verify that the cylinder made direct contact with all eight rods. These impressions were the most pronounced near the most severely

Figure 5.19 Photograph of assembled uniaxial test apparatus after failure test of $[90/0/\pm45]_s$ cylinder with 50.8 mm slit.

damaged rods, rods 'H' and 'G'. As shown in Figure 5.19, the edges of the cylinder along the main fracture path wrapped themselves around these two bars during the cylinder explosion so that they were on the outside of the apparatus. Due to the high degree of contact between the cylinder and the rods and the high force levels required for this to happen, it is understandable why rods 'H' and 'G' were damaged more than the other rods. To prevent rod damage and possible endplate damage in subsequent tests, most of which involved cylinders with higher predicted failure pressures, the previously described rod support plates were added to the AALD design. A new set of rods was also purchased and was used for the remaining tests in this investigation.

The damage to the rods caused by the cylinder explosion raises questions concerning the role of the rods in damage initiation and propagation in the cylinder. This potential role is addressed further in the following chapters. However, it is important to note that the analysis of the damage state in the $[90/0/\pm45]_s$ cylinder with the 50.8 mm slit indicates that the propagating damage in a cylinder, but not the initial damage mechanism, may be modified or intensified due to the close proximity of the rods. Similar effects caused by the rod support plates are also expected and were observed in the subsequent uniaxial failure tests. The types of cylinder damage that were observed in these tests which were most likely influenced by the rods and rod support plates and the consequences of these effects on the interpretation of the test results are described in detail in Chapters 6 and 7.

The analyses of the strain data from the verification tests support the assertion that the AALD functions as designed. Following the verification tests and the manufacture of the rod support plates, general failure testing of cylinders with axial slits was conducted in the uniaxial test apparatus

according to the test matrix described in Chapter 3. The apparatus set-up was conducted as described earlier in this chapter, and the same testing procedures were used as described in Chapter 4. The results of these tests, as well as those for the coupons and biaxially loaded cylinders tested in this investigation, are described in detail in the following chapter.

CHAPTER 6

Results

Experimental results from failure tests on coupons, uniaxially loaded cylinders (pressurized in the AALD), and biaxially loaded cylinders (pressurized in the normal configuration) are provided in this chapter. Correlations of the coupon failure stresses and cylinder failure pressure predictions are also presented. The methodology used to generate these predictions from the notched coupon failure stresses is summarized in Section 3.4 and is described in detail in Chapter 2. Nominal radius and thickness values for the cylinders, nominal thicknesses and widths for the coupons, and measured slit lengths for both specimen types were used in all calculations related to the results presented in this section. Whenever an average value, such as an average failure stress or an average value of the composite fracture parameter for the coupons, is cited, values for individual specimens may be found in Appendix A.

In the slit tip strain plots that are presented in this chapter, Slit Tip Gage 1 refers to the circumferential gage located on the side of the slit closer to End 1 of the cylinder, as defined in Figure 4.14. In the far-field strain plots for the uniaxially loaded cylinders, Hoop Gage 1 refers to the original far-field circumferential gage which is located in or near paint grid square 'D10' in Figure 4.14. Stress-strain and strain-strain data for both coupons and cylinders were used to determine experimental in-plane moduli and Poisson's ratios. Each experimental laminate property is the initial slope of either the stress-strain or strain-strain data determined using a least squares linear curve fitting program known as LIN6 [36]. For

all average moduli and Poisson's ratios cited in this chapter, values for individual specimens may be found in Appendix A.

Discontinuities are observed in the slit tip strain data for all of the tape cylinders tested in the current investigation. In all cases, strains at the first discontinuity are well within the operational range of the gage and the slit tip strains remain within the operational range until the gages fail. Thus, the discontinuities in the slit tip strain readings are most likely a result of localized damage to the cylinder near the slit tips before the ultimate cylinder failure. However, it is important to note that as a result of this cylinder damage, the strain readings after the first discontinuity may also be affected by direct damage to the gages or partial debonding of the gages from the cylinder surface. Since the slit tip strain gages only measure strain at the surface, the strain results do not provide any insight into the types and quantities of slit tip damage and only indicate that such damage is present. The corresponding effects of this damage on the stress state at the slit tips are also unknown. The slit tip gages are located in high gradient regions so that the magnitudes of the measured strains are highly sensitive to the location and orientation of the gage. Thus, trends in the slit tip strain behavior for different laminates, as opposed to direct comparisons of the strain magnitudes, may be the best indicator of the role of the slit tip damage in the failure of these cylinders. Such trends are noted herein.

Damage descriptions are presented in this chapter for both coupons and cylinders. Except where noted, angles which are cited to describe the direction of failure in these specimens are referenced to the laminate axes, as defined in Figure 3.1 for coupons and in Figure 3.2 for cylinders. The damage descriptions for the uniaxially and biaxially loaded cylinders refer to damage schematics which are presented for each cylinder. Each

damage schematic is a scale drawing of the damage state in the cylinder with axial position from the midpoint of the slit referenced along the horizontal direction and hoop angular position from the axial slit location line referenced along the vertical direction. In each damage schematic, cylinder material that was not damaged is shown in white, fragments which were not recovered are indicated by a hatch pattern, delamination is indicated by gray shading, and through-thickness fracture paths are shown as black lines. All delamination is indicated by one pattern due to the large variation in the through-thickness locations and quantities (in terms of the number of plies effected at a given location) of delamination that were observed between cylinders and even on one cylinder. The original location of the slit is indicated by a straight gray line located circumferentially at 0° and centered on the axial position of 0 mm. A common element of the damage observed in the uniaxially loaded cylinders, which is not discussed further in the damage descriptions but is observable in the damage schematics, is the presence of a high degree of secondary damage induced by cylinder contact with the rods and rod support plates in the uniaxial test apparatus. This damage becomes more prominent with decreasing slit length, but it generally takes the form of circumferential damage and discoloration marks on the cylinder at the axial locations of the rods support plates. Scratch marks with varying degrees of severity and, in many cases, longitudinal damage are also present on the cylinder surface at hoop angular positions which roughly correspond to the locations of the continuously threaded rods. While it is clear that the propagating damage in the uniaxially loaded cylinders was modified and intensified by the test apparatus, the initial damage mechanisms were not affected.

6.1 [0/±45/90]s Coupons and Cylinders

Representative plots of the far-field longitudinal stress versus longitudinal strain data and far-field transverse strain versus longitudinal strain data for the unnotched coupons are provided in Figures 6.1 and 6.2, respectively. These curves for the unnotched specimens are generally smooth. Furthermore, the stress-strain curves for the unnotched specimens are linear for approximately the first third of each test, as can be seen in Figure 6.1. The far-field stress-strain curves for the notched specimens are similar and remained linear through approximately the first three-quarters of the test. The average initial slope of these curves, E_{11}, for the unnotched specimens is 53.6 GPa with a coefficient of variation of 2.1%. For the notched specimens, the average longitudinal modulus is 54.5 GPa with a coefficient of variation of 1.2%. These values compare well to a value of 55.5 GPa calculated using Classical Laminated Plate Theory (CLPT) and the basic material properties of Table 3.1. The strain-strain curves for the unnotched coupons are generally linear throughout the first three quarters of each test, as can be seen in Figure 6.2. The average value of the Poisson's ratio, ν_{12}, for the unnotched specimens is 0.32 with a coefficient of variation of 2.6%. This compares to the calculated value of 0.30.

Average failure stresses for the $[0/\pm45/90]_s$ coupons are indicated in Table 6.1. Average values of H_c calculated from these stresses using the Mar-Lin equation (equation 3.1) for the notched specimens are also shown in this table. The average value of H_c for all the notched $[0/\pm45/90]_s$ coupons is 632 $MPa*mm^{0.28}$ with a coefficient of variation of 6.0%. The coupon correlation curve for the $[0/\pm45/90]_s$ layup and individual data points used to establish this curve are plotted in Figure 6.3.

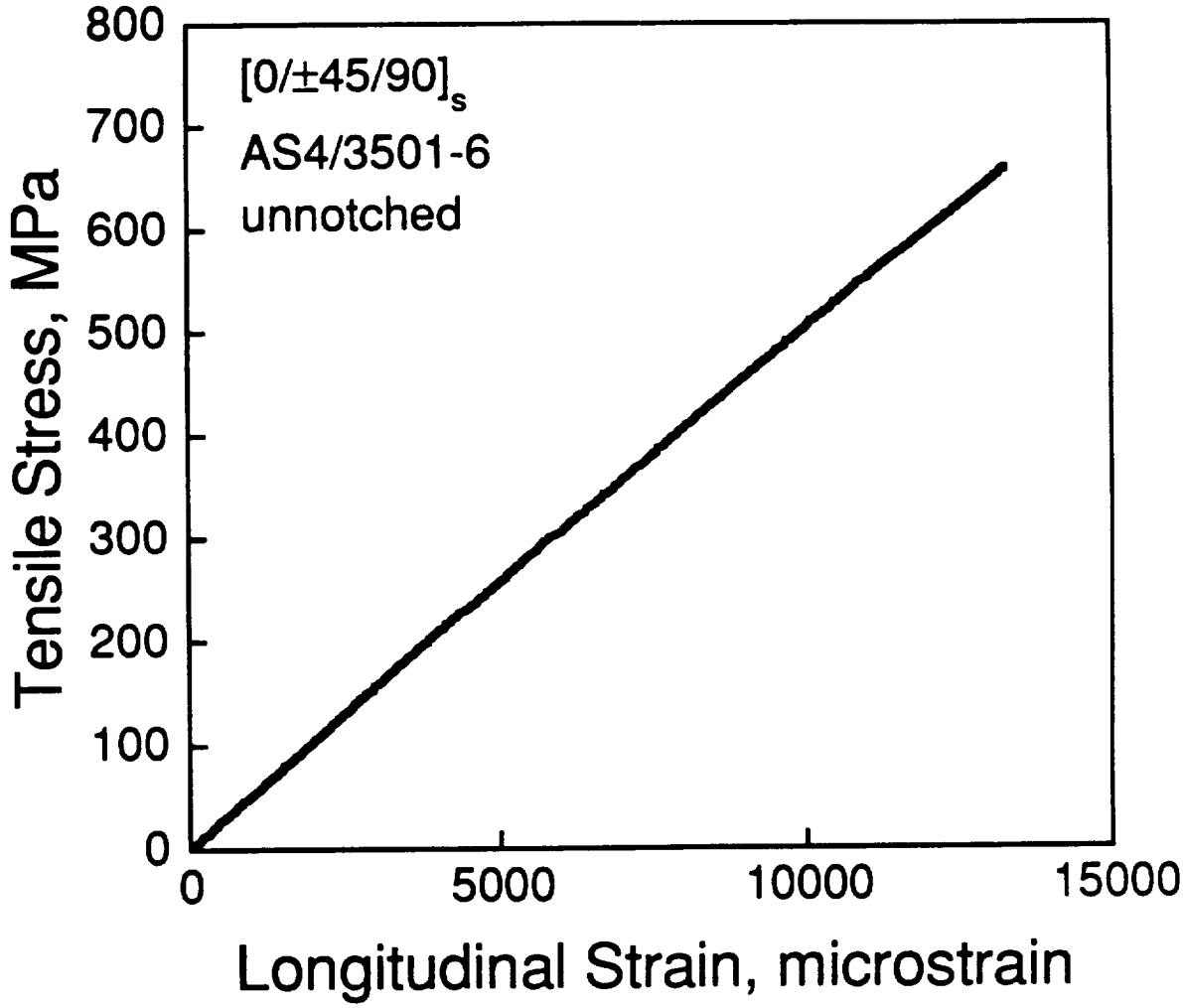

Figure 6.1 Tensile stress versus longitudinal strain for typical $[0/\pm45/90]_s$ coupon.

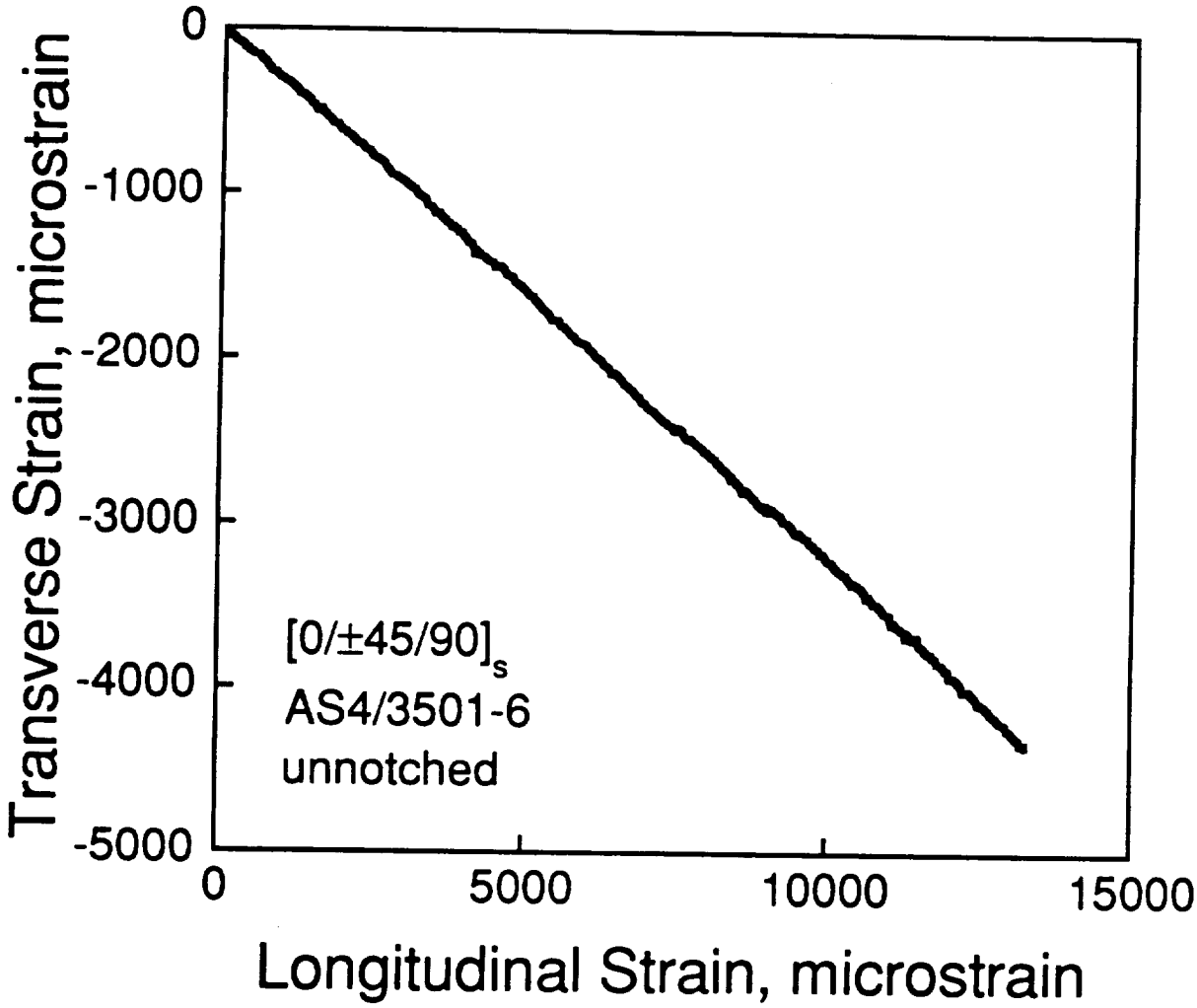

Figure 6.2 Transverse strain versus longitudinal strain for typical $[0/\pm45/90]_s$ coupon.

Table 6.1 Failure Data for $[0/\pm45/90]_s$ Coupons

Slit Length [mm]	Average Failure Stress [MPa]	Average H_c [MPa*mm$^{0.28}$]
unnotched	726 (6.0%)[a]	--
9.5	349 (7.7%)	656 (7.5%)
12.7	312 (6.2%)	640 (5.8%)
15.9	290 (3.4%)	630 (3.4%)
19.1	263 (3.8%)	602 (4.1%)

[a] Numbers in parentheses are coefficients of variation.

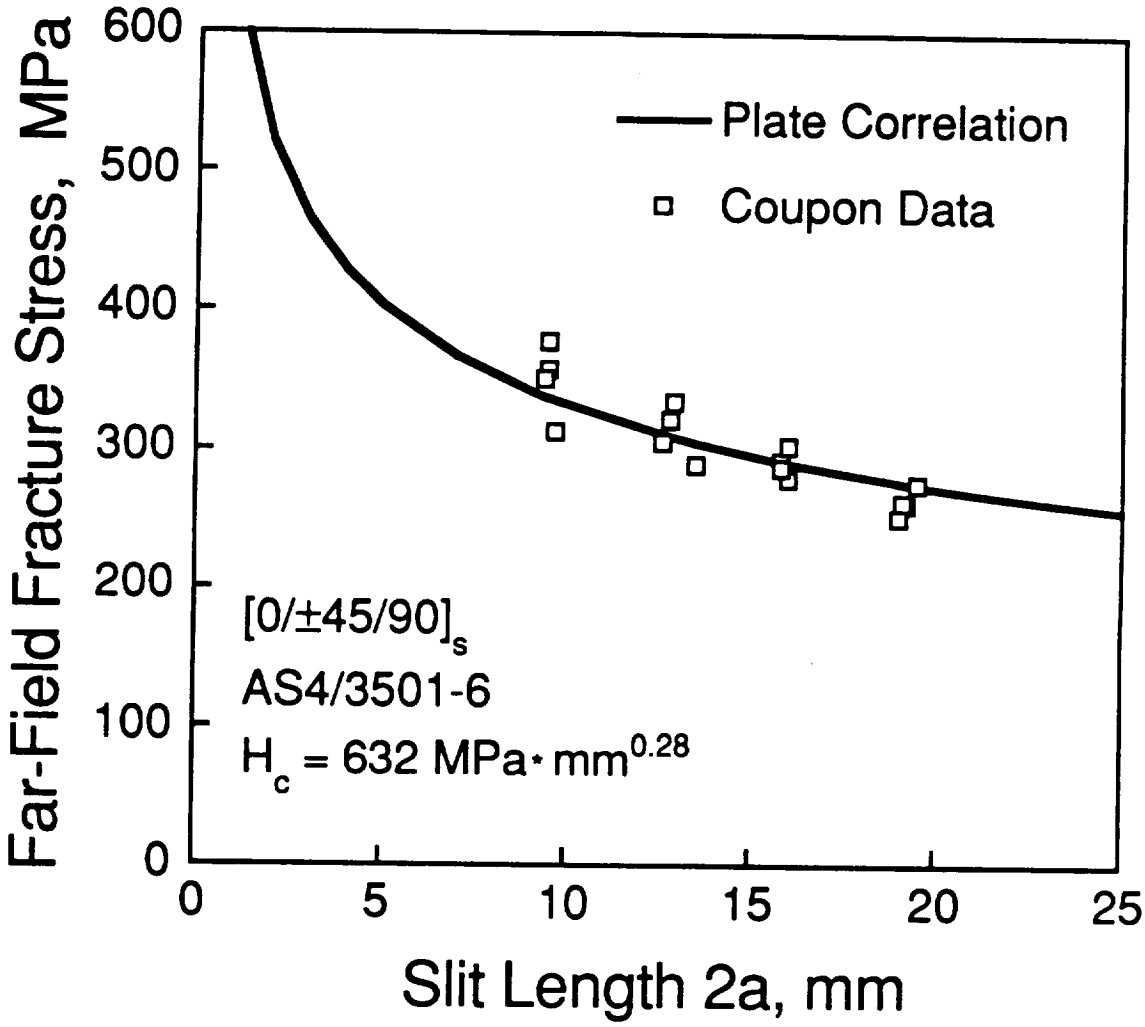

Figure 6.3 Individual failure stresses and failure stress correlation curve for notched $[0/\pm45/90]_s$ coupons.

A representative post-test photograph of an unnotched specimen is shown in Figure 6.4. Primary failure usually occurred in two locations approximately 30 mm from the ends of the specimen test section. However, an additional primary failure path was observed near the center of the test section in one specimen. The primary damage visible on the surface varies somewhat from specimen to specimen. Starting from the left side at the top of the coupon, a fairly clean, straight primary fracture path extends approximately halfway across the specimen along the 90° direction at which point it generally bifurcates. One branched path curves up slightly toward the loading tab as it continues all the way across the specimen while the other branched path extends away from the original path along the direction of the -45° fibers. The -45° path generally turns back toward the 90° direction as it approaches the edge of the specimen and it sometimes does not reach the specimen edge. Similar damage exists at the bottom of the specimen except that it starts from the right side. The 0° plies fractured cleanly, but show some minor secondary splitting and delamination along the primary fracture paths. Extensive secondary delamination and splitting of the ±45° plies is observed in the region between the branched paths and, as a result of this delamination, sections of the 0° and +45° plies are missing between the branched paths near the branching point. Similar secondary delamination in the ±45° plies is present near all of the fracture paths. Secondary delamination between the 90° plies and extensive splitting of these plies was usually observed all along both sides of the test section. These delaminations extend approximately 15 mm into the specimen from the edges. Some secondary splitting of the 90° plies along the fracture paths is also apparent.

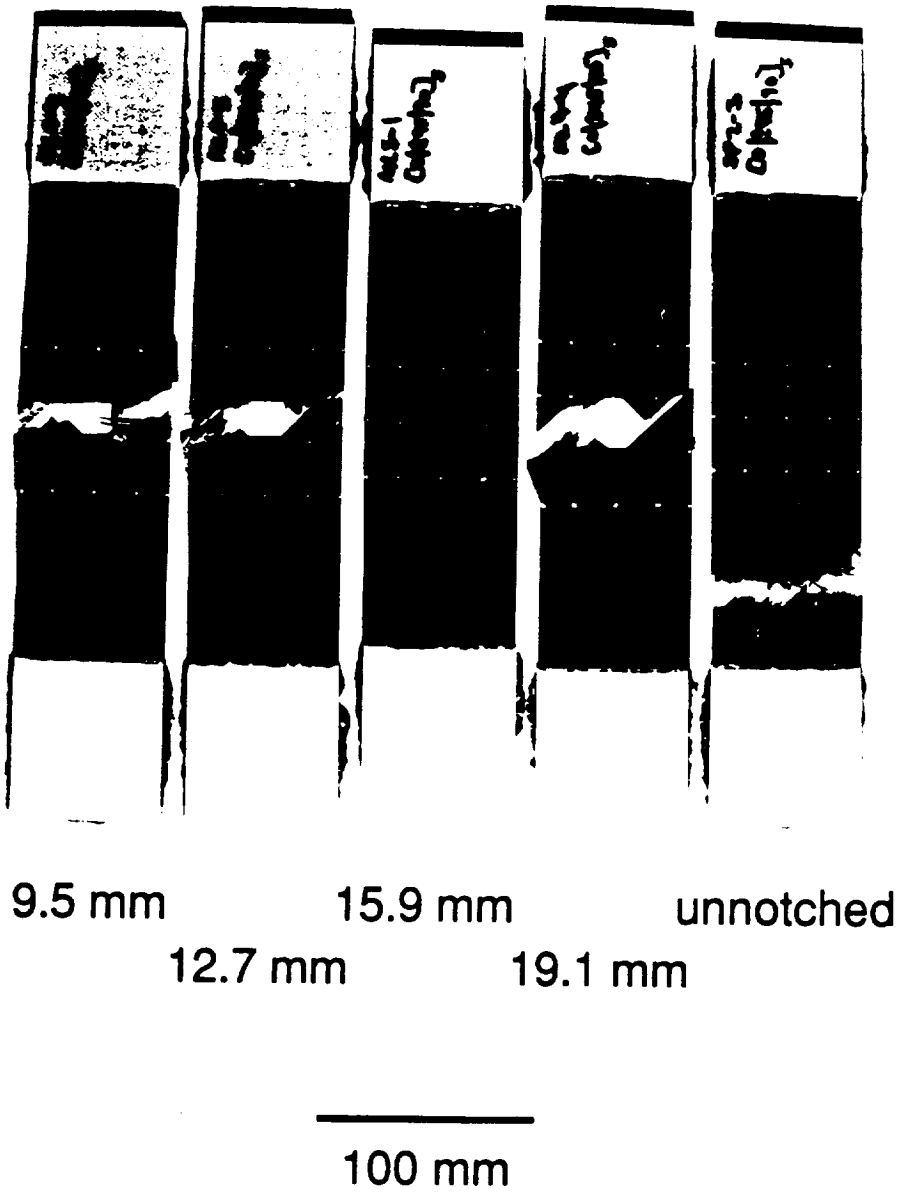

Figure 6.4 Post-test photograph of representative $[0/\pm45/90]_s$ coupons.

A photograph of representative notched $[0/\pm45/90]_s$ coupons after failure is shown in Figure 6.4. In all cases, fracture initiated at the slit tips and progressed all the way to the sides of the specimen. The 0° and +45° plies fractured cleanly along a path that initially extends away from the slit tips along the direction of the +45° fibers. After reaching points that are approximately 5 mm along the length of the specimen from the slit, the paths turn abruptly to the direction of the -45° plies and proceed back toward the center of the specimen. When the paths are approximately in line with the slit, they again change direction abruptly and curve gently out to the edges of the specimen at an angle close to -90°. This fracture path results in a triangular shaped region approximately 5 mm high and 10 mm wide in the 0° and +45° plies on both sides of the specimen at both slit tips. There is, however, some variation in the sizes of these triangular regions. A sharp, straight primary fracture through the -45° and 90° plies extends from both slit tips in the direction parallel to the -45° fibers. In many cases, this fracture extends all the way to the specimen edge. Secondary delamination between the ±45° plies is present in the region between the fracture through the -45° and 90° plies, the fracture surface of the 0° and +45° plies, and the edge of the specimen. Consequently, in some specimens, the two ends of the coupon can be pulled apart easily to reveal large triangular shaped regions of the -45° and 90° plies which jut out between the slit tips and the edges of the specimen. Extensive secondary splitting of the -45° and 90° plies near the fracture surface of the 0° and +45° plies caused the triangles to break off in some specimens.

Results for the biaxially loaded $[0/\pm45/90]_s$ cylinders are presented starting with representative strains from the tests of these cylinders. The far-field (axial and circumferential) and circumferential patch gage strain

data from the test of the cylinder with the 25.4 mm slit are shown in Figure 6.5. Each pressure versus strain curve is essentially linear. In addition, the close agreement between the circumferential far-field and patch gage strains indicates that far-field conditions were achieved between the slit and the patch. As discussed in Chapter 4, this condition verifies that the patch did not interfere with the loading condition near the slit. The slopes of the pressure versus strain data for the far-field gages in the cylinder with the 12.7 mm slit (not shown) are essentially the same as those for the cylinder with the 25.4 mm slit and these curves are also highly linear and smooth.

The quality of the $[0/\pm45/90]_s$ cylinders was checked by using LIN6 to determine the initial slope of the pressure, p, versus hoop strain, ε_{11}, data and comparing this slope to a predicted value. The predicted values were calculated using the following equation:

$$\frac{p}{\varepsilon_{11}} = \frac{E_{11}t}{r(1-\nu_{12}/2)} \tag{6.1}$$

where E_{11} and ν_{12} are the in-plane hoop modulus and major Poisson's ratio of the laminate from Classical Laminated Plate Theory, t is the cylinder thickness, and r is the cylinder radius. This equation is a modified form of the constitutive equation for ε_{11} where the hoop stress, σ_{11}, has been replaced by equation (5.1) and the axial stress, half of the hoop stress, is replaced by equation (5.1) divided by two. Equation (5.1) relates the effective far-field membrane hoop stress in a cylinder to the applied internal pressure. The predicted value of p/ε_{11} for the $[0/\pm45/90]_s$ layup is 460 MPa. The experimental value for the cylinder with the 12.7 mm slit is 467 MPa and the value for the cylinder with the 25.4 mm slit is 457 MPa. Both

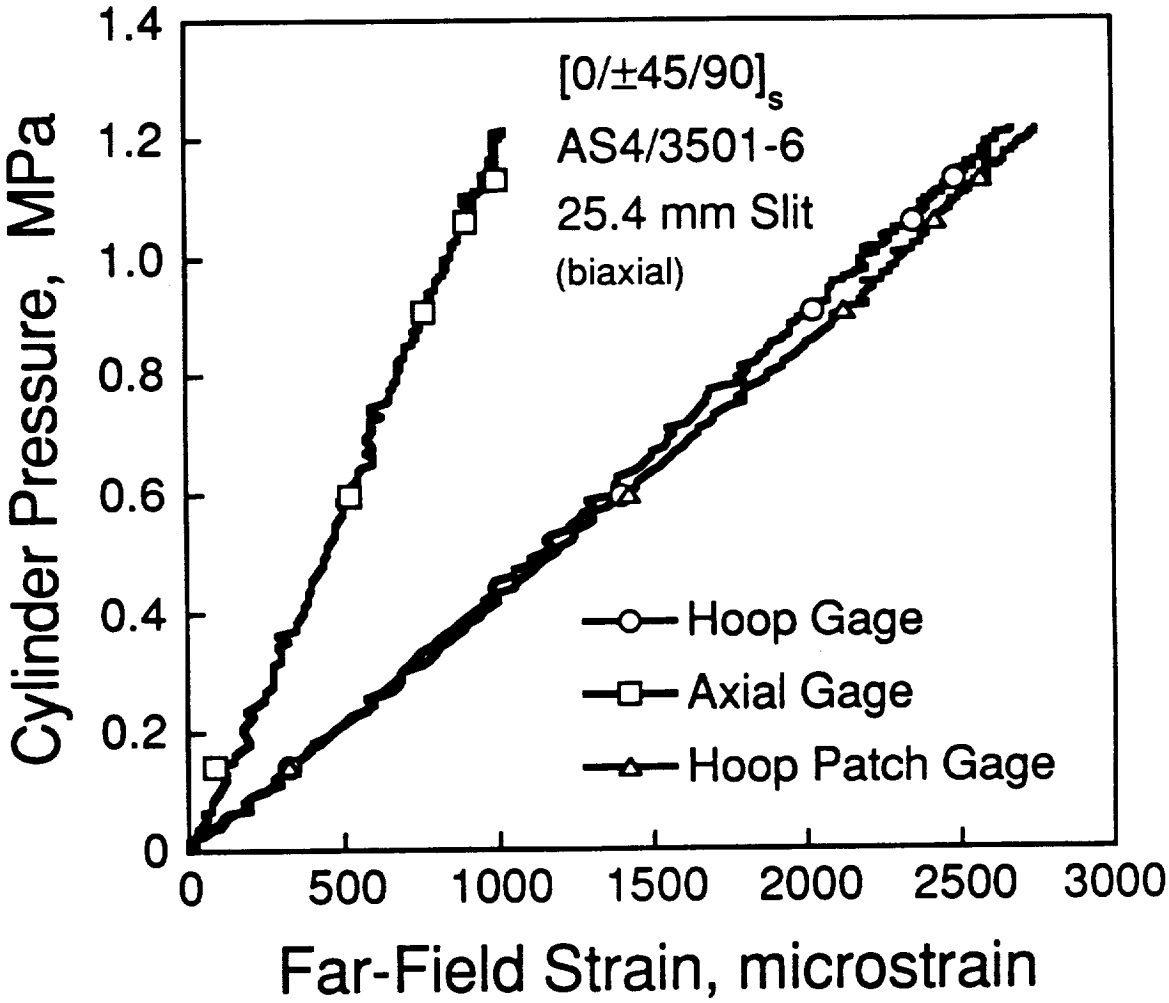

Figure 6.5 Cylinder pressure versus far-field and circumferential patch gage strains from failure test of biaxially loaded $[0/\pm45/90]_s$ cylinder with 25.4 mm slit.

experimental values agree well with the predicted value indicating the quality of the specimens.

Strain data from the slit tip hoop gages on the biaxially loaded $[0/\pm45/90]_s$ cylinders are shown in Figures 6.6 and 6.7. As mentioned previously, Slit Tip Gage 1 is the gage on the end of the slit closest to End 1 of the cylinder, as defined in Chapter 4. Slit Tip Gage 2 is located at the other end of the slit. The pressure-strain curves for the slit tip gages on the cylinder with the 12.7 mm slit are generally linear and smooth, except for a slight discontinuity in the readings from Slit Tip Gage 2. These gages remained active throughout the test. In contrast, the pressure-strain curves for the slit tip gages on the cylinder with the 25.4 mm slit show several discontinuities in the strain readings, with the curves being essentially linear between these discontinuities. Both gages failed at approximately 85% of the failure pressure. Pressures and strains corresponding to the first discontinuity observed in the readings from each gage are shown in Table 6.2. As can be seen in this table, pressures and strains at the first discontinuity are lower for the gages on the cylinder with the 25.4 mm slit and are higher for Slit Tip Gage 1. As mentioned in Chapter 4, the presence of discontinuities in the slit tip pressure-strain curves is significant since this indicates that cylinder (and/or gage) damage occurs at the slit tips prior to the ultimate cylinder failure.

Failure pressures for the biaxially loaded $[0/\pm45/90]_s$ cylinders with the 12.7 and 25.4 mm slits are shown in Table 6.3 and are plotted versus slit length in Figure 6.8. Also shown in this figure are the coupon correlation curve from Figure 6.3, expressed in terms of equivalent pressures, and the cylinder failure pressure prediction curve obtained by mitigating the coupon correlation curve using the Folias curvature correction factor. Both

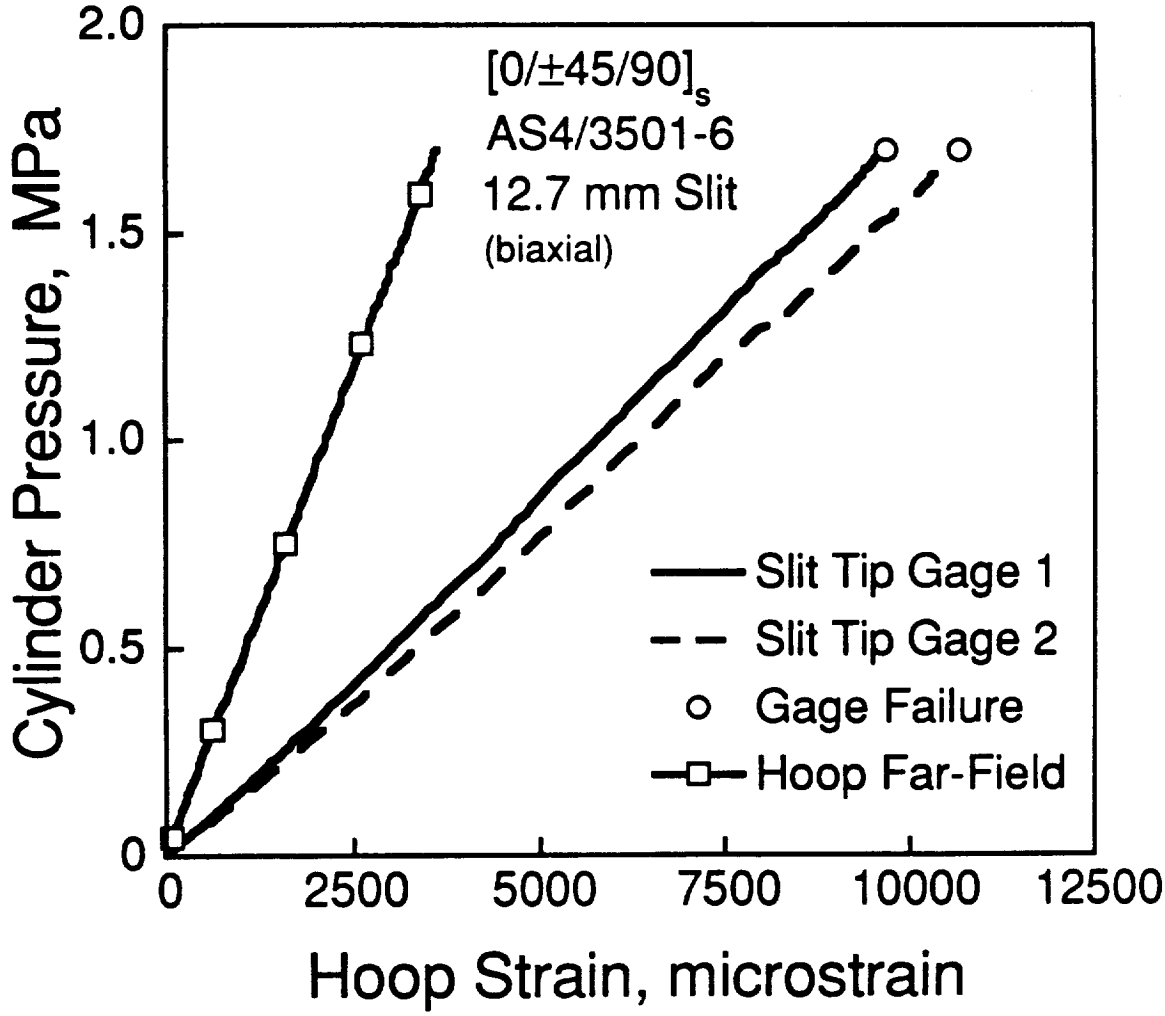

Figure 6.6 Cylinder pressure versus slit tip gage and far-field circumferential strains from failure test of biaxially loaded $[0/\pm45/90]_s$ cylinder with 12.7 mm slit.

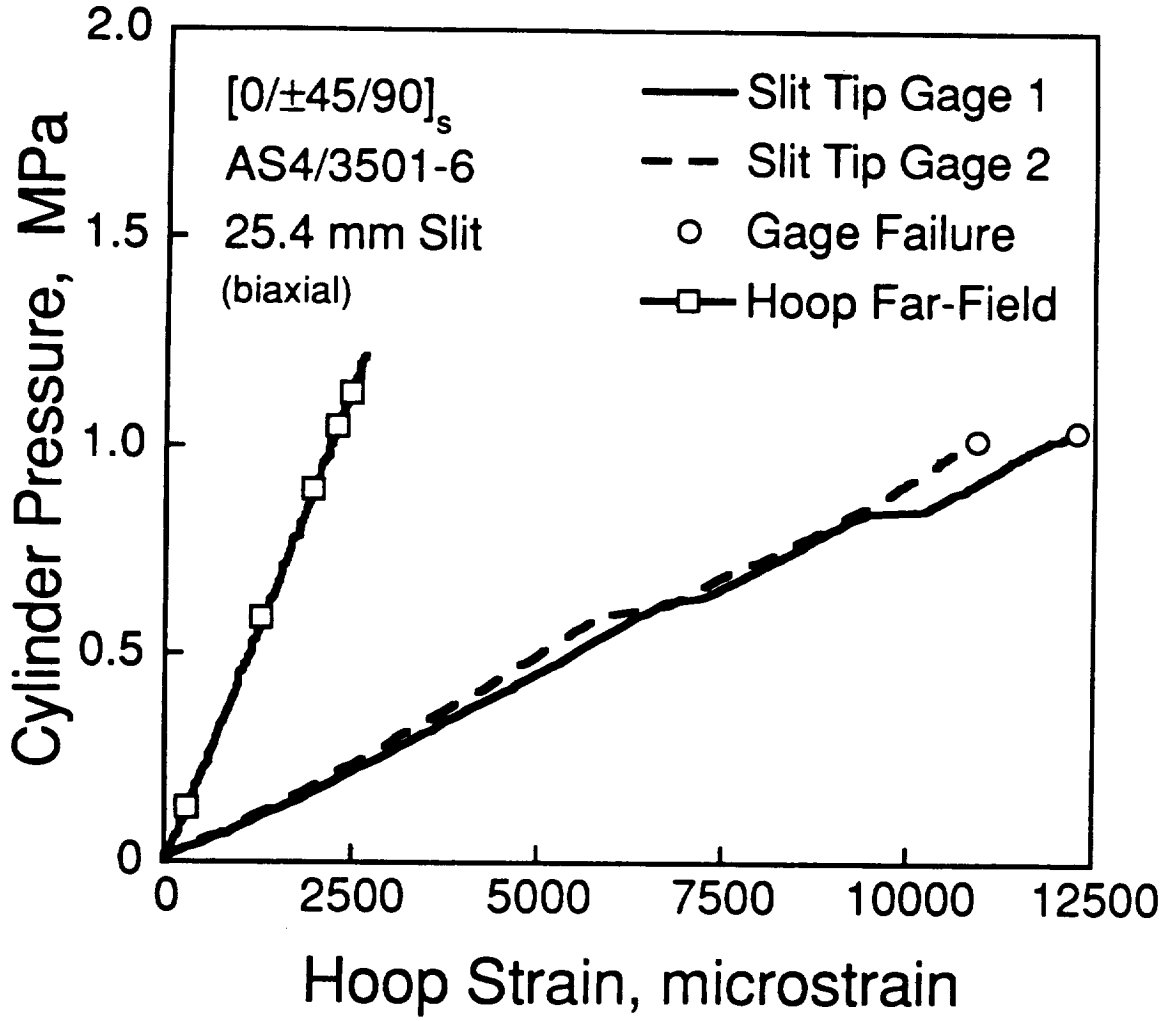

Figure 6.7 Cylinder pressure versus slit tip gage and far-field circumferential strains from failure test of biaxially loaded $[0/\pm45/90]_s$ cylinder with 25.4 mm slit.

Table 6.2 Hoop Strain and Cylinder Pressure at First Discontinuity Observed in Slit Tip Strain Gage Data for Biaxially Loaded $[0/\pm45/90]_s$ Cylinders

Slit Length [mm]	Gage	Pressure [MPa]	Slit Tip Hoop Strain [microstrain]
12.7	1	1.70	9688
	2	1.26	7950
25.4	1	0.63	6750
	2	0.60	5950

Table 6.3 Failure Pressures of Biaxially Loaded $[0/\pm45/90]_s$ Cylinders

Slit Length, mm	Failure Pressure, MPa
12.7	1.70
25.4	1.21

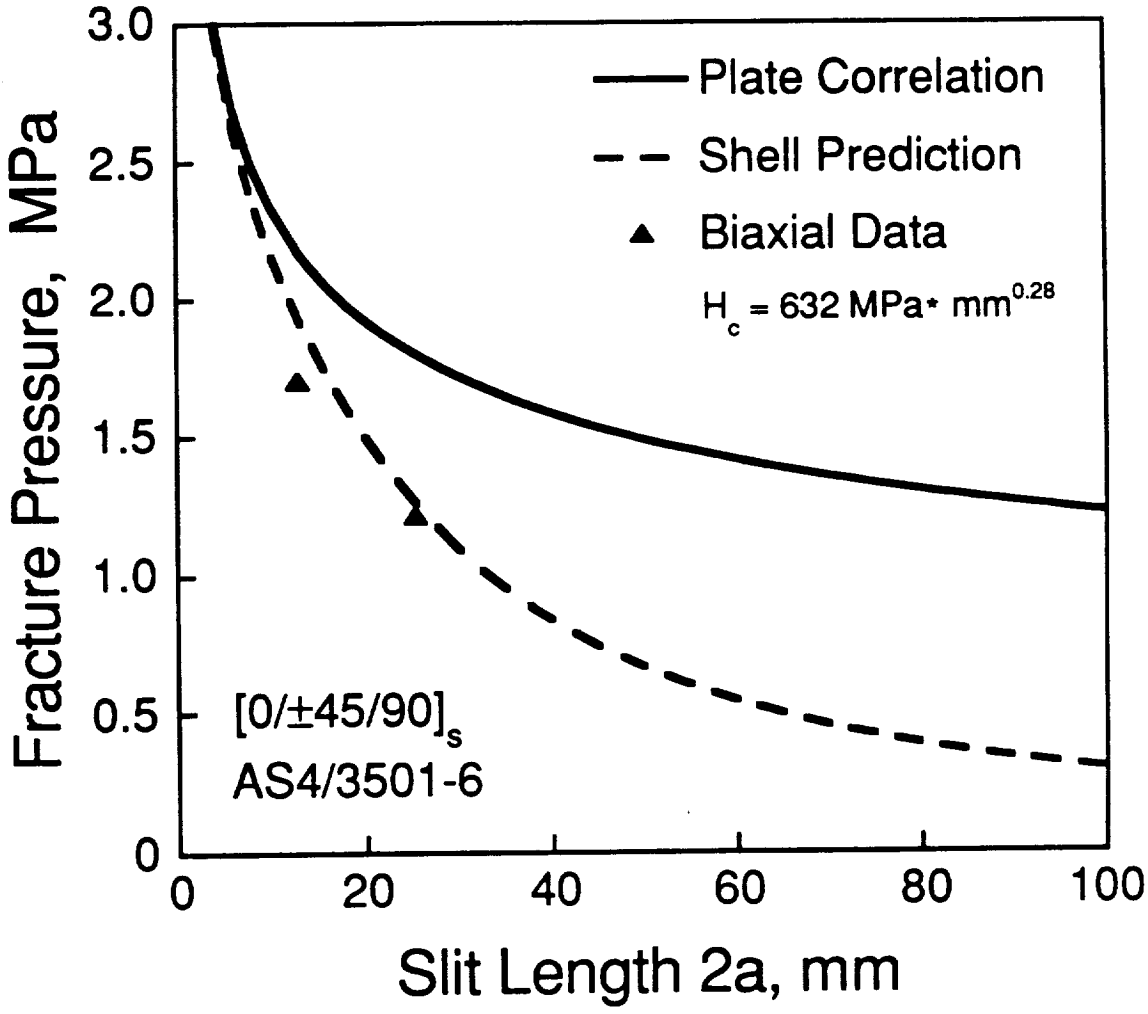

Figure 6.8 Experimental and predicted failure pressures for biaxially loaded $[0/\pm45/90]_s$ tape cylinders.

cylinders failed at pressures slightly below the predicted values. However, the experimental pressures correlate fairly well with these predictions.

Photographs after failure are shown for the $[0/\pm45/90]_s$ cylinders with the 12.7 and 25.4 mm slits in Figures 6.9 and 6.11, respectively. Damage schematics for these cylinders are provided in Figures 6.10 and 6.12 for more clarity. Since the cylinder with the 25.4 mm slit was patched, the slit in this cylinder is located along the line between paint grid squares 'O8' and 'P8' instead of in the normal location between squares 'S8' and 'A8', as can be seen in Figure 6.11.

The damage states observed directly at the slit tips in the $[0/\pm45/90]_s$ cylinders with the 12.7 and 25.4 mm slits show strong similarities to each other as well as to those which were described previously for notched coupons with the same layup. In the cylinder with the 25.4 mm slit, several small triangular-shaped fractures in the 0° and +45° plies, like those described for the notched coupons, are distinctly visible at both slit tips. However, the first triangle at each slit tip is smaller than the average triangle size for the coupons (1 mm high and 3 mm wide in the cylinder compared to 5 mm high and 10 mm wide in the coupons). The fracture paths near the slit tips in this cylinder are also more ragged than those in the coupons. In the cylinder with the 12.7 mm slit, the small triangular fractures in the 0° and +45° plies at both slit tips are larger and more well defined even though these regions are still smaller than the average size observed for the notched coupons. The triangular region on the left end of the slit in this cylinder is approximately 6 mm wide and 2 mm high and the one on the right end is 4 mm wide and 2 mm high. The failure paths extending away from the triangular fractures are also less ragged than those observed in the cylinder with the 25.4 mm slit which makes them

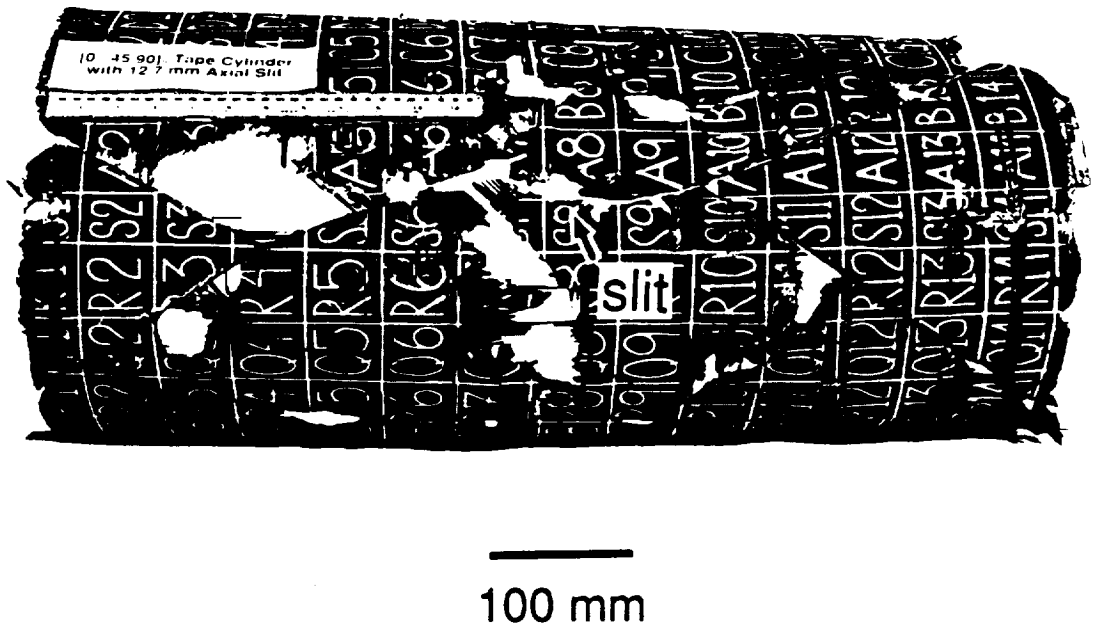

Figure 6.9 Post-test photograph of biaxially loaded $[0/\pm45/90]_s$ cylinder with 12.7 mm slit.

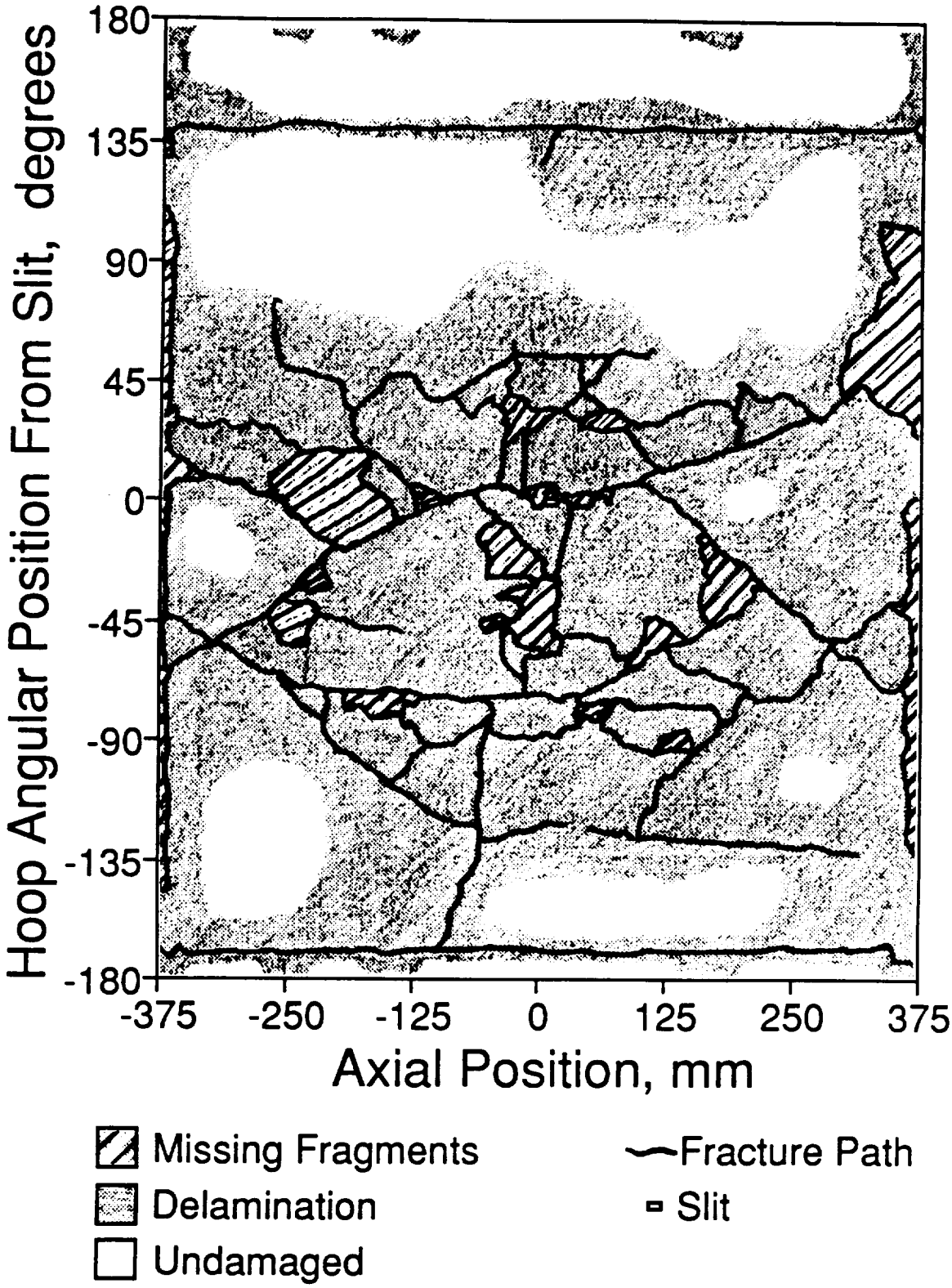

Figure 6.10 Schematic of damage in biaxially loaded $[0/\pm45/90]_s$ cylinder with 12.7 mm slit.

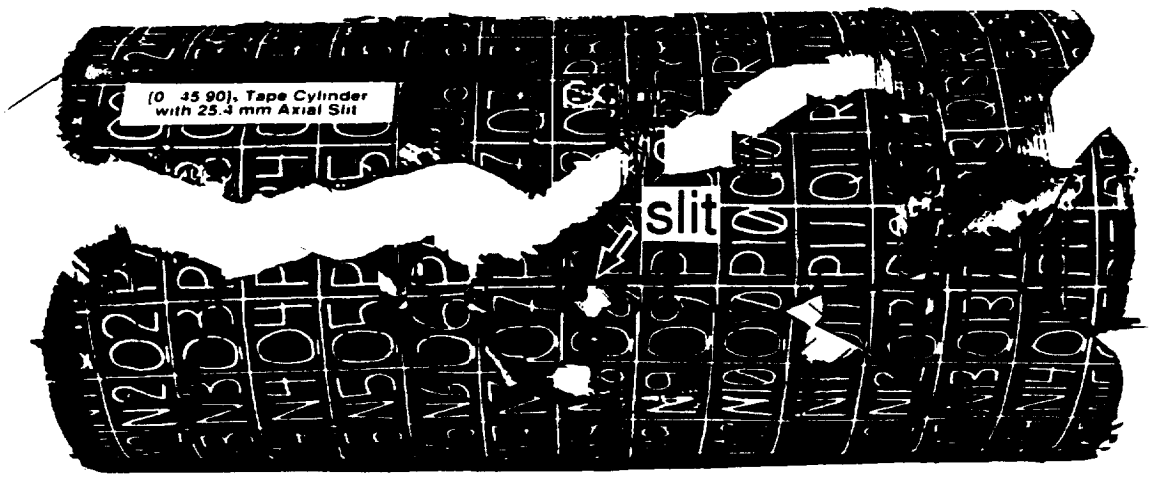

Figure 6.11 Post-test photograph of biaxially loaded $[0/\pm45/90]_s$ cylinder with 25.4 mm slit.

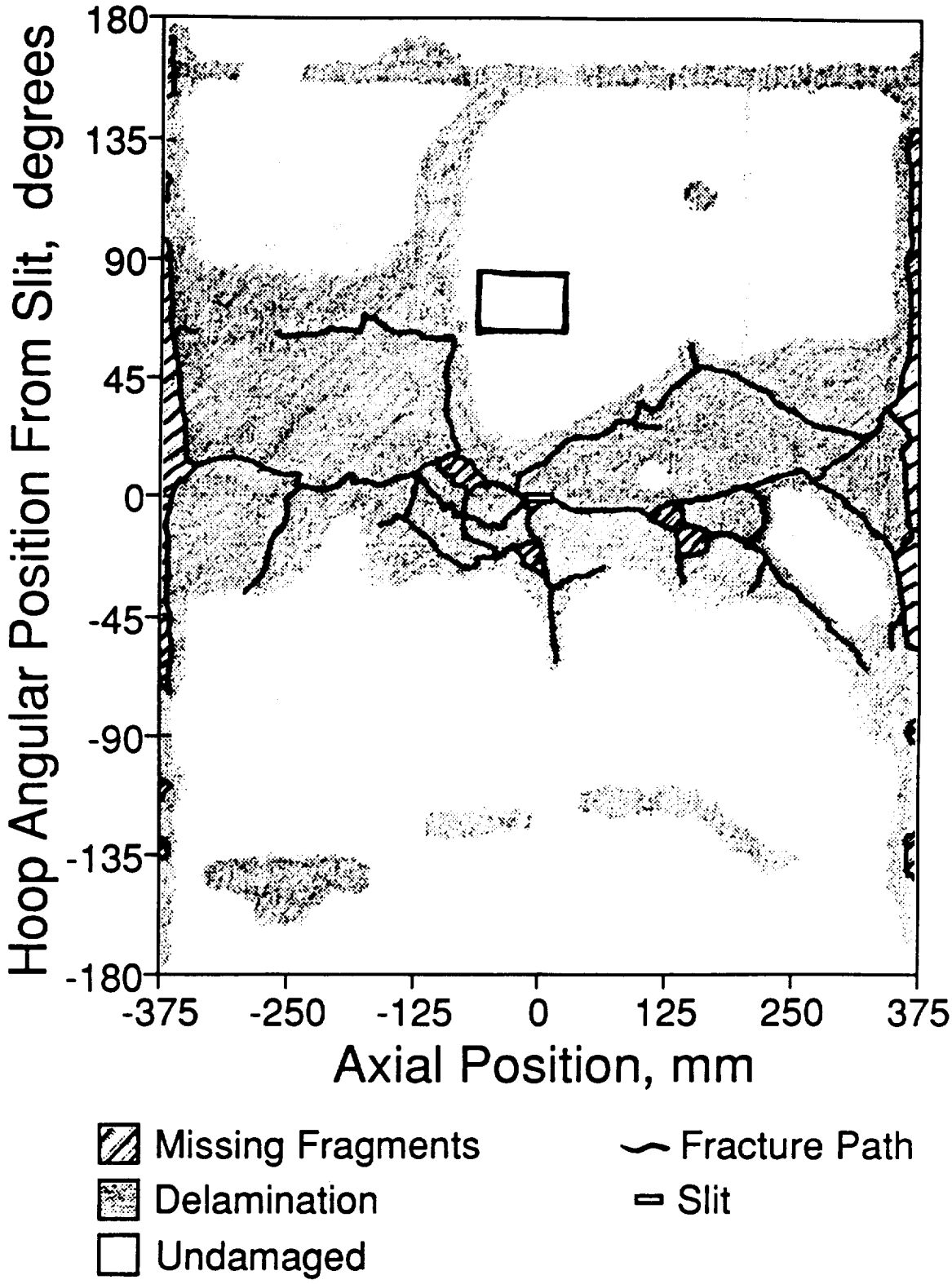

Figure 6.12 Schematic of damage in biaxially loaded $[0/\pm45/90]_s$ cylinder with 25.4 mm slit.

more similar to the coupon failure paths. In both cylinders, the primary failure paths extend away from the triangular fractures along an angle that is initially close to -70°. This compares to the direction observed in the notched coupons. In the cylinder with the 25.4 mm slit, there is some evidence of a crack through the -45° and 90° plies emanating from both slit tips and delamination between the ±45° plies near the crack, as was observed in the coupons. However, many of the back plies near the slit delaminated and their original locations are not identifiable and it is, therefore, difficult to determine how these cracks and the accompanying delamination progressed away from the slit. In the cylinder with the 12.7 mm slit, a straight crack along the fibers of the -45° ply closest to the outside surface of the cylinder extends from the right slit tip. It is unknown if this crack also extended through the 90° plies and the other -45° ply, as it did in the coupons, since most of the back plies were not recovered due to extensive delamination between the ±45° plies in the region below the slit. In both cylinders, very little damage was observed on the outside surface directly above or below the slit, depending on which slit fragment was recovered, except for some splitting and delamination of the 0° ply.

The damage observed outside the immediate region of the slit is also similar in both biaxially loaded $[0/\pm45/90]_s$ cylinders. The primary fracture paths initially leave the slit region along the -70° direction and the magnitude of this angle generally becomes smaller with increasing distance from the slit. The main paths in both cylinders eventually change direction abruptly and run toward the ends of the cylinder along the positive angular direction (with respect to the laminate axes). These paths bifurcate, in some cases several times, as they approach the ends of the cylinders. Secondary damage in the form of fracture paths, multiple-ply

delamination, and missing fragments are also present in both cylinders. However, this secondary damage is much more abundant in the cylinder with the 12.7 mm slit. In both cylinders, delamination is more severe near the fracture paths and the fracture surfaces are generally very clean. In the cylinder with the 12.7 mm slit, two sharp, longitudinal fracture paths visible near the top and bottom of Figure 6.10 were caused when the back of the cylinder hit the I-beam that was used to support the endcaps during the test. In the cylinder with the 25.4 mm slit, only a longitudinal strip of delamination is present in the back of the cylinder since this cylinder failed at a lower pressure and, thus, did not hit the I-beam with as much force. Primary and secondary fracture paths which reached the endcaps turned and ran around the circumference. Thus, the endcaps were completely separated from both cylinders.

6.2 [90/0/±45]s Coupons and Cylinders

A representative plot of the longitudinal stress versus far-field longitudinal strain data for a notched $[90/0/\pm45]_s$ coupon is provided in Figure 6.13 (unnotched coupons of this layup were not tested). The far-field stress-strain curves are generally smooth. Furthermore, these curves are linear through approximately 90% of the test. The average initial slope of the stress-strain curves, E_{11}, for the notched specimens is 55.8 GPa with a coefficient of variation of 5.1%. This compares well with the value of 55.5 GPa calculated via Classical Laminated Plate Theory (CLPT) using the ply properties listed in Table 3.1.

The average failure stresses and value of H_c calculated from these stresses using the Mar-Lin equation (equation 3.1) for the coupons are shown in Table 6.4. The average value of H_c for all the notched $[90/0/\pm45]_s$

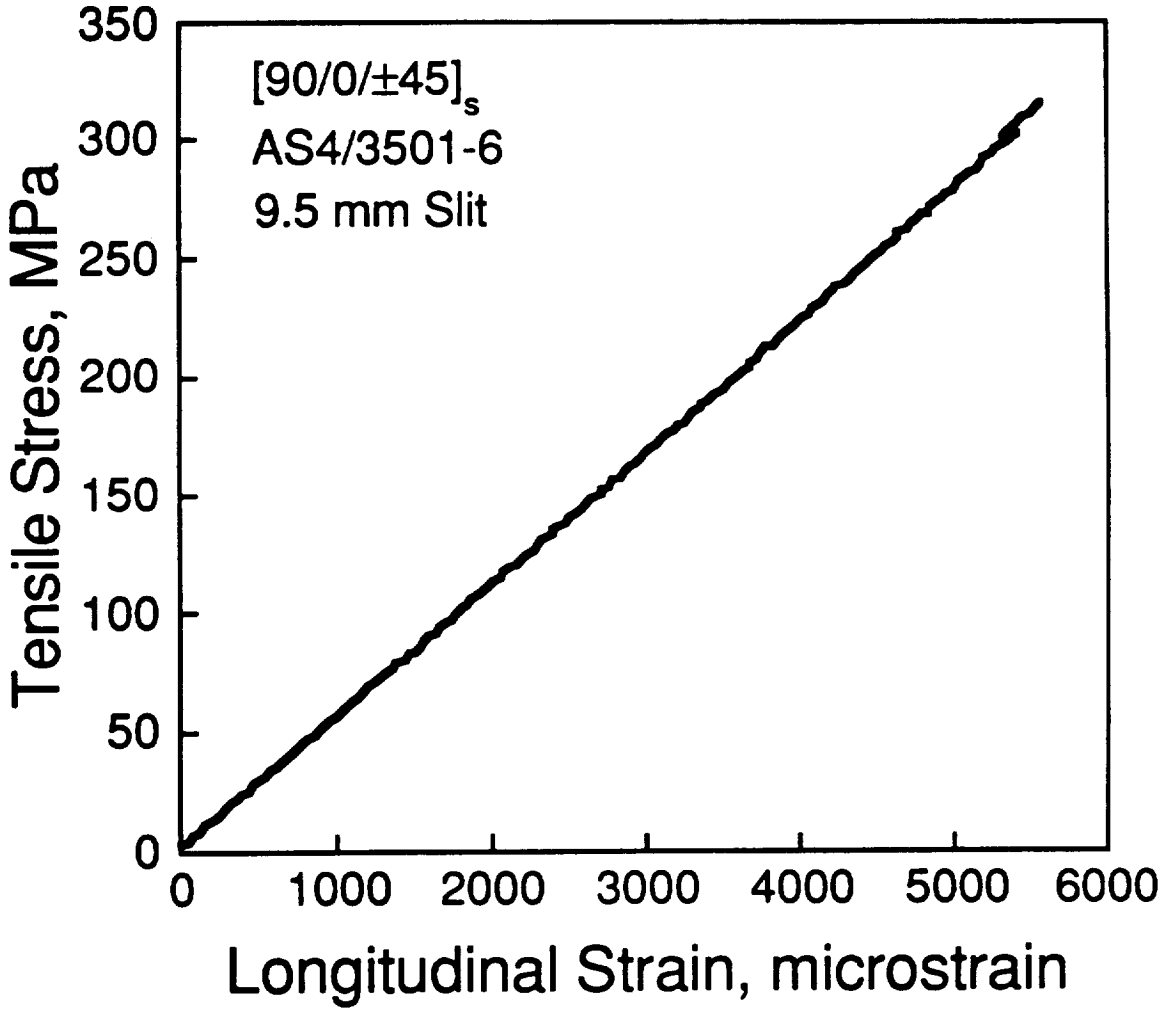

Figure 6.13 Tensile stress versus longitudinal strain for typical notched $[90/0/\pm45]_s$ coupon.

Table 6.4 Failure Data for $[90/0/\pm45]_s$ Coupons

Slit Length [mm]	Average Failure Stress [MPa]	Average H_c [MPa*mm$^{0.28}$]
9.5	314 (1.3%)[a]	593 (1.3%)
12.7	299 (1.1%)	609 (1.2%)
15.9	271 (3.3%)	592 (3.3%)
19.1	262 (6.9%)	601 (6.8%)

[a] Numbers in parentheses are coefficients of variation.

coupons is 599 MPa*mm$^{0.28}$ with a coefficient of variation of 3.2%. This H_c value is 9.8% lower than the value of 664 MPa*mm$^{0.28}$ obtained in past work [31] for the $[90/0/\pm45]_s$ layup. The coupon correlation curve for this layup generated using the average calculated H_c value from the current work is shown in Figure 6.14. Individual data points used to establish this curve are also shown in this figure for comparison purposes.

A representative photograph of the notched $[90/0/\pm45]_s$ coupons after failure is shown in Figure 6.15. In all cases, the fracture paths originate at the slit tips and extend all the way to the sides of the specimen. The damage surrounding these fracture paths and the shapes of the paths are similar in many respects to those described previously for the $[0/\pm45/90]_s$ coupons. A clean fracture path in the 90°, 0°, and +45° plies extends from each slit tip along an angle between +45° and +80°. However, the most common path direction is parallel to the +45° fibers. After running in this direction for an average of 9 mm, the paths change direction abruptly and curve gently out to the sides of the specimen along an angle between -70° and -90°. In the case of the $[0/\pm45/90]_s$ coupons, the fracture paths proceed back toward the center of the specimen along the -45° direction before they curve to the edges of the specimen in the same manner, as described previously. There is evidence of a primary split through the -45° plies that extends away from each slit tip in the direction parallel to the -45° fibers. Secondary delamination of the ±45° plies is present in the region between the split, the fracture surface of the 90°, 0°, and +45° plies, and the edge of the specimen. This damage pattern is similar to the clean fracture through the -45° and 90° plies and the delamination between the ±45° plies observed in the $[0/\pm45/90]_s$ coupons. Extensive splitting of the -45° plies is visible in the delaminated region and many of the -45° fibers broke raggedly.

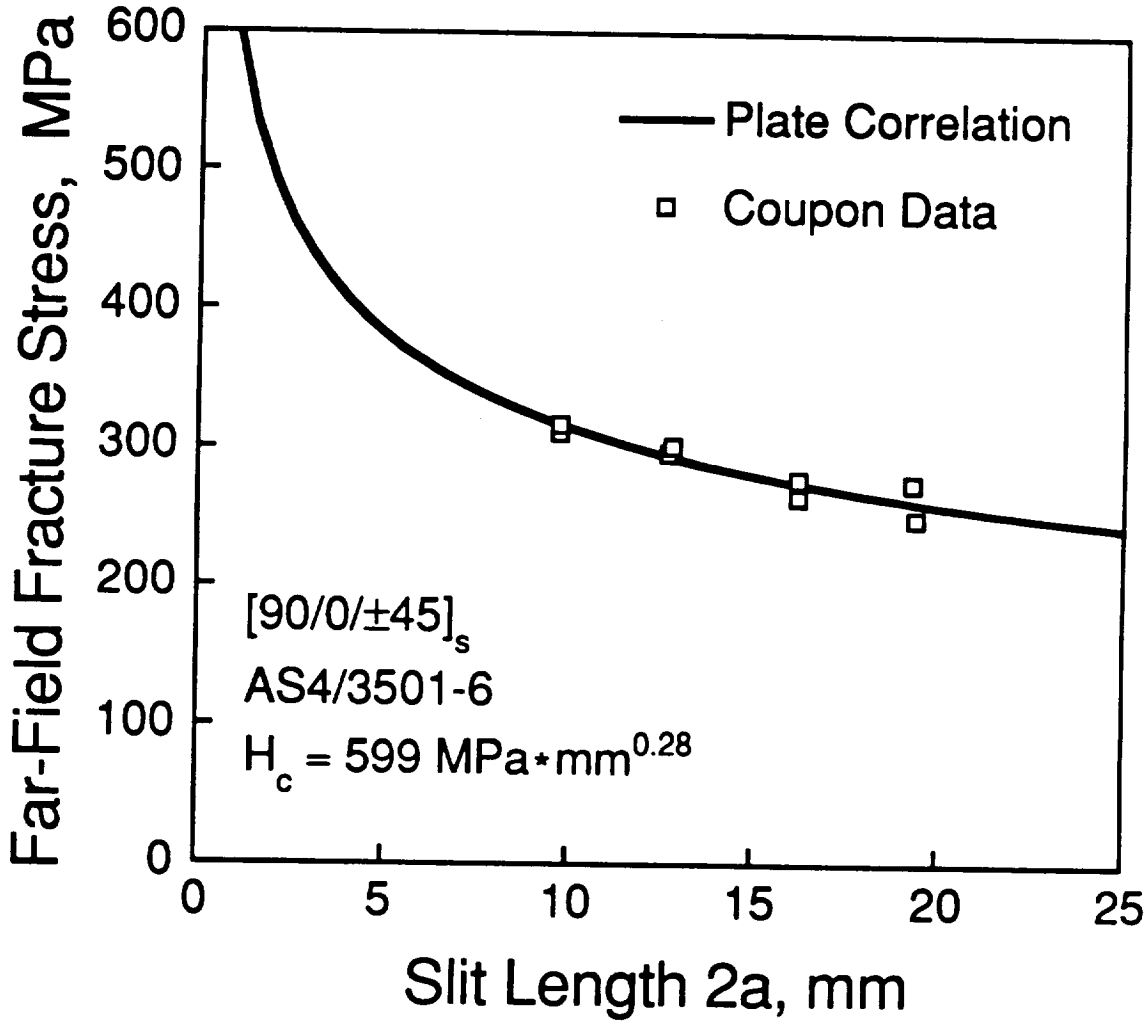

Figure 6.14 Individual failure stresses and failure stress correlation curve for notched $[90/0/\pm45]_s$ coupons.

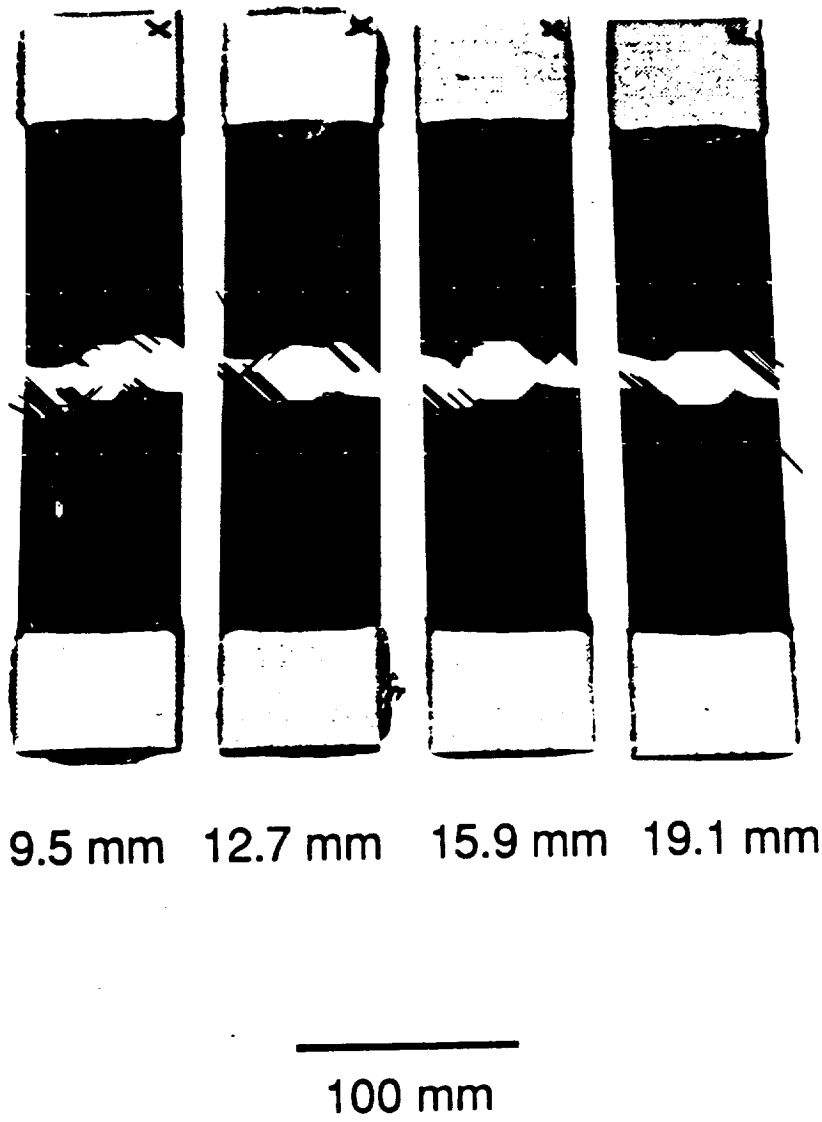

Figure 6.15 Post-test photograph of representative $[90/0/\pm45]_s$ coupons.

In some specimens, secondary delamination between the ±45° plies is also visible directly above and below the slit and on the opposite sides of the main fracture paths from the delaminations described above.

Results for the uniaxially and biaxially loaded $[90/0/\pm45]_s$ cylinders are presented separately starting with the latter cylinders. The far-field and circumferential patch gage strain data for the biaxially loaded cylinder with the 12.7 mm slit that failed at the lower pressure are shown in Figure 6.16. This cylinder is also referred to as the 'second tested cylinder'. The pressure versus strain curves for the gages on both biaxially loaded cylinders with the 12.7 mm slits are essentially linear. The far-field hoop strains for the second tested cylinder are, on the average, 8.9% higher than the patch gage hoop strains. The fair agreement between these strains suggests that far-field conditions were achieved between the slit and the patch and, thus, the patch did not interfere with the loading condition near the slit. The far-field hoop strains for the first tested cylinder and the patch gage strains for the second tested cylinder are virtually identical. However, the axial strains for the first tested cylinder are somewhat higher than those presented in Figure 6.16 for the second tested cylinder.

The quality of each biaxially loaded $[90/0/\pm45]_s$ cylinder was checked by comparing the initial slope of the pressure versus far-field hoop strain data to the predicted value calculated using equation (6.1). The predicted value of p/ε_{11} for the $[90/0/\pm45]_s$ layup is 460 MPa. Both experimental values agree well with the predicted value as the experimental value for the first tested cylinder (with the higher failure pressure) is 488 MPa and the value for the second tested cylinder is 446 MPa.

The slit tip strain data for the biaxially loaded $[90/0/\pm45]_s$ cylinders are shown in Figures 6.17 and 6.18. The pressure-strain curves for the slit

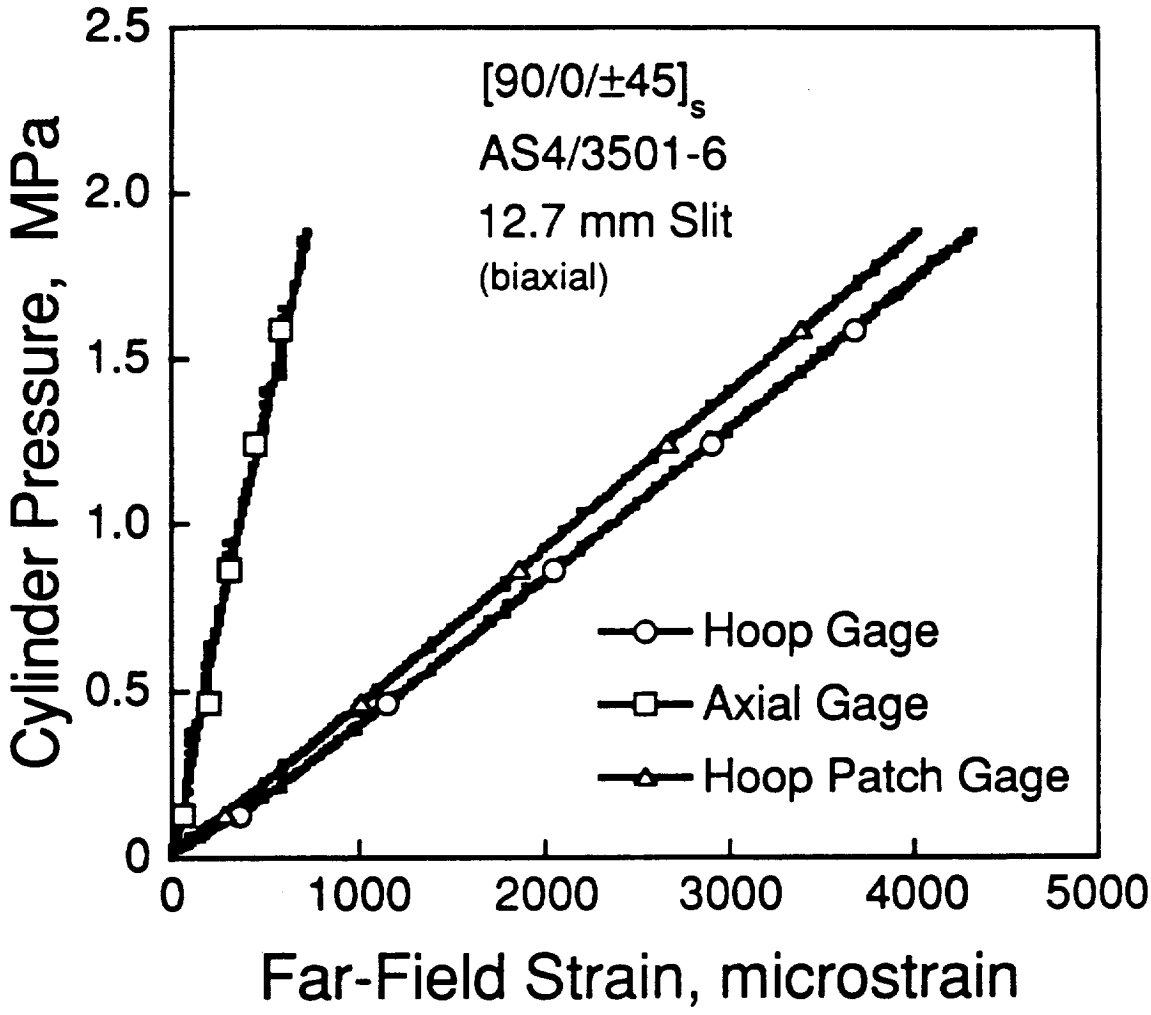

Figure 6.16 Cylinder pressure versus far-field and circumferential patch gage strains from failure test of second biaxially loaded $[90/0/\pm45]_s$ cylinder with 12.7 mm slit.

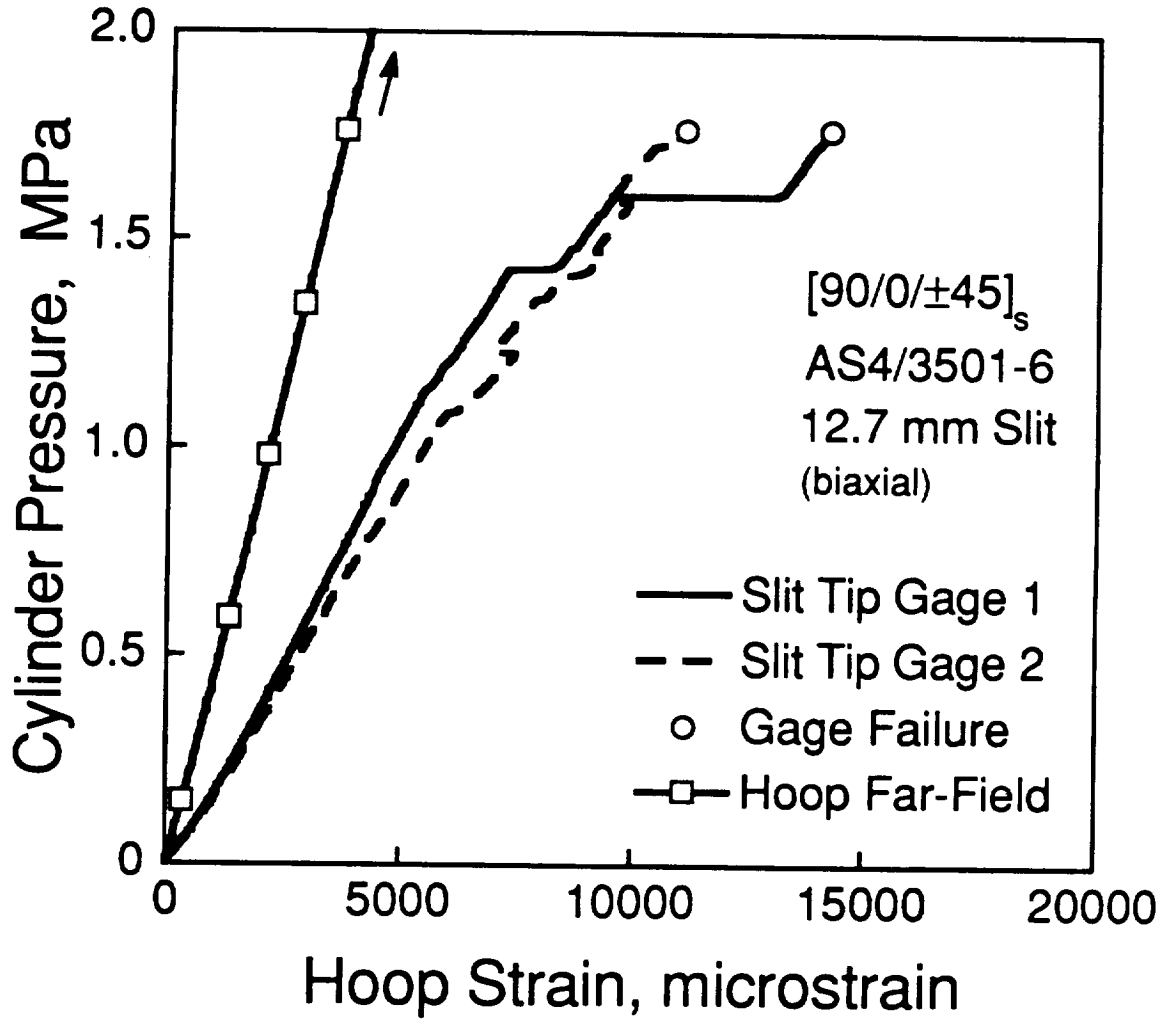

Figure 6.17 Cylinder pressure versus slit tip gage and far-field circumferential strains from failure test of first biaxially loaded $[90/0/\pm45]_s$ cylinder with 12.7 mm slit.

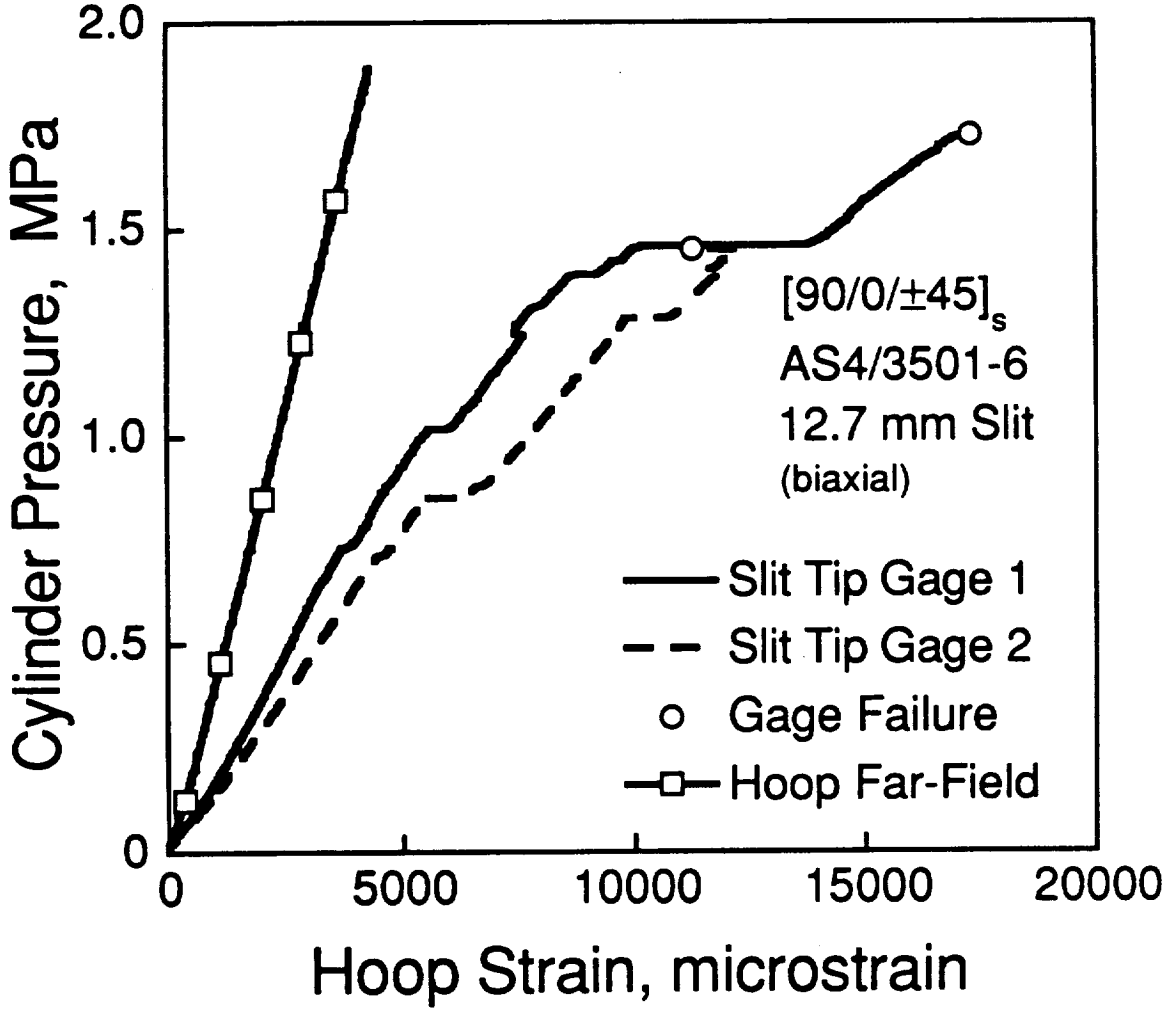

Figure 6.18 Cylinder pressure versus slit tip gage and far-field circumferential strains from failure test of second biaxially loaded $[90/0/\pm45]_s$ cylinder with 12.7 mm slit.

tip gages on these cylinders show several discontinuities in the strain readings with the curves being essentially linear between these discontinuities. The pressure and strain levels at which the first discontinuity is observed are indicated in Table 6.5 for each gage. As can be seen in this table, the pressure at which the first discontinuity is observed is essentially the same for both slit tip gages on each cylinder. However, the pressures for the second tested cylinder (which failed at a lower pressure) are approximately 35% lower than those for the first tested cylinder. Hoop strains corresponding to the first discontinuity are somewhat lower and pressures are slightly higher for Slit Tip Gage 1. The hoop strain values for the second tested cylinder are approximately 28% lower than those for the other cylinder. An abrupt jump of approximately 4000 μstrain was observed for Slit Tip Gage 1 on both cylinders shortly before the slit tip gages failed. The slit tip gages on the first tested cylinder both failed at 87% of the failure pressure. Slit Tip Gage 1 on the second tested cylinder failed at 92% and Slit Tip Gage 2 failed at 77% of the cylinder failure pressure.

The failure pressures of the biaxially loaded $[90/0/\pm45]_s$ cylinders are listed in Table 6.6. A full discussion of these pressures is delayed until the end of this section where the experimental values for the uniaxially and biaxially loaded $[90/0/\pm45]_s$ cylinders are compared to each other as well as to the predicted values.

A post-test photograph and damage schematic are shown in Figures 6.19 and 6.20 for the first biaxially loaded $[90/0/\pm45]_s$ cylinder and in Figures 6.21 and 6.22 for the second tested cylinder. The first slit cut into the latter cylinder was patched, as described in Chapter 4, and the new slit was located on the line between paint grid squares 'E8' and 'F8', as can be seen in Figure 6.21.

Table 6.5 Hoop Strain and Cylinder Pressure at First Discontinuity Observed in Slit Tip Strain Gage Data for Biaxially Loaded $[90/0/\pm45]_s$ Cylinders

Slit Length [mm]	Gage	Pressure [MPa]	Slit Tip Hoop Strain [microstrain]
12.7[a]	1	1.14	5500
	2	1.08	5988
12.7	1	0.73	3738
	2	0.71	4500

[a] indicates first tested cylinder

Table 6.6 Failure Pressures of Biaxially Loaded $[90/0/\pm45]_s$ Cylinders

Slit Length, mm	Failure Pressure, MPa
12.7[a]	2.03
12.7	1.89

[a] indicates first tested cylinder

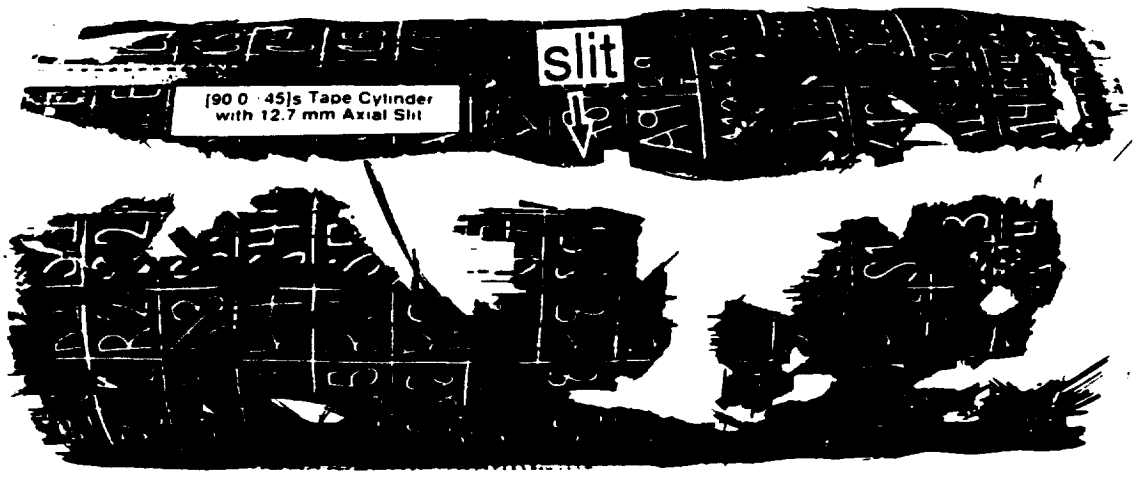

100 mm

Figure 6.19 Post-test photograph of first biaxially loaded $[90/0/\pm45]_s$ cylinder with 12.7 mm slit.

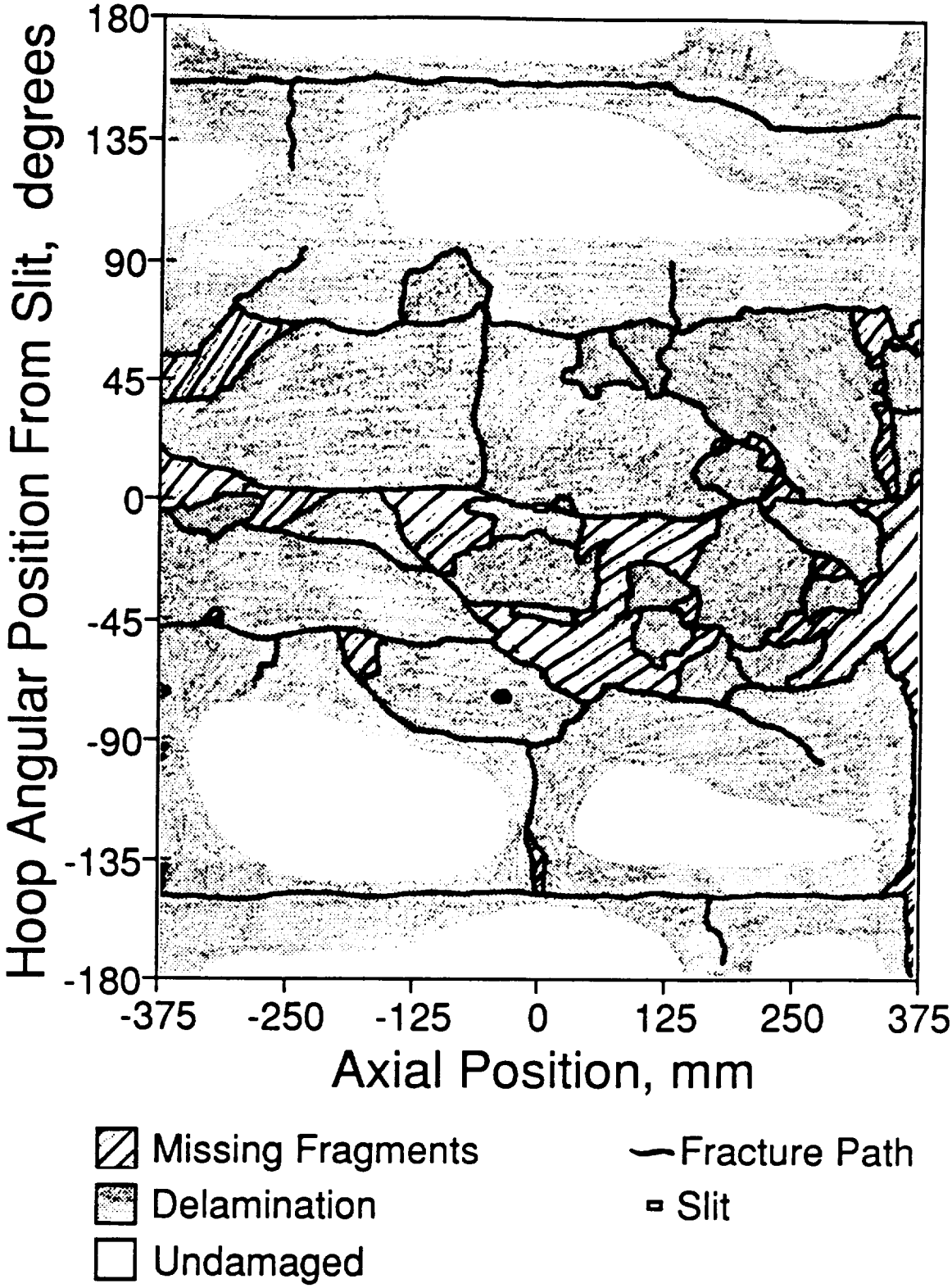

Figure 6.20 Schematic of damage in first biaxially loaded $[90/0/\pm45]_s$ cylinder with 12.7 mm slit.

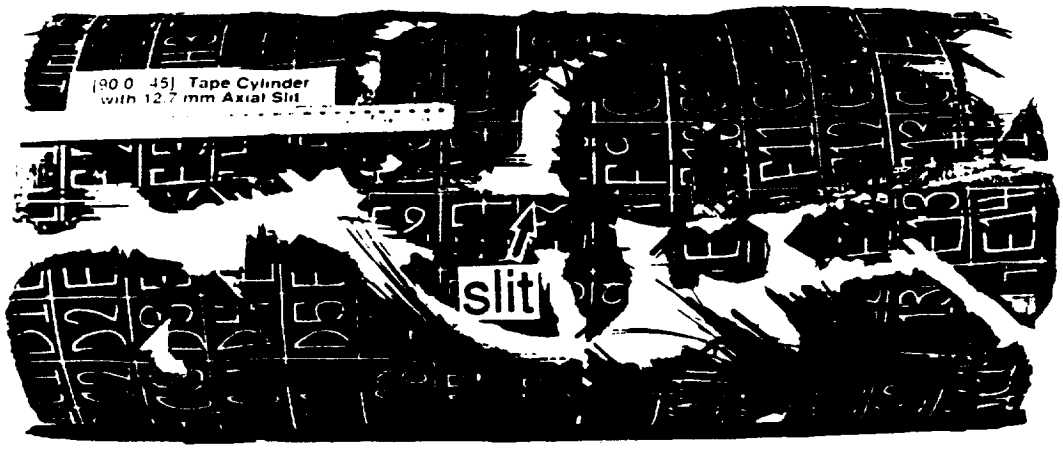

Figure 6.21 Post-test photograph of second biaxially loaded $[90/0/\pm45]_s$ cylinder with 12.7 mm slit.

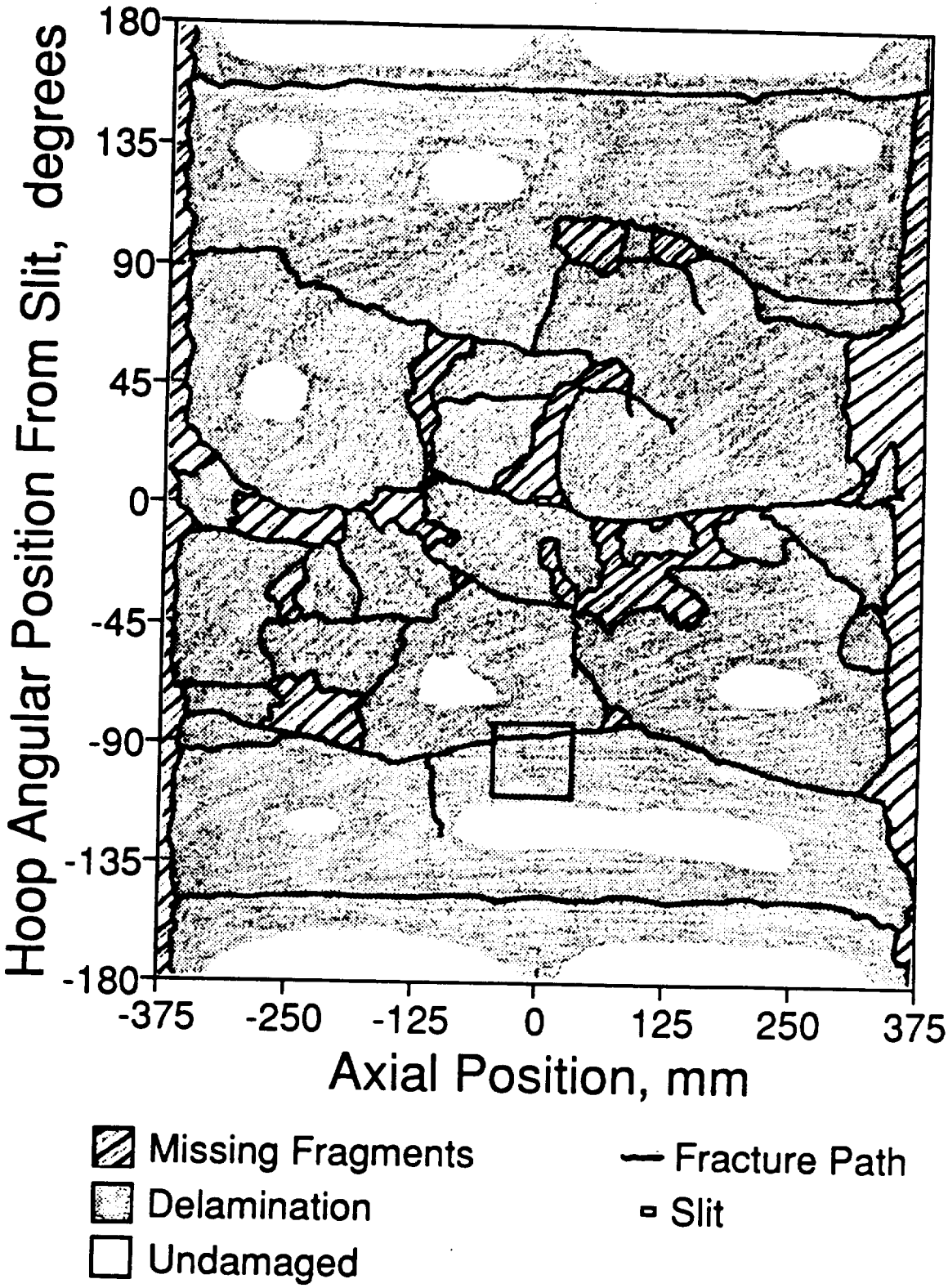

Figure 6.22 Schematic of damage in second biaxially loaded $[90/0/\pm45]_s$ cylinder with 12.7 mm slit.

The initial failure modes near the slits in the biaxially loaded $[90/0/\pm45]_s$ cylinders are similar to each other as well as to those observed in the $[90/0/\pm45]_s$ coupons. As in the coupons, a clean fracture path in the 90°, 0°, and +45° plies extends from each slit tip. However, the initial direction of this path in the cylinders is along an angle between +65° and +80° rather than along the direction of the +45° fibers, as was usually observed in the coupons. The path extending from the left slit tip in the second tested cylinder is somewhat unusual since it runs along the 90° (axial) direction for approximately 10 mm before it turns to the +70° direction. The primary fracture paths progress along the angle between +65° and +80° for approximately 6 mm before they change direction abruptly and curve away from the slit location along an angle between -70° and -90°. The angled path length of 6 mm matches that observed in several of the coupons even though it is slightly shorter than the average length of 9 mm cited for these specimens. The path to the left of the slit in the second tested cylinder is again different from the other cylinder paths and from those observed in the coupons in that it is relatively jagged in the region within 30 mm of the slit tip in the axial direction. Due to a high degree of secondary delamination between the ±45 plies, most of the plies behind the +45° ply closer to the outside surface of the cylinders were not recovered in the regions near the slits. In both cylinders, secondary delamination of the outer 90° ply is visible near the fracture paths and along the sides of the slit. Directly above the slit in the first tested cylinder, only fragments of the 0° and +45° plies closer to the outside surface of the cylinder remain. Secondary splitting of the 0° ply in this cylinder is observed extending away from the top edge of the slit.

The damage near the slits in the biaxially loaded $[90/0/\pm45]_s$ cylinders with the 12.7 mm slits tested in the current investigation is similar in many respects to that observed in the biaxially loaded $[90/0/\pm45]_s$ cylinders tested in the past investigation [31]. However, the cylinder with the 12.7 mm slit tested in the past work is unique in that a primary circumferential fracture path extends directly from Slit Tip 2 in the negative hoop angular direction. This path runs for approximately 70 mm before it splits into several secondary paths. No similar circumferential path was observed in any of the other biaxially loaded cylinders tested in the previous or current investigations.

The damage states in the biaxially loaded $[90/0/\pm45]_s$ cylinders with the 12.7 mm slits are also similar outside the immediate slit region. The previously mentioned main fracture paths which extend away from the slit vicinity along an angle close to -90° stay near the axial slit location line as they progress all the way to the endcaps. The main paths bifurcate into two diverging paths approximately 150 mm from the ends of each cylinder. Many additional failure paths emanate from the main paths and result in large scale secondary damage all over both cylinders in the form of fracture paths and multiple-ply delamination. Secondary delamination of the surface 90° plies on both sides of the cylinder is apparent near most of the fracture paths. Several sections of each cylinder, many of which border on the main fracture paths, could not be identified. The characteristic longitudinal fracture lines near the back of biaxially loaded cylinders with small slit sizes can be seen at the top and bottom of Figures 6.20 and 6.22. As was discussed previously for the $[0/\pm45/90]_s$ cylinders, these fracture lines were caused by cylinder contact with the I-beam that is used to support the endcaps during the test. The second tested cylinder also

contains a fracture path that extends axially along the entire length of the cylinder and passes below the patch near the hoop angular position of -90°, as can be seen in Figure 6.22. Fracture paths which reached the endcaps turned to the circumferential direction and completely separated the endcaps from both cylinders.

Results for the uniaxially loaded $[90/0/\pm45]_s$ cylinders are presented starting with sample plots of the strain data for these cylinders. Strain readings from the original circumferential 'far-field' gage and the extra hoop gage on the cylinder with the 12.7 mm slit are shown in Figure 6.23. Strains from the axial 'far-field' gage on the same cylinder are shown in Figure 6.24. As mentioned previously, Hoop Gage 2 refers to the extra circumferential gage. The strain readings from the pair of axial and hoop gages on the other two cylinders (not shown) show the same general trends. As can be seen in Figures 6.23 and 6.24, the pressure-strain curves are all highly linear. The hoop strains measured by the gage closer to the slit on the cylinder with the 12.7 mm slit are, on the average, 9.4% lower than those measured farther from the slit. This result verifies that the first set of 'far-field' gages on this cylinder were placed inside the region of influence of the slit. As discussed in Chapter 4, the extra circumferential gage was added to all of the uniaxially loaded cylinders tested after the $[90/0/\pm45]_s$ cylinders with the 50.8 and 25.4 mm slits and the $[\pm45/90]_s$ cylinder with the 50.8 mm slit precisely because there was concern that the original pairs of 'far-field' gages on the uniaxially loaded cylinders were placed too close to the slits.

The initial slope of the hoop stress versus hoop strain data, or E_{11}, was determined for the circumferential gage(s) on each cylinder. Hoop stresses were calculated from the cylinder pressures using equation (5.1).

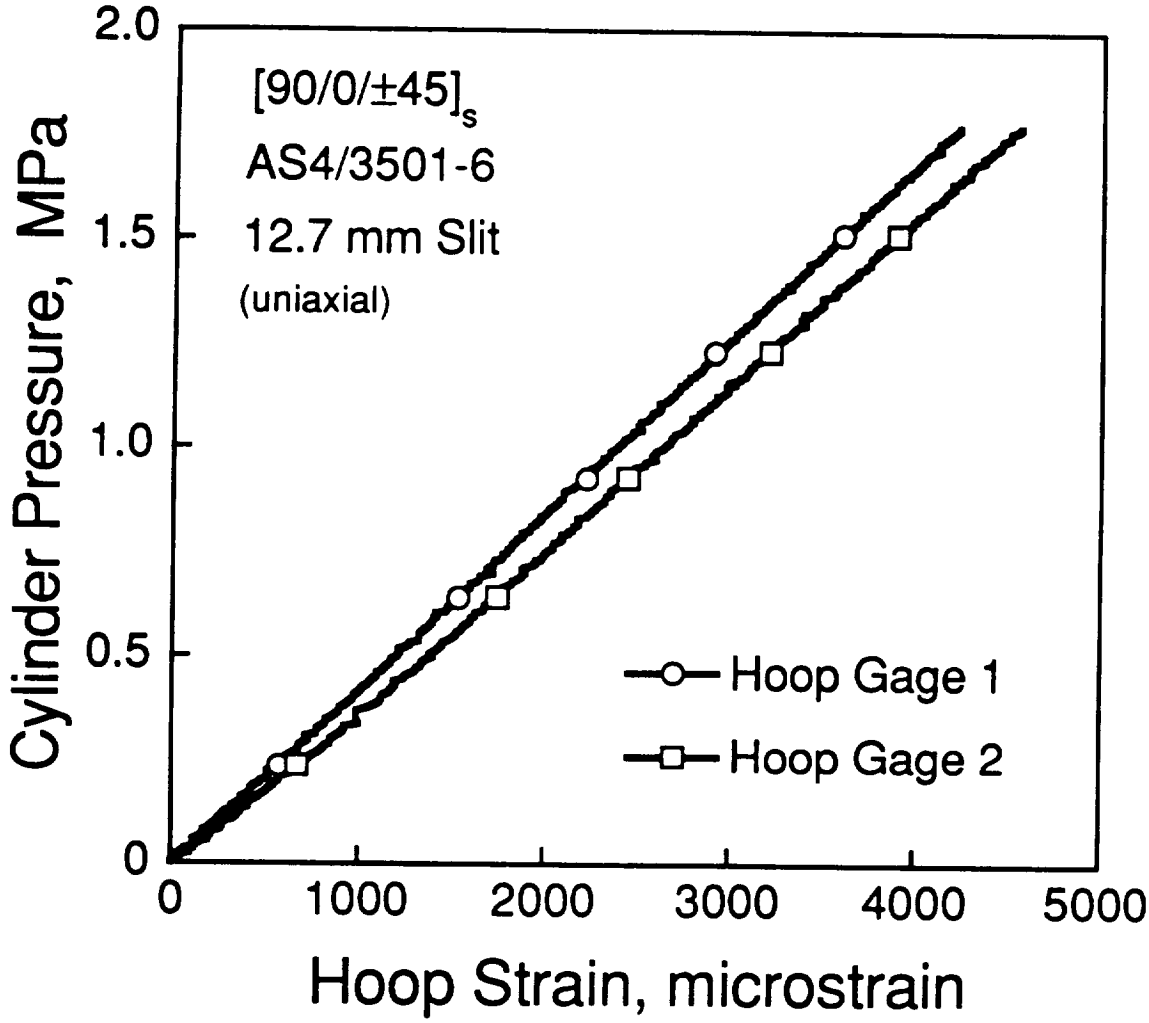

Figure 6.23 Cylinder pressure versus far-field circumferential strain from failure test of uniaxially loaded $[90/0/\pm45]_s$ cylinder with 12.7 mm slit.

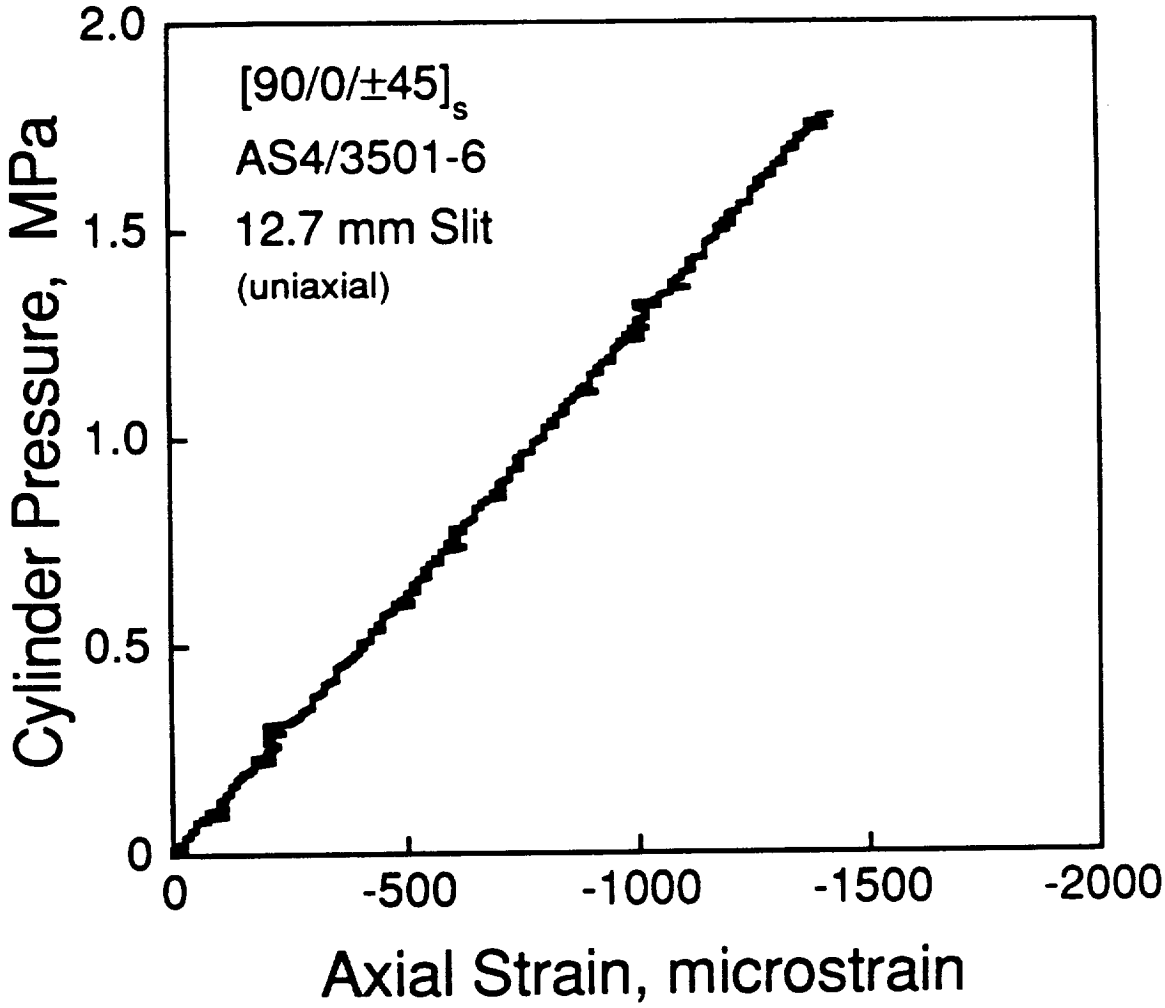

Figure 6.24 Cylinder pressure versus far-field longitudinal strain from failure test of uniaxially loaded $[90/0/\pm45]_s$ cylinder with 12.7 mm slit.

The average value of E_{11} for the uniaxially loaded $[90/0/\pm45]_s$ cylinders is 58.2 GPa with a coefficient of variation of 2.8%. The average initial slope of the axial strain versus hoop strain data, or ν_{12}, for the original pair of far-field gages on each cylinder is 0.33 with a coefficient of variation of 5.5%. The average experimental in-plane modulus and Poisson's ratio compare well with the values of 55.5 GPa and 0.30 calculated from CLPT using the ply properties listed in Table 3.1. However, the experimental modulus of 59.4 GPa for the cylinder with the 50.8 mm slit is 7.0% higher than the calculated value which suggests that the 'far-field' gages on this cylinder may be too close to the slit. The experimental modulus and Poisson's ratio for the pair of axial and hoop gages on the cylinder with the 25.4 mm slit are both less than 2% higher than the calculated values which indicates that these gages read true far-field values. The experimental modulus of 59.7 GPa for Hoop Gage 1 on the cylinder with the 12.7 mm slit is 7.6% higher than that calculated which supports the previous conclusion that the original 'far-field' gages on this cylinder are not located in a region that experienced far-field loading.

The pressure-strain plots for the slit tip gages on all three cylinders are shown in Figures 6.25, 6.26, and 6.27. The curves in these plots are generally smooth. However, there are a few discontinuities that result in increases as well as decreases in the strain readings. The magnitude of the largest abrupt strain jump observed in each plot increases with slit length. The pressure and strain at which the first discontinuity in each curve occurs are indicated in Table 6.7. As can be seen in this table, the pressure at which the first discontinuity is observed is the same for both slit tip gages on each cylinder except for the one with the 12.7 mm slit. The pressure at the first discontinuity also tends to increase with decreasing slit

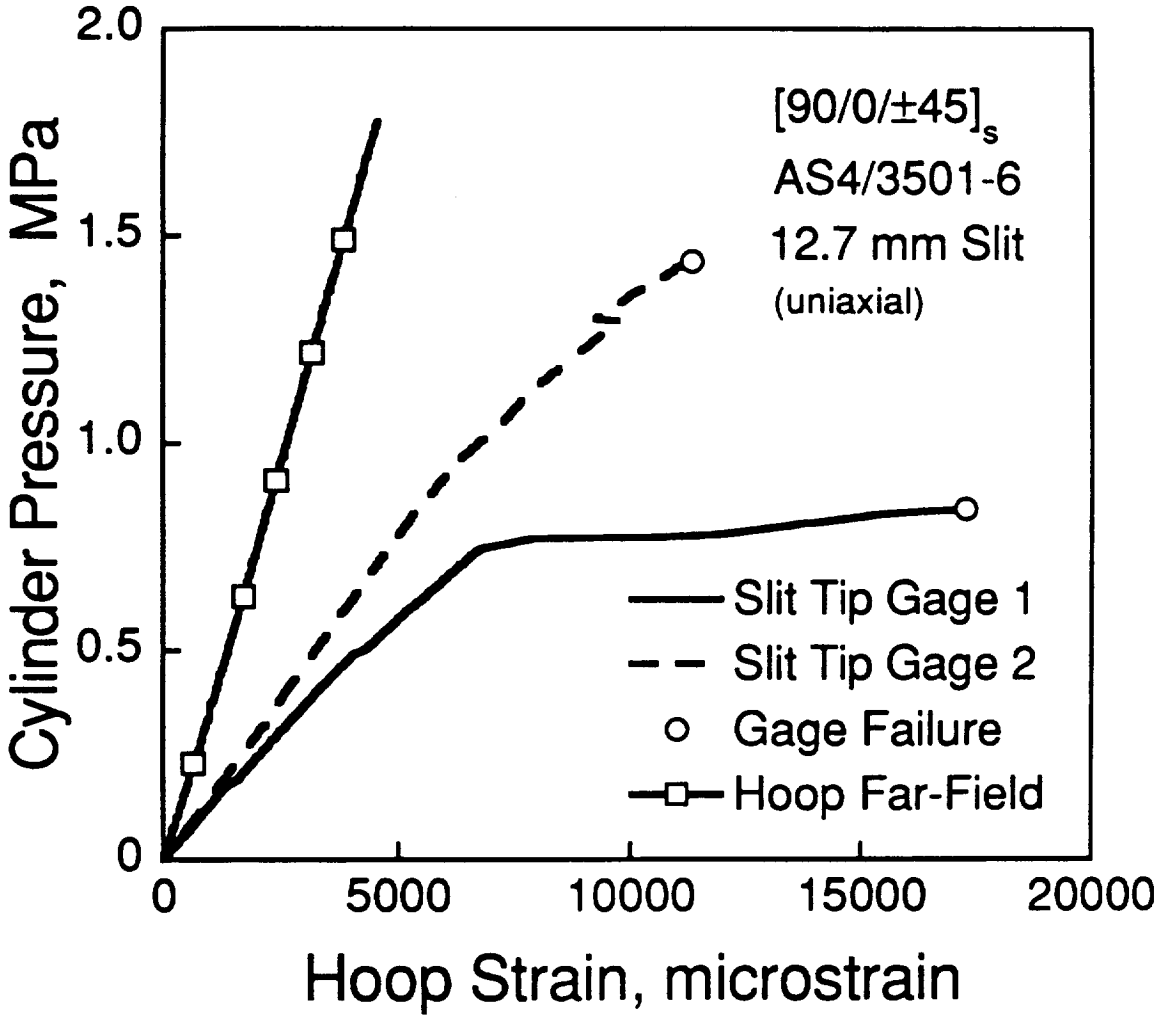

Figure 6.25 Cylinder pressure versus slit tip gage and far-field circumferential strains from failure test of uniaxially loaded $[90/0/\pm45]_s$ cylinder with 12.7 mm slit.

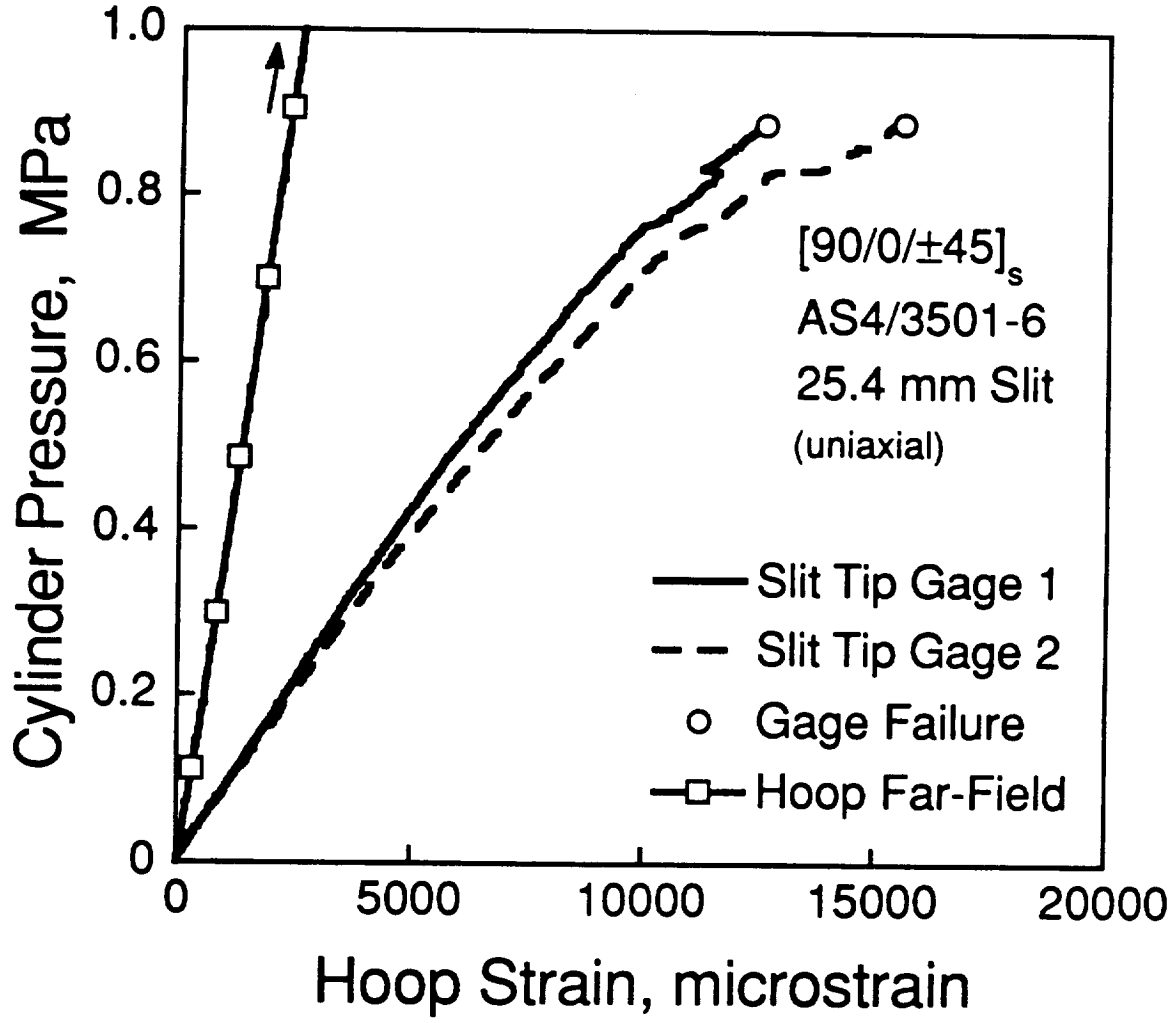

Figure 6.26 Cylinder pressure versus slit tip gage and far-field circumferential strains from failure test of uniaxially loaded $[90/0/\pm45]_s$ cylinder with 25.4 mm slit.

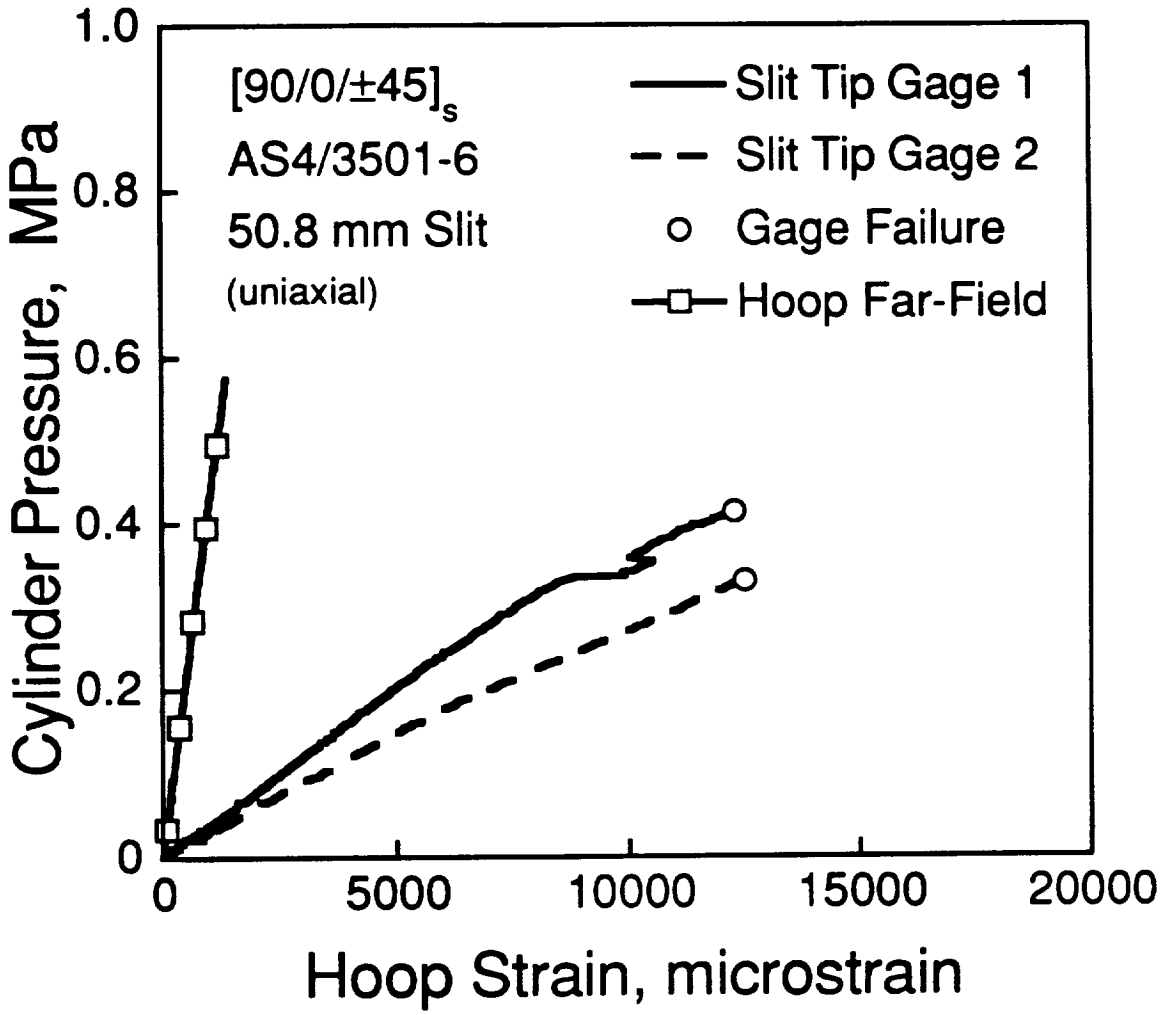

Figure 6.27 Cylinder pressure versus slit tip gage and far-field circumferential strains from failure test of uniaxially loaded $[90/0/\pm45]_s$ cylinder with 50.8 mm slit.

Table 6.7 Hoop Strain and Cylinder Pressure at First Discontinuity Observed in Slit Tip Strain Gage Data for Uniaxially Loaded $[90/0/\pm45]_s$ Cylinders

Slit Length [mm]	Gage	Pressure [MPa]	Slit Tip Hoop Strain [microstrain]
12.7	1	0.18	1375
	2	1.00	6750
25.4	1	0.76	9988
	2	0.76	10900
50.8	1	0.33	8813
	2	0.33	12513

length except in the case of Slit Tip Gage 1 on the cylinder with the 12.7 mm slit. Hoop strains corresponding to the first discontinuity are lower for Slit Tip Gage 1 in all three cases. The maximum hoop strain value at the first discontinuity for each cylinder increases with slit length. Slit Tip Gages 1 and 2 on the cylinder with the 50.8 mm slit went inactive at pressures that are 72% and 57% of the failure pressure, respectively. The corresponding values for the cylinder with the 25.4 mm slit are 82% and 83% and the corresponding values for the cylinder with the 12.7 mm slit are 48% and 81%.

Post-test photographs and damage schematics for the uniaxially loaded $[90/0/\pm45]_s$ cylinders with the 12.7, 25.4, and 50.8 mm slits are shown in Figures 6.28 through 6.33. It is relatively difficult to comment on the initial failure modes in the uniaxially loaded $[90/0/\pm45]_s$ cylinders since fragments containing only three of the six slit tips were recovered. However, the damage visible on the small number of remaining slit fragments is very similar to that observed in the biaxially loaded cylinders from the past [31] and current investigations as well as for the coupons with the same layup. A clean fracture path through the 90°, 0°, and +45° plies extends from each of the three recovered slit tips along an angle of approximately +45°. This direction matches that observed most often in the $[90/0/\pm45]_s$ coupons. The primary fracture paths progress along this angle for approximately 7 mm before they change direction abruptly and curve away from the slit location in the manner described previously for the coupons and biaxially loaded cylinders. The angled path length of 7 mm is approximately the same at that observed in the biaxially loaded cylinders tested in the current investigation. As described previously, this length matches that observed in several of the coupons even though it is slightly

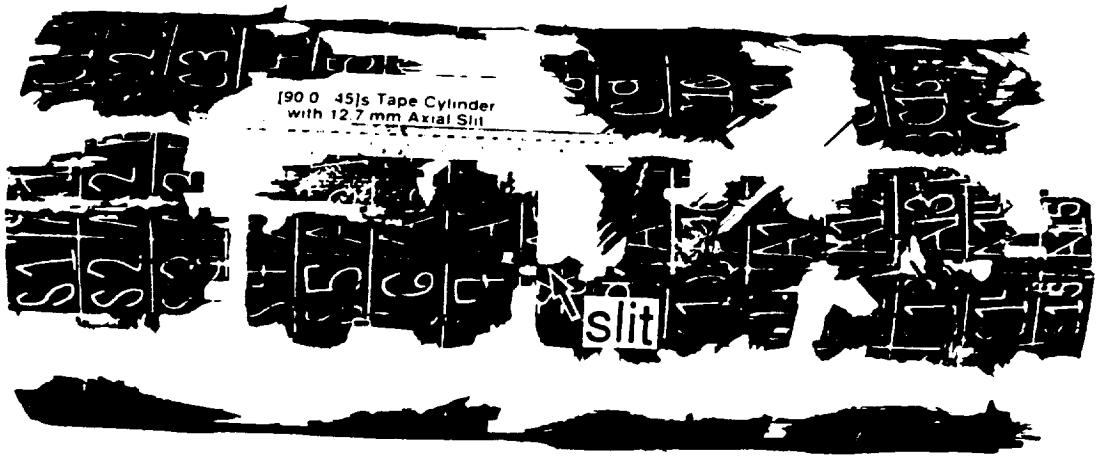

Figure 6.28 Post-test photograph of uniaxially loaded $[90/0/\pm45]_s$ cylinder with 12.7 mm slit.

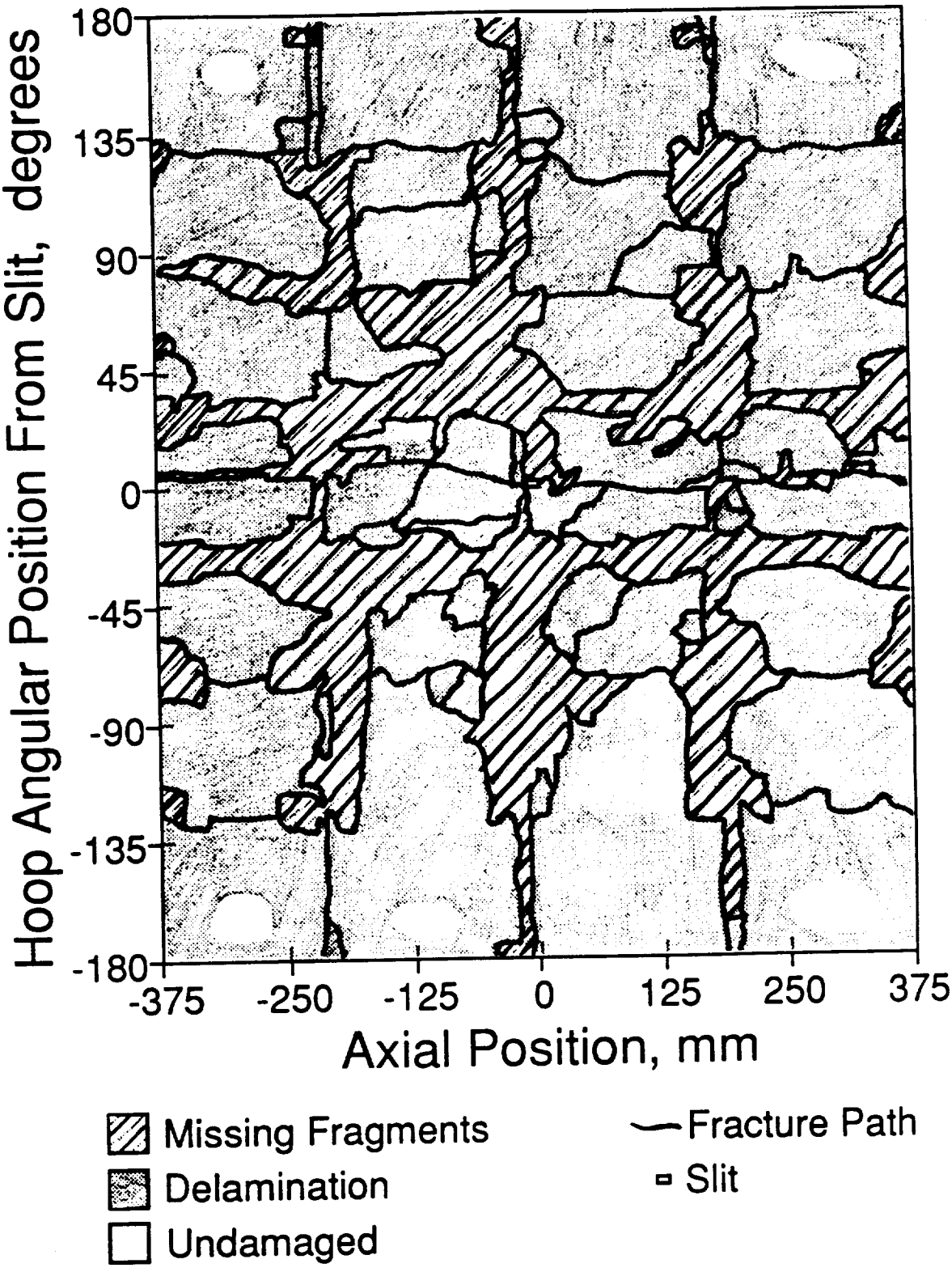

Figure 6.29 Schematic of damage in uniaxially loaded $[90/0/\pm45]_s$ cylinder with 12.7 mm slit.

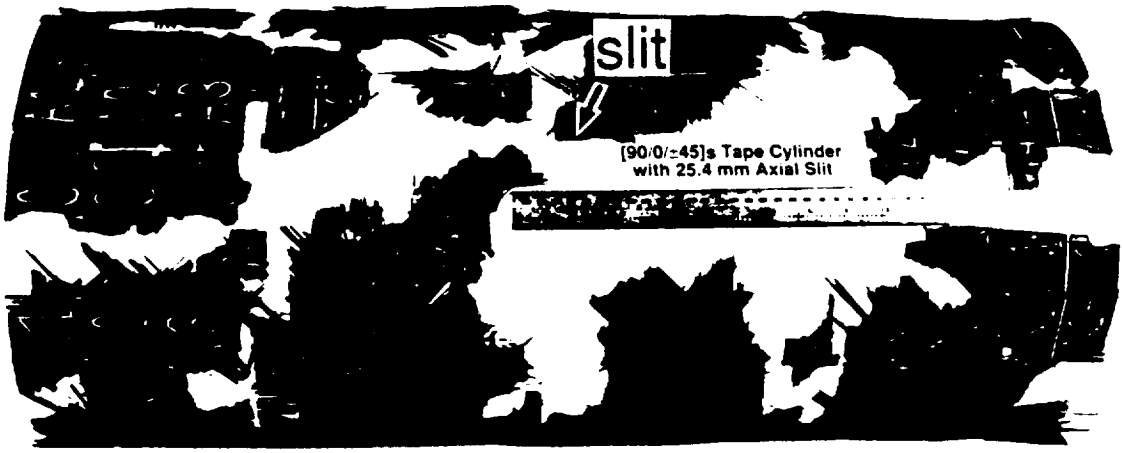

Figure 6.30 Post-test photograph of uniaxially loaded $[90/0/\pm45]_s$ cylinder with 25.4 mm slit.

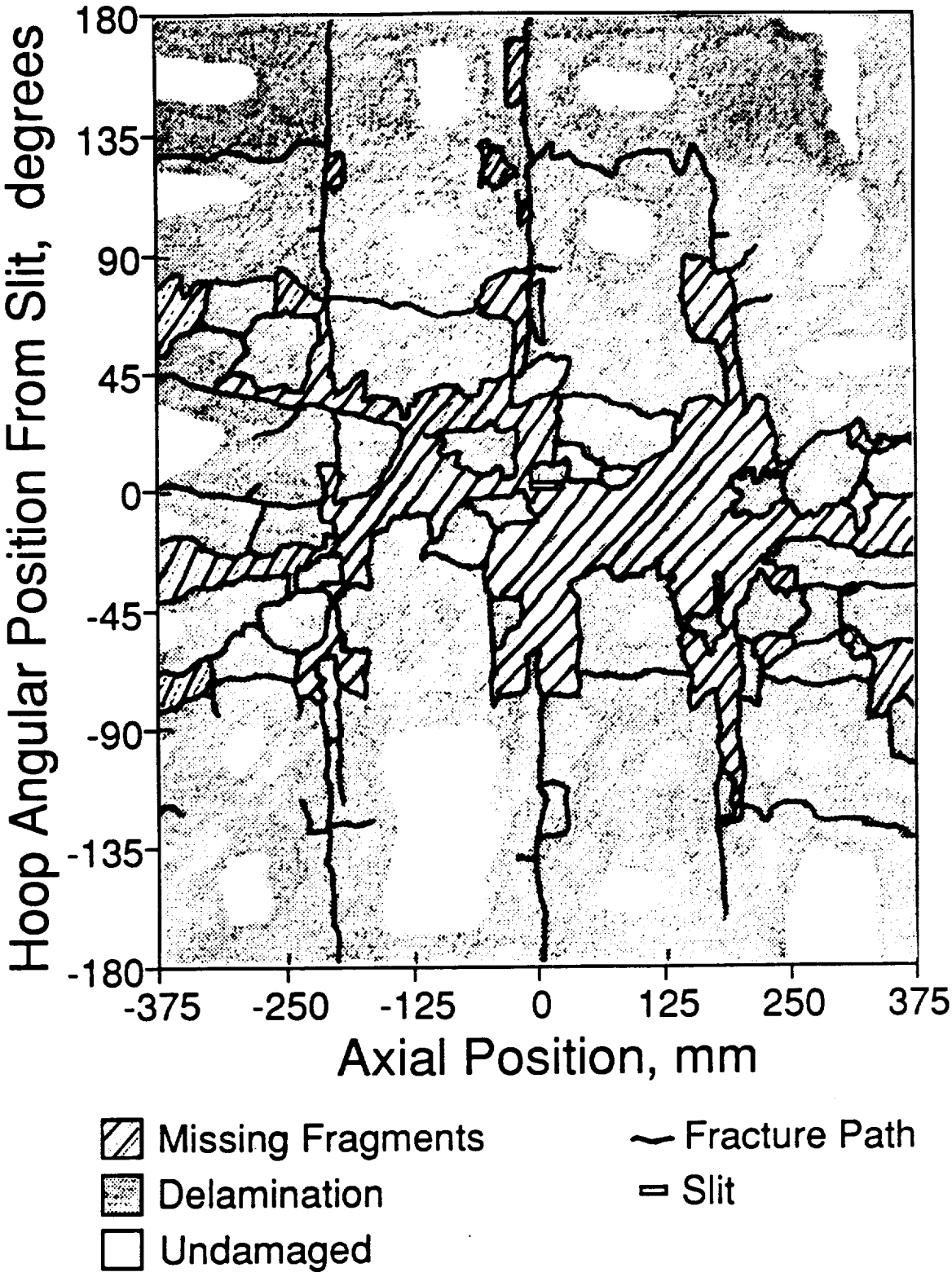

Figure 6.31 Schematic of damage in uniaxially loaded $[90/0/\pm45]_s$ cylinder with 25.4 mm slit.

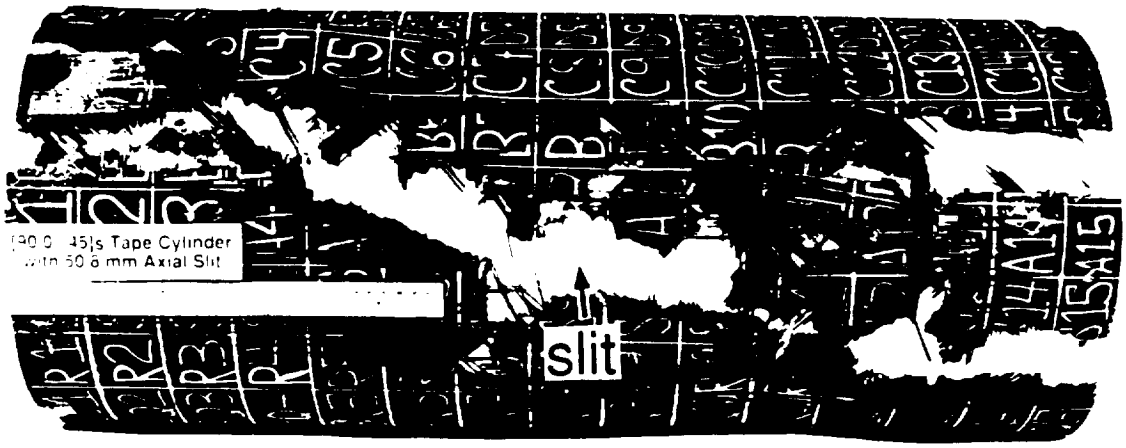

Figure 6.32 Post-test photograph of uniaxially loaded $[90/0/\pm45]_s$ cylinder with 50.8 mm slit.

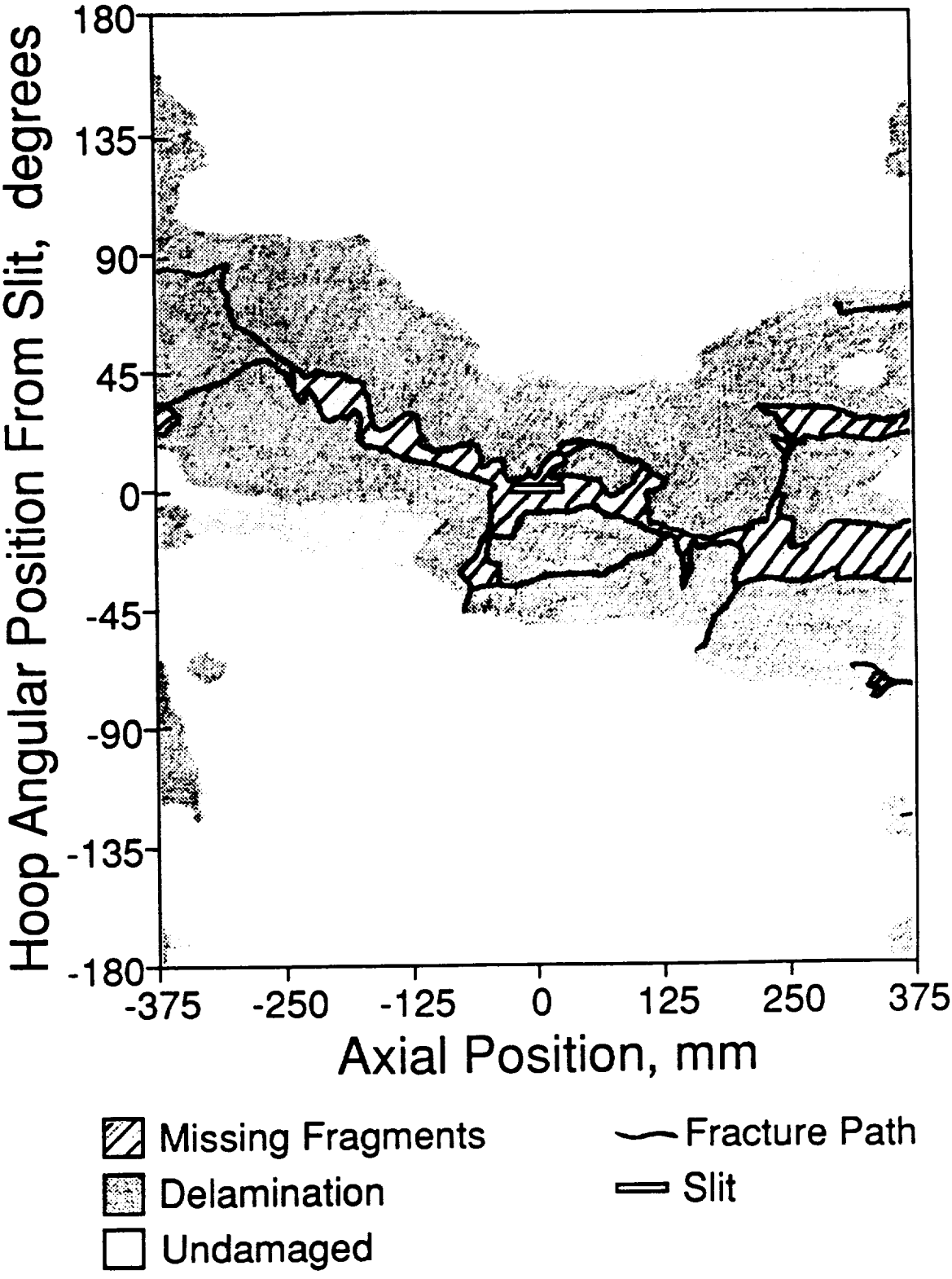

Figure 6.33 Schematic of damage in uniaxially loaded $[90/0/\pm45]_s$ cylinder with 50.8 mm slit.

shorter than the average length of 9 mm. A sharp, secondary circumferential fracture path from the center rod support plate passes through the left slit tip in the cylinder with the 12.7 mm slit and intersects the top edge of the slit in the cylinder with the 25.4 mm slit, 23 mm from the right slit tip. Other secondary damage near the slits in the uniaxially loaded cylinders is similar to that described previously for the biaxially loaded cylinders with the 12.7 mm slits. No primary circumferential fracture paths similar to the one observed in the past investigation [31] at Slit Tip 2 in the biaxially loaded cylinder with the 12.7 mm slit are visible at the slit tips in the uniaxially loaded $[90/0/\pm45]_s$ cylinders.

The primary damage away from the slit regions in the uniaxially loaded $[90/0/\pm45]_s$ cylinders with the 12.7 and 25.4 mm slits is similar in many respects to that described previously for the biaxially loaded $[90/0/\pm45]_s$ cylinders with the 12.7 mm slits. However, secondary damage in the uniaxially loaded cylinders with the 12.7 and 25.4 mm slits, and the damage in the uniaxially loaded cylinder with the 50.8 mm slit, differs somewhat from that observed in the biaxially loaded cylinders. The primary fracture paths in the uniaxially loaded cylinders with the 12.7 and 25.4 mm slits differ from those described previously for the biaxially loaded cylinders with the 12.7 mm slits only in that they do not bifurcate as they approach the endplates. In addition, fracture paths which reached the ends of the uniaxially loaded cylinders did not turn to the circumferential direction, as they do when the endcaps are bonded. A higher degree of secondary fragmentation and a much larger number of unidentified fragments resulting from cylinder contact with the test apparatus (AALD) are observed in the uniaxially loaded cylinders with the 12.7 mm and 25.4 mm slits as compared to the biaxially loaded cylinders. Of the two

uniaxially loaded cylinders, the cylinder with the 12.7 mm slit experienced the most secondary damage in the form of fracture paths, unidentified fragments, and multiple-ply delamination. However, many more fragments were recovered along the main fracture paths in the cylinder with the 12.7 mm slit. The main fracture paths in the cylinder with the 50.8 mm slit are oriented along essentially the -70° direction. This agrees with the initial portion of the paths observed in the biaxially loaded and other uniaxially loaded cylinders. However, the paths in the other cylinders do not continue along this direction, as described previously. The main failure paths in the cylinder with the 50.8 mm slit are very uneven and relatively nondistinct since sections of the material are missing all along the main fracture paths. Multiple-ply delaminations are localized in a band approximately 250 mm wide around the main failure paths and very little damage is apparent on most of the cylinder.

Failure pressures for the uniaxially loaded $[90/0/\pm45]_s$ cylinders are listed in Table 6.8. These failure pressures, as well as those for the biaxially loaded $[90/0/\pm45]_s$ cylinders tested in the past and current investigations, are plotted versus slit length in Figure 6.34. This figure also shows the correlation curves for the $[90/0/\pm45]_s$ coupons tested in the past and current investigations, expressed in terms of equivalent pressures, and the corresponding cylinder failure pressure prediction curves. The failure stresses in both coupon data sets were correlated separately since the average H_c value obtained for the notched $[90/0/\pm45]_s$ coupons in the current investigation is 10% lower than that obtained in the past work. Both correlation curves were used with the same Folias curvature correction factor to establish two separate cylinder failure pressure prediction curves which are valid for cylinders tested uniaxially or biaxially. As can be seen

Table 6.8 Failure Pressures of Uniaxially Loaded $[90/0/\pm45]_s$ Cylinders

Slit Length, mm	Failure Pressure, MPa
12.7	1.77
25.4	1.08
50.8	0.57

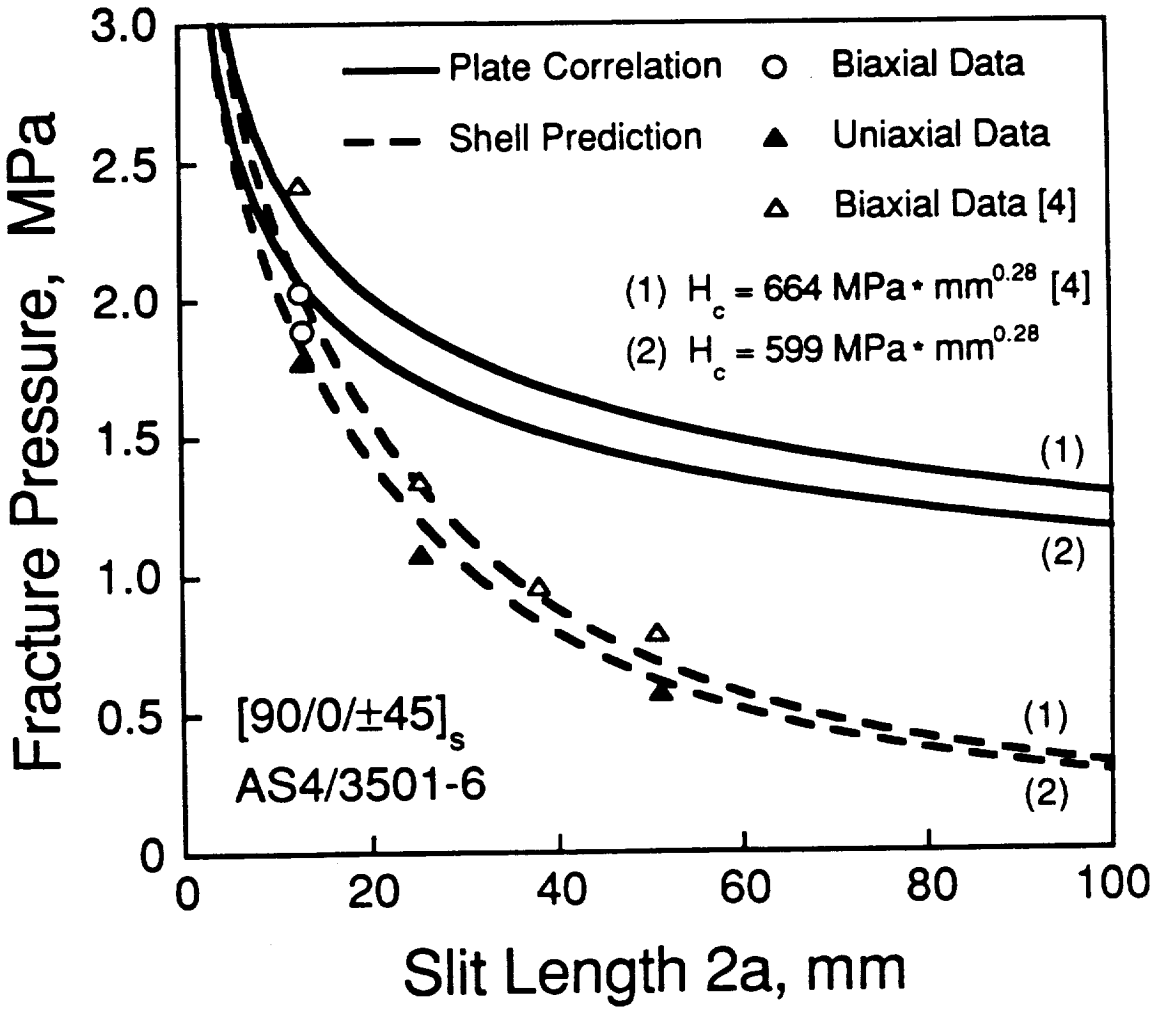

Figure 6.34 Experimental and predicted failure pressures for biaxially and uniaxially loaded $[90/0/\pm45]_s$ tape cylinders.

in Figure 6.34, the experimental failure pressures of the biaxially loaded cylinders tested in the current investigation are both located in the region between the two failure pressure prediction curves. The failure pressures of these cylinders agree well with each other and correlate well with the predicted values. The uniaxial failure pressures are less than the values predicted using the lower H_c value (599 MPa*mm$^{0.28}$) by only 3% to 10%. Thus, there is fairly good correlation between the experimental failure pressures for the uniaxially loaded cylinders and the predicted values. However, the failure pressures of the uniaxially loaded $[90/0/\pm45]_s$ cylinders are lower than the experimental failure pressures for the biaxially loaded cylinders in all cases. Furthermore, the failure pressures for all three biaxially loaded cylinders with the 12.7 mm slit size from the current investigation are significantly different from the failure pressure of the corresponding cylinder from the past investigation which is 18% above the value predicted using the higher H_c value (664 MPa*mm$^{0.28}$) and is also above the equivalent pressure for a flat plate with the same slit size. All of the biaxial values from the past investigation also differ from the current uniaxial and biaxial values in that they are all above, although very close to, the higher predictions.

6.3 $[\pm45/0]_s$ Cylinders

Representative plots of the strain data for the $[\pm45/0]_s$ cylinders are provided in Figures 6.35 and 6.36. Strain readings from the original circumferential far-field gage and the extra hoop gage on the cylinder with the 25.4 mm slit are shown in Figure 6.35. Axial far-field strains for the same cylinder are shown in Figure 6.36. The strain readings from the axial and hoop gages on the other two cylinders (not shown) show the same

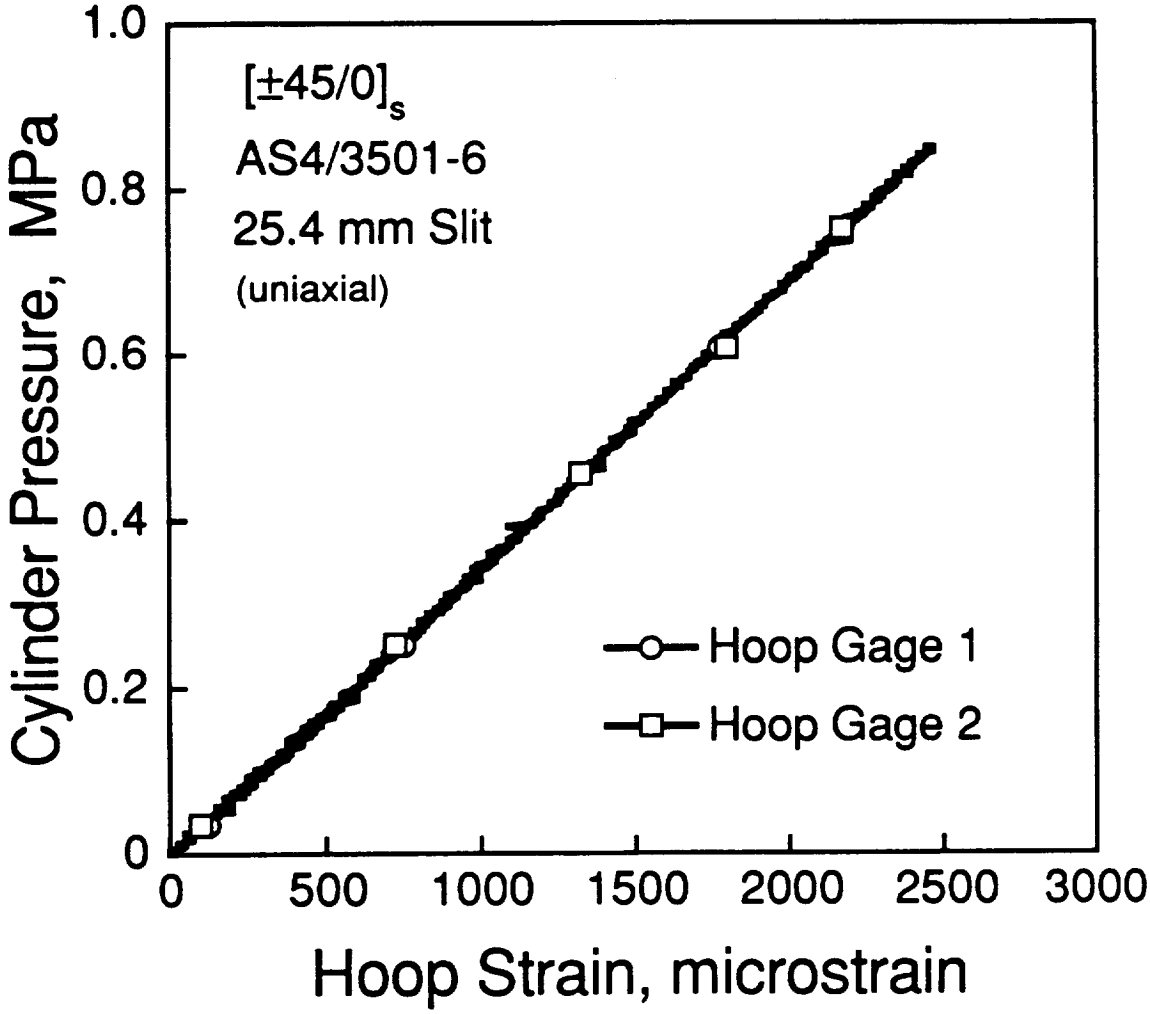

Figure 6.35 Cylinder pressure versus far-field circumferential strain from failure test of uniaxially loaded $[\pm 45/0]_s$ cylinder with 25.4 mm slit.

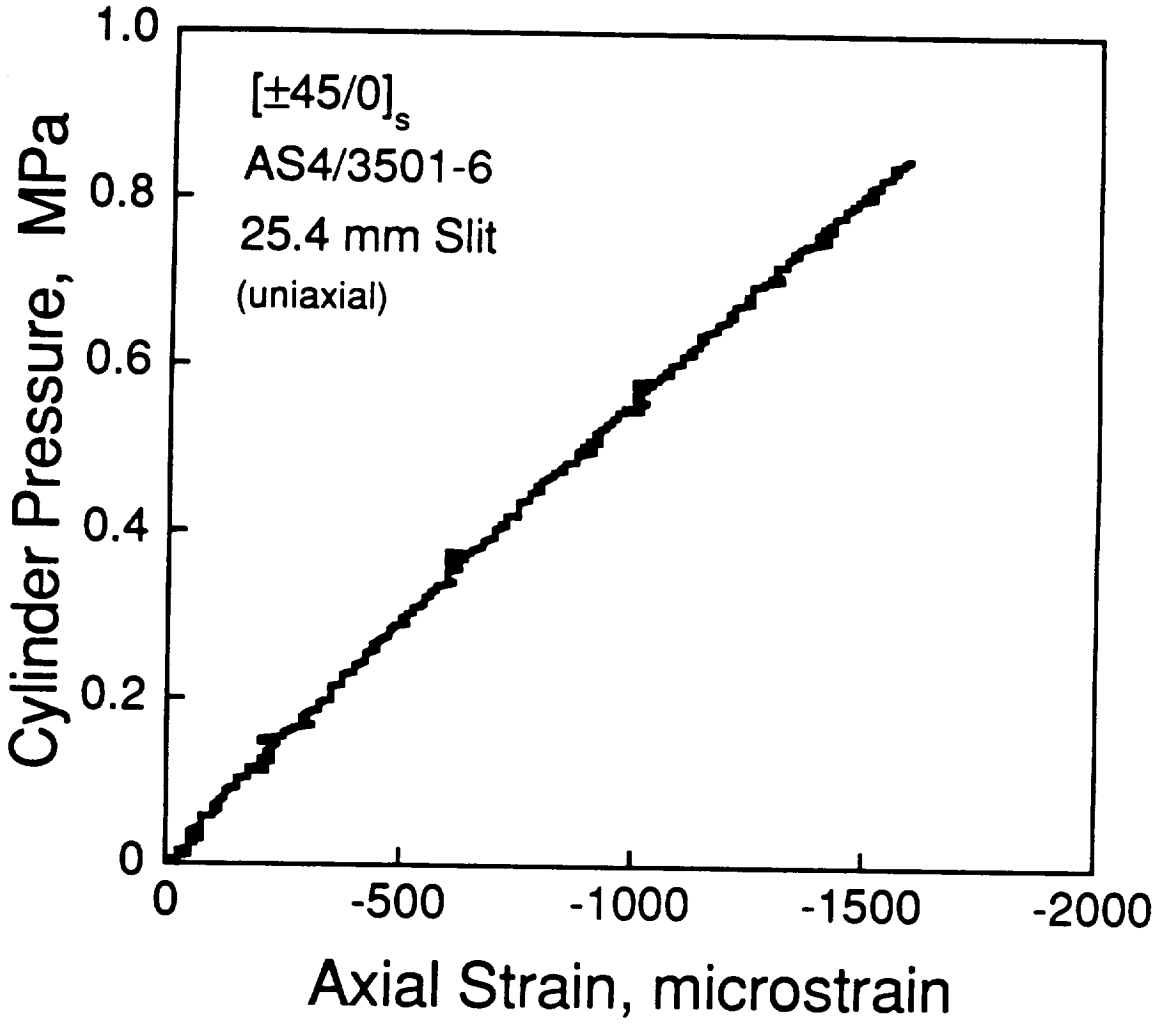

Figure 6.36 Cylinder pressure versus far-field longitudinal strain from failure test of uniaxially loaded $[\pm 45/0]_s$ cylinder with 25.4 mm slit.

general trends. However, the Hoop Gage 1 and Hoop Gage 2 strains for the cylinders with the 12.7 and 50.8 mm slit do not agree with each other as well as they do for the cylinder with the 25.4 mm slit. This lower degree of correlation between the hoop strains suggests that the original pair of 'far-field' gages on the cylinders with the 12.7 and 50.8 mm slits may be located slightly inside the region of influence of the slit. As can be seen in Figure 6.35, the pressure-hoop strain curves are highly linear. However, the axial strains shown in Figure 6.36 do not show the same degree of linearity as the hoop strains, particularly at the lower end of the curve. The excellent correlation between the Hoop Gage 1 and Hoop Gage 2 strains for the cylinder with the 25.4 mm slit indicates that the original axial and hoop gages on this cylinder are truly far-field gages.

The average experimental value of E_{11} for the $[\pm 45/0]_s$ cylinders, or the average initial slope of the hoop stress versus hoop strain data, is 66.0 GPa with a coefficient of variation of 4.5%. The average experimental value of ν_{12} determined using strain data from the original 'far-field' gage pair on each cylinder is 0.65 with a coefficient of variation of 12.9%. The average experimental hoop modulus and major Poisson's ratio compare with the values of 61.8 GPa and 0.69 calculated using CLPT and the ply properties listed in Table 3.1. The experimental modulus for Hoop Gage 1 on the cylinder with the 50.8 mm slit is virtually identical to the calculated modulus, however, the experimental Poisson's ratio of 0.56 is 19% below the calculated value. The experimental modulus for Hoop Gage 2 on the same cylinder is 7.7% above predicted and, thus, it is difficult to determine if the original 'far-field' gages on the cylinder with the 50.8 mm slit are too close to the slit. The original gages on the cylinder with the 12.7 mm slit are too close to the slit since the experimental modulus of 71.1 GPa for Hoop Gage 1

is 15% above the calculated value. The readings from the axial and hoop gages on the cylinder with the 25.4 mm slit are true far-field values since the experimental moduli of 66.1 and 65.1 GPa for Hoop Gage 1 and Hoop Gage 2, respectively, agree with each other and the experimental Poisson's ratio of 0.67 is 3% lower than calculated.

The pressure-strain plots for the slit tip gages on the uniaxially loaded $[\pm 45/0]_s$ cylinders are shown in Figures 6.37, 6.38, and 6.39. The curves for Slit Tip Gage 2 are all generally smooth and show slight discontinuities only near the point where the gage failed. The slope of each Slit Tip Gage 2 curve continuously decreases throughout the test. The curves for Slit Tip Gage 1 also show an initial smooth increase in strain, however, the slope of both curves continuously increases until it becomes close to infinite. At this point, a discontinuity in the strain readings is observed and the strains start to decrease with increasing pressure. The Slit Tip Gage 1 strains decrease or hold steady as the pressure increases until a discontinuity is reached which results in a large, abrupt increase in strain. For the cylinder with the 50.8 mm slit, this strain jump is followed by a relatively large nonlinear increase in strain which ends with the gage failure. Slit Tip Gage 1 on the cylinder with the 12.7 mm slit fails shortly after the sudden strain increase. No Slit Tip Gage 1 data is presented for the cylinder with the 25.4 mm slit since this gage was damaged prior to the test. Pressure and strain values which correspond to the first observed discontinuity in the strain readings from each gage are listed in Table 6.9. As can be seen in this table, pressures and strains for Slit Tip Gage 2 decrease with increasing slit length. Strains for Slit Tip Gage 1 are lower than those for Slit Tip Gage 2 on the cylinders with the 12.7 and 50.8 mm slits, however, the strains for Slit Tip Gage 1 do not change significantly for

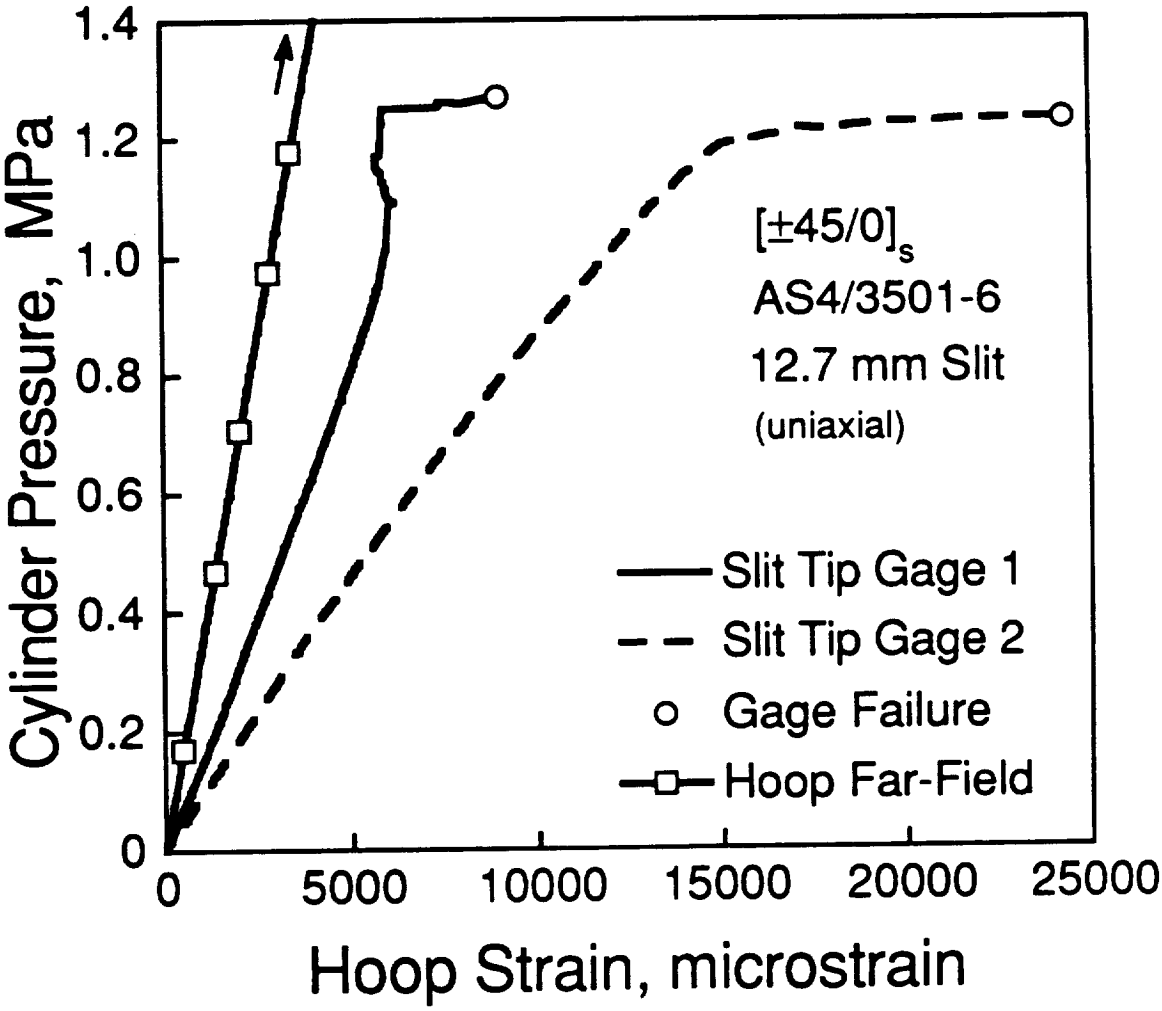

Figure 6.37 Cylinder pressure versus slit tip gage and far-field circumferential strains from failure test of uniaxially loaded $[\pm 45/0]_s$ cylinder with 12.7 mm slit.

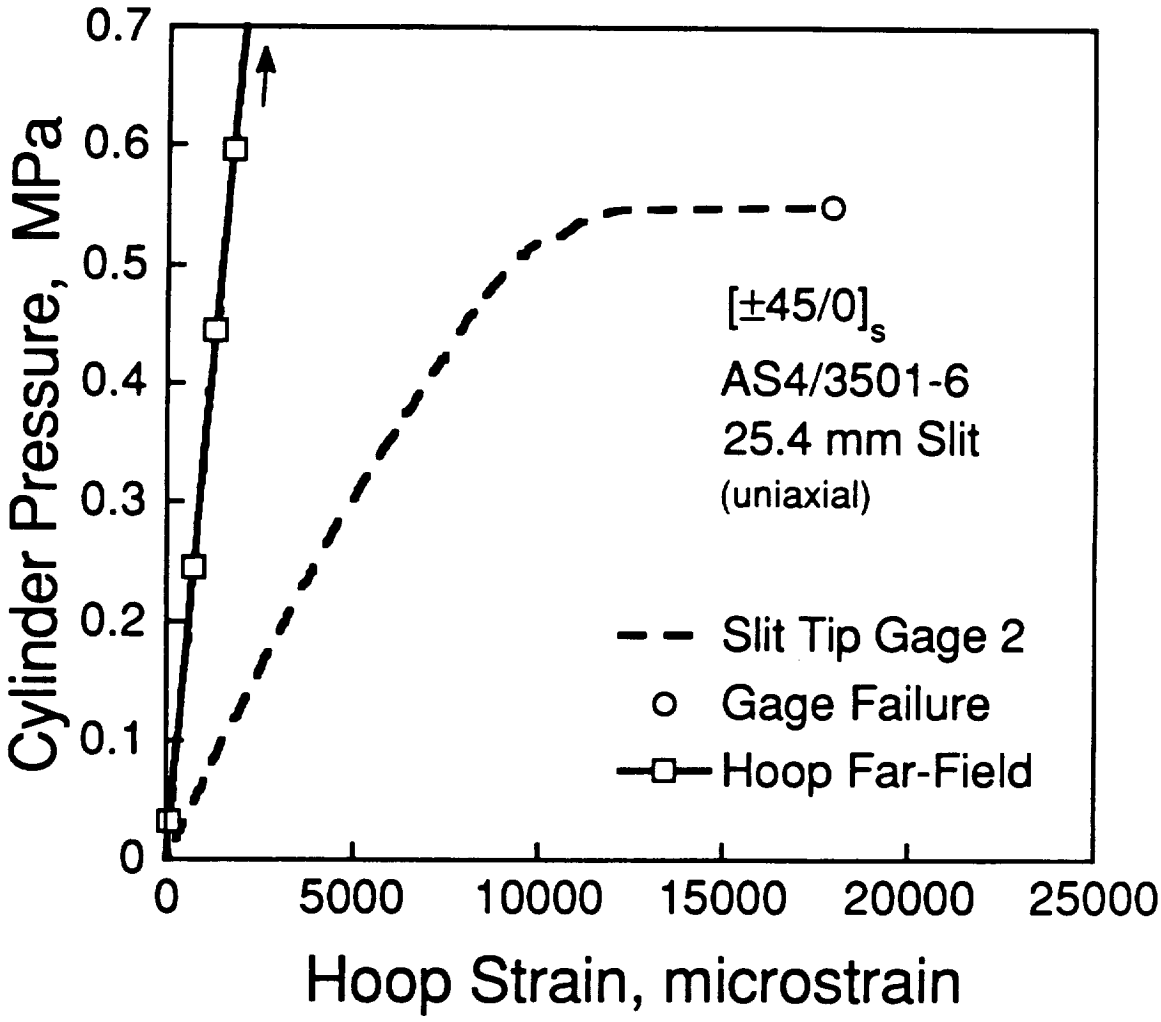

Figure 6.38 Cylinder pressure versus slit tip gage and far-field circumferential strains from failure test of uniaxially loaded $[\pm 45/0]_s$ cylinder with 25.4 mm slit.

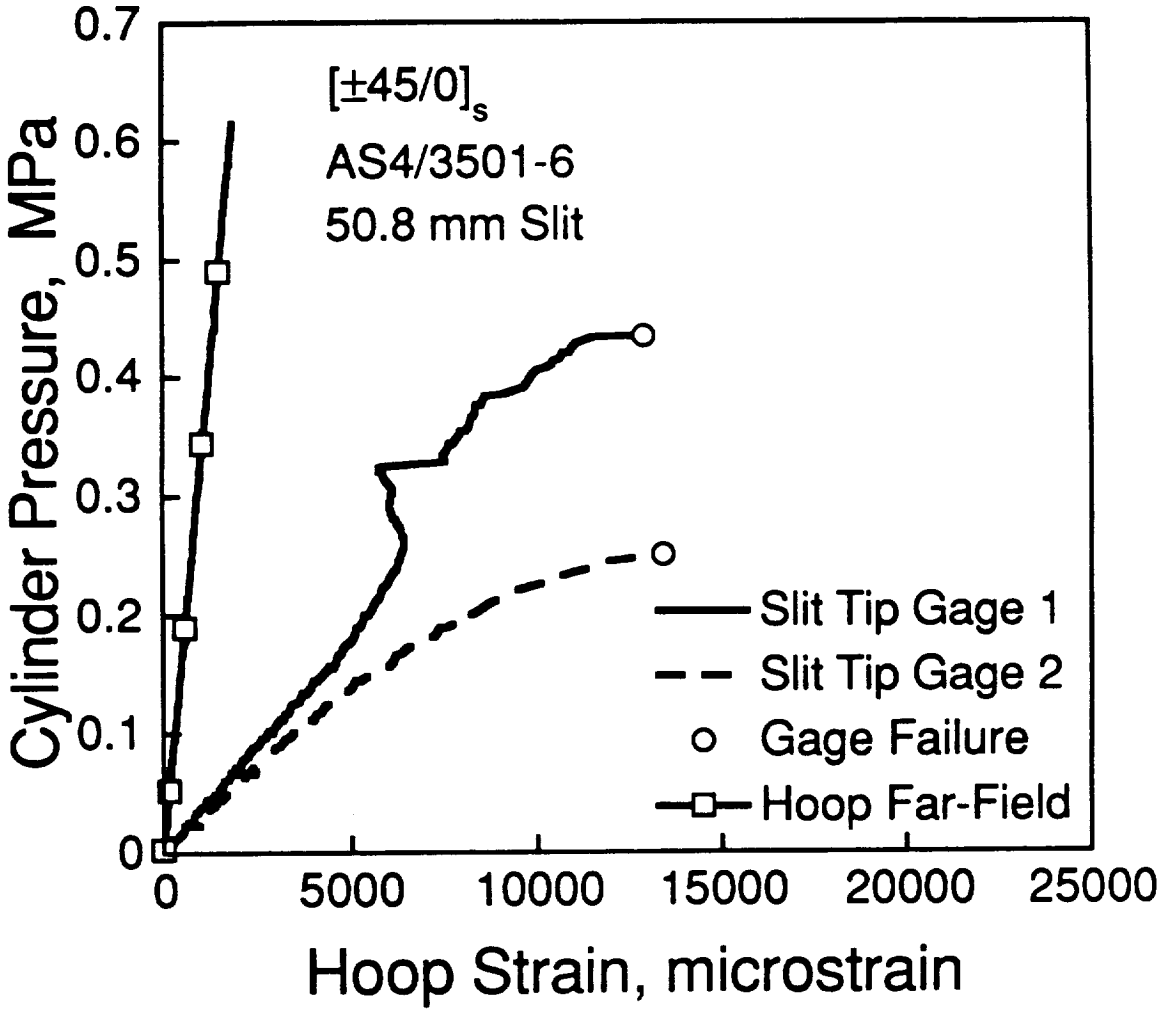

Figure 6.39 Cylinder pressure versus slit tip gage and far-field circumferential strains from failure test of uniaxially loaded $[\pm 45/0]_s$ cylinder with 50.8 mm slit.

Table 6.9 Hoop Strain and Cylinder Pressure at First Discontinuity Observed in Slit Tip Strain Gage Data for Uniaxially Loaded $[\pm 45/0]_s$ Cylinders

Slit Length [mm]	Gage	Pressure [MPa]	Slit Tip Hoop Strain [microstrain]
12.7	1	1.09	6063
	2	1.19	15075
25.4	1	--[a]	--
	2	0.55	12100
50.8	1	0.26	6450
	2	0.24	11638

[a] gage damaged prior to test

the two slit lengths. The pressure at the first discontinuity is comparable at both ends of the slit in the cylinders with the 12.7 and 50.8 mm slits. The largest strain jump of approximately 1750 μstrain was observed in the Slit Tip Gage 1 data for the cylinder with the 50.8 mm slit and the Slit Tip Gage 1 strains for this cylinder are much more erratic than those for the cylinder with the 12.7 mm slit. Slit Tip Gages 1 and 2 on the cylinder with the 50.8 mm slit failed at pressures that are 71% and 41% of the failure pressure, respectively. The corresponding values for the cylinder with the 12.7 mm slit are 89% and 86%. Slit Tip Gage 2 on the cylinder with the 25.4 mm slit failed at 65% of the failure pressure.

The failure pressures of the $[\pm 45/0]_s$ cylinders tested in the current investigation are shown in Table 6.10. These pressures are also plotted versus slit length in Figure 6.40 along with the coupon correlation curve expressed in terms of equivalent pressures, the cylinder failure pressure prediction curve, and Ranniger's data [31] for biaxially loaded cylinders of this layup with slit lengths from 12.7 to 63.5 mm. The value of the composite fracture parameter, H_c, used for the coupon correlation curve is 715 $MPa*mm^{0.28}$ [31]. The failure pressures of the uniaxially loaded $[\pm 45/0]_s$ cylinders with the 12.7 and 25.4 mm slits are lower than those of the biaxially loaded cylinders with the same slit lengths by 33% and 41%, respectively, which is a significant decrease. In contrast, the failure pressure of the uniaxially loaded cylinder with the 50.8 mm slit is only 15% lower than the biaxial value. The failure pressures of the cylinders with the 12.7 and 25.4 mm slits are both below the predicted values by approximately 14%. The failure pressure of the cylinder with the 50.8 mm slit differs in that it is higher than the predicted value by 21%.

Table 6.10 Failure Pressures of Uniaxially Loaded $[\pm 45/0]_s$ Cylinders

Slit Length, mm	Failure Pressure, MPa
12.7	1.43
25.4	0.85
50.8	0.62

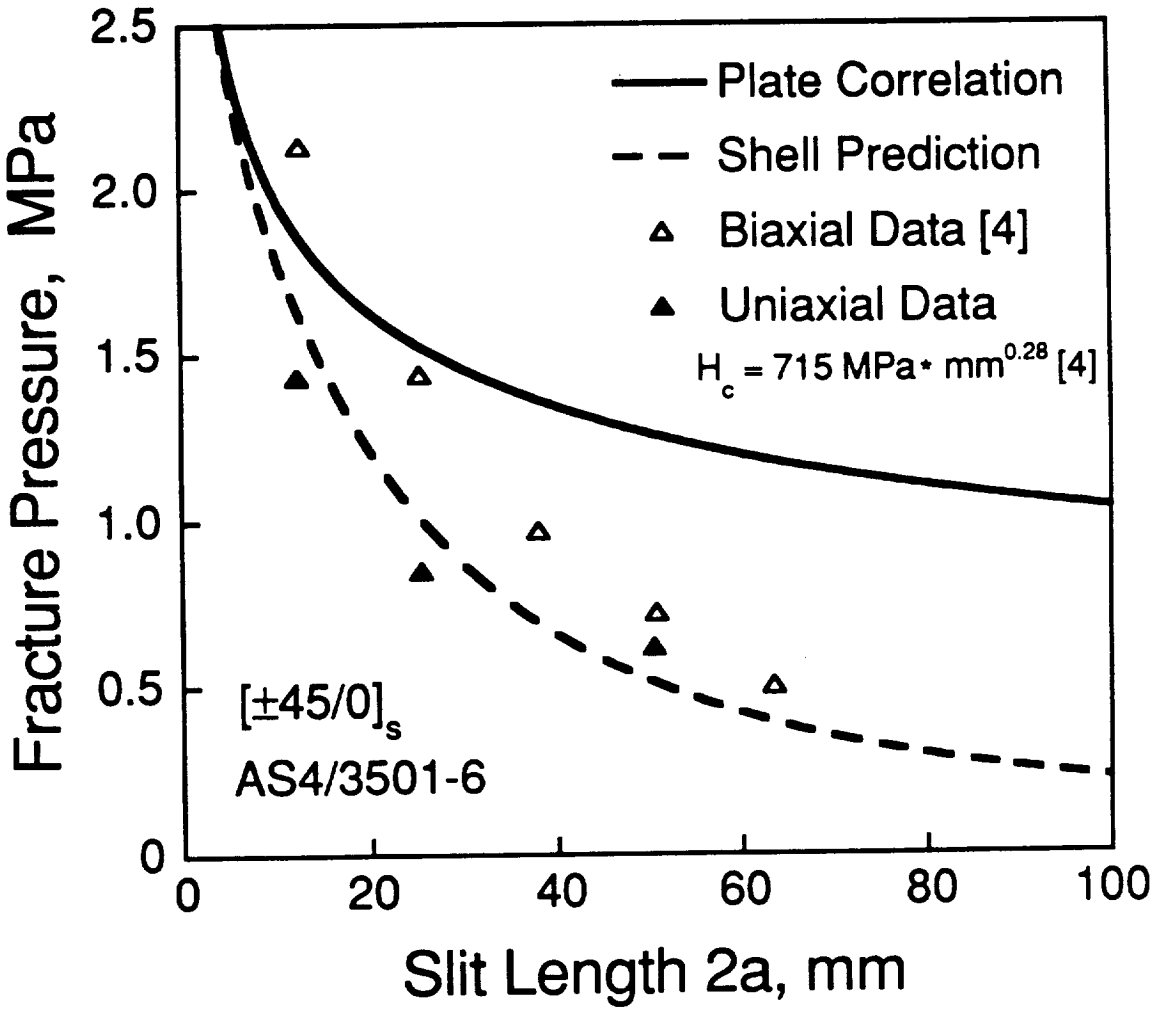

Figure 6.40 Experimental and predicted failure pressures for uniaxially loaded $[\pm 45/0]_s$ tape cylinders.

Photographs of the uniaxially loaded $[\pm 45/0]_s$ cylinders with the 12.7, 25.4, and 50.8 mm slits after failure are shown in Figures 6.41, 6.43, and 6.45, respectively. Drawings of damage states in these cylinders are presented in Figures 6.42, 6.44, and 6.46. As can be seen in these figures, the initial damage states in the uniaxially loaded $[\pm 45/0]_s$ cylinders vary somewhat from cylinder to cylinder. In the cylinders with the 25.4 and 50.8 mm slits, a primary fracture path extends away from each slit tip along the direction of the +45° fibers. In the cylinder with the 50.8 mm slit, an additional primary fracture path leaves each slit tip along the -45° direction. It is difficult to tell if these additional paths are present at the slit tips in the cylinder with the 25.4 mm slit due to missing fragments which include the fragment(s) containing the entire bottom half of the slit. However, there is some evidence of a fracture path along the -45° direction at the left slit tip in this cylinder. In the cylinders with the 25.4 and 50.8 mm slits, the paths extending from the slit tips are ragged due to delamination between the ±45° and splitting of these plies. The paths are, however, much more ragged in the cylinder with the 50.8 mm slit. In the triangular region between the two paths at each slit tip in the cylinder with the 50.8 mm slit, most of the plies behind the -45° ply closest to the outside of the cylinder were not recovered. Sharp, secondary circumferential fracture paths from the center rod support plate intersect the slit 6 mm from the left slit tip in the cylinder with the 25.4 mm slit and 8.5 mm from the left slit tip in the cylinder with the 50.8 mm slit. The bottom half of the slit in the cylinder with the 50.8 mm slit to the left of the circumferential fracture path is damaged and shows evidence of secondary splitting in the 0° plies. It is impossible to comment on the initial damage state in the cylinder with the 12.7 mm slit since no fragments from the slit region were recovered.

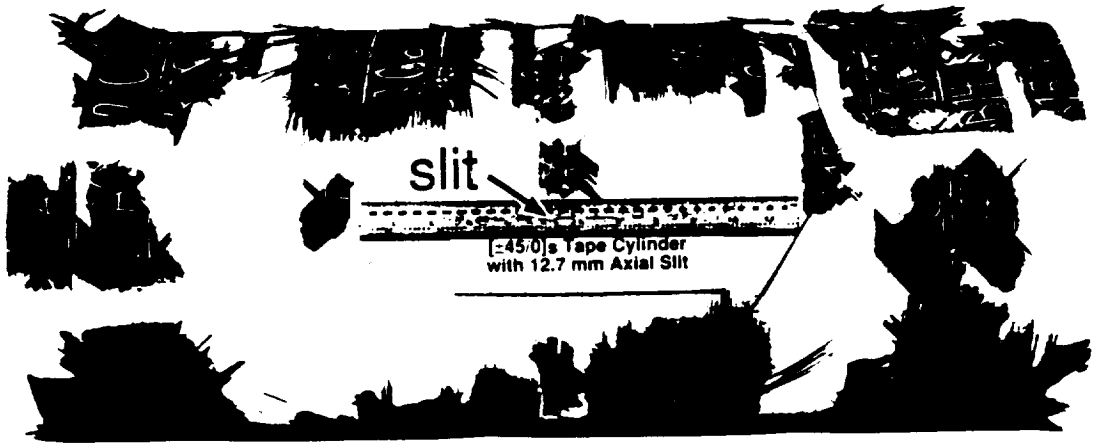

Figure 6.41 Post-test photograph of uniaxially loaded $[\pm 45/0]_s$ cylinder with 12.7 mm slit.

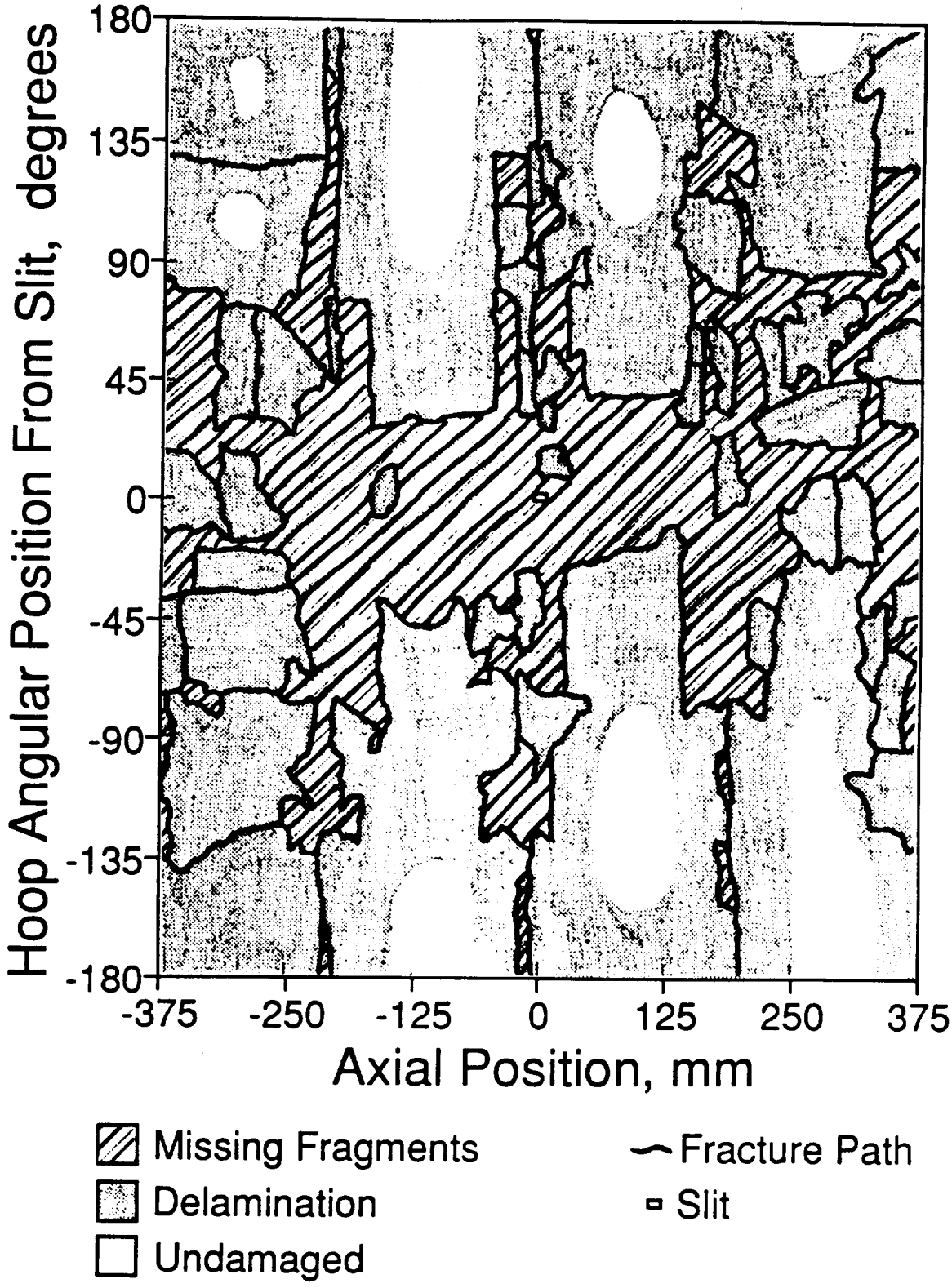

Figure 6.42 Schematic of damage in uniaxially loaded $[\pm 45/0]_s$ cylinder with 12.7 mm slit.

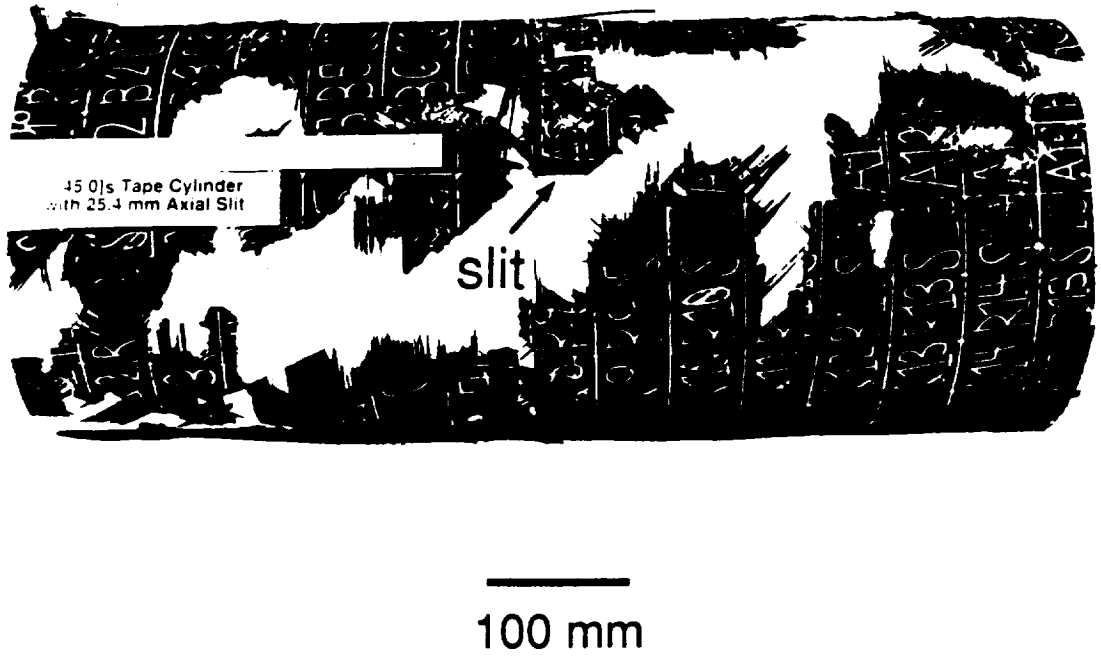

Figure 6.43 Post-test photograph of uniaxially loaded $[\pm 45/0]_s$ cylinder with 25.4 mm slit.

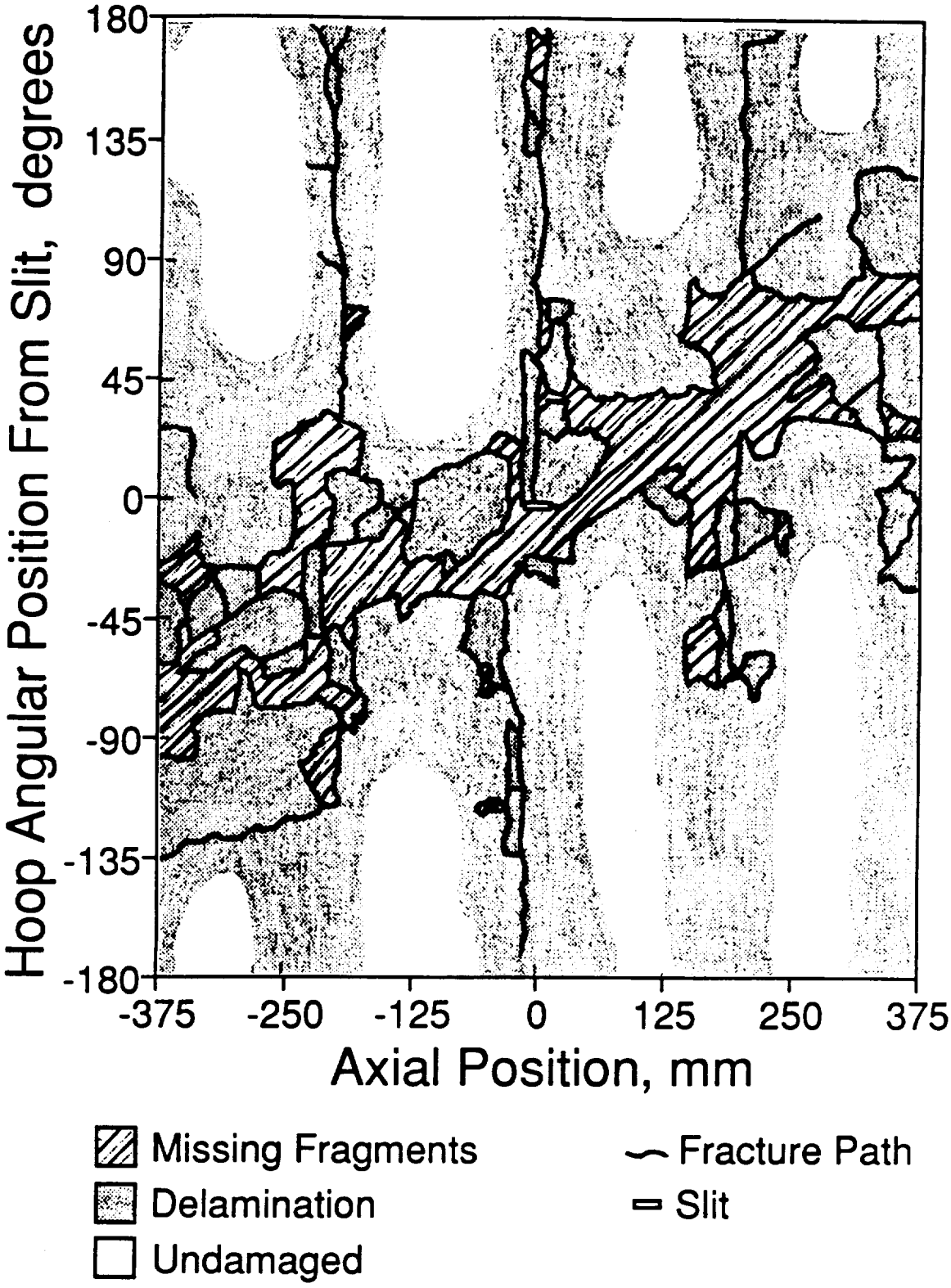

Figure 6.44 Schematic of damage in uniaxially loaded $[\pm 45/0]_s$ cylinder with 25.4 mm slit.

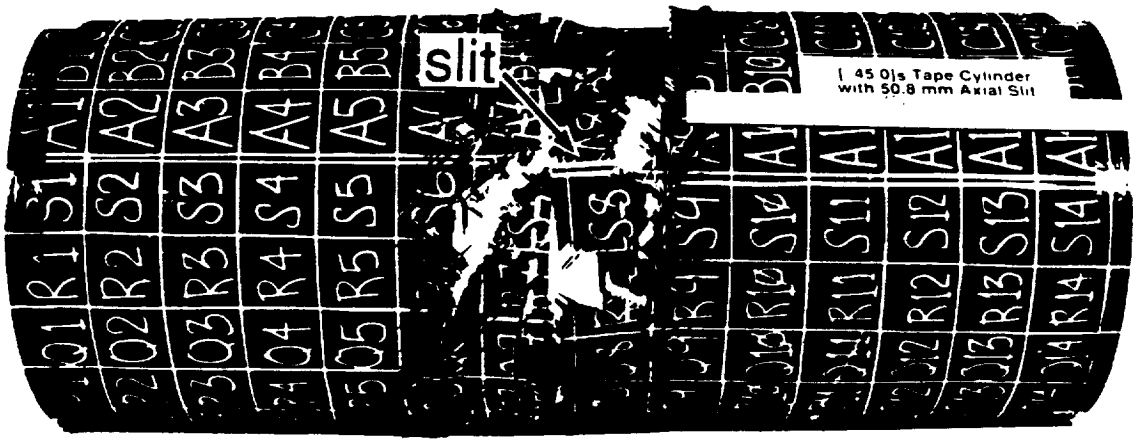

Figure 6.45 Post-test photograph of uniaxially loaded $[\pm 45/0]_s$ cylinder with 50.8 mm slit.

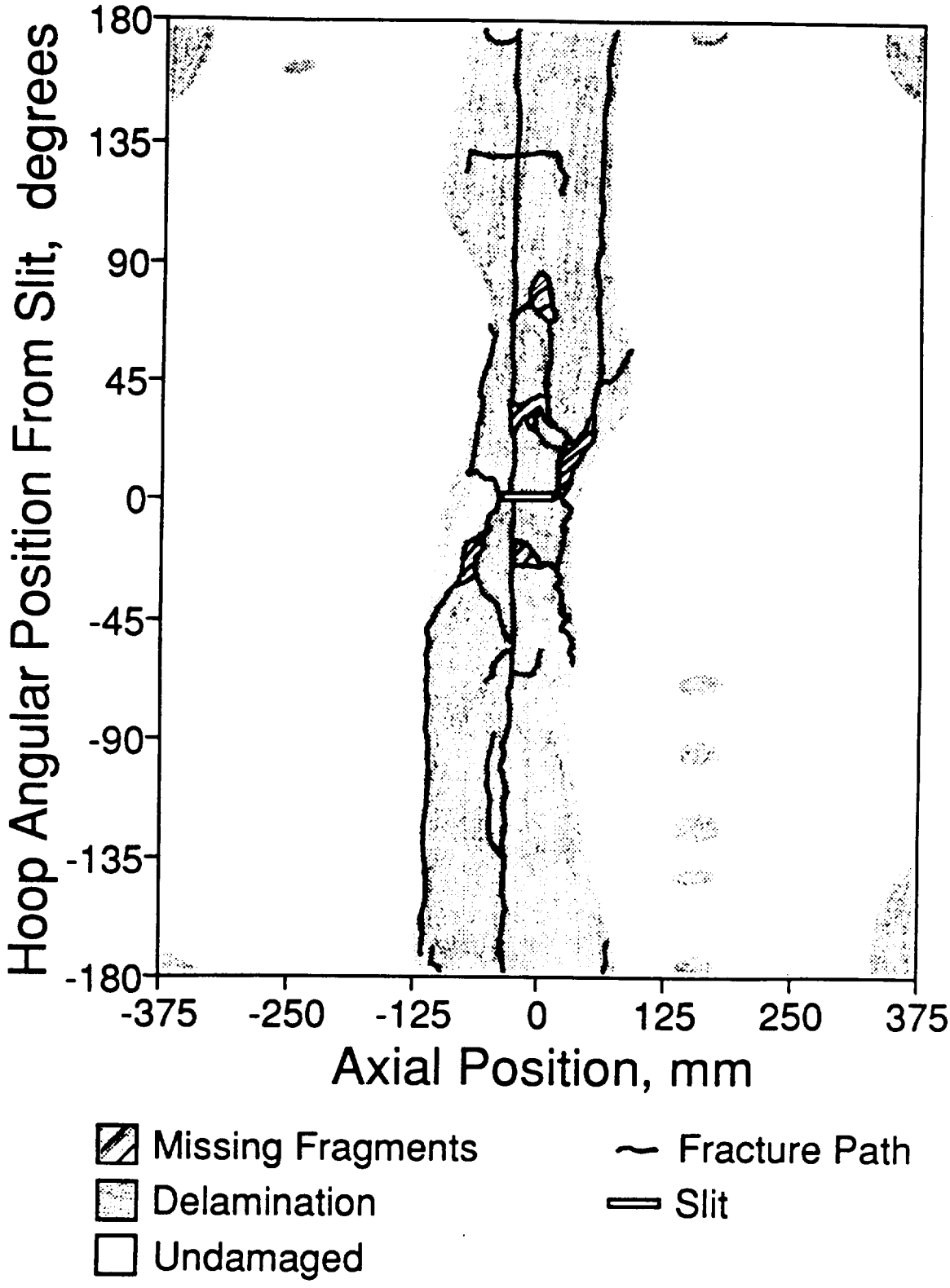

Figure 6.46 Schematic of damage in uniaxially loaded $[\pm 45/0]_s$ cylinder with 50.8 mm slit.

The damage visible near the slits in the uniaxially loaded $[\pm 45/0]_s$ cylinders is not similar to that observed in the $[\pm 45/0]_s$ coupons tested in the past investigation [31]. This cylinder damage is also different in some cases from that noted in the past investigation for biaxially loaded cylinders with the same layup and slit lengths. As discussed in the previous work, the initial damage modes of $[\pm 45/0]_s$ coupons and biaxially loaded cylinders also are not similar. In the coupons, a clean, primary fracture path through the -45° and 0° plies runs along the -45° direction from each slit tip to the edge of the specimen. Secondary delamination of the external +45° plies extends away from the primary fracture paths along the +45° direction. In contrast, two primary fracture paths usually emanate from the slit tips in the uniaxially and biaxially loaded cylinders. When only one path is present at each slit tip, these paths are oriented along the +45° or 90° direction as opposed to the -45° direction observed in the coupons. In the uniaxially and biaxially loaded cylinders with the 50.8 mm slit length, the primary fracture paths extending from the slit tips along essentially the ±45° directions are highly similar and the main difference between the damage states is that the uniaxially loaded cylinder experienced a higher degree of secondary damage. In contrast, both the primary fracture paths and the secondary damage differ for the cylinders with the 25.4 mm slit length tested under both loading conditions. While four fracture paths extend from the slit tips along angles between 0° and ±45° in the biaxially loaded cylinder with the 25.4 mm slit, only two +45° paths are clearly identifiable in the uniaxially loaded cylinder, as previously mentioned. The fracture paths are also more jagged in the biaxially loaded cylinder with the 25.4 mm slit. The initial damage states in the uniaxially and biaxially loaded cylinders with the 12.7 mm slit length cannot be compared since no

fragments were recovered from the slit region in the uniaxially loaded cylinder, as previously mentioned. However, it is interesting to note that the primary fracture path at each slit tip in the biaxially loaded cylinder with the 12.7 mm slit is oriented along essentially the 90° (axial) direction.

The damage states in the uniaxially loaded $[\pm 45/0]_s$ cylinders differ significantly from each other outside the immediate region of the slit. In the cylinder with the 50.8 mm slit, the fracture paths emanating from the slit tips along the ±45° directions turn to the circumferential direction and define the boundaries of a circumferential damage band, approximately 150 mm wide, that is centered axially on the slit. Some of the circumferential damage in this band is secondary damage caused by cylinder contact with test apparatus and most of the cylinder material outside of this band is undamaged. The circumferential extensions of the -45° paths are relatively clean compared to the angled portions of the paths and these extensions end approximately +65° in the circumferential direction on either side of the slit. The extensions of the +45° paths are characterized by secondary delamination and splitting of the +45° ply on the outside surface of the cylinder and a clean fracture through the other plies. The extensions of the +45° paths continue halfway around the circumference of the cylinder. In contrast, the paths emanating from the slit tips along the +45° direction in the cylinder with the 25.4 mm slit continue to extend along essentially the same direction all the way to the ends of the cylinder. The exact orientation of these paths becomes obscured at axial positions of approximately ±80 mm due to the large number of unidentified fragments along the primary direction of failure. The boundaries of the missing fragment region are oriented primarily along the 0° and 90° directions and are ragged due to secondary splitting and fiber breakage in the 0° and +45° plies. The

cylinder with the 12.7 mm slit differs from the others in that a large percentage of the material was damaged beyond recognition, especially in the region between the hoop angular positions of -45° and +45°. The boundaries of the main missing fragment region in this cylinder are oriented along essentially the axial direction and a high degree of secondary splitting in the 0° plies is apparent along these boundaries.

6.4 [±45/90]s Cylinders

Representative plots of the strain data for the $[\pm 45/90]_s$ cylinders are presented in Figures 6.47 and 6.48. Strain readings from the original and extra far-field hoop gages on the cylinder with the 12.7 mm slit are shown in Figure 6.47. Strain data from the axial 'far-field' gage on this cylinder are shown in Figure 6.48. The strain readings from the axial and hoop gages on the other two cylinders (not shown) show the same general trends. As can be seen in Figures 6.47 and 6.48, the pressure-strain curves for the axial and hoop gages are generally nonlinear. A small jump in the strain readings from Hoop Gage 1 and the axial gage on the cylinder with the 12.7 mm slit, and a change in the slope of the pressure-strain curves for these gages, are observed at a pressure of approximately 0.85 MPa. This pressure corresponds to a hoop strain value of 6200 μstrain and an axial strain of -2050 μstrain. It is possible that this strain behavior is indicative of damage near the slit in the cylinder with the 12.7 mm slit. The close agreement between the Hoop Gage 1 and Hoop Gage 2 strains for the cylinder with the 12.7 mm slit indicates that the original pair of far-field gages on this cylinder were placed far enough away from the slit. The Hoop Gage 1 strains for the cylinder with the 25.4 mm slit are slightly higher than the Hoop Gage 2 strains even though the correlation between these

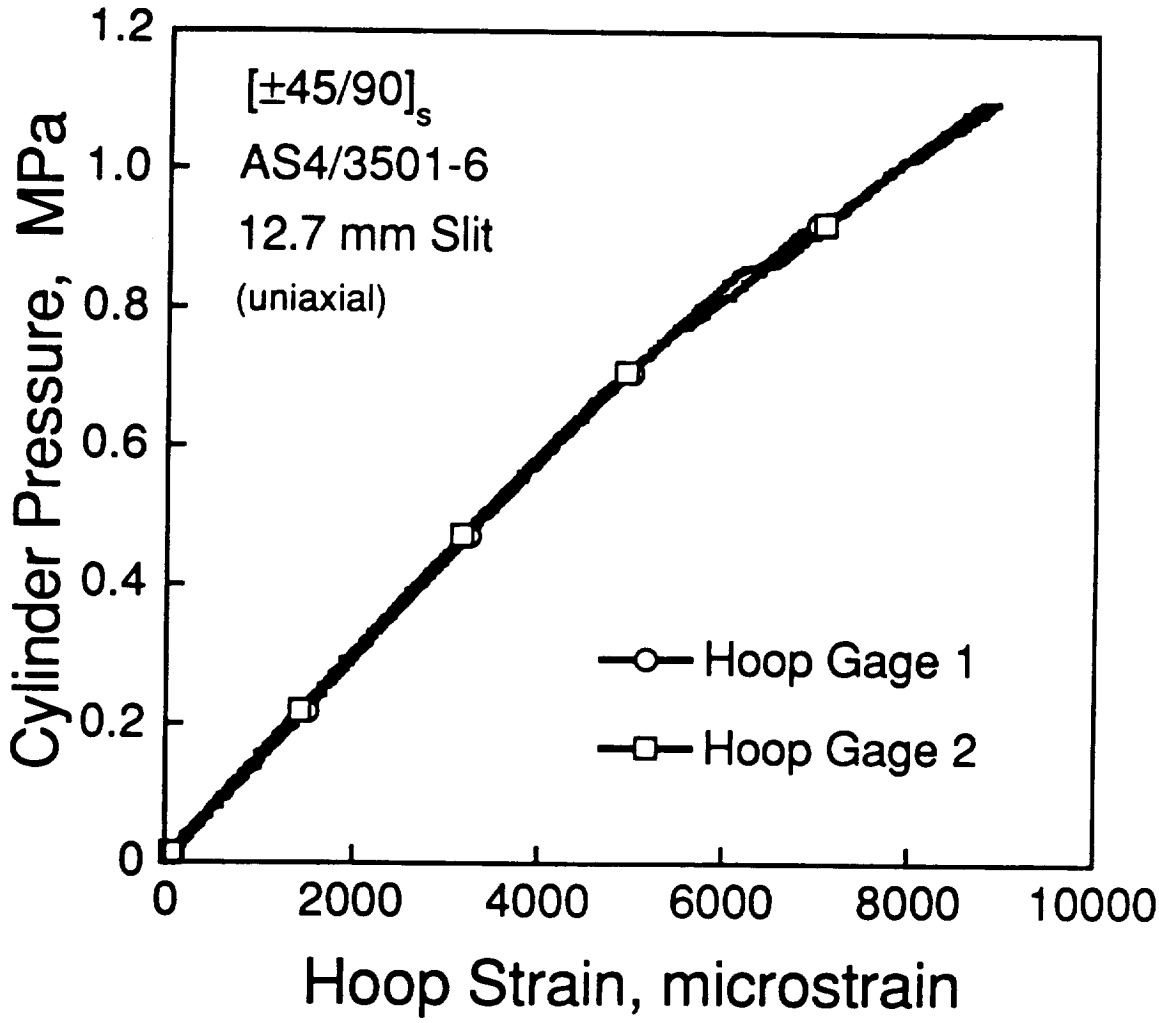

Figure 6.47 Cylinder pressure versus far-field circumferential strain from failure test of uniaxially loaded $[\pm 45/90]_s$ cylinder with 12.7 mm slit.

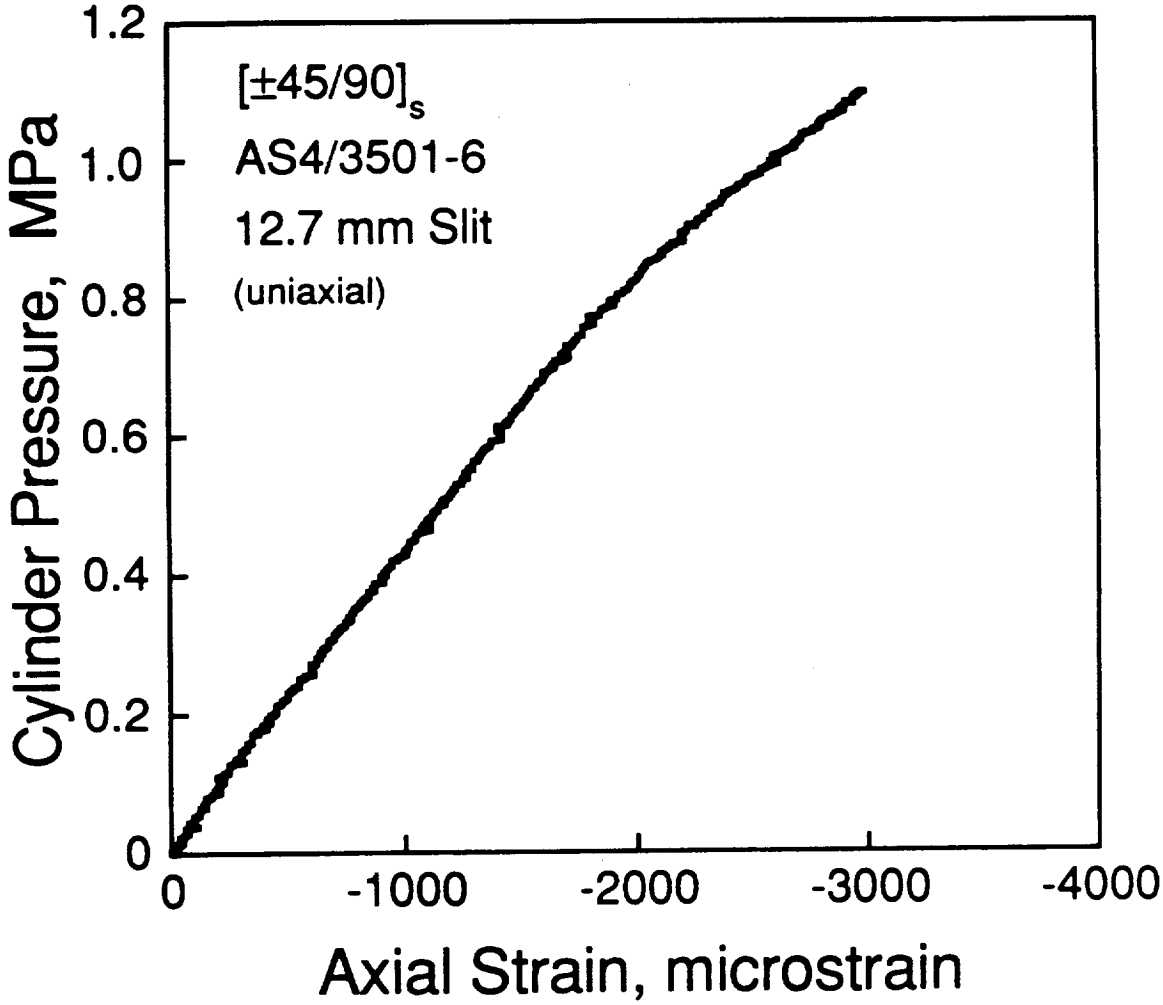

Figure 6.48 Cylinder pressure versus far-field longitudinal strain from failure test of uniaxially loaded $[\pm 45/90]_s$ cylinder with 12.7 mm slit.

strains is still fairly good. This suggests that the original pair of axial and hoop gages on the cylinder with the 25.4 mm slit are also located outside the region of influence of the slit.

The average initial slope of the hoop stress versus hoop strain data for the $[\pm 45/90]_s$ cylinders, or average experimental E_{11}, is 27.4 GPa with a coefficient of variation of 5.1%. The average experimental value of ν_{12} for these cylinders, determined using the strain data from the original pair of axial and hoop gages, is 0.33 with a coefficient of variation of 6.9%. These experimental values compare with the values of 26.7 GPa and 0.30 calculated for the $[\pm 45/90]_s$ layup using CLPT and the ply properties indicated in Table 3.1. However, the experimental hoop modulus of 29.2 GPa for the cylinder with the 50.8 mm slit is 9.4% higher than predicted which indicates that the pair of hoop and axial gages on this cylinder were located too close to the slit. The experimental modulus of 27.6 GPa for Hoop Gage 1 on the cylinder with the 12.7 mm slit is virtually identical to the modulus for Hoop Gage 2 and is only 3.2% higher than the calculated modulus. For the cylinder with the 25.4 mm slit, the experimental modulus of 25.3 GPa for Hoop Gage 1 is 5.3% lower than the calculated modulus and the experimental Poisson's ratio equals the calculated value. These results confirm that the original hoop and axial gages on the cylinders with the 12.7 and 25.4 mm slits are located in far-field regions.

Plots of the strain data from the slit tip hoop gages on the uniaxially loaded $[\pm 45/90]_s$ cylinders are shown in Figures 6.49, 6.50, and 6.51. The curves in these plots are nonlinear and initially smooth. However, a few discontinuities are also observed which become more pronounced with increasing slit length. The strains from Slit Tip Gage 2 on the cylinder with the 50.8 are the most irregular and behave similarly to the Slit Tip

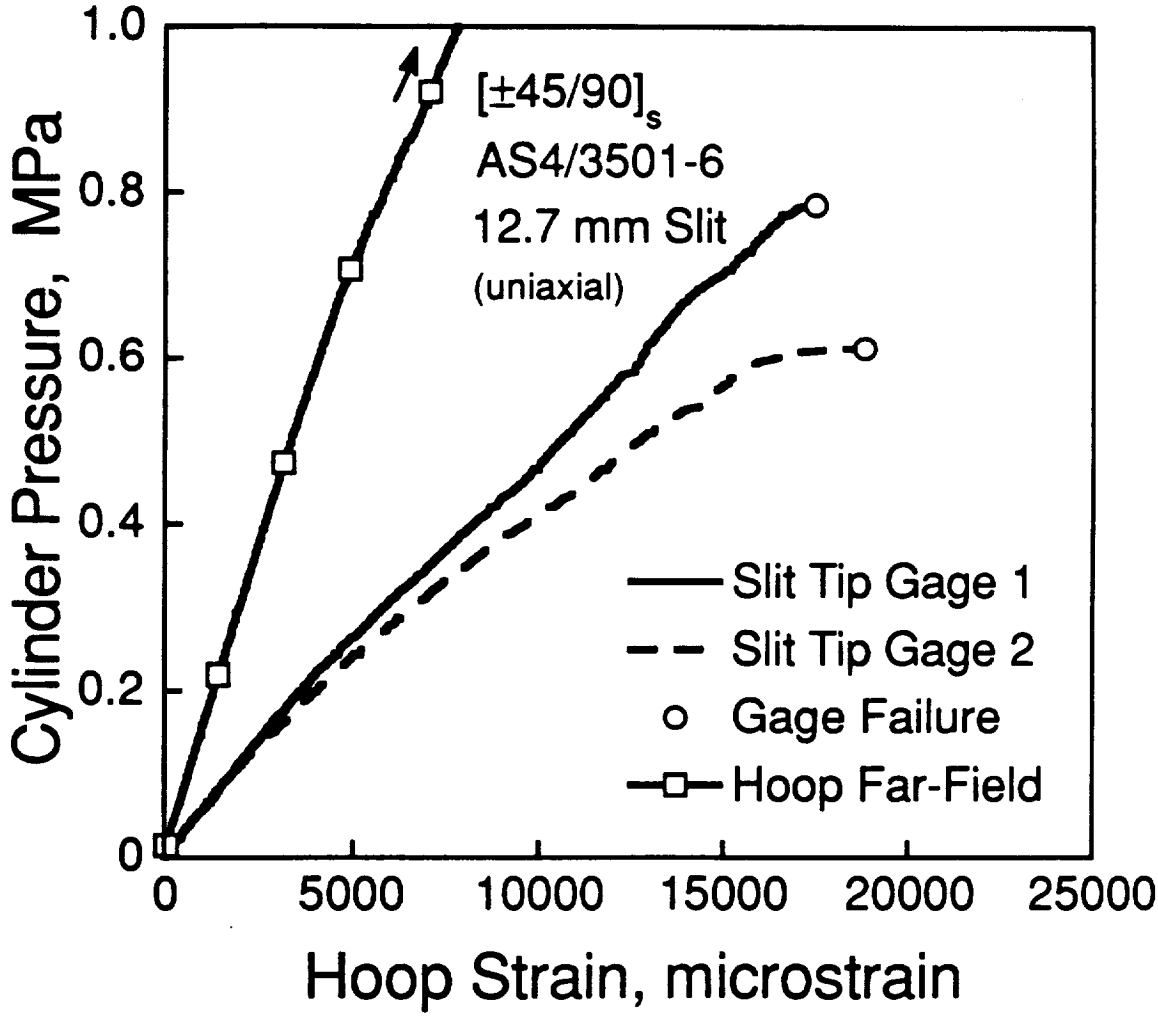

Figure 6.49 Cylinder pressure versus slit tip gage and far-field circumferential strains from failure test of uniaxially loaded $[\pm 45/90]_s$ cylinder with 12.7 mm slit.

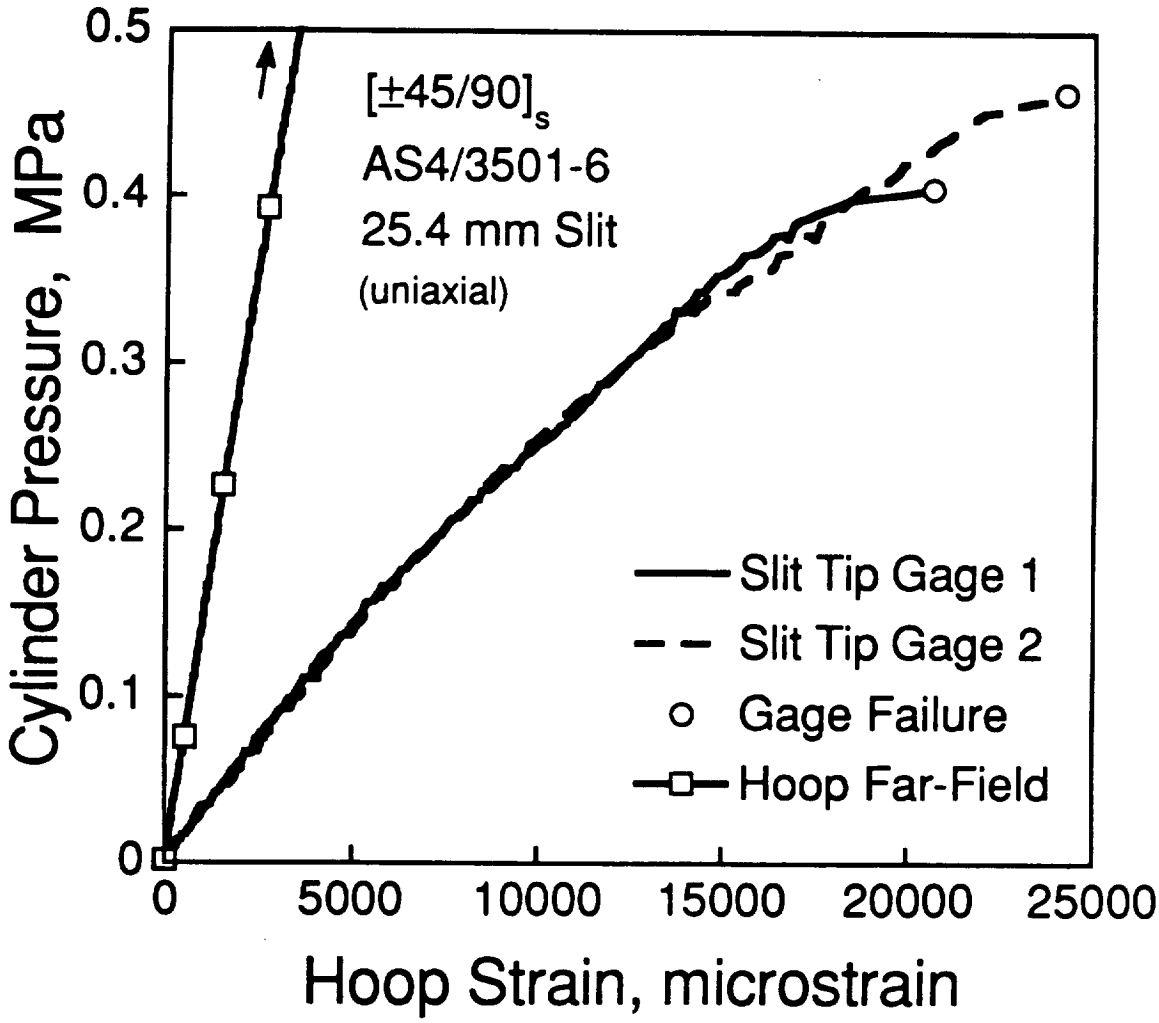

Figure 6.50 Cylinder pressure versus slit tip gage and far-field circumferential strains from failure test of uniaxially loaded $[\pm 45/90]_s$ cylinder with 25.4 mm slit.

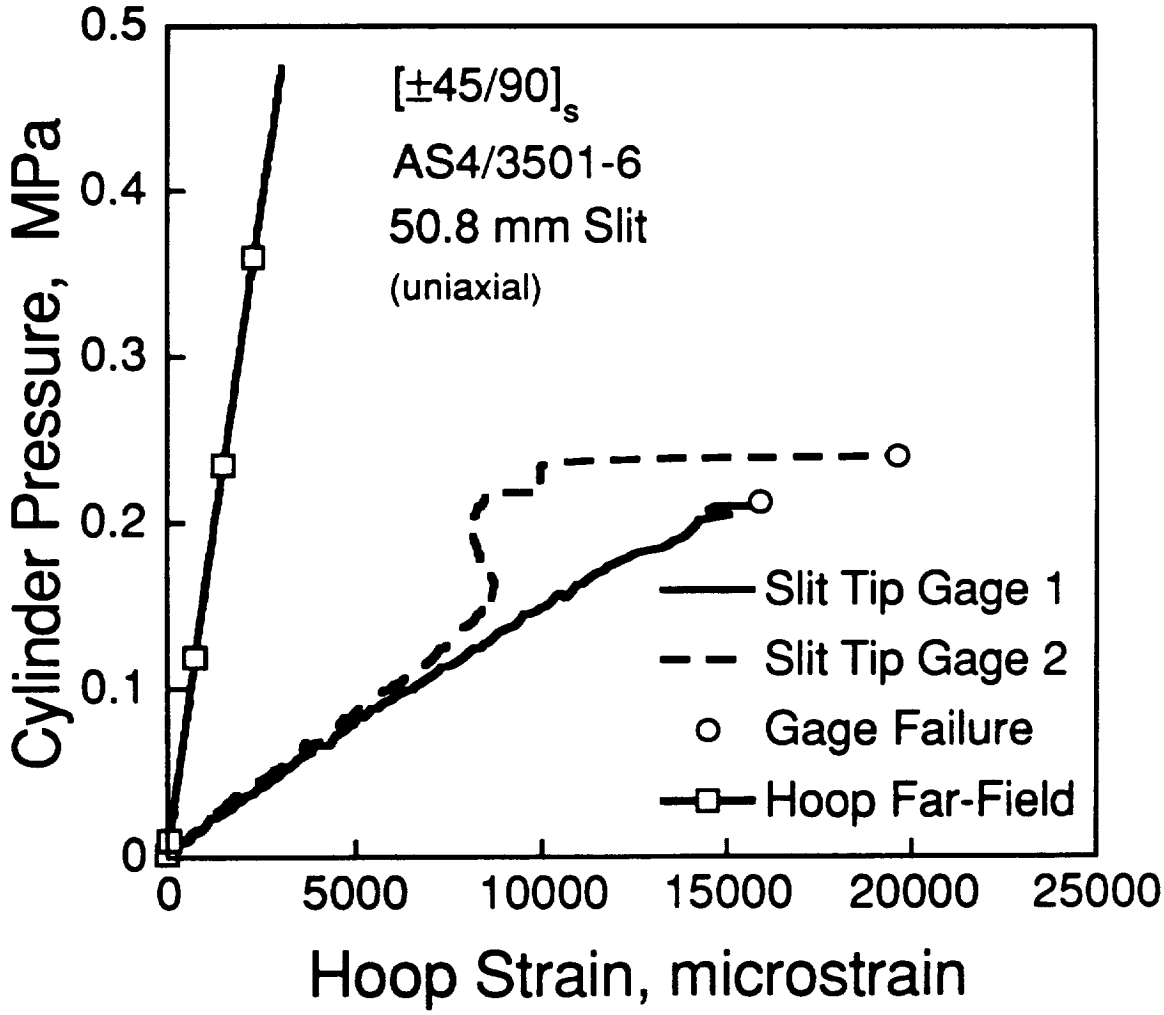

Figure 6.51 Cylinder pressure versus slit tip gage and far-field circumferential strains from failure test of uniaxially loaded $[\pm 45/90]_s$ cylinder with 50.8 mm slit.

Gage 1 strains for the $[\pm 45/0]_s$ cylinders. The pressure-strain curves for the Slit Tip Gage 1 strains on the cylinder with the 50.8 mm slit and both sets of slit tip strains for the other two cylinders are similar in that the slopes of these curves generally decrease, then increase, and then decrease again. These subtle slope changes result in a slight 'wave' in each curve. The pressure and strain values at the first discontinuity observed in the strain readings for each gage are shown in Table 6.11. As can be seen in this table, the pressure at which the first discontinuity is observed is comparable for both slit tip gages on each cylinder. However, the pressures are slightly higher for Slit Tip Gage 1. The only other trends observed in the values presented in Table 6.11 are that strains at the first discontinuity are highest for the cylinder with the 25.4 mm slit and pressures at the first discontinuity decrease with increasing slit length. Slit Tip Gages 1 and 2 on the cylinder with the 50.8 mm slit failed at pressures that are 45% and 51% of the failure pressure, respectively. The corresponding values for the cylinder with the 25.4 mm slit are 60% and 68%. On the cylinder with the 12.7 mm slit, Slit Tip Gage 1 failed at 72% of the failure pressure while the corresponding value for Slit Tip Gage 2 is 56%.

The failure pressures of the $[\pm 45/90]_s$ cylinders tested in the current investigation are indicated in Table 6.12 and are plotted versus slit length in Figure 6.52. The coupon correlation curve expressed in terms of equivalent pressures, the cylinder failure pressure prediction curve, and Ranniger's data for biaxially loaded cylinders [31] of this layup with slit lengths from 12.7 to 63.5 mm are also presented in this figure. The value of the composite fracture parameter, H_c, used for the coupon correlation curve is 422 $MPa*mm^{0.28}$ [31]. The failure pressures of the uniaxially loaded $[\pm 45/90]_s$ cylinders are lower than those of biaxially loaded cylinders with the same

Table 6.11 Hoop Strain and Cylinder Pressure at First Discontinuity Observed in Slit Tip Strain Gage Data for Uniaxially Loaded $[\pm 45/90]_s$ Cylinders

Slit Length [mm]	Gage	Pressure [MPa]	Slit Tip Hoop Strain [microstrain]
12.7	1	0.58	12300
	2	0.54	14063
25.4	1	0.40	18425
	2	0.34	14688
50.8	1	0.18	12588
	2	0.16	8763

Table 6.12 Failure Pressures of Uniaxially Loaded $[\pm 45/90]_s$ Cylinders

Slit Length, mm	Failure Pressure, MPa
12.7	1.10
25.4	0.68
50.8	0.47

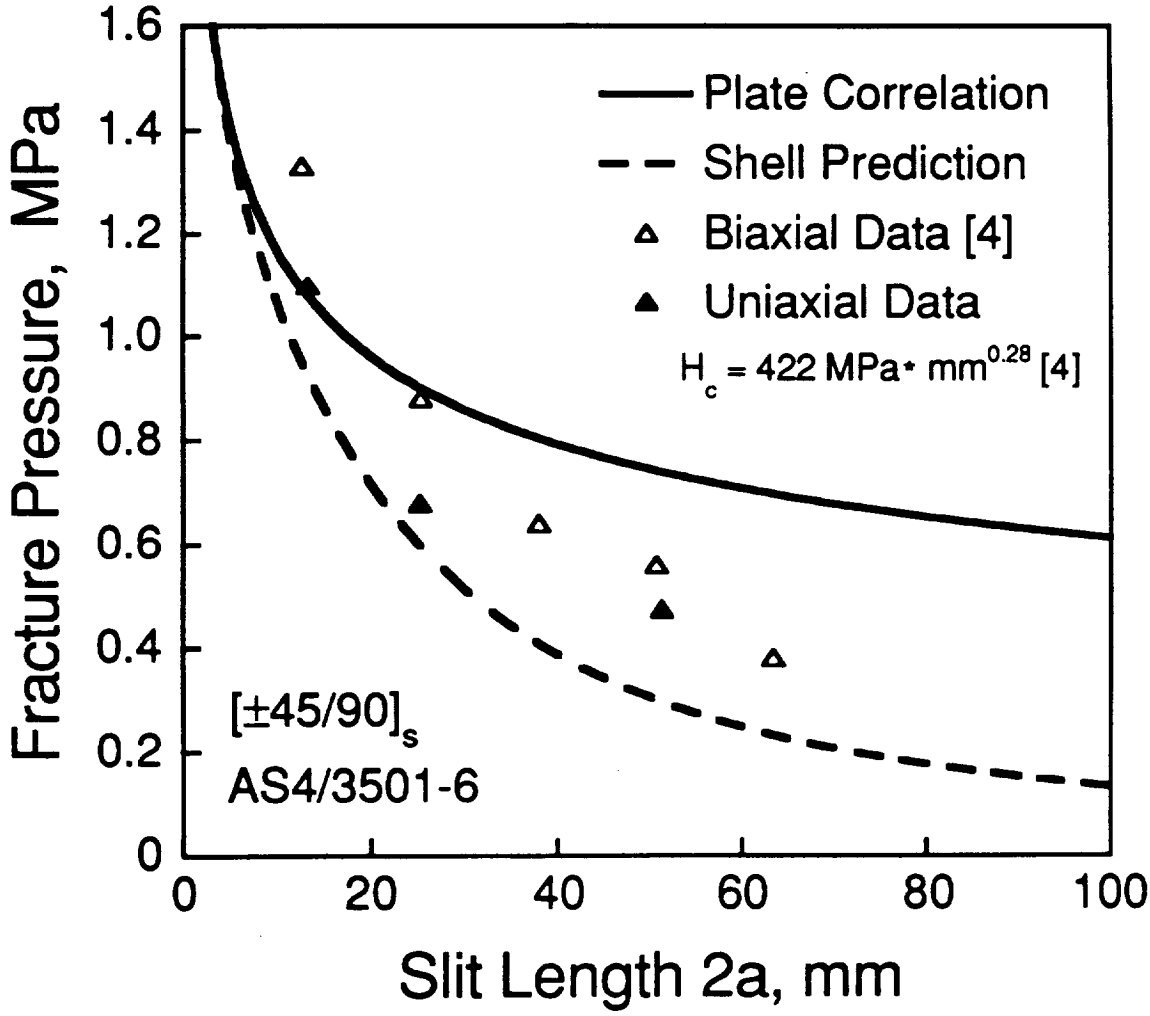

Figure 6.52 Experimental and predicted failure pressures for uniaxially loaded $[\pm 45/90]_s$ tape cylinders.

slit lengths by 15% to 23% which is a fairly consistent decrease. However, the failure pressures of all three cylinders are still well above the predicted values (by 14% to 61%). The maximum percent decrease in failure pressure is observed for the cylinder with the 25.4 mm slit and this failure pressure also exceeds the predicted value by the lowest percentage. The failure pressure of the cylinder with the 12.7 mm slit is slightly higher than, but is virtually identical to, the equivalent coupon failure pressure.

Post-test photographs and damage schematics for the uniaxially loaded $[\pm 45/90]_s$ cylinders are shown in Figures 6.53 through 6.58. As can be seen in these figures, the initial damage states are generally similar in the cylinders with the 12.7, 25.4, and 50.8 mm slits. In all three cylinders, a clean primary fracture path extends away from each slit tip along the axial direction. However, these axial paths are not always well defined. Only 8 mm of the primary path is visible at the left slit tip in the cylinder with the 50.8 mm slit since fragments to the left as well as below the slit were not recovered. In the cylinder with the 12.7 mm slit, only 13 mm of the path on the left end of the slit and approximately one millimeter of the path on the right end of the slit are visible due to unretrieved fragments. However, an axial path does extend 50 mm into the nearest fragment to the left of the 12.7 mm slit at a hoop angular position of 0° which suggests that the axial paths do extend farther from this slit than can be determined from the one recovered slit fragment. Sharp, secondary circumferential damage paths from the center rod support plate intersect the slit, or the 90° fracture path slightly to the left of the left slit tip, in all three cylinders. Some secondary delamination and splitting of the +45° plies and delamination between the -45° and 90° plies is present near the slits.

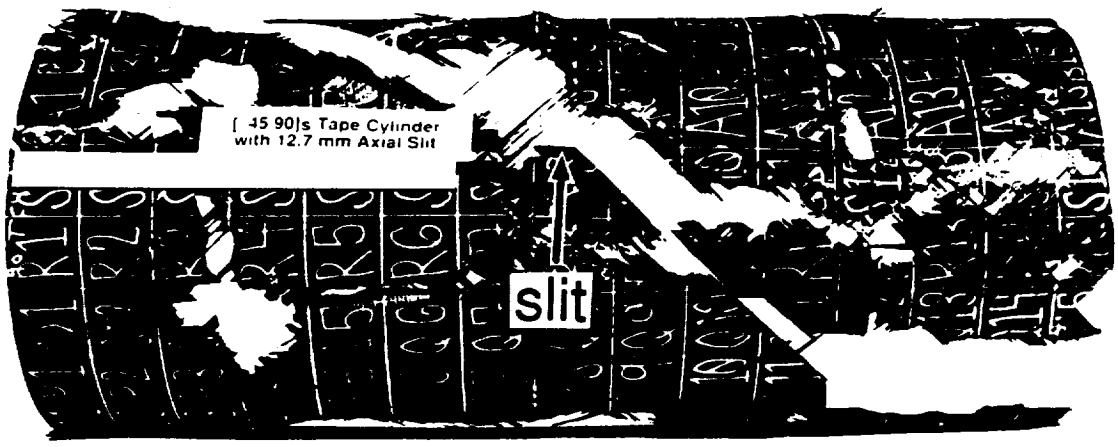

Figure 6.53 Post-test photograph of uniaxially loaded $[\pm 45/90]_s$ cylinder with 12.7 mm slit.

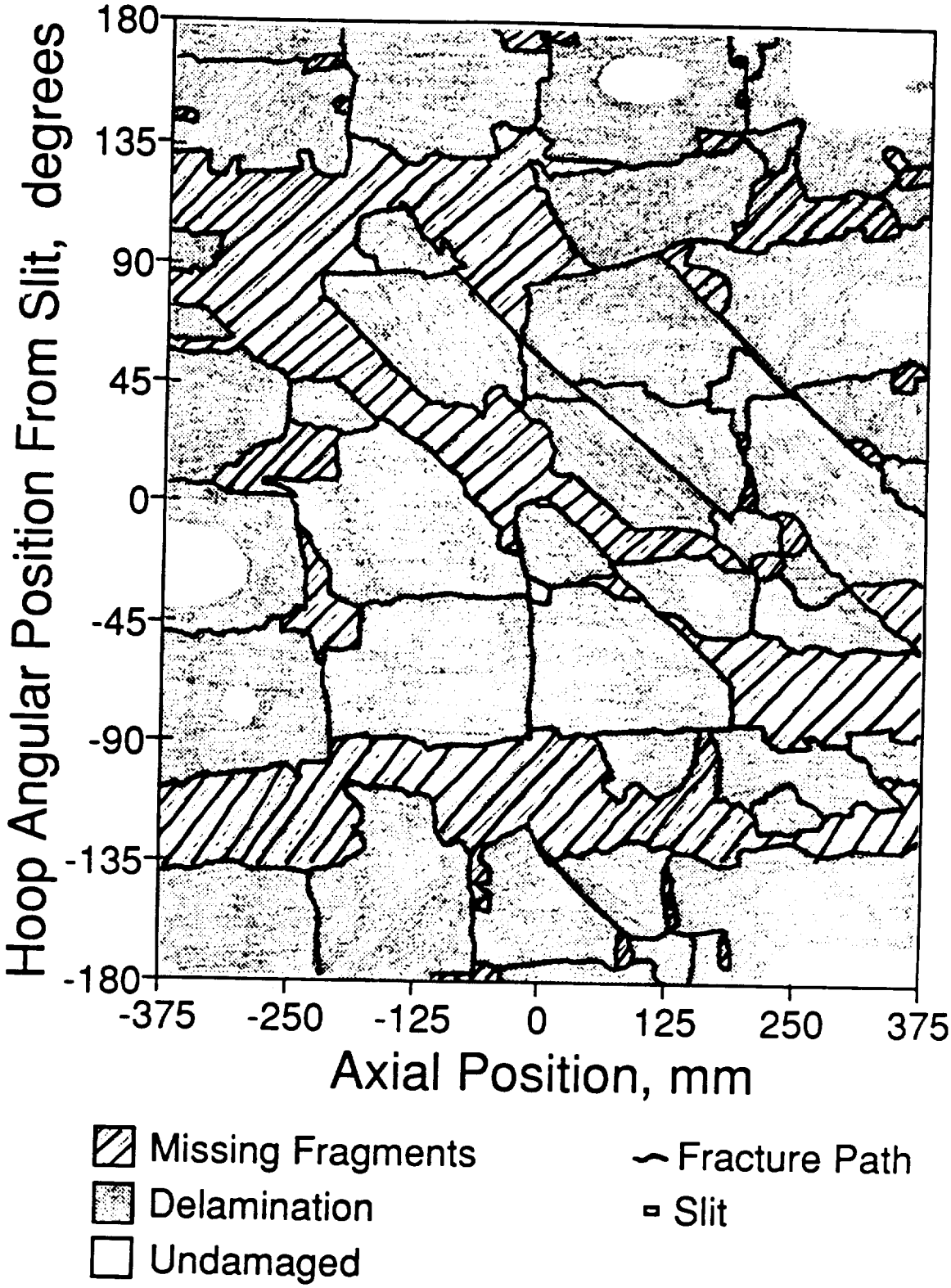

Figure 6.54 Schematic of damage in uniaxially loaded $[\pm 45/90]_s$ cylinder with 12.7 mm slit.

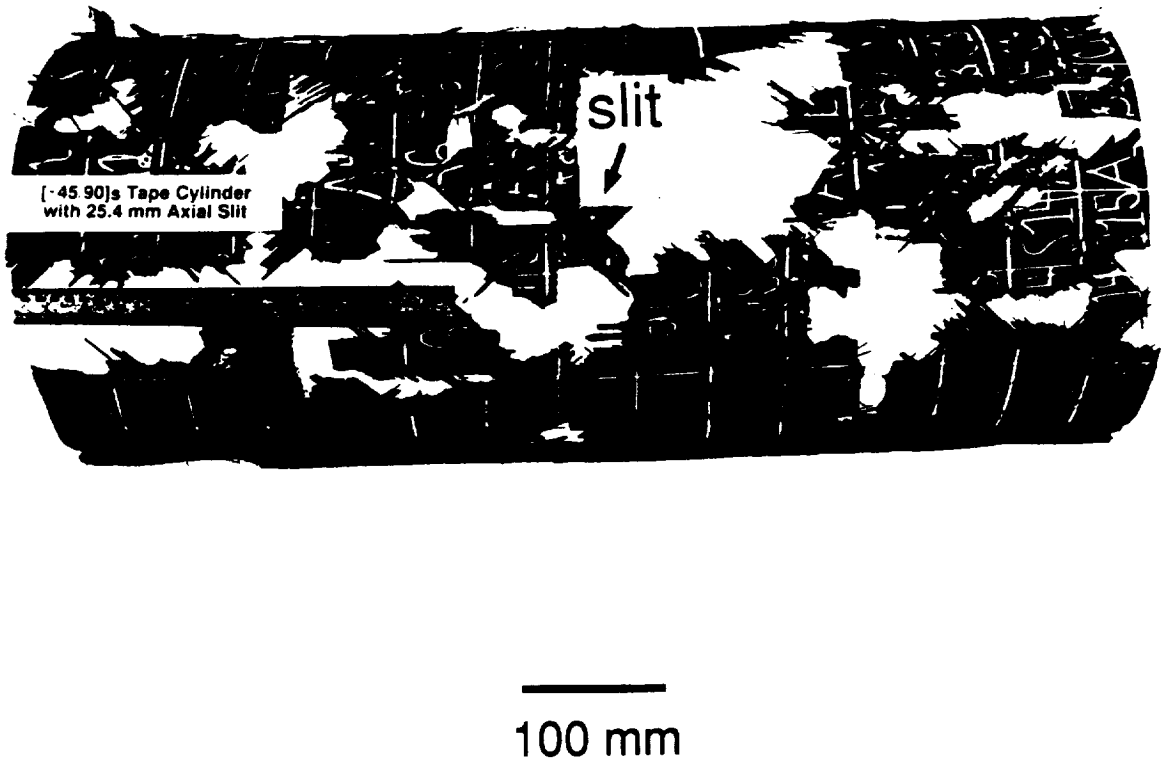

Figure 6.55 Post-test photograph of uniaxially loaded $[\pm 45/90]_s$ cylinder with 25.4 mm slit.

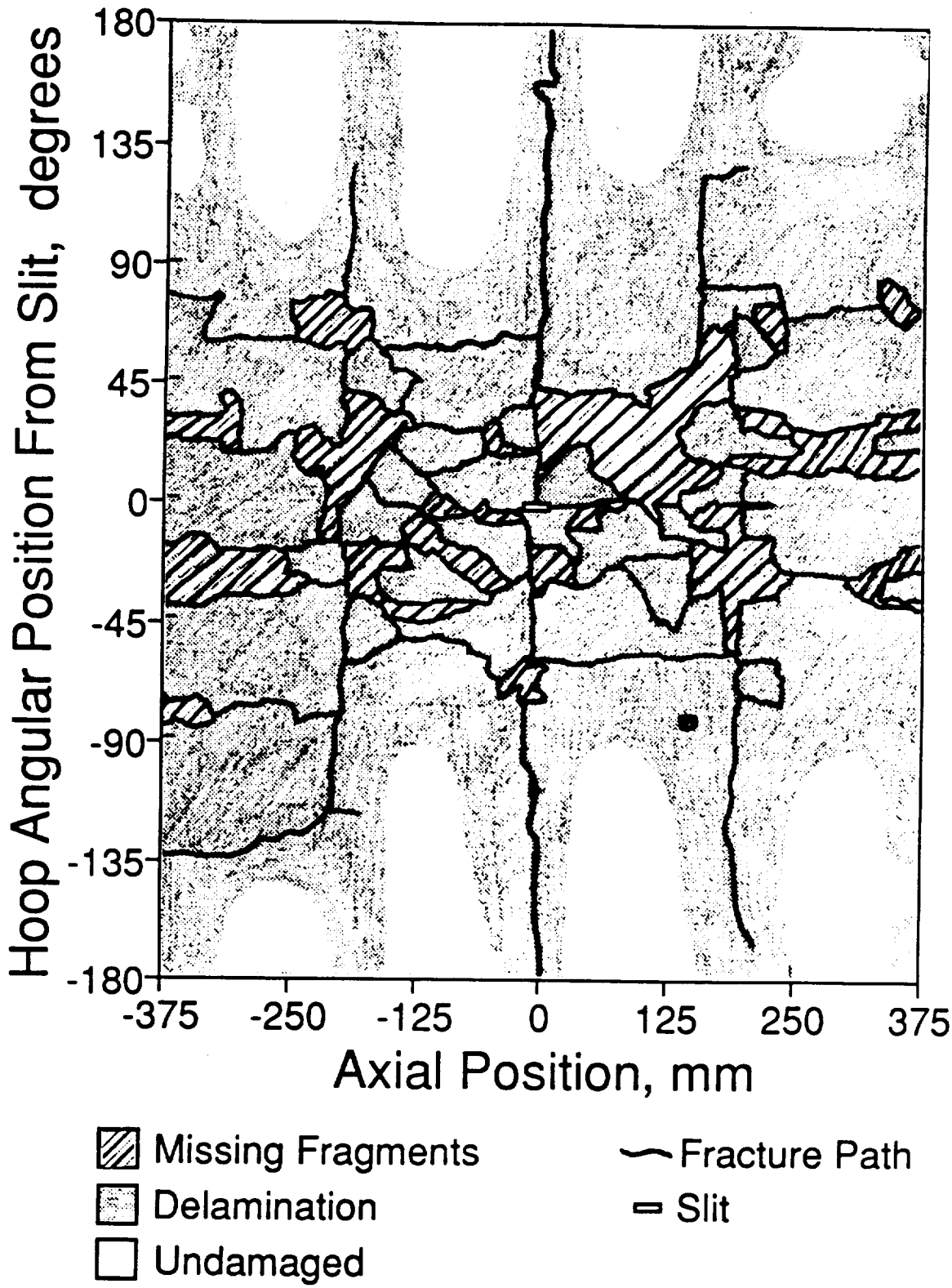

Figure 6.56 Schematic of damage in uniaxially loaded $[\pm 45/90]_s$ cylinder with 25.4 mm slit.

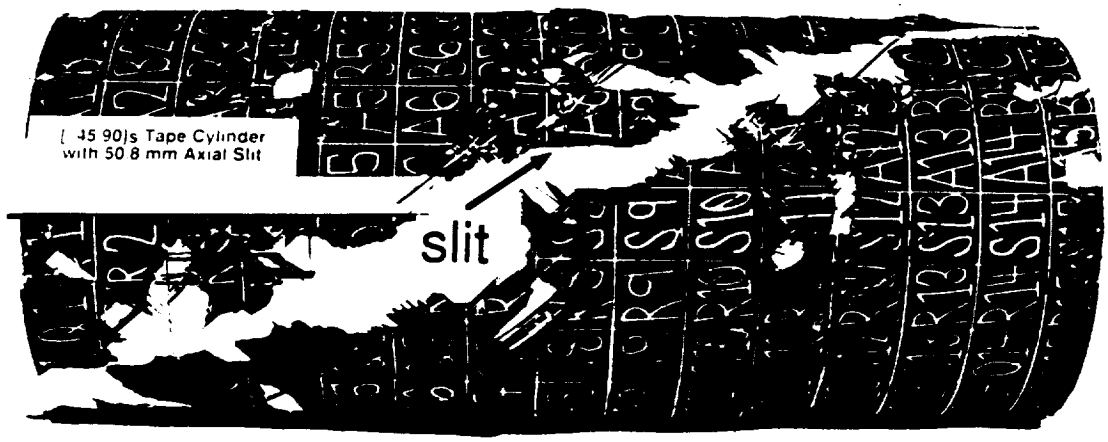

Figure 6.57 Post-test photograph of uniaxially loaded $[\pm 45/90]_s$ cylinder with 50.8 mm slit.

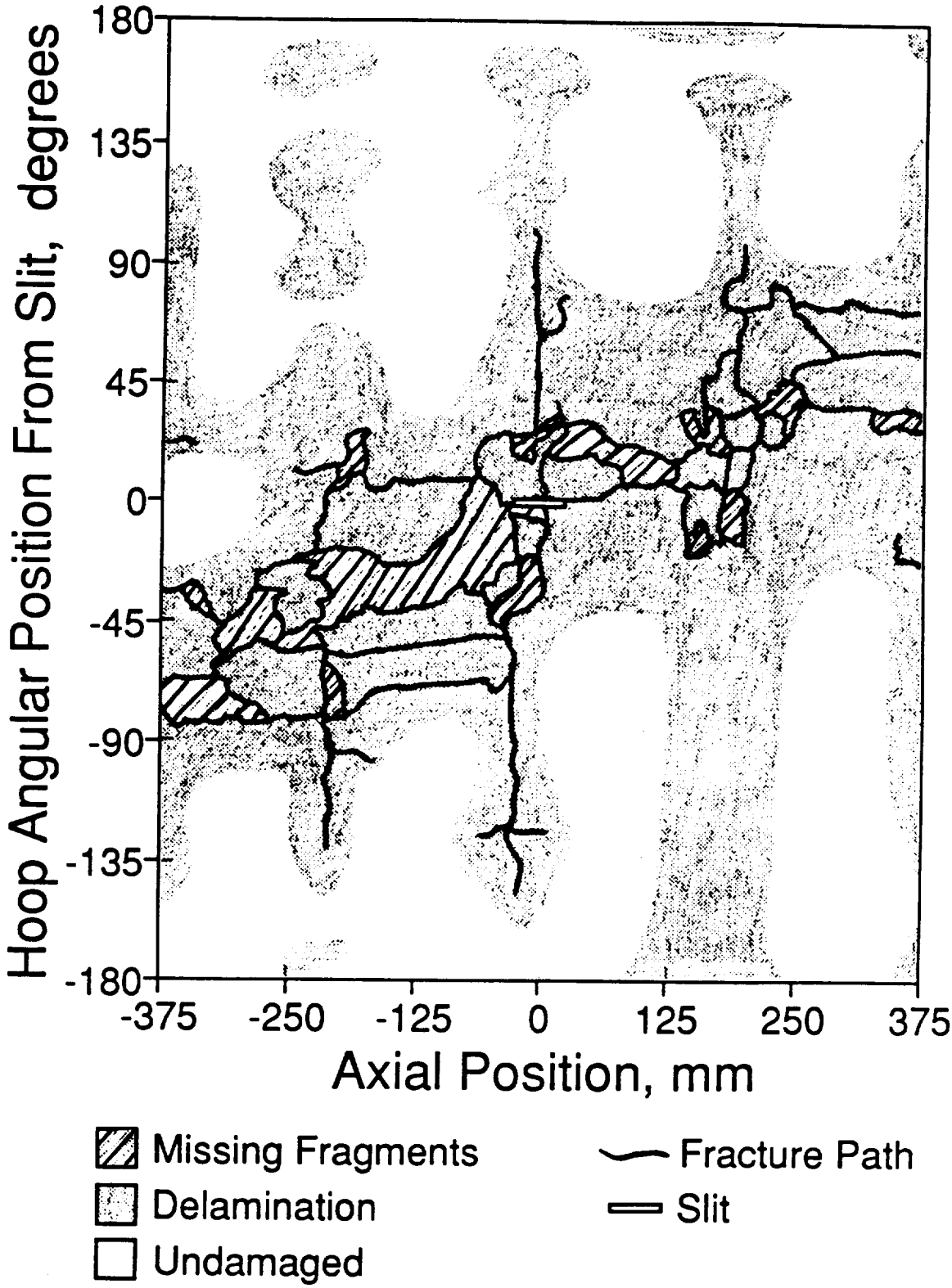

Figure 6.58 Schematic of damage in uniaxially loaded $[\pm 45/90]_s$ cylinder with 50.8 mm slit.

The damage near the slits in the uniaxially loaded $[\pm 45/90]_s$ cylinders is similar to that observed in the biaxially loaded cylinders from the past investigation with the same layup and slit lengths [31]. However, this damage is quite different from that present in the $[\pm 45/90]_s$ coupons tested in the same investigation. In the coupons, a clean, primary fracture path through the -45° and 90° plies runs from each slit tip to the edge of the specimen along the -45° direction. Secondary delamination of the external +45° plies extends all the way from the primary fracture to the edge of the specimen along the +45° direction. In contrast, the primary fracture paths near the slits in the uniaxially and biaxially loaded cylinders are oriented in the 90° (axial) direction and delamination of the +45° plies near these fracture paths is less extensive than it is in the coupons.

The damage states in the uniaxially loaded $[\pm 45/90]_s$ cylinders are less similar to each other in the regions away from slits. The axial fracture paths emanating from the slit tips in the cylinder with the 50.8 mm slit turn and progress out toward the ends of the cylinder along an angle of approximately +65°. The angled extensions of the axial fracture paths in this cylinder are jagged and not well defined due to the high degree of secondary fragmentation and the numerous unidentified pieces along the primary direction of failure. Most of the fracture surfaces in the cylinder with the 50.8 mm slit are ragged from delamination, splitting, and fiber breakage of the ±45° and 90° plies. The axial fracture paths extending from the slit tips in the cylinder with the 25.4 mm slit also turn toward the positive angular direction (along an angle of approximately +45°). However, these paths only reach hoop angular positions of approximately ±15° before they turn back to the axial direction and progress all the way to the ends of the cylinder. The cylinder with the 25.4 mm slit experienced

more secondary fragmentation than the cylinder with the 50.8 mm slit. However, the fracture surfaces in both cylinders are qualitatively similar. The primary direction of failure away from the slit region in the cylinder with the 12.7 mm slit is along the -45° fibers. This direction is opposite in sign to the directions observed in the other two $[\pm 45/90]_s$ cylinders. A band of missing fragments with a varying width extends along the direction of primary fracture to the ends of the cylinder with the 12.7 mm slit and this band is bordered by several sharp, straight -45° fracture paths. One such path intersects the previously described 90° path extending from the right slit tip approximately 1 mm from this slit tip. Several of the secondary failure paths are also sharp, straight, and oriented along the -45° direction. As in the other two $[\pm 45/90]_s$ cylinders, many of the fracture paths, with the exception of the sharp -45° fractures mentioned above, are ragged due to delamination and splitting of the ±45° plies. Some minor secondary splitting of the +45° plies is also visible along the sharp -45° fractures.

CHAPTER 7

Discussion

The basic objectives of this research are to better understand the failure processes in tape cylinders with axial slits and to further explore the limitations of the current failure prediction methodology for these cylinders. In this chapter, the results presented in Chapter 6 are summarized and discussed in terms of these objectives. Specifically, the effects of axial stress, subcritical damage, and structural anisotropy, as well as the interactions of these factors, are addressed. An assessment of the apparatus used to test the uniaxially loaded cylinders, which is described in detail in Chapter 5, is also presented in this chapter.

7.1 Assessment of AALD

The uniaxial test apparatus, or AALD, has been shown in this investigation to be a valid means to test pressurized cylinders to failure in hoop loading only. As discussed in Chapter 5, far-field strains from the four AALD verification tests of the unnotched $[90/0/\pm45]_s$ cylinder and the failure test of the same cylinder with a 50.8 mm slit were used to calculate experimental hoop moduli and Poisson's ratios assuming that only hoop stress was applied to the cylinder. The experimental stresses agree with the predicted values and the experimental laminate properties compare well with calculated values from Classical Laminated Plate Theory which confirms that the AALD provides the desired hoop-loading-only condition in the cylinders. Comparisons of far-field, edge zone, and boundary zone cylinder strains and longitudinal rod strains from the various verification

tests indicate that highly repeatable results were achieved. Repeatability of the strain results was confirmed even when the cylinder was removed from the apparatus between tests and the axial slit location line was located at different angular orientations with respect to the continuously threaded rods.

In this investigation, the AALD operated properly for cylinders with a length of 750 mm and failure pressures up to 2.03 MPa. While the device is expected to perform as well for cylinders with shorter lengths, no tests have been conducted which support this claim. The strain results from the verification tests confirm the presence of boundary zones, or regions of high stress and strain gradients, which are located in the areas within approximately 75 mm of the ends of the cylinder. Thus, cylinder lengths must be chosen carefully to ensure that these boundary zones are outside the region of influence of the slit. No damage to the AALD with the rod support plates was observed at the maximum test failure pressure of 2.03 MPa. However, it is not known how much the failure pressure may be increased without causing permanent damage to the device. Such permanent damage, in the form of yielding in most of the continuously threaded rods, was observed in the early version of the AALD without the rod support plates at a relatively low failure pressure of only 0.57 MPa.

Secondary damage from the rods and rod support plates in the AALD is distinctly visible on all of the uniaxially loaded cylinders. Thus, while the initial failure mechanisms are not affected, it is clear that the uniaxial test apparatus interferes with the propagating damage in a cylinder. Since the manner in which the test apparatus modifies and intensifies the propagating damage is not known, the use of the device to study damage propagation and arrest in uniaxially loaded cylinders is currently not

recommended. However, it is possible that the effects of the test apparatus on the propagating damage could be minimized by testing shorter cylinders since the use of the rod support plates might no longer be necessary. The test apparatus may also affect propagating damage less, or the effects might be easier to isolate, in fabric cylinders which usually have only a few well defined fracture paths and remain relatively intact compared to tape cylinders. The influence of the test apparatus on the propagating damage is expected to be less for tape cylinders with longer slit lengths which generally fail at lower failure pressures and experience relatively little damage as a result of the failures [4].

7.2 Factors in Failure of Pressurized Cylinders

From the results of the past and current investigations, axial stress, subcritical damage, and structural anisotropy have been identified as factors which may significantly influence the failure of pressurized tape cylinders with axial slits. The effects of these factors are discussed separately in the following sections. However, it should be noted that there are possibly varying degrees of interaction amongst these effects. It is also important to mention that since axial stress, subcritical damage, and structural anisotropy are not taken into account in the current failure prediction methodology, the manner in which these factors affect tape cylinder failure may limit the use of the current predictive methodology for tape cylinders of general configuration.

7.2.1 Importance of Axial Load

The primary means of assessing the influence of axial stress on the failure of tape cylinders is to compare the failure pressures and initial

failure modes of cylinders loaded uniaxially to the failure pressures and initial failure modes of biaxially loaded cylinders with the same layups and slit lengths from the past investigation. Additionally, the experimental failure pressures for the uniaxially and biaxially loaded cylinders are compared to values predicted from the methodology using coupon failure data from the past and, in the case of the $[90/0/\pm45]_s$ layup, the current works. The aforementioned failure pressure comparisons are complicated by the fact that the value of the composite fracture parameter, H_c, for the $[90/0/\pm45]_s$ coupons tested in the current investigation is 10% lower than that obtained in the past work [4]. This difference in the value of H_c for coupons with the same layup likely encompasses general material variability. However, the difference should be kept in mind in evaluating the influence of the axial stress in the $[90/0/\pm45]_s$, $[\pm45/0]_s$, and $[\pm45/90]_s$ cylinders as well as the applicability of the methodology to the uniaxially loaded cylinders with these layups.

The failure pressures of the $[90/0/\pm45]_s$, $[\pm45/0]_s$, and $[\pm45/90]_s$ cylinders are consistently lower when the cylinders are loaded uniaxially. A summary of these differences is shown in Table 7.1 as compared to the biaxial case. The relative effects of the removal of the axial stress differ with layup, and possibly with slit length. These effects do not, however, generally depend on the degree of structural coupling in terms of the ratios of D_{16} and D_{26} to D_{11} and the absolute magnitudes of D_{16} and D_{26}. The failure pressures of the $[\pm45/90]_s$ cylinders are affected the least (15% to 23% below the biaxial values) by the removal of the axial stress. This layup also has the highest ratios of D_{16} and D_{26} to D_{11}. Even accounting for basic material variability, the biaxial failure pressures still clearly exceed the uniaxial values. The same is true for the $[90/0/\pm45]_s$ cylinders where

Table 7.1 Absolute and Percent[a] Differences in Failure Pressure between Uniaxially and Biaxially Loaded Tape Cylinders[b]

Slit Size, mm	Laminate		
	$[\pm 45/90]_s$	$[\pm 45/0]_s$	$[90/0/\pm 45]_s$
12.7	-0.23[c] (-18%)[a]	-0.70 (-33%)	-0.34[d] (-16%)[d]
25.4	-0.20 (-23%)	-0.59 (-41%)	-0.26 (-20%)
50.8	-0.09 (-15%)	-0.10 (-15%)	-0.22 (-27%)

[a] Numbers in parentheses are percent differences

[b] Differences referenced to biaxial failure pressures

[c] Units are MPa

[d] Average difference from three biaxial failure pressures

removal of the axial stress generally results in comparable, but slightly greater, decreases in the failure pressures (16% to 27% below the biaxial values). This layup has the lowest ratios of D_{16} and D_{26} to D_{11} which are approximately one-fifth of the ratios for the structurally anisotropic layups. It should be noted that while the failure pressure of the uniaxially loaded $[90/0/\pm45]_s$ cylinder with the 12.7 mm slit is 16% below the average value from three biaxial tests, the difference ranges from 27% below the biaxial failure pressure from the past investigation [4] to only 6% and 13% below the corresponding biaxial failure pressures from the current investigation. This wide range in the failure pressure differences may be related to differences in the role of subcritical damage in the failure of the three biaxially loaded cylinders with the 12.7 mm slits, as is discussed in Section 7.2.2. The lowest percent decrease in failure pressure for the $[90/0/\pm45]_s$ cylinders is observed at the 12.7 mm slit size (between the uniaxial and biaxial values from the current investigation) and the greatest decrease is observed at the 50.8 mm slit size. This is quite different than the trend observed in the failure pressures for the $[\pm45/90]_s$ cylinders, which have the lowest percent decrease in failure pressure at the 50.8 mm slit size and the greatest decrease at the 25.4 mm slit size.

The greatest variation in the percent differences between the failure pressures for the uniaxially and biaxially loaded cylinders is observed for the $[\pm45/0]_s$ cylinders (from 15% to 41%). This layup has the same D_{16} and D_{26} terms as the $[\pm45/90]_s$ layup but the ratios of D_{16} and D_{26} to D_{11} are 10% lower for the $[\pm45/0]_s$ layup. The decrease in failure pressure is largest at the 25.4 mm slit size and smallest at the 50.8 mm slit size, which is the same trend observed for the $[\pm45/90]_s$ layup. The uniaxially loaded $[\pm45/0]_s$

and $[\pm 45/90]_s$ cylinders with the 50.8 mm slit length also experienced approximately the same percent decrease in failure pressure.

The relative effects of the removal of the axial stress on the failure pressures do not correlate with the magnitudes of the ratios of D_{16} and D_{26} to D_{11}. Furthermore, different effects are observed for the two structurally anisotropic layups which have the same values for the bending-twisting coupling terms (D_{16} and D_{26}). Thus, although these observations suggest it is unlikely that the observed effects are only a result of the influence that the axial stress has on the stress state near the slit through the structural coupling mechanisms, the results do indicate that structural coupling is a possible important factor in the role of the axial stress, as discussed more in Section 7.2.3. This is shown in the trends of the percent differences in failure pressure between the uniaxially and biaxially loaded cases. It is observed that the structurally anisotropic layups which have a similar degree of structural coupling have the lowest percent difference in failure pressure at the longest slit length (50.8 mm). In contrast, the quasi-isotropic $[90/0/\pm 45]_s$ layup which has a much lower degree of structural coupling compared to the structurally anisotropic layups has the highest percent difference in failure pressure at this slit length. Finite element analyses should thus be conducted in order to determine how the stress state surrounding the slit tips in quasi-isotropic and structurally anisotropic cylinders is modified by the addition of axial stress in order to better understand the potential contribution of this effect.

As discussed previously, discontinuities in the slit tip strain data for the uniaxially loaded cylinders indicate that damage occurred near the slit tips prior to the ultimate failure of these cylinders. The role of such subcritical damage in the failure of tape cylinders is discussed more in

Section 7.2.2. However, what is important to note here in terms of understanding the importance of the axial stress is that the relative influence of the axial stress on the cylinder failure pressures may depend on the types and quantities of slit tip damage, as well as on the degree of structural coupling. The axial stress may also play a role in the initiation and subsequent development of the slit tip damage and, thus, this damage may not be the same in cylinders that differ only in loading condition. In some laminates, the contributions of structural anisotropy and subcritical damage effects may be functions of slit length which would explain why there is a greater influence of the axial stress at some slit lengths rather than at others. If the loading condition effects on the failure pressures of tape cylinders are only related to structural anisotropy and subcritical damage, quasi-isotropic fabric cylinders, which have zero D_{16} and D_{26} terms and are less susceptible to subcritical damage (i.e. matrix cracking/splitting and subsequent delamination) due to the woven nature of the fibers, should have essentially the same failure pressures whether they are loaded uniaxially or biaxially. In order to test this hypothesis, fabric cylinders with the same layup, slit lengths, and material system as in the past work [3,29] should be tested to failure in uniaxial loading and their failure pressures compared to the biaxial values. Slit tip strain gages should be used in these tests to see if subcritical damage may also be a factor in the failure of fabric cylinders.

Removal of the axial stress affects the applicability of the predictive methodology to tape cylinders with the $[90/0/\pm45]_s$ layup. In the past [4] and current investigations, the methodology was concluded to be valid for biaxially loaded $[90/0/\pm45]_s$ cylinders with slit lengths from 12.7 to 50.8 mm since good agreement was observed between the experimental and

predicted failure pressures as well as between the initial damage states in the coupons and cylinders. Although the experimental failure pressures for the uniaxially loaded $[90/0/\pm45]_s$ cylinders with slit lengths from 12.7 to 50.8 mm are consistently lower than the corresponding biaxial values (as indicated in Table 7.1), they do agree fairly well with the predicted values. As discussed in Chapter 6, the initial damage states in the uniaxially loaded cylinders appear to be even more similar to the coupon fracture mode than the initial damage states in the biaxially loaded cylinders. Additionally, the general trend in the cylinder failure pressure with slit length is similar for the cylinders with both loading conditions. Since failure pressures of the biaxially loaded $[90/0/\pm45]_s$ cylinders are higher, and closer to the predictions, than the failure pressures of the uniaxially loaded $[90/0/\pm45]_s$ cylinders and the initial angle of the fracture paths leaving the slit tips in the uniaxially, as opposed to the biaxially, loaded cylinders is closer to that observed in the coupons, there is clearly a difference in the applicability of the methodology to $[90/0/\pm45]_s$ cylinders for different loading conditions. However, since the extent of similarity between the experimental and predicted failure pressures, the coupon and cylinder failure modes, and the coupon and cylinder slit tip stress states are all indicators of the degree of applicability of the predictive methodology, it is not currently possible to say for which loading condition the methodology is more valid. Thus, finite element analyses are needed to determine for which cylinder loading condition the slit tip stress states in $[90/0/\pm45]_s$ cylinders most closely resemble those observed in $[90/0/\pm45]_s$ coupons.

The methodology was shown to be invalid in the past investigation for biaxially loaded $[\pm45/0]_s$ and $[\pm45/90]_s$ cylinders with slit lengths from 12.7 to 63.5 mm since the failure pressures of these cylinders are not predicted and

the initial damage states in the coupons and cylinders with the same layup differ. Failure pressures of the uniaxially loaded $[\pm 45/0]_s$ and $[\pm 45/90]_s$ cylinders, and especially the failure pressures of the former cylinders, are closer to the predictions than the corresponding biaxial values. However, the trends in the experimental failure pressure with slit length for the uniaxially loaded cylinders with both layups do not match those of the corresponding prediction curves. Furthermore, these trends are observed to be different for uniaxially and biaxially loaded cylinders with the same layup. Differences in the failure pressure trends with slit length for uniaxially and biaxially loaded cylinders with the same layup suggest that there may also be differences in the applicability of the methodology to cylinders with both loading conditions. However, since similarity of the trends in the experimental and predicted failure pressures with slit length is required for the methodology to be valid, the methodology is not applicable for uniaxially loaded cylinders with the $[\pm 45/0]_s$ and $[\pm 45/90]_s$ layups as it was not for the biaxially loaded cases.

A fundamental assumption of the predictive methodology is that the initial damage modes in coupons and cylinders with the same layup and slit length agree. Thus, if the applicability of the predictive methodology to cylinders with the $[\pm 45/0]_s$ and $[\pm 45/90]_s$ layups were improved by the removal of the axial stress, the initial fracture modes in the uniaxially loaded, as opposed to the biaxially, loaded cylinders should also agree better with the coupon fracture mode. The damage visible near the slits is highly similar in the failed uniaxially and biaxially loaded $[\pm 45/90]_s$ cylinders. Thus, removal of the axial stress in cylinders with the $[\pm 45/90]_s$ layup does not improve the correlation between the initial damage states in the coupons and cylinders. Initial damage states for the uniaxially and

biaxially loaded $[\pm 45/0]_s$ cylinders differ at the 12.7 and 25.4 mm slit lengths and agree at the 50.8 mm slit length where the uniaxial and biaxial failure pressures are also the most similar. However, as in the case of the $[\pm 45/90]_s$ cylinders, neither the uniaxial nor the biaxial loading condition clearly results in more similar initial fracture modes in the coupons and cylinders. Thus, as with the failure pressure comparisons described above, damage comparisons indicate that the methodology is not valid for uniaxially loaded cylinders with the $[\pm 45/0]_s$ and $[\pm 45/90]_s$ layups.

7.2.2 Role of Subcritical Damage

The presence of subcritical damage, or damage which occurs before the ultimate cylinder failure, at the slit tips in tape cylinders may play an important role in the failure of these cylinders. As discussed previously, the presence of such damage in all of the cylinders tested in this investigation is confirmed by the discontinuities observed in the slit tip strain data.

In the case of the biaxially loaded $[90/0/\pm 45]_s$ cylinders with the 12.7 mm slit size from the past [4] and current investigations, differences in subcritical damage may explain the large degree of scatter in the experimental failure pressures, even after standard material variation is taken into account. Such differences in subcritical damage should correlate with differences in the damage observed near the slits after the cylinder failures. Thus, if failure pressure scatter is affected by differences in subcritical damage, there should also be correlation between the cylinder failure pressures and the post-failure damage visible near the slits. In the biaxially loaded $[90/0/\pm 45]_s$ cylinder with the 12.7 mm slit tested in the past investigation, the initial damage mode at each slit tip is similar in many

respects to that observed in the $[90/0/\pm45]_s$ coupons and both biaxially loaded cylinders with the same slit length tested in the current investigation. However, in the cylinder from the past investigation, an extra circumferential fracture path is observed at one slit tip. This difference may be observed by comparing Figures 7.1, 7.2, and 7.3 which are post-failure close-up photographs of the slit region in the biaxially loaded cylinder from the past investigation, the first biaxially loaded cylinder from the current investigation, and the second biaxially loaded cylinder from the current investigation, respectively (overall photographs for the cylinders tested in the current investigation are shown in Figures 6.19 and 6.21). The cylinder with the circumferential fracture path has a relatively high failure pressure (23% higher than the average value for the other two cylinders) while the failure pressures of the other two cylinders without a circumferential slit tip fracture path are lower and comparable in magnitude (2.03 MPa for the first tested cylinder versus 1.89 MPa for the second tested cylinder). Thus, by induction, there is clearly a relationship between subcritical damage and scatter in the cylinder failure pressures. For the biaxially loaded $[90/0/\pm45]_s$ cylinders with the 12.7 mm slits, the initial coupon and cylinder failure modes are not similar and the experimental and predicted failure pressures do not agree when the circumferential fracture path is present. This dissimilarity between the coupon and cylinder fracture modes violates a fundamental assumption of the methodology since it implies that the parameter used to characterize the fracture behavior, H_c, is unlikely to have the same value for both the coupons and cylinders when the controlling fracture mechanisms change. Thus, subcritical damage also influences the applicability of the predictive methodology to the cylinders considered. Since the cylinder with the

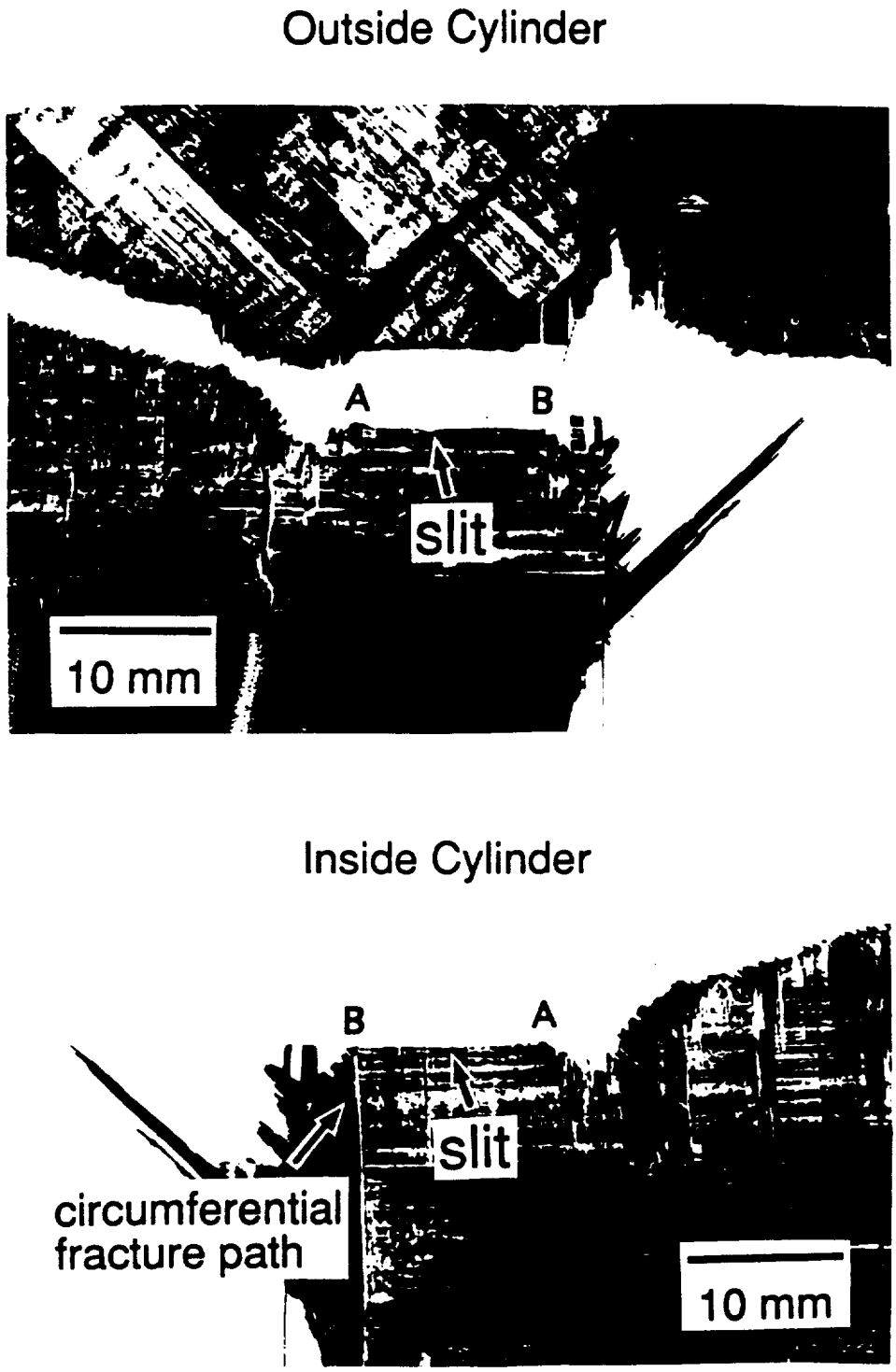

Figure 7.1 Post-test photograph of slit region in biaxially loaded $[90/0/\pm45]_s$ cylinder with 12.7 mm slit [31].

Figure 7.2 Post-test photograph of slit region in first biaxially loaded $[90/0/\pm45]_s$ cylinder with 12.7 mm slit.

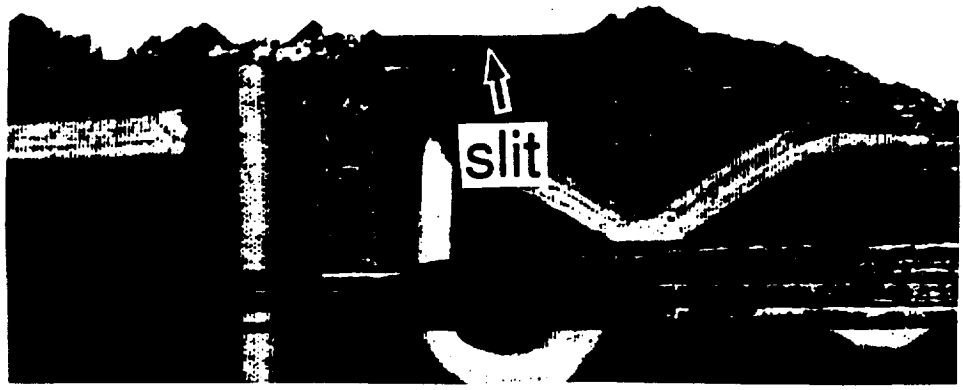

10 mm

Figure 7.3 Post-test photograph of slit region in second biaxially loaded $[90/0/\pm45]_s$ cylinder with 12.7 mm slit.

circumferential fracture path has the highest failure pressure of the three $[90/0/\pm45]_s$ cylinders with the 12.7 mm slits, the subcritical damage mechanism responsible for the formation of this path was apparently more effective in mitigating the notch-tip stresses and, thereby, reducing the notch sensitivity of the cylinder than such a mechanism in the other two cylinders.

The slit tip hoop strain discontinuities and post-failure damage near the slits for the two biaxially loaded $[90/0/\pm45]_s$ cylinders tested in the current investigation provide support for the claim that subcritical damage played somewhat of a different role in the failure of these cylinders. While pressures at the first strain discontinuity are slightly higher and the strains are slightly lower for Slit Tip Gage 1 on both cylinders, there is a large discrepancy between the two cylinders as to the magnitudes of these pressures and strains. As discussed in Chapter 6, the pressures and strains at the first discontinuities are approximately 35% and 28% lower, respectively, for the second tested cylinder. This difference in subcritical damage behavior, with such damage being observed earlier in the second tested cylinder, may be related to the fact that the failure pressure of the second tested cylinder is 7% lower than that for the first tested cylinder. As mentioned previously, the fracture path emanating from the left slit tip in the second biaxially loaded $[90/0/\pm45]_s$ cylinder is somewhat unusual since it is initially oriented along an angle of 90° as opposed to an angle between +65° and +80° as was observed at the other end of the slit in the second tested cylinder and at both ends of the slit in the first tested cylinder. The fracture path at the left slit tip in the second tested cylinder is also relatively jagged compared to the other slit tip paths. Thus, the assertion that the slit tip strain discontinuities for the two biaxially loaded $[90/0/\pm45]_s$ cylinders

tested in the current investigation reflect a discernible difference in the subcritical damage behavior in both cylinders is substantiated by the observed differences in the damage visible near the slits after the cylinder failures.

Differences in the post-failure damage near the slits in the biaxially loaded $[90/0/\pm45]_s$ cylinders with the 12.7 mm slits from the past and current investigations suggest that competing damage mechanisms may be present and that the one that becomes critical first may not always be the same. Depending on which mechanism causes the first subcritical damage and when this damage occurs, the subsequent damage and the corresponding effect that this damage has on the failure pressure and the damage that is observable near the slit after the test may be different. Thus, while difficult, it would be useful to compare the observed damage near the slits after failure and the failure pressures of similar cylinders with the initial subcritical damage mechanisms and the pressures (and/or strains) at which they occur.

In an analogous manner to how differences in subcritical damage may be related to scatter in the experimental failure pressures for cylinders with the same layup, loading condition, and slit length, differences in the role of subcritical damage might be linked to the observed discrepancies between the failure pressures of cylinders that differ only in loading condition (uniaxial or biaxial). As in the case of the two biaxially loaded $[90/0/\pm45]_s$ cylinders tested in the current investigation, differences in the slit tip hoop strain discontinuities and the post-failure damage visible near the slits are indicative of differences in the role of subcritical damage and are observed for the uniaxially and biaxially loaded $[90/0/\pm45]_s$ cylinders with the 12.7 mm slits tested in the current investigation. These are the

only cylinders for which comparisons between the discontinuities in the slit tip strains for cylinders that differ only in loading condition may currently be made. As previously mentioned, pressures and strains at the first discontinuity are similar at both ends of the slits in the biaxially loaded cylinders. However, pressures are slightly higher and strains are slightly lower for Slit Tip Gage 1. In contrast, the pressure, as well as the strain, at the first discontinuity are lower for Slit Tip Gage 1 than for Slit Tip Gage 2 in the uniaxially loaded cylinder. In this cylinder, there are also relatively large differences between the pressures and strains at the first discontinuity at both ends of the slit of 0.82 MPa and 5375 μstrain, respectively. The post-failure damage near the slits in the uniaxially and biaxially loaded $[90/0/\pm45]_s$ cylinders differs primarily in that the initial fracture path in the latter cylinders is generally oriented along an angle between +65° and +80° as opposed to an angle of approximately +45° as is observed in the former cylinders. The existence of differences in the role of subcritical damage in the failure of the uniaxially and biaxially loaded $[90/0/\pm45]_s$ cylinders with the 12.7 mm slits from the current work, which is supported by the differences in the post-failure slit region damage and the slit tip strain discontinuity behavior described above, may be related to the fact that the failure pressure of the uniaxially loaded cylinder is approximately 10% lower than the biaxial values.

The results of previous work [32,37,38,39] involving notched tape laminates loaded uniaxially indicate that some types of subcritical damage, especially 0° ply splitting accompanied by delamination, can mitigate stresses at the notch tips resulting in reduced notch sensitivity. The relative effects of the axial stress on the cylinder failure pressures correlate with the percentage of 0° plies in the layups considered, with the greatest

differences in the uniaxial and biaxial failure pressures being observed for the $[\pm 45/0]_s$ cylinders which have the highest percentage (33%) of 0° plies. Thus, in the biaxially loaded $[90/0/\pm 45]_s$ and $[\pm 45/0]_s$ cylinders, and particularly in the latter cylinders, the axial stress may contribute to the formation of 0° (hoopwise) ply splitting at the slit tips which reduces the local stress concentration and leads to higher failure pressures than those which are observed for the uniaxially loaded cylinders with the same layups. The $[\pm 45/90]_s$ cylinders do not contain any 0° plies and their failure pressures are affected the least by the removal of the axial stress. Thus, a similar, but less effective, stress-mitigating subcritical damage mechanism than 0° ply splitting may be involved which leads to reduced notch sensitivity when the axial stress is present.

The circumferential fracture path observed at the slit tip in the biaxially loaded $[90/0/\pm 45]_s$ cylinder with the 12.7 mm slit from the past work is highly suggestive of a 0° ply split. Since 0° ply splitting accompanied by delamination can be a highly effective stress-mitigating subcritical damage mechanism in notched tape configurations, the presence of the circumferential fracture path indicates that 0° ply splitting may have played a particularly strong role in the notch-tip load redistribution in the cylinder where this path is located. This would explain why the notch sensitivity of the biaxially loaded $[90/0/\pm 45]_s$ cylinder with the 12.7 mm slit and extra circumferential fracture path at one slit tip was observed to be lower than that of the other two biaxially loaded cylinders with the same layup, loading condition, and slit length.

The biaxially loaded $[90/0/\pm 45]_s$ cylinder with a 12.7 mm slit is, to date, the only case (slit length, layup, and loading condition) for which multiple tests have been conducted. Thus, it is currently not known if a

similar degree of scatter in the experimental failure pressures is present for biaxially loaded cylinders with the same layup and other slit lengths or for biaxially loaded cylinders with other layups. Additionally, no comparisons of the degree of scatter are currently available for uniaxially and biaxially loaded cylinders with the same layup. Since determining the variations in the degree of experimental failure pressure scatter may help clarify the role of subcritical damage in the failure of tape cylinders, research addressing this issue should be pursued. Discontinuities in slit tip strains should also be compared for similar cylinders to see if there is any correlation between the scatter in the pressure and strain levels at these discontinuities and the scatter in the cylinder failure pressures.

In Section 7.2.1, it was suggested that slit tip damage occurring before the ultimate cylinder failure may play a different role in different laminates. This claim is supported by the fact that while definite trends are observed in the discontinuities in the slit tip strain data for the cylinders tested in the current investigation, these trends are generally not the same for cylinders with different layups and loading conditions. In fact, the only consistent trend noted in the pressures and strains at the first discontinuities in the slit tip strain readings is that the pressures generally decrease with increasing slit length. In past work [32,37,38,39] using uniaxially loaded tape coupons with notches, it has been shown that the effects of subcritical damage on load redistribution at the notch tips and the subsequent effects on the coupon failure behavior are indeed highly dependent on loading condition, material, and laminate, even when only changes in stacking sequence are involved. The effects of subcritical damage can range from detrimental to beneficial, in terms of increasing or decreasing notch sensitivity, depending on the degree to which the localized

damage relieves the stress concentration on the primary load bearing plies [37]. The trends in the slit tip strain data for the biaxially loaded cylinders with the $[90/0/\pm45]_s$ and $[0/\pm45/90]_s$ layups are not well-defined since so few of these cylinders were tested. Thus, more biaxially loaded $[90/0/\pm45]_s$ and $[0/\pm45/90]_s$ cylinders with a variety of slit lengths should be tested and the trends in the slit tip strain discontinuities should be determined and compared in order to better understand the potential differences in the role of slit tip damage in both layups. Subcritical damage effects are likely coupled to effects of structural anisotropy since the formation of a slit tip damage zone results in load redistribution in the region around the slit. Therefore, attempts should be made in additional investigations to isolate these damage effects by focusing on tape layups with zero D_{16} and D_{26} terms.

Within the limitations of the damage comparisons, it appears that when the post-failure damage near the slit tips in uniaxially and biaxially loaded cylinders with the same layup are more similar, lower percent changes in cylinder failure pressure are also observed. In the uniaxially and biaxially loaded $[\pm45/90]_s$ cylinders, a primary fracture path leaves each slit tip along essentially the 90° direction . The narrowest range of percent failure pressure differences (15% to 23%) between the uniaxially and biaxially loaded cylinders and the percent differences with the lowest magnitudes are observed for the $[\pm45/90]_s$ layup. For the $[90/0/\pm45]_s$ layup, the initial angle of the fracture paths is generally between +65° and +80° in the biaxially loaded cylinders, as opposed to an angle of approximately +45° as is observed in the uniaxially loaded cylinders, while the length of the paths along the initial angle is approximately 7 mm in cylinders with both loading conditions. A greater range of percent failure pressure differences

(6% to 27%) and percent differences with greater magnitudes are observed for the $[90/0/\pm45]_s$ layup than for the $[\pm45/90]_s$ layup. The greatest range of percent failure pressure differences (15% to 41%) and percent differences with the greatest magnitudes are observed for the $[\pm45/0]_s$ layup. At the 50.8 mm slit length where the lowest percent failure pressure difference for the $[\pm45/0]_s$ layup and one of the lowest percent differences in the entire investigation is observed (15%), the fracture paths leaving the slit tips in the uniaxially and biaxially loaded cylinders along angles of approximately ±45° are very similar. For the $[\pm45/0]_s$ layup at the 12.7 and 25.4 mm slit lengths, relatively large differences in the primary damage at the slit tips are observed between the cylinders with both loading conditions. The percent differences between the uniaxial and biaxial failure pressures for the $[\pm45/0]_s$ cylinders with the 12.7 and 25.4 mm slits are also the largest such differences observed in the current work.

The damage visible near the slit after the cylinder failure is likely related to the types and quantities of subcritical damage. Thus, the observed correlation between similarity of initial damage modes and similarity of failure pressures in cylinders that differ only in loading condition suggests that the axial stress may play less of a role when the subcritical damage in cylinders with a given layup and both loading conditions is similar or minimal. Differences in the slit region stress states for a uniaxially and biaxially loaded cylinder with the same layup and slit length, which are manifested as differences in failure pressure and post-failure damage visible near the slits, are expected to be less when the slit tip damage zone is similar or minimal in both cylinders since changes in subcritical damage by themselves may result in fundamental differences in the way that loads are distributed at the slit tips. To further establish the

relationship between subcritical damage and the role of the axial stress in the failure of tape cylinders, differences in the slit tip strain discontinuity trends for uniaxially and biaxially loaded cylinders with the same layup need to be compared for a variety of laminates. These comparisons should be coupled with those of the relative effects of the axial stress on the cylinder failure pressures and the damage visible near the slits after the cylinder failures. It might also be useful to compare the trends in the slit tip strain discontinuities for cylinders and coupons with the same layup to see if there is any connection between the degree of correlation of the trends and the degree of applicability of the predictive methodology.

Since the information provided by the slit tip strain readings is limited, progressive damage studies, whereby cylinders are loaded once or multiple times to pressures below the failure pressure and the damage at the slit tips is evaluated using destructive or nondestructive inspection, should also be conducted on uniaxially and biaxially loaded tape cylinders. These studies are necessary in order to determine if and how the types and quantities of subcritical damage vary for different laminates and for the same laminate with two different loading conditions. Once the subcritical slit tip damage in uniaxially and biaxially loaded tape cylinders is more clearly identified and quantified, the role of this damage in the failure of tape cylinders can be better assessed.

7.2.3 Effects of Structural Anisotropy

The predictive methodology has been shown in the past [4] and current investigations to be invalid for structurally anisotropic $[\pm 45/0]_s$ and $[\pm 45/90]_s$ tape cylinders loaded uniaxially and biaxially. The failure pressures of these cylinders generally do not agree with the predicted

values and differences are observed between the initial damage states, or the damage visible near the slits after failure, in the coupons and cylinders with the same layup. The methodology is applicable for biaxially loaded $[0/\pm45/90]_s$ cylinders and, as discussed in Section 7.2.1, the methodology could be applicable for either the uniaxially or the biaxially loaded $[90/0/\pm45]_s$ cylinders although the uniaxially loaded cylinders fail at consistently lower pressures than their biaxially loaded counterparts. However, some slight differences between the experimental and predicted failure pressures and the initial damage modes in the coupons and cylinders are also observed for these quasi-isotropic layups which have a small degree of bending-twisting coupling. In some cases, differences have also been observed between the failure pressures and failure modes of uniaxially and biaxially loaded cylinders with the $[\pm45/0]_s$, $[\pm45/90]_s$, and $[90/0/\pm45]_s$ layups. Since structural anisotropy is a common element of the properties of all the cylinders tested in the current investigation, it must be considered as a possible important factor in the observed failure behavior of these cylinders.

As mentioned above, the results presented in Chapter 6 indicate that the predictive methodology is applicable for the biaxially loaded, quasi-isotropic $[0/\pm45/90]_s$ cylinders with the 12.7 and 25.4 mm slits. This applicability is confirmed by the observed agreement between the experimental and predicted failure pressures and the initial damage states in the $[0/\pm45/90]_s$ coupons and biaxially loaded cylinders. As discussed in Chapter 3, the $[0/\pm45/90]_s$ layup has values of D_{16} and D_{26} with twice the magnitudes of those for the $[90/0/\pm45]_s$ layup for which the methodology has also been shown to be valid. However, the ratios of D_{16} and D_{26} to D_{11} for both layups are essentially the same. Thus, if a structural anisotropy effect

is present in cylinders with these quasi-isotropic layups, this may indicate that the ratios of D_{16} and D_{26} to D_{11}, and not the absolute magnitudes of D_{16} and D_{26}, may be important. However, as discussed in Section 7.2.2, it is not clear that the effects of structural anisotropy are independent of other potential effects such as subcritical damage. As mentioned previously, these two effects are likely related because they both influence the slit tip stress state. In order to further clarify the significance of the ratios of the bending-twisting coupling terms to the hoop direction bending stiffness, additional comparisons should be made between the failure results for tape cylinders with layups that differ only in stacking sequence and represent a wide range of ratios of D_{16} and D_{26} to D_{11}. Since only two $[0/\pm45/90]_s$ cylinders with similar slit lengths, one cylinder radius, and one loading condition were tested, more cylinder tests may also be necessary in order to confirm the general applicability of the methodology to tape cylinders with this layup.

A known limitation on the use of the current predictive methodology for tape cylinders is that the structurally anisotropy that these laminates generally exhibit is not accounted for in the isotropic curvature correction factor. The major and minor Poisson's ratios are also not accounted for properly in the curvature correction factor if these ratios differ from each other, as they do for the $[\pm45/0]_s$ and $[\pm45/90]_s$ layups, since only an average Poisson's ratio is used. Additionally, as discussed in Chapter 2, two fundamental assumptions of the methodology which may be violated when a laminate exhibits structural anisotropy are that the stress states near the slits in a cylinder and coupon are similar in nature and that the extensional stresses near and perpendicular to the slits in both specimen types are responsible for failure. The first assumption is automatically

violated if structural anisotropy significantly alters the stress state near the slit in the cylinder from that in the flat plate. As discussed in Chapter 3, the second assumption might also not be met if nonnegligible bending stresses supplement the extensional stresses in the cylinder in the direction perpendicular to the slit or if the stress state surrounding the slit is favorable to inducing failure through tearing or shearing action. This second assumption that the extensional stresses near and perpendicular to the slit cause failure in both cylinders and coupons is coupled to an additional assumption that the initial failure mode is the same in both specimen types for a given layup.

Some differences were observed in the current investigation between the failure modes of coupons and cylinders with the same layup. This suggests that, in addition to the improper representation of the material properties in the isotropic curvature correction factor, the tape laminates considered in the current investigation may also violate the fundamental assumptions of the methodology to varying extents. The structurally anisotropic $[\pm 45/0]_s$ and $[\pm 45/90]_s$ layups clearly violate these assumptions since the initial failure modes in the uniaxially and biaxially loaded cylinders with these layups are not similar to the corresponding coupon fracture modes. Failure mode differences near the slit tips between coupons and cylinders are relatively minor for the quasi-isotropic $[90/0/\pm 45]_s$ and $[0/\pm 45/90]_s$ layups, with the primary difference for the $[0/\pm 45/90]_s$ layup being that the average size of the triangular shaped fractures through the 0° and +45° plies in the cylinders is slightly smaller than in the coupons. For the $[90/0/\pm 45]_s$ layup, the initial fracture path angle and the length of the fracture path along this angle are slightly smaller and greater in magnitude, respectively, in the coupons as compared to the uniaxially and

biaxially loaded cylinders. As mentioned previously, the initial fracture mode in the uniaxially loaded, as opposed to the biaxially loaded, $[90/0/\pm45]_s$ cylinders agrees the best with the coupon fracture mode. The high degree of similarity between the initial damage modes in the coupons and cylinders with the $[90/0/\pm45]_s$ and $[0/\pm45/90]_s$ layups indicates that these laminates likely comply with the fundamental assumptions of the methodology.

The small differences between the initial damage modes in cylinders and coupons with the quasi-isotropic $[90/0/\pm45]_s$ and $[0/\pm45/90]_s$ layups suggest that there may be slight differences in the slit tip stress states in the two specimen types as a result of structural anisotropy. Thus, there may be a range of magnitudes of D_{16} and D_{26}, or of ratios of D_{16} and D_{26} to D_{11} if these are the more important parameters, for which the changes in the stress state in the cylinder from that in the flat plate are limited to such a degree that the methodology may still be considered valid. The lack of similarity between the initial cylinder and coupon fracture modes for the $[\pm45/0]_s$ and $[\pm45/90]_s$ layups suggests that differences between the slit tip stress states in both specimen types are significant for these layups. Differences between the failure modes of uniaxially and biaxially loaded cylinders with the same layup suggest that in some cases the effect of structural anisotropy on the stress state in a cylinder may depend on the loading condition. However, it is not clear whether a uniaxial or biaxial loading condition results in more similar stress states near the slit in coupons and cylinders with the same layup. Thus, in order to address these issues and determine how structural anisotropy affects the stress states in uniaxially loaded cylinders, biaxially loaded cylinders, and coupons, detailed finite element analyses of uniaxially and biaxially loaded

cylinders and coupons with layups representing a wide range of structural coupling magnitudes are required. These finite element analyses should be accompanied by additional cylinder tests so that the effects of varying degrees of structural anisotropy on the stress states in the cylinders may be compared to the corresponding effects on the applicability of the current methodology.

In summary, axial stress, subcritical damage, and structural anisotropy are factors which can affect the failure of notched pressurized cylinders. The relative effects of each of these factors vary with parameters such as layup, loading condition, and slit length. Interaction amongst the effects of these factors also occurs.

Axial stress, subcritical damage, and structural anisotropy are not taken into account in the current predictive methodology. Thus, this methodology, which employs an isotropic curvature correction factor derived from a linear analysis and only accounts for hoopwise loading, is not expected to be generally applicable for axially-slit tape cylinders loaded uniaxially and biaxially. The methodology has, however, been successfully used to predict the failure pressures of some fabric and tape cylinders with quasi-isotropic layups. This is not surprising since, as mentioned above, the curvature correction factor used in the methodology is derived for isotropic materials.

In the case of quasi-isotropic $[90/0/\pm45]_s$ cylinders with the 12.7 mm slit length loaded biaxially, the methodology has been shown to be both valid and invalid depending on the effect of subcritical damage in the cylinder considered. A circumferential fracture path suggestive of a 0° ply split is observed at one slit tip in the biaxially loaded $[90/0/\pm45]_s$ cylinder with the

12.7 mm slit tested in the past investigation and the methodology is not applicable for this cylinder. The two cylinders with the same layup, slit length, and loading condition tested in the current investigation do not have such a slit tip fracture path and their failure pressures are predicted by the methodology. This indicates that the early damage mechanisms at the slit tips are key in determining the ultimate failure behavior of a cylinder. It may also demonstrate the importance of the axial stress with regard to the formation and growth of subcritical damage.

The experimental failure pressures of the uniaxially and biaxially loaded tape cylinders with structurally anisotropic layups that have been tested to date all exceed the predicted values. Thus, while the current methodology may not be valid for tape cylinders with a wide variety of layups, it might be useful in providing conservative failure pressure estimates for these cylinders. Any new predictive methodology or revised version of the one currently used must account for the effects of axial stress, subcritical damage, and structural anisotropy as well as the interactions amongst these effects. Thus, additional work is recommended to further establish the roles of these factors in the failure of axially-slit tape cylinders and to identify any other factors which should be included in a failure prediction methodology for these cylinders.

The uniaxial cylinder tests in this investigation cover only one cylinder radius and a relatively narrow selection of slit lengths and layups. Thus, it is important to determine how the roles of the axial stress and the other factors in the failure of tape cylinders may change with these parameters. It may be especially revealing to test the same structurally anisotropic cylinders considered in the current investigation with longer slit lengths since the general trend in the experimental failure pressures

for each set of cylinders suggests that a curve drawn through these pressures would converge with, or possibly cross over, one drawn through the experimental failure pressures for the biaxially loaded cylinders with the same layup. In the case of convergence, it would suggest that factors influencing the role of the axial stress, such as subcritical damage and structural anisotropy, may become less important with increasing slit length. Since the current investigation does not reveal a consistent trend in the degree of structural anisotropy and the effect of the axial stress, it may also be important to consider other tape layups with different degrees of structural anisotropy. Cylinders with these layups should be tested in uniaxial and biaxial loading in order to determine how the differences in the failure pressures compare to those observed for the three layups considered here.

CHAPTER 8

Conclusions and Recommendations

In this investigation, three factors which can influence the failure behavior of pressurized tape cylinders with axial slits have been examined. Axial stress effects have been evaluated by comparing the failure behavior of uniaxially and biaxially loaded cylinders with the $[90/0/\pm45]_s$, $[\pm45/0]_s$, and $[\pm45/90]_s$ layups. The failure behavior of biaxially loaded cylinders with the $[90/0/\pm45]_s$ and $[0/\pm45/90]_s$ layups have been compared to better understand the role of structural anisotropy. Additionally, the influence of subcritical damage in the failure of all the cylinders considered has been explored through comparisons of slit tip hoop strain discontinuities and post-failure damage visible near the slits. The limitations of a failure prediction methodology which uses coupon fracture data to predict cylinder failure were also examined by applying the predictive methodology to all the cylinders considered. The results of this investigation, as presented and discussed in previous chapters, have led to the following conclusions:

1. The uniaxial test apparatus designed and built for this work enables cylinders to be tested to failure in uniaxial (hoop) far-field loading via internal pressurization. The rods and rod support plates in the device affect the propagating damage, but not the initial damage mechanisms, in the cylinders.

2. Removal of the axial stress in $[90/0/\pm45]_s$, $[\pm45/0]_s$, and $[\pm45/90]_s$ cylinders with 12.7, 25.4, and 50.8 mm slits consistently results in lower failure pressures. The relative effects of the removal of the

axial stress on the cylinder failure pressures differ with layup and possibly with slit length.

3. Although the magnitudes of the percent decreases in failure pressure resulting from the removal of the axial stress do not correlate directly with the degree of structural coupling (i.e. the magnitudes of D_{16}, D_{26}, and the ratios of D_{16} and D_{26} to D_{11}), such structural coupling is a possible important factor in the role of the axial stress since the trends in the percent failure pressure differences between the uniaxially and biaxially loaded cases with slit length appear to correlate with the degree of this coupling. Specifically, the lowest percent difference in failure pressure for the $[\pm 45/0]_s$ and $[\pm 45/90]_s$ layups, which have a similar degree of structural coupling, is observed at the longest slit length (50.8 mm) while the highest such difference for the quasi-isotropic $[90/0/\pm 45]_s$ layup is observed at the same slit length.

4. The role of structural anisotropy may depend more on the ratios of D_{16} and D_{26} to D_{11} than on the absolute magnitudes of D_{16} and D_{26}. This is shown by the biaxially loaded $[0/\pm 45/90]_s$ and $[90/0/\pm 45]_s$ cylinders, for which the methodology is valid, since the $[0/\pm 45/90]_s$ layup has higher values of D_{16} and D_{26} but both layups have similar ratios of D_{16} and D_{26} to D_{11}. This assumes that structural anisotropy affects the failure of cylinders with both layups.

5. The applicability of the predictive methodology to $[90/0/\pm 45]_s$ cylinders with slit lengths from 12.7 to 50.8 mm differs somewhat with loading

condition since experimental and predicted failure pressures agree better when the cylinders are loaded biaxially and initial cylinder and coupon fracture modes agree better when the cylinders are loaded uniaxially. It is not currently known for which loading condition the methodology is more valid.

6. The predictive methodology is applicable for biaxially loaded $[0/\pm45/90]_s$ cylinders with 12.7 and 25.4 mm slits.

7. The predictive methodology is not applicable for uniaxially or biaxially loaded $[\pm45/0]_s$ and $[\pm45/90]_s$ cylinders with slit lengths from 12.7 to 50.8 mm. Experimental and predicted failure pressures, as well as coupon and cylinder initial fracture modes, for these layups do not agree and, thus, little similarity is also expected between the slit tip stress states in coupons and cylinders with these layups.

8. Discontinuities observed in the slit tip hoop strains indicate that subcritical damage occurred at the slit tips in all the cylinders tested in the current investigation. The initial fracture mechanism and the pressure (and/or strain level) at which it occurs are key in determining the ultimate effect of this subcritical damage on the cylinder failure behavior.

9. Differences in the subcritical damage behavior in cylinders with the same layup, loading condition, and slit length can lead to differences in the experimental failure pressures and associated differences in the post-failure damage visible near the slits. These effects were

observed for the biaxially loaded $[90/0/\pm45]_s$ cylinders with the 12.7 mm slit size from the past and current investigations.

10. Differences in the role of subcritical damage in cylinders with the same layup, slit length, and loading condition can affect the applicability of the methodology to these cylinders. This is shown by the biaxially loaded $[90/0/\pm45]_s$ cylinders with the 12.7 mm slits since the methodology is not valid for the cylinder with the 0° fracture path at one slit tip but is valid for the two cylinders without this path.

11. The axial stress may contribute to the formation of stress-mitigating subcritical damage at the cylinder slit tips leading to higher failure pressures than when the cylinders are loaded uniaxially. Such damage is likely 0° ply splitting accompanied by delamination in the $[\pm45/0]_s$ and $[90/0/\pm45]_s$ cylinders. A similar, but less effective, subcritical damage mechanism may operate in the $[\pm45/90]_s$ cylinders which have the lowest percent differences between the uniaxial and biaxial failure pressures.

12. Splitting of 0° plies and associated delamination is an important stress-mitigating subcritical damage mechanism in tape laminates. This is supported by the fact that a circumferential fracture path suggestive of a 0° ply split is observed at one slit tip in the biaxially loaded $[90/0/\pm45]_s$ cylinder with a 12.7 mm that has the highest failure pressure of the three such cylinders that have been tested.

Based on the work conducted, the following recommendations are made for further work:

1. The uniaxial test apparatus should not be used to study damage propagation and arrest in uniaxially loaded cylinders (unless the design is reformed for this purpose) since the manner in which the apparatus modifies the propagating damage in a cylinder is currently not known.

2. Additional tests of uniaxially and biaxially loaded cylinders with the $[90/0/\pm45]_s$, $[\pm45/0]_s$, $[\pm45/90]_s$ layups should be conducted in order to determine how the role of the axial stress varies at slit lengths greater than 50.8 mm. Greater similarity between the failure pressures and fracture modes of cylinders that differ only in loading condition might indicate that factors influencing the role of the axial stress become less important with increasing slit length.

3. The effects of axial stress on the failure pressures, failure modes, and slit tip strain behavior of quasi-isotropic fabric cylinders, which have zero D_{16} and D_{26} terms and are less susceptible to subcritical damage due to the woven nature of the fibers, should be investigated to determine if the loading condition effects on the failure pressures of tape cylinders are only related to structural anisotropy and subcritical damage.

4. Additional experiments should be conducted using tape laminates with zero D_{16} and D_{26} terms so that the effects of subcritical damage

on tape cylinder failure may be isolated from the effects of structural anisotropy.

5. The significance of the ratios of the bending-twisting coupling terms to the hoop direction bending stiffness should be further evaluated by comparing the failure results for tape cylinders with layups that differ only in stacking sequence and represent a wide range of ratios of D_{16} and D_{26} to D_{11}.

6. In order to establish the effects of structural anisotropy and axial stress on the slit tip stress states in pressurized cylinders and to determine how the slit tip stress states in coupons and cylinders differ, detailed finite element analyses of uniaxially loaded cylinders, biaxially loaded cylinders, and coupons with the same layup should be conducted for a variety of laminates. Uniaxial and biaxial cylinder tests, including strain surveys, should accompany the finite element analyses so that the results of these analyses may be compared to the corresponding effects on the applicability of the predictive methodology.

7. More work is needed to determine how subcritical damage influences the role of the axial stress as well as scatter in the experimental failure pressures for similar cylinders. Such work should involve a variety of comparisons of the slit tip strain discontinuity behavior for uniaxially and biaxially loaded cylinders with the same layup and for cylinders with the same layup, slit length, and loading condition. These comparisons should be coupled with those of the cylinder failure pressures and the post-failure damage visible near the slits.

8. In order to more clearly identify and quantify the subcritical slit tip damage in the uniaxially and biaxially loaded cylinders considered in the current investigation, progressive damage studies should be conducted. Such studies would show if and how the types and quantities of subcritical damage vary for different laminates and for the same laminate with two different loading conditions and would make it possible to compare the post-failure damage near the slits and the failure pressures of similar cylinders with the initial subcritical damage mechanisms and the pressures (and/or strains) at which they occur.

9. Differences in the roles of structural anisotropy, subcritical damage, and axial stress as a result of changes in the cylinder curvature should be assessed. Cylinders with larger radii are preferred since they are more representative of the real-world structures (such as fuselages or pipelines) to which the results of such research could be applied.

Bibliography

1. Smith, P. J., Thomson, L. W., and Wilson, R. D., "Development of Pressure Containment and Damage Tolerance Technology for Composite Fuselage Structures in Large Transport Aircraft", NASA CR-3996, 1986.

2. Ilcewicz, L. B., Smith, P. J., and Horton, R. E., "Advanced Composite Fuselage Technology", *Third NASA Advanced Composites Technology Conference, Volume I*, Long Beach, CA, 1992, pp. 97-156.

3. Graves, M. J. and Lagace, P. A., "Damage Tolerance of Composite Cylinders", *Composite Structures*, Vol. 4, No. 1, 1985, pp. 75-91.

4. Ranniger, C. U., Lagace, P. A., and Graves, M. J., "Damage Tolerance and Arrest Characteristics of Pressurized Graphite/Epoxy Tape Cylinders", to appear in *Proceedings of the ASTM Fifth Symposium on Composite Materials: Fatigue and Fracture*, May, 1993.

5. Awerbach, J. and Madhukar, M. S., "Notched Strength of Composite Laminates Predictions and Experiments - A Review", *Journal of Reinforced Plastics and Composites*, Vol. 4, January, 1985, pp. 3-159.

6. Fenner, D. N., "Stress Singularities in Composite Materials with an Arbitrarily Oriented Crack Meeting an Interface", *International Journal of Fracture*, Vol. 12, No. 5, October, 1986, pp. 705-721.

7. Lo, K. H., Wu, E. M., and Konishi, D. Y., "Failure Strength of Notched Composite Laminates", *Journal of Composite Materials*, Vol. 17, September, 1983, pp. 384-398.

8. Mar, J. W. and Lin, K. Y., "Fracture of Boron/Aluminum Composites with Discontinuities", *Journal of Composite Materials*, Vol. 11, October, 1977, pp. 405-421.

9. Whitney, J. M. and Nuismer, R. J., "Stress Fracture Criteria for Composite Laminates Containing Stress Concentrations", *Journal of Composite Materials*, Vol. 8, July, 1974, pp. 253-265.

10. Corten, H. T., "Fracture Mechanics of Composites", in *Fracture*, ed. Liebowitz, H., Vol. VII, 1972, pp. 676-767.

11. Lagace, P. A., "Notch Sensitivity and Stacking Sequence of Laminated Composites", *Composite Materials: Testing and Design (Seventh Conference), ASTM STP 893*, ASTM, 1986, pp. 161-176.

12. Saeger, K. J. and Lagace, P. A., "Fracture of Pressurized Composite Cylinders with a High Strain-to-Failure Matrix System", *Composite Materials: Fatigue and Fracture, Second Volume, ASTM STP 1012*, ASTM, 1989, pp. 326-337.

13. Graves, M. J., "The Catastrophic Failure of Pressurized Graphite/Epoxy Cylinders", TELAC Report 82-10, Massachusetts Institute of Technology, September, 1982.

14. Brewer, J. C., "Tensile Fracture of Graphite/Epoxy with Angled Slits", TELAC Report 82-16, Massachusetts Institute of Technology, December, 1982.

15. Lagace, P. A., "Notch Sensitivity of Graphite/Epoxy Fabric Laminates", *Composites Science and Technology*, Vol. 26, 1986, pp. 95-117.

16. Mar, J. W. and Lagace, P. A., "Tensile Fracture of Graphite/Epoxy Laminates with Holes", *Third International Conference on Composite Materials*, Paris, France, 1980, pp. 130-145.

17. Ranniger, C., "Effect of Cylinder Diameter on the Damage Tolerance of Graphite/Epoxy Cylinders with Axial Notches", TELAC Report 91-10, Massachusetts Institute of Technology, May, 1991.

18. Folias, E. S., "Asymptotic Approximations to Crack Problems in Shells", in *Mechanics of Fracture - Plates and shells with cracks*, ed. Sih, G. C., Vol. 3, Noordhoff International Publishing, Leyden, 1977, pp. 117-160.

19. Folias, E. S., "On the Effect of Initial Curvature on Cracked Flat Sheets", *International Journal of Fracture Mechanics*, Vol. 5, No. 4, 1969, pp. 327-346.

20. Folias, E. S., "An Axial Crack in a Pressurized Cylindrical Shell", *International Journal of Fracture Mechanics*, Vol. 1, No. 2, 1965, pp. 104-113.

21. Folias, E. S., "On the Prediction of Catastrophic Failures in Pressurized Vessels", in *Prospects of Fracture Mechanics*, ed. Sih, G. C., van Elst, H. C., and Broek, D., Noordhoff International, Leyden, 1974, pp. 405-418.

22. Krenk, S., "Influence of Transverse Shear on an Axial Crack in a Cylindrical Shell", *International Journal of Fracture*, Vol. 14, No. 2, April, 1978, pp. 123-143.

23. Saeger, K. J., "A Comparison of the Damage Tolerance of Pressurized Graphite/Epoxy and Aluminum Cylinders", TELAC Report 85-24, Massachusetts Institute of Technology, November, 1985.

24. Getz, D. L., Pierce, W. S., and Calvert, H. F., "Correlation of Uniaxial Notch Tensile Data With Pressure-Vessel Fracture Characteristics", ASME 63 WA-187, 1963.

25. Anderson, R. B. and Sullivan, T. L., "Fracture Mechanics of Through-Cracked Cylindrical Pressure Vessels", NASA TN D-3252, 1966.

26. Broek, D., *Elementary Engineering Fracture Mechanics*, Fourth revised ed., Kluwer Academic Publishers, Dordrecht, 1991, pp. 392-396.

27. Rogers, J. D., "An Investigation of the Damage Tolerance Characteristics of Graphite/Epoxy Pressure Vessels", TELAC Report 81-12, Massachusetts Institute of Technology, September, 1981.

28. Chang, S. G. and Mar, J. W., "The Catastrophic Failure of Pressurized Graphite/Epoxy Cylinders Initiated by Slits at Various Angles", *Journal of Aircraft*, Vol. 22, No. 6, June, 1985, pp. 462-466.

29. Sawicki, A. J., "Damage Tolerance of Integrally Stiffened Composite Plates and Cylinders", TELAC Report 90-17, Massachusetts Institute of Technology, September, 1990.

30. Saeger, K. J. and Lagace, P. A., "Effect of Localized Bending at Through-Flaws in Pressurized Composite Cylinders", *Journal of Aerospace Engineering*, Vol. 6, No. 4, October, 1993, pp. 381-393.

31. Ranniger, C. U., "Damage Tolerance and Arrest Characteristics of Pressurized Graphite/Epoxy Tape Cylinders", TELAC Report 91-11, Massachusetts Institute of Technology, June, 1991.

32. Harris, C. E. and Morris, D. H., "A Fractographic Investigation of the Influence of Stacking Sequence on the Strength of Notched Laminated Composites", *Fractography of Modern Engineering Materials: Composites and Metals, ASTM STP 948*, ASTM, 1987, pp. 154-173.

33. Lagace, P. A., Brewer, J. C., Varnerin, C. F., and Beaumont, M., "TELAC Manufacturing Course Class Notes", TELAC Report 88-4b, Massachusetts Institute of Technology, September, 1991.

34. Ranniger, C. and Forbes, K., "Air Bladder Manufacturing Process for Cylindrical Graphite/Epoxy Pressure Vessels", Internal TELAC Document, Massachusetts Institute of Technology, October, 1990.

35. Priest, S. M., "Set-Up Procedure for Cylinder Uniaxial Test Apparatus", Internal TELAC Document, Massachusetts Institute of Technology, 1994.

36. Vizzini, A. J., "An Efficient Algorithm to Characterize Stress/Strain Data Using Piecewise Linear Curves", *Journal of Testing and Evaluation*, Vol. 20, No. 2, March, 1992, pp. 126-131.

37. Lagace, P. A., Bhat, N. V., and Gundogdu, A., "Response of Notched Graphite/Epoxy and Graphite/PEEK Systems", *Composite Materials: Fatigue and Fracture, Fourth Volume, ASTM STP 1156*, ASTM, 1993, pp. 55-71.

38. Lagace, P. A. and Nolet, S. C., "The Effect of Ply Thickness on Longitudinal Splitting and Delamination in Graphite/Epoxy under Compressive Cyclic Load", *Composite Materials: Fatigue and Fracture, ASTM STP 907*, ASTM, 1986, pp. 335-360.

39. Simonds, R. A. and Stinchcomb, W. W., "Response of Notched AS4/PEEK Laminates to Tension/Compression Loading", *Advances in Thermoplastic Matrix Composite Materials, ASTM STP 1044*, ASTM, 1989, pp. 133-145.

Appendix A

Table A.1 $[0/\pm45/90]_s$ Coupon Data

Slit Length [mm]	Average Width [mm]	Average Thickness [mm]	Failure Stress [MPa]	H_c[a]	E_{11} [GPa]	ν_{12}
0.0	70.0	1.09	748	--	53.2	0.31
0.0	70.0	1.09	735	--	54.1	0.32
0.0	70.1	1.08	662	--	52.4	0.32
0.0	70.1	1.12	758	--	54.9	0.32
9.5	70.1	1.10	377	708	55.6	--
9.5	70.1	1.09	357	670	53.1	--
9.4	70.1	1.10	350	656	55.0	--
9.7	70.0	1.09	312	590	54.7	--
12.8	70.1	1.08	321	656	54.9	--
12.6	70.2	1.09	305	621	53.2	--
12.9	70.2	1.11	334	683	55.1	--
13.5	70.1	1.10	289	600	55.1	--
15.8	70.1	1.10	292	633	56.5	--
16.0	70.3	1.10	303	658	54.4	--
16.0	70.2	1.09	279	607	54.4	--
15.8	70.0	1.10	288	623	55.7	--
19.2	70.1	1.08	261	598	54.3	--
19.0	70.1	1.10	252	575	54.0	--
19.1	70.1	1.10	263	601	52.6	--
19.5	70.1	1.09	276	635	54.0	--

[a] units are $MPa*mm^{0.28}$

Table A.2 $[90/0/\pm45]_s$ Coupon Data

Slit Length [mm]	Average Width [mm]	Average Thickness [mm]	Failure Stress [MPa]	H_C[a]	E_{11} [GPa]
9.8	70.3	1.08	311	588	51.0
9.8	70.2	1.09	317	599	55.4
12.8	70.2	1.08	301	614	55.6
12.7	70.3	1.11	296	604	59.5
16.2	70.2	1.07	265	578	57.2
16.2	70.3	1.10	277	605	58.1
19.4	70.1	1.04	250	572	51.5
19.3	70.3	1.08	275	630	58.3

[a] units are $MPa*mm^{0.28}$

Table A.3 Biaxially Loaded Cylinder Data

Laminate	Slit Size [mm]	Average Length [mm]	Average Thickness [mm]	Failure Pressure [MPa]
$[0/\pm45/90]_s$	12.9	29.3	1.06	1.70
	25.4	29.8	1.07	1.21
$[90/0/\pm45]_s$	12.7[a]	29.7	1.07	2.03
	13.0	29.0	1.09	1.89

[a] indicates first tested cylinder

Table A.4 Uniaxially Loaded Cylinder Data

Laminate	Slit Size [mm]	Average Length [mm]	Average Thickness [mm]	Failure Pressure [MPa]
$[\pm 45/90]_s$	13.4	29.5	0.81	1.10
	25.3	29.9	0.81	0.68
	51.4	29.5	0.82	0.47
$[\pm 45/0]_s$	12.3	29.5	0.80	1.43
	25.5	29.5	0.81	0.85
	50.6	28.8	0.81	0.62
$[90/0/\pm 45]_s$	12.9	29.5	1.08	1.77
	25.5	29.6	1.10	1.08
	51.2	29.7	1.10	0.57

Table A.5 Experimental Hoop Moduli and Major Poisson's Ratios for Uniaxially Loaded Cylinders

Laminate	Slit Size [mm]	Failure Pressure [MPa]	Hoop Gage	E_{11} [GPa]	ν_{12}
$[\pm 45/90]_s$	13.4	1.10	1	27.6	0.34
			2	27.6	--
	25.3	0.68	1	25.3	0.30
			2	27.4	--
	51.3	0.47	1	29.2	0.34
			2	--	--
$[\pm 45/0]_s$	12.3	1.43	1	71.1	0.73
			2	64.9	--
	25.5	0.85	1	66.2	0.67
			2	65.2	--
	50.6	0.62	1	62.1	0.56
			2	66.5	--
$[90/0/\pm 45]_s$	12.9	1.77	1	59.7	0.33
			2	57.3	--
	25.5	1.08	1	56.4	0.31
			2	--	--
	51.2	0.57	1	59.4	0.34
			2	--	--